Mathematical and numerical modelling of high-speed rarefied flow of binary gas mixtures

Blaga Nenkova Todorova
BEng

Submitted in fulfilment of the requirements for the
Degree of Doctor of Philosophy

James Watt School of Engineering
College of Science and Engineering
University of Glasgow

August 2020

Abstract

Engineering applications that include flows with thermodynamic non-equilibrium and rarefaction effects require modelling with an increased level of physical detail. Practical problems often involve more than one constituent in the flow and therefore the capability to analyse gas mixtures is important. Extending kinetic model equations of the Bhatnagar-Gross-Krook (BGK)-type from a single-species gas to a gas mixture presents a number of difficulties. These are further pronounced when diatomic gas mixtures are considered, due to the addition of internal energy. This is a challenging research area and available models present a number of shortcomings.

This thesis presents new mathematical models for high-speed flow applications with moderate levels of rarefaction. The novel kinetic models are derived for mixtures of binary gases: two new models for mixtures of monoatomic gases and a model for mixtures of diatomic gases are introduced. The novel kinetic models are shown to have good mathematical properties and demonstrate significant advances over models in the literature. Transport properties in the continuum limit are obtained through the Chapman-Enskog (CE) type expansion and shown for each model. The models account for separate species-mean velocity such that the species diffusion and velocity drift are accurately represented. For mixtures of monoatomic gases a Shakhov-based model and an Ellipsoidal-Statistical (ES)-based model are derived. The main advantage of the newly introduced models is the recovery of three correct transport coefficients in the hydrodynamic limit and as a result having a correct Prandtl number for the mixture. For the diatomic mixture model, the key improvement is the inclusion of separate species velocities, species- translational, -rotational and -vibrational temperatures and three-step relaxation process.

Furthermore, the new models are numerically evaluated for a range of high-speed flows with strong thermodynamic non-equilibrium. Validation and good agreement with results from the Boltzmann model and the direct simulation Monte Carlo (DSMC) demonstrates the models' capabilities and limitations. A parametric study shows the variation of flow properties under varied free-stream conditions. A numerically efficient gas-kinetic scheme (GKS) based on the monoatomic Shakhov-based mixture model is also presented and the results show good accuracy, while reducing the required computational time. Overall, the newly-introduced gas mixture models demonstrate promising computational results for relevant applications. The current work can form the basis for further work on improved kinetic modelling of high-speed non-equilibrium flows.

List of Publications

In Journals

- B.N. Todorova and R. Steijl, "Derivation and Numerical Comparison of Shakhov and Ellipsoidal Statistical Kinetic Models for a Monotoatomic Gas Mixture", April 2019, European Journal of Mechanics - B/Fluids, DOI: 10.1016/j.euromechflu.2019.04.001

- B.N. Todorova and R. Steijl, "Comparative Study of Discrete Velocity Method and Gas-Kinetic Method for Binary Gas Mixture", Journal of Thermophysics and Heat Transfer,Aug 2019, Journal of Thermophysics and Heat Transfer,DOI: 10.2514/1.T5741

- B.N. Todorova, C. White and R. Steijl, "Numerical Evaluation of Novel Kinetic Models for Binary Gas Mixture Flows", Jan 2020, Physics of Fluids, DOI: 10.1063/1.5134040

Journal Articles Under Review

- B.N. Todorova, C. White and R. Steijl, "Modelling of Nitrogen and Oxygen Gas Mixture with a Novel Diatomic Kinetic Model", AIP Advances, Aug 2020, DOI: 10.1063/5.0021672

In Conference Proceedings

- B.N. Todorova, C. White, R. Steijl, "Discrete-Velocity Simulations of High-speed Flows Based on Binary Gas Mixture Kinetic Models", Proceedings of 31st International Symposium of Rarefied Gas Dynamics, AIP Publishing, (peer-reviewed and accepted)

- B.N. Todorova and R.Steijl, "A Comparative Study of a Discrete Velocity Method and a Gas-Kinetic Method for a Binary Gas Mixture", 2019, Proceedings of AIAA Scitech 2019 Forum, DOI: 10.2514/6.2019-1052

Presentations without Proceedings

- B.N. Todorova and R.Steijl, "Modelling of Non-equilibrium Hypersonic Flow Using Novel Gas-kinetic Methods", 30th Scottish Fluid Mechanics Meeting, Glasgow, UK, May 2017
- B.N. Todorova and R.Steijl, "Kinetic Models for a Binary Mixture of Monoatomic Gases", Methods and Models on Kinetic Theory Workshop, Porto Ercole, Italy, June 2018

Contents

List of Tables

List of Figures

Nomenclature

Latin symbols

a	spatial derivative of the Maxwellian distribution function
a	speed of sound
A	temporal derivative of the Maxwellian distribution function
A^*_{12}	non-dimensional coefficient
c_p	specific heat at constant pressure
c_V	specific heat at constant volume
d	molecular diameter
D_T	thermal diffusion coefficient
e	internal energy
f	gas distribution function
f^M	Maxwellian gas distribution function
f^0_s	initial non-equilibrium gas distribution function
f^{eq}	equilibrium gas distribution function
$f_s(x_{i+\frac{1}{2}}, t, u_i)$	time-dependent gas distribution function at cell face
$\underline{F}_{i+\frac{1}{2}}$	numerical flux of macroscopic variables at cell face
F_s	species equilibrium function, representing G_s, G^{Sh}_s, G^{ES}_s
g	equilibrium gas distribution function
g^{Sh}	Shakhov equilibrium gas distribution function
g_s & h_s	species reduced distribution functions
G_s & H_s	species reduced distribution functions (Chapter 5)
G_s	Modified Maxwellian distribution function per species s
G^{Sh}_s	Shakhov Modified distribution function per species s
H	H-functional
i	quantised level of energy
I	rotational energy
j	cell
$\underline{j}_s$	mass flux
k	Boltzmann's constant

Kn	local Knudsen number
L_{ref}	characteristic length
m	molecular mass
m	equilibrium distribution functions
m_{mix}	mass of the gas mixture $m_{mix} = \rho/n$
m_2/m_1	mass ratio between species 2 and 1
M	Mach number
M	reduced equilibrium functions
n	gas number density
n_s	species number density
n_1/n	concentration of light species in the gas mixture
N_2	nitrogen molecule
O_2	oxygen molecule
p	pressure
Pr	Prandtl number
Pr^*	target Prandtl number
Pr_{mix}	gas mixture Prandtl number
q_D	Dufour effect
q_x	heat flux in the x-direction
q^{corr}	heat flux correction
Q	collision term
R	cylinder radius
R	specific gas constant
S_s	species source term in continuum flow
S	entropy $S = -kH$
ΔS	small area
t	time
Δt	time step
T	gas temperature
T_∞	free-stream temperature
$\hat{T}$	target translational gas temperature
T_{ref}	reference gas temperature
u, v, w	molecular velocity components
$\underline{u}_0$	mean gas velocity
$\underline{u}_s$	species mean velocity
$\underline{u}_s^{(g)}$	modified species velocity
u_{ref}	reference velocity (most probable speed) $u_{ref} = \sqrt{2kT_r/m_1}$
u_{min} & u_{max}	velocity bounds for DVM

Δu	velocity step
ΔV	small volume
$\underline{W}_j$	vector of conserved macroscopic variables in cell j
Z_r	rotational collision number
Z_v	vibrational collision number

Greek symbols

β	mass ratio between species $\beta = m_2/m_1$
γ	specific heat ratio
δ	vibrational degrees of freedom
$\mathscr{D}_{sr}$	binary diffusion coefficients $r \in \{1,2\}$ and $r \neq s$
ε	small parameter of the order of the Knudsen number
η	relaxation parameter, equalizing the species mean velocities
θ_v	characteristic temperature for vibrational excitation
$\underline{\underline{\Theta}}$	velocity tensor (ES model)
κ	thermal conductivity
λ	mean free path
λ_{11}, λ_{22}, etc.	components of the tensor $\underline{\underline{\Lambda}}$
$\underline{\underline{\Lambda}}$	temperature tensor (ES model)
μ	gas viscosity
ν	collision rate
ν_{ES}	ES-based relaxation parameter where $Pr = 1/(1-\nu_{ES})$
ω	coefficient in viscosity power law model
π	3.14159
ρ	gas density
$\sigma(\mu_B)$	normal stress due to bulk viscosity
τ	relaxation time $\tau = 1/\nu$
$\hat{\tau}$	non-dimensional relaxation time $\tau = \varepsilon\hat{\tau}$
τ_{xx}	normal stress
$\underline{\Psi}$	collision invariants

Acronyms

AAP	Andries, Aoki and Perthame
BGK	Bhatnagar- Gross- Krook
CE	Chapman- Enskog
CFD	Computational Fluid Dynamics
CFL	Courant–Friedrichs–Lewy condition
CL	Characteristic Length
CPU	Central processing unit
deg	degrees
DoF	Degrees of Freedom
DSMC	Direct Simulation Monte Carlo
DUGKS	Discrete Unified Gas-Kinetic Scheme
DVM	Discrete Velocity Method
ES	Ellipsoidal Statistical
FVM	Finite Volume Method
GBE	Generalized Boltzmann Equation
GKS	Gas Kinetic Scheme
HS	Hard-sphere
LHS	Left Hand Side
MD	Molecular dynamics
MEMS	Microelectromechanical systems
МФС	Multi Physics Code
NS	Navier-Stokes
RHS	Right Hand Side
TVD	Total Variation Diminishing
UGKS	Unified Gas-Kinetic Scheme
VDF	Velocity Distribution Function
WCU	Wang-Chang-Uhlenbeck
w.r.t	with respect to
1D	one-dimensional

Subscripts

$()_j$	cell
$()_{diff}$	difference
$()_{ref}$	reference value
$()_r$	rotational
$()_s$	species variables
$()_t$	translational
$()_{tr}$	translational and rotational
$()_v$	vibrational
$()_\infty$	free-stream
$()_0$	gas mixture
$()_1$	species 1
$()_2$	species 2
$()_-$	pre-shock value
$()_+$	post-shock value
$()\|_m$	at discrete velocity with index m

Superscripts

$()^{eq}$	Equilibrium
$()^{ES}$	Ellipsoidal Statistical
$()^{M}$	Maxwellian
$()^{n}$	time step n
$()^{rot}$	Rotational
$()^{Sh}$	Shakhov
$()^{tran}$	Translational
$()^{vib}$	Vibrational
$()^0$, $()^1$, $()^2$	0-th, 1-st, 2-nd order expansion (CE)

Acknowledgements

First and foremost, I would like to thank my supervisor Dr. Rene Steijl for his help, guidance and vast technical knowledge. His door was always open for all the questions and ideas I brought to him. I am also grateful to my second supervisor Prof. George Barakos for the provided advice and discussions and to Dr. Mark Woodgate for the computational support throughout this process. I would like to thank all the members of the Aerospace PhD lab for creating a positive and friendly work environment. A special mention to Ross Higgins with whom I started and shared this journey.

The financial support for this project was provided by the University of Glasgow and the James Watt School of Engineering and is gratefully acknowledged. The opportunity to use EPSRC funded ARCHIE-WeSt High Performance Computer (www.archie-west.ac.uk). EPSRC grant no. EP/K000586/1 is also acknowledged. I would like to thank the Zonta Foundation for the Amelia Earhart Fellowship.

In addition, I would like to acknowledge the University Volleyball Club, my coach Tom Rooney and all my teammates for all the fun moments we had together. Moreover, I would like to thank my closest friends- Marina, Nikoleta, Pavlina and Vilyana for their love, understanding and patience during these years.

Above all, a massive thank you to my family in Bulgaria and Austria, to my parents Meri and Nenko, to my brother Martin and to mi Número Uno for supporting me and helping me in every challenge I faced. Without you I could not have gone through this journey. I will always be there for you!

Declaration

I certify that the thesis presented here for examination for a PhD degree of the University of Glasgow is solely my own work other than where I have clearly indicated that it is the work of others (in which case the extent of any work carried out jointly by me and any other person is clearly identified in it) and that the thesis has not been edited by a third party beyond what is permitted by the University's PGR Code of Practice.

I declare that the thesis does not include work forming part of a thesis presented successfully for another degree.

I declare that this thesis has been produced in accordance with the University of Glasgow's Code of Good Practice in Research.

I acknowledge that if any issues are raised regarding good research practice based on review of the thesis, the examination may be postponed pending the outcome of any investigation of the issues.

August 2020

.....

Blaga Nenkova Todorova

2024108

Chapter 1

Introduction

1.1 Motivation

Continuum flow modelling dominates industrial aerodynamics [1]. Computational fluid dynamics (CFD) based on the Navier-Stokes (NS) equations is traditionally used for aeronautical applications. However, advances in engineering sciences have led to an increasing amount of complex products in all length scales: from nanoscale devices to spacecrafts. Many of these applications involve a rarefied gas environment.

In order to identify if the flow is in the continuum or rarefied regime, the concept of characteristic length scale is introduced. This means that a consideration of the distance between molecules is taken in reference to the characteristic length (CL) of the flowfield considered. The ratio of these two lengths is an important quantity in rarefied gas dynamics and is known as Knudsen number, which is defined in more detail in Section 1.3.4. For example, an airliner cruising at approximately $10-11$ km altitude will have an average distance between molecules of 10^{-6} m [10]. A typical characteristic length of an airliner is the chord of the wing which is of the order of meters. Therefore, at this altitude and at that characteristic length, the number of molecules and collisions is large enough to consider the flow a continuum fluid. Another example of aerospace interest is the Space Shuttle orbiter. At reentry it passes from altitudes where the distance between particles is of the order of $20,000$ m (at 300km altitude) to 0.3 m (at 100km) and then to sea level with distance of $0.6\text{x}10^{-7}$ m between molecules [1], [10]. If the characteristic length of the Space Shuttle is chosen to be the fuselage length, the overall flow can be considered continuum below 100 km. However, a continuum assumption is not accurate when localized effects need to be considered, e.g. for the flow at the nose, flaps or trailing edges of the shuttle, a more appropriate CL is to be considered, e.g. the nose radius of the shuttle or the flap chord. The number of molecules present in these regions are so low that continuum concepts cannot be applied and rarefaction effects are considered. The characteristic length is selected for each individual test case and is an important variable. Moreover, due the to low number of molecules a low number of collisions occur. Thermodynamic equilibrium is established in a gas through

molecular collisions and a reduced collision rate means the flow requires more time to relax to equilibrium than in a higher density environment. Non-equilibrium thermodynamic effects are to be considered. These effects will be described in detail in the theoretical background section. Conventional computational methods (e.g. modern-day CFD methods) are based on the Navier-Stokes equations and are limited to the continuum limit, i.e. with the mean-free path between successive molecular collisions much smaller than the characteristic length scales of the flow. The Navier-Stokes equations stop working at a Knudsen number (ratio between the mean-free path and CL) around 0.001, which can be extended upto 0.1 when applying the slip boundary conditions [3]. Classical solvers based on continuum equations find a the solution for the flow-field macroscopically: by considering changes in pressure, density, velocity, etc. They are based on the concept of mass, momentum and energy conservation for the fluid. In rarefied gas flows this type of modelling is not sufficient and is inaccurate.

Furthermore, the failure of the Navier-Stokes equations is further pronounced for high Knudsen number flows combined with high Mach number flows, e.g. shockwaves will create larger deviation from thermal equilibrium. Therefore, for some practical applications a more detailed level of modelling is required.

An important first question to pose is when rarefaction effects actually appear. It occurs in one of two occasions. The first is when the characteristic length of the device is reduced to the distance between particles while air density is close to sea-level conditions, e.g. nanoscale devices. The second occasion is caused by the opposite effect: when the distance between molecules is increased to the characteristic length of a macroscopic device, e.g. a reduction in the density in the upper stages of the atmosphere during a spacecraft launch or re-entry. Matter on the microscopic level is composed of atoms and molecules, which are in constant motion, and the most detailed level modelling means inspecting the individual movement of each particle. Such modelling is governed by molecular dynamics (MD) and suitable applications are e.g. devices on the micro- and nanoscale and also modelling of liquids and liquid-vapor mixtures. This is a very detailed approach and is very accurate for all flow regimes. However the computational time (CPU) and memory required limit its applicability to very small flow domains so that number of particle remains acceptable for MD simulations. For gas flows, MD is computationally inefficient due to the combination of the small time-steps required to model the collisions and the relatively long macroscopic time scales at which flow changes take place. Most practical flows include a wide range of sizes of the flow domain and combine regions of both continuum and rarefied flows, often referred to as transitional regime. Therefore, accounting for each particle movement and collision is computationally unfeasible for most engineering applications due to excessively large number of particles that needs to be considered. The direct simulation Monte Carlo (DSMC) is a statistical approach simulating a large number of particles and their behaviour, which will be discussed in more detail later in this Chapter. The link between molecular dynamics and classical hydrodynamics is provided by kinetic theory of gases. It is capable

of modelling the motion of all particles, based on probability and statistical physics. What kinetic theory does is that it considers the behaviour of particles on the microscopic level to find a solution for the overall behaviour of the gas on the macroscopic level [2].
Kinetic modelling has been widely studied, due to the increasing number of possible applications. The focus of this thesis is on applying kinetic modelling to aerospace applications, more specifically on vehicles experiencing rarefied flow conditions. Examples include supersonic and hypersonic vehicles, e.g. SR-71, X-15, X-51 etc., shown in Fig. (1.1). These vehicles will encounter different levels of rarefaction related to their corresponding flight altitude. Note that the cruising altitudes of SR-71 and X-51 are lower in comparison to X-15 due to the requirements imposed by their air-breathing engine.The thermodynamic non-equilibrium effects will vary, but chemical reactions are unlikely. The flow around these vehicles at high altitudes (above 20 km),

(a) SR-71

(b) X-15

(c) X-51

Figure 1.1: Supersonic and hypersonic aircraft: applications of kinetic models

which is the domain of hypersonic vehicles, can be characterised as partly continuum with regions of rarefaction. Therefore, the non-equilibrium effects are localised to parts of the vehicle. Modelling this flow is a challenging task, since computational modelling requires code coupling or the development of a new efficient methodology for multi-scale problems. The capability to model the flow around these vehicles accurately is vital to their design and development. A rocket launched from Earth and a re-entry vehicle coming back to Earth (Fig. 1.2) are examples

of applications where all regimes are experienced: from continuum through transitional to free-molecular flow. Such vehicles experience equilibrium thermodynamics as well as high levels of non-equilibrium thermodynamics, including high levels of chemistry in the flow. These flows are often solved by coupled solvers, e.g. [11–14], while alternatively different techniques try to build a single solver that models the whole spectrum of regimes, e.g. [15, 16]. Kinetic models provide the basis of many of these solvers. Therefore, all challenges that kinetic models face, e.g. including chemical reactions, are inherited by the solvers.

(a) Rocket Launch

(b) Capsule

Figure 1.2: Spacecrafts: applications of kinetic models

Outside the scope of aerospace science (Fig. 1.3), other engineering applications of kinetic theory include nanoscale devices, e.g. microelectromechanical systems (MEMS) are being used as biochips in biotechnology, pressure sensors in medicine, accelerometers and gyroscopes in inertial sensing, etc. These are only a few of many examples of nanodevices and the possible

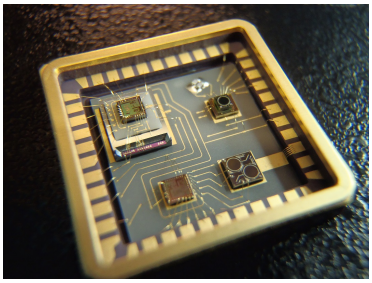

(a) MEMS

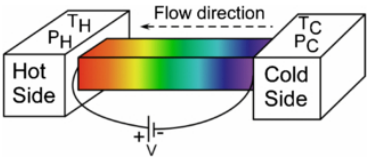

(b) Knudsen Pump

(c) Plasma

Figure 1.3: Engineering devices: applications of kinetic models

applications. The current industry of MEMS has been identified as one of the most promising of the century with the prediction of market value reaching £105.8 billion by 2026 [17]. Other common uses of kinetic modelling study is utilised for flows including plasmas, gas purification, Knudsen pumps, etc. Kinetic models can go a step further, outside of engineering applications, with capabilities in social and natural sciences (Fig. 1.4). Models are used for radiotherapy, bacteria, traffic flow calculations, opinion formation, financial and economic market applications, etc. see for example [18–21] and references therein.

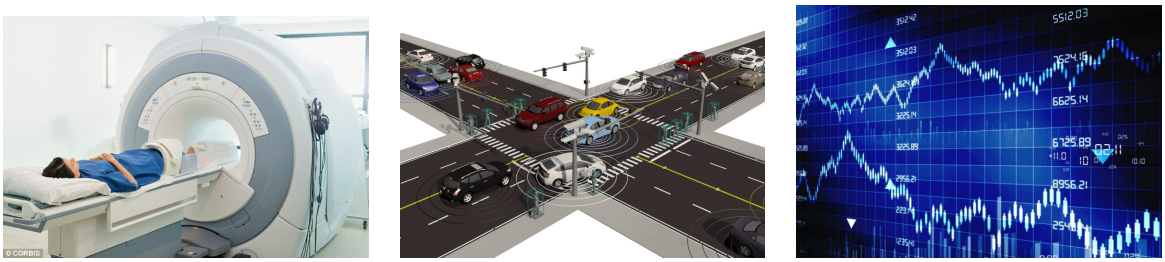

(a) Radiotherapy (b) Traffic Flow (c) Financial Market

Figure 1.4: Social and natural sciences: applications of kinetic models

In summary, since kinetic models consider the microscopic level in order to model macroscopic properties, many systems that require statistical analysis of large data can utilise such modelling. There are many applications in numerous disciplines, some of which were detailed in this section, but many more can be found in the literature. In this thesis the focus is on aerospace-related applications, in particular high-speed flows.

1.2 Scope of the Thesis

The goal of this thesis is to propose new modelling solutions for flows consisting of mixtures of gases, since these are of practical interest. For aerospace engineering that gas mixture is comprised of diatomic molecules. However, due to the challenging nature of kinetic modelling, the majority of available models in the literature is for a single-species monoatomic gas.
Therefore, the scope of this thesis is to create and apply numerically a new kinetic model for a gas mixture comprised of diatomic molecules. This will allow a significant improvement over existing models. The model is to posses good mathematical properties (i.e. continuity, compatibility, positive macroscopic fields, etc.) and be consistent with other models and kinetic theories in the literature. Furthermore, beyond defining and proving the model mathematically, the model is to be applied numerically in order to test its capabilities.
All of the above criteria will be addressed and analysed in this thesis. A multi-step approach is applied and is described in greater detail in the objectives of the thesis, which are presented at the end of this chapter. Before that, the next sections will briefly review some of the vital

theoretical definitions forming the basis of high-speed kinetic modelling and also provide an extensive review of the available kinetic models and their capabilities.

1.3 Theory

This theoretical section briefly reviews basic concepts that are well-established and a full account can be found in standard books on hypersonic flight and kinetic modelling, e.g. [22], [1], [23], [2], [24] etc. It presents the background of this thesis and is an important stepping stone in the literature survey.

1.3.1 High-speed Flow Properties

In aerodynamics the velocity of a fluid is often used to define the flowfield and it's main properties. It is often expressed with a non-dimensional quantity: the Mach number, defined as the magnitude of the gas velocity $\underline{u}_0$ divided by the local speed of sound a as: $M = \frac{|u_0|}{a} = \frac{|u_0|}{\sqrt{\gamma RT}}$, where γ is the ratio of specific heats, R is the gas constant and T the temperature of the gas. Even though the definition of a Mach number is a well-established concept, for cases where the fixed γ assumption is not valid or R is defined for a mixture, the definition of the speed of sound a and consequently the Mach number definition is a more involved process.
The different flow regimes are characterised according to the Mach number: from subsonic to hypervelocity regimes. In this thesis the focus is on supersonic and hypersonic flows. The normal shock wave is the simplest form of non-equilibrium phenomena and are an essential part of many high-speed flows.Through a shock wave the variables defining the flow field, i.e. density, velocity, pressure, temperature etc., change drastically in a short period of time. The change in variables though the shock is solely dependent on the free-stream Mach number and expressed through the Rankine-Hugoniot relationship [22]. Note these equations are strictly valid for ideal gases. Increasing the Mach number leads to a higher jump in the flow conditions with the limiting case for $M_- \to \infty$ resulting in:

$$\frac{\rho_+}{\rho_-} = \frac{(\gamma+1)}{(\gamma-1)} \qquad \frac{u_+}{u_-} = \frac{(\gamma-1)}{(\gamma+1)} \qquad \frac{T_+}{T_-} \to \infty \tag{1.1}$$

The Rankine-Hugoniot equations are used to initialize the flow in the normal shock simulations in this thesis for monoatomic gases. The equations are valid only for calorically perfect gases and to accommodate the jump conditions for a diatomic gas with excited vibrational degrees of freedom and with a variable γ, an iterative procedure, detailed in [1] is required.
When a high-speed flow meets a solid surface an oblique or bow shock is created. Additional complexity is added by the interactions between the flow and the wall of the solid in the boundary layer. In contrast to slower speeds, boundary layers thickens. This is due to the higher kinetic energy inducing a higher temperature close to the wall, which in turn propagates viscous effects.

It is inherent to high-speed flows to have a thin shock layer (bow and oblique shocks move close to the body) and the higher the Mach number, the closer the shock wave lies to the surface [1].

1.3.2 Molecular Motion & Energy Modes

Clearly, the definition of the free-stream Mach number and the flowfield variables are dependant on the specific heat ratio γ, which is a function of the excited degrees of freedom of the considered gas. For air the focus is on nitrogen and oxygen which are both diatomic molecules that can be modelled using a "dumbbell" model [1], i.e. two spheres connected with a spring. There are four types of motion for a molecular gas that also correspond to the four types of energy, comprising the total energy of a molecule: translational, rotational, vibrational and electronic (shown in Fig. 1.5). Energy is quantised and the different types of energy have different spacing between each quantised level. How many levels of energy levels are populated depends on how excited that state is, which is directly related to the temperature of the gas [25]. The transla-

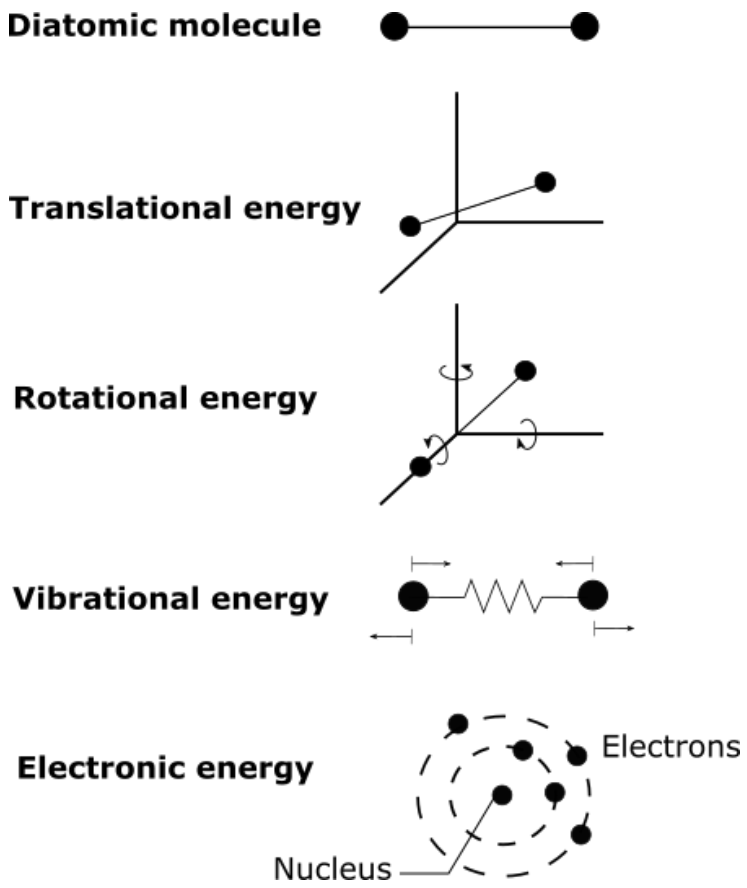

Figure 1.5: Modes of energy (adapted from Anderson [1])

tional kinetic energy is based on the movement of the molecule in the three space coordinates and corresponds to three degrees of freedom. The quantised levels of translational energy are so close to each other that it is considered a continuous range. The rotational energy is due to the rotational motion of the molecule. The number of degrees of freedom for a diatomic molecules

is two, since the rotation along the axis of the molecule is ignored, since the moment of inertia in the third direction is negligible. The spacing between rotational energy levels is bigger in comparison to the translational energy. However, for most aerospace applications the temperature of the gas is high enough to assume the rotational energy fully excited and treat it as continuous. Vibrational energy is due to the movement of the atoms of the molecule with respect to each other as if they are connected by a spring [1]. Two degrees of freedom are associated with this energy type for diatomic molecules due to the kinetic energy of the moving atoms and the potential energy of the intermolecular forces.
The most commonly used model for these forces is demonstrated by the harmonic oscillator, while the anharmonic oscillator represents a more realistic modelling method. The internal potential energy is shown to depend on the distance between the atoms of the molecule. The harmonic oscillator is an idealised case and is shown as an infinite parabola (see Fig. 1.6). In

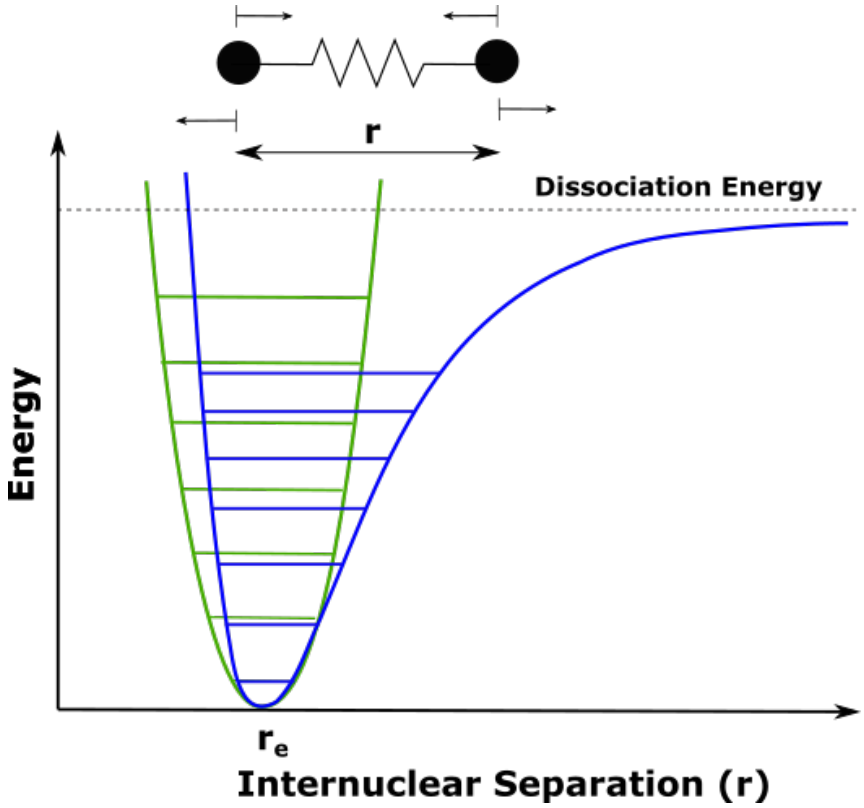

Figure 1.6: Potential energy with respect to distance between atoms in a vibrating molecule (adapted from Vincenti and Kruger [2])

reality there is a limiting energy at which dissociation occurs when the harmonic oscillator will fail to provide accurate results. The corresponding temperature associated with the dissociation of oxygen molecules starts at approximately $2500K$ and for nitrogen at around $4000K$, as demonstrated in Fig. (1.7). The harmonic oscillator is often used since the provided results are accurate for most cases, in which the temperature is sufficiently low that no chemical reactions occur. It is Therefore, used in the derivation of the diatomic kinetic model in this thesis.

Electronic energy is an internal energy mode and and its detailed modelling is essential for very high temperatures as shown in Fig. 1.7, conditions that occur for example in re-entry flows. However, since the quantised levels are so spaced out and for the flow fields of interest (su-

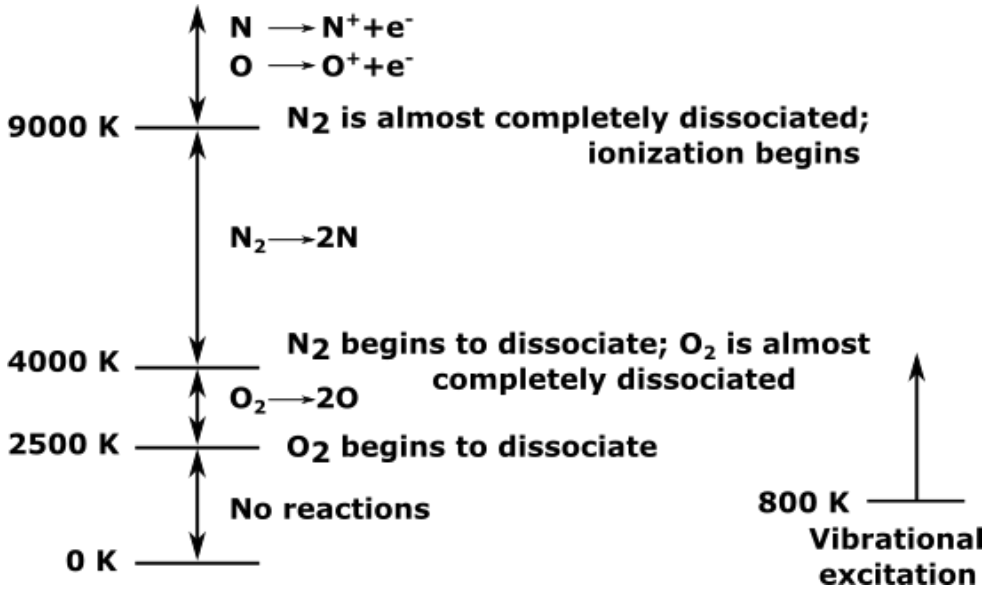

Figure 1.7: Temperature range for non-reacting, vibrational, dissociation and ionization processes (adapted from Anderson [1])

personic and hypersonic) the gas temperatures considered are unlikely to excite any levels of electronic energy beyond the ground state level, it will not be considered in this thesis.
Clearly, monoatomic gases posses only translational and electronic energies, since at least two atoms in a molecule are required for rotational and vibrational degrees of freedom to be possible. Further, electronic energy is often neglected, as described previously. Such monoatomic flows are referred to as inert and only the translational motion is accounted for. However, for inert diatomic gases, the translational, rotational and vibrational temperatures are to be accounted for. The rotational and vibrational DoF are referred to as internal DoF. Rotation is fully excited for aerospace applications and the degrees of freedom are constant and equal to 2. However, the vibrational energy is excited above 800K for air (Fig. 1.7). This means for some applications it will not be excited and for others it can be partially excited. The degrees of freedom of vibrational motion are a function of the gas temperature. It is important to note that vibrational energy cannot be treated like translational or rotational, since a 'fully excited' vibrational state will dissociate the molecule before it is reached. The number of degrees of freedom are directly related to the amount of energy through the characteristic specific heats c_p and c_V, with $c_p = c_V + k/m$.

$$c_V^{tran} = \frac{3}{2}\frac{k}{m} \qquad c_V^{rot} = \frac{2}{2}\frac{k}{m} \qquad c_V^{vib} = \frac{\delta(T)}{2}\frac{k}{m}, \tag{1.2}$$

where $\delta(T)$ corresponds to the degrees of freedom excited by vibration, which typically is a non-integer number and depends on the temperature. The total c_V is the sum of the different

contributions and for diatomic vibrationally excited gas is $c_V = c_V^{tran} + c_V^{rot} + c_V^{vib}$. Figure 1.8 demonstrates the activation of rotational and vibrational degrees of freedom with temperature for a diatomic molecule. The activation temperature for rotation is very low and can easily be reached for nitrogen (2.9K) and oxygen (2.1K) [2], which are the two species of main interest to aerospace engineering. It is considered very similar, if not the same for both gases. However, it is different for vibrational excitation. There is no single temperature after which a gas is considered fully excited. Instead the level of excitation is dependent on the temperature of the gas as is the number of degrees of freedom. This can be observed in the figure as well, where the process of vibrational excitation is a slope and there is no such regime of a vibrationally fully excited gas.

Since γ is the specific heats ratio $\gamma = c_p/c_V$, it is fixed for a monoatomic gas,i.e. $\gamma = 5/3$ and

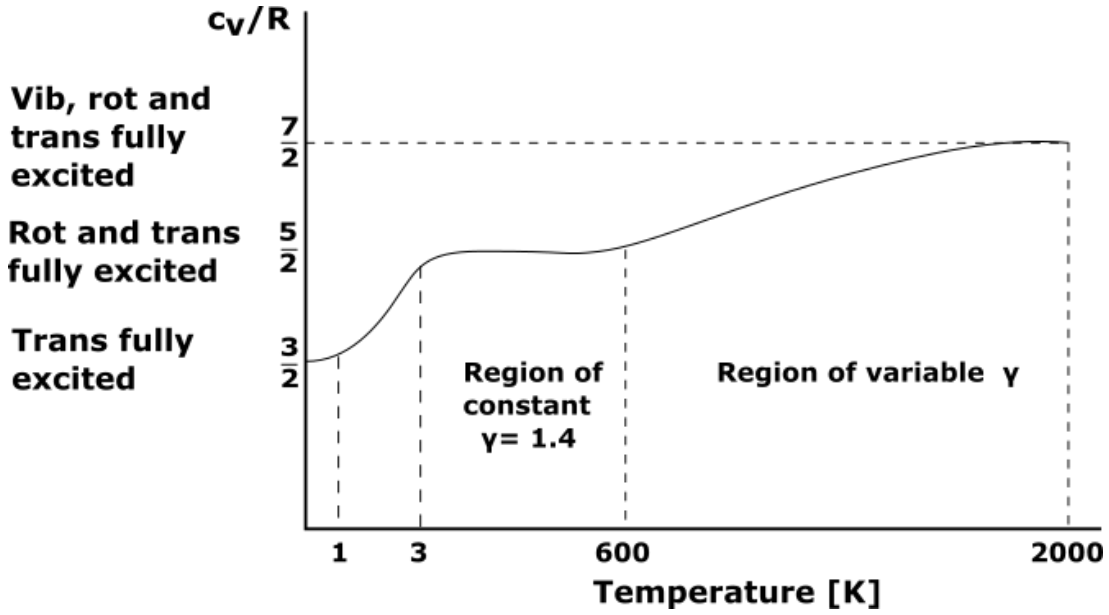

Figure 1.8: Specific heat at constant volume c_v for different temperatures (adapted from Anderson [1]).

for a diatomic gas with only translational and rotational energies fully excited, i.e. $\gamma = 7/5$. It is more complex when the vibrational energy is excited since γ is no longer a constant and depends on the temperature of the gas. In that case the expression becomes:

$$\gamma = \frac{7+\delta(T)}{5+\delta(T)} \tag{1.3}$$

Diatomic dissociation and ionization occur at different temperatures for oxygen and for nitrogen. Characteristic temperatures for chemical reactions are detailed in Fig. 1.7 and discussed in detail in the literature [1], [23], [25], etc. They are beyond the scope of this thesis.

1.3.3 Non-equilibrium Thermodynamics

The changes of pressure, temperature and composition of a gas follow the principles of thermodynamics. These fundamental principles are linked to the assumption that a given system is in equilibrium. While most systems have a tendency towards equilibrium, it does not mean that using the equilibrium assumption is an accurate representation of said systems. Systems which are in a non-equilibrium state have irregular and time-dependent patterns, which are often hard to predict.

In the context of high-speed aerodynamics, it is important to note that high-temperature effects (vibrational excitation, chemical reactions) do not necessarily mean the flow is non-equilibrium. If these effects occur quickly, i.e. for a length of time much smaller relative to the fluid convecting through the flowfield, we have vibrational and chemical equilibrium flow [1]. At the same time, even though the flow is in equilibrium, it is no longer calorically perfect, since the constant γ assumption no longer holds. In Fig. 1.9 the difference between calorically perfect gas and a gas in vibrational and chemical equilibrium is demonstrated by comparing the shock-layer temperature for a number of re-entry vehicles at different re-entry velocity [1].

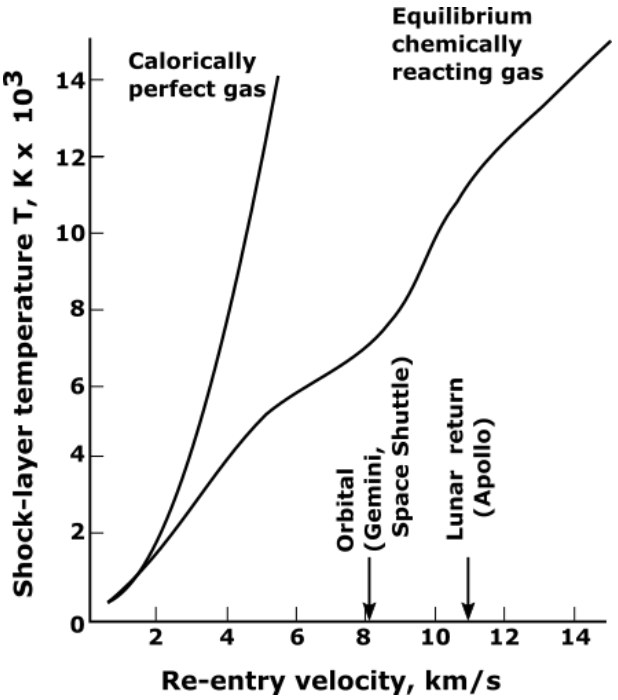

Figure 1.9: Velocity-amplitude map, demonstrating the importance of accounting for vibrational excitation, dissociation and ionization (adapted from Anderson [1])

Next, it is important to establish when a flow is out of equilibrium. The length of time for thermodynamic processes to take place is connected to the number of molecular collisions, which redistribute the internal energy between the molecular states. The number of required collisions for each type of molecular process to reach equilibrium differ, with the translational and rotational needing significantly less collisions and having shorter characteristic times [2]. Also,

the equipartition of energy principle guarantees that no matter the cause of energy exchange, the equilibrium state of the gas will split the energy equally between all degrees of freedom. If translational energy is excited, the rotational and vibrational energies will slowly increase (with different relaxation rates) to find a balanced state. The state in which these energies are not balanced and the corresponding temperatures are not equalised is referred to as thermodynamic non-equilibrium. Flows at low density, experiencing high-temperature effects (vibrational excitation and chemical reactions) will have extensive non-equilibrium regions, e.g. re-entry vehicles for aerospace applications.
Furthermore, the non-equilibrium that occurs related to the translational and rotational molecular motions is typically due to large gradients in the flow (e.g in a boundary layer or a shock wave), rather than low collision frequency. Examples of such transport effects due to molecular motion are viscous stresses, heat conduction and bulk viscosity, which are discussed in great detail in Section 1.3.11.
It is clear from this discussion that accurate modelling of non-equilibrium processes needs to account for the different energies, dependent on the different types of temperatures. If a single temperature is used to describe a diatomic gas, the gas temperature is significantly overestimated [25]. Therefore, mathematical models with different temperatures and relaxation rates for each type of molecular motion are of great interest. Moreover, flow rarefaction is in important factor when establishing the length of time for sufficient collisions to occur to achieve equilibrium and will be discussed next.

1.3.4 Rarefied Flow

A number of key aspects of high-speed flows were summarized previously. It is important to note that flow rarefaction is not one of them. The typical domain for most classes of hypersonic vehicles is the outer region of the atmosphere, where low - density effects occur [1]. These effects are important and determine the choice of modelling equations.
Figure 1.10 summarises the different levels of modelling options and the laws that govern them. A gas flow can be modelled on any of these levels. The macroscopic level regards the flow as a continuum and a classical CFD solver considers the changes in the macroscopic variables: pressure, density, velocity, temperature, etc. On a microscopic level matter is composed of atoms and molecules, which are in constant motion [2] and are defined by the three dimensions in physical space and three dimensions in velocity. Accounting for their individual movement is a subject of molecular dynamics [23]. The middle ground between continuum flow and individual particle modelling is governed by the laws of kinetic theory. It is based on statistical mechanics, which is subject to probability theory and fluctuations around the average. Kinetic theory of gases considers the behaviour of particles on the microscopic level to find a solution for the macroscopic properties of the flow. As such kinetic theory governs the mesoscopic level of modelling, illustrated in Fig. 1.10. The variables in a flow are nothing more than a macroscopic

reflection of microscopic molecular motions [2]. These variables are local averages or statistical moments over all molecules and that leads to defining density, velocity, pressure, etc. The particle collisions cause molecules to change direction and velocity magnitude and as a result to exchange momentum and energy and Therefore, cause change in the macroscopic properties.

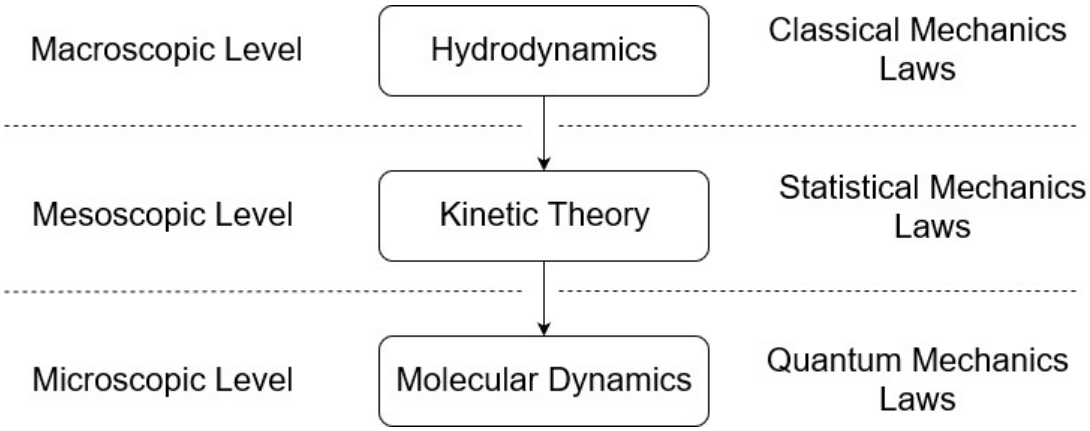

Figure 1.10: Levels of flows modelling

Continuum flow theory is based on the principle that particles collide very often and equilibrium in a gas is reached quickly relative to macroscopic changes of the flow and typically during this relaxation a particle travels a couple of nanometres [26]. This is induced by the molecules being in close proximity to each other. However, at lower densities the distance a molecule travels before colliding with another increases, which delays equilibration of gas properties through the flow. It is evident that the distance between molecules is crucial in defining the gas flow modelling level (Fig. 1.10) and the laws that govern it. The mean free path of a molecule is used to determine the density of a gas. It is defined as the average distance between successive collisions [2] and it is illustrated in Fig. 1.11.

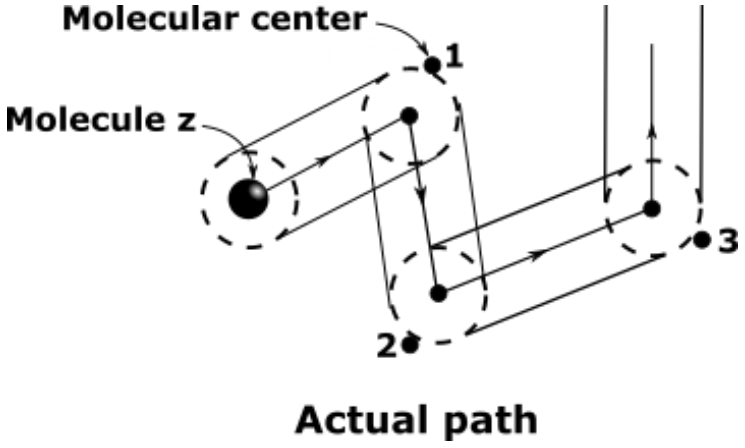

Figure 1.11: Mean free path illustration (adapted from Vincenti and Kruger [2])

For the hard-sphere (HS) molecular model, the expression for the mean free path λ is in the

form:

$$\lambda = \frac{1}{\sqrt{2}\pi d^2 n}, \tag{1.4}$$

where d is the molecular diameter and n the number density of the gas. Based on the mean free path, the Knudsen number Kn is commonly used to assess the level of rarefaction in a gas, where the non-dimensional Knudsen number is defined as: $Kn = \lambda / L_{ref}$ with L_{ref} the characteristic length (CL) of the problem.

Figure 1.12 presents the correlation between the Knudsen number and the modelling equations required for the different levels of rarefaction. Classical CFD solvers are based on the Navier - Stokes equations and model air as a continuum flow and for flows with a small Knudsen number ($Kn \to 0$), this is sufficient. The NS equations have been modified to include slip regime and temperature jump condition at the solid wall in order to extend their validity up to $Kn \sim 0.1$ [27]. However, for higher Knudsen numbers continuum hypothesis breaks down and the Navier - Stokes solvers cannot be used to accurately predict the flow-field and a more detailed level of modelling is required. This occurs when the mean free path is of the same order of magnitude as the characteristic length of the problem [28], either on nanoscale or at low densities. Practical applications were detailed previously in the Motivation section of this thesis.

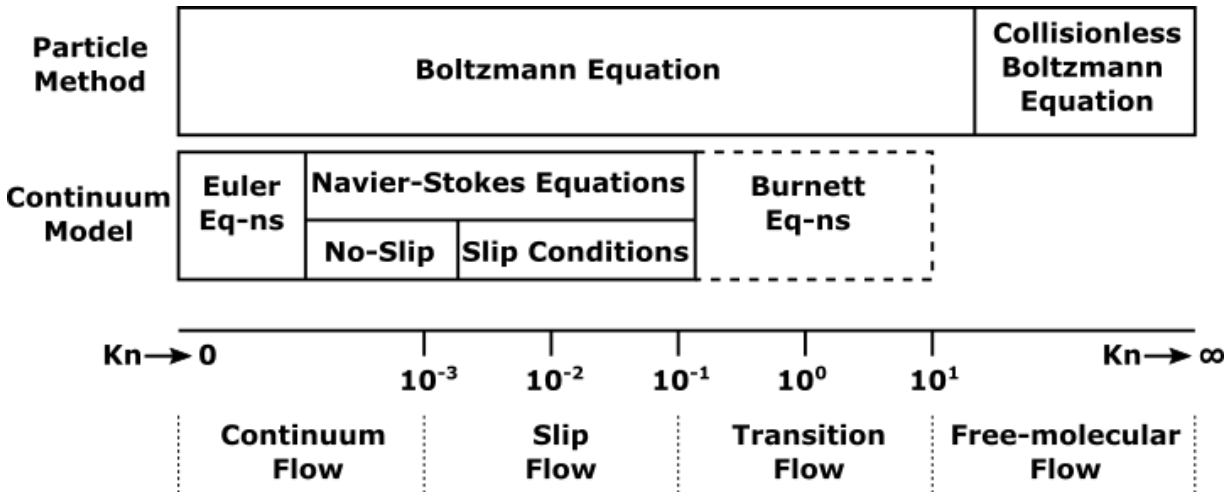

Figure 1.12: Model equations according to the flow rarefaction (adapted from Ivanov [3])

The Boltzmann equation is capable of governing all Knudsen number regimes: from continuum ($Kn \to 0$) to collisionless flows ($Kn \to \infty$). Both ends of this spectrum are extensively studied and well-defined in the literature, while the transitional regimes still represents a challenging research task. Most aerodynamics of high-speed vehicles require the modelling of the flow as a combination of continuum, transitional and rarefied flow. For this reason, the Boltzmann equation, simplified models of the equation and methodologies to solve the flow both efficiently and accurately have been developed in the literature and are the main focus of this thesis.

1.3.5 Boltzmann equation

The Boltzmann equation is a governing equation capable of modelling a variety of rarefaction regimes and is a governing equation for a particle distribution that defines for each location in space, the likelihood of finding a particle with a certain velocity. This distribution function is therefore a 6-dimensional function for a monatomic gas, while for polyatomic gas (requiring an extended form of Boltzmann equation) extra dimensions representing internal energy modes need to be added. It considers the rate of change of a distribution function with respect to time and position by accounting for the collision processes that take place [2], as shown in Eq. (1.5). The Boltzmann equation is a non-linear integro-differential equation and is complex to solve. For a monatomic gas, the Boltzmann equation can be written as:

$$\frac{\partial f(\underline{x},\underline{u},t)}{\partial t} + \underline{u} \cdot \frac{\partial f(\underline{x},\underline{u},t)}{\partial \underline{x}} + \frac{\partial}{\partial \underline{u}}(F_i f(\underline{x},\underline{u},t)) = \left[\frac{\partial f(\underline{x},\underline{u},t)}{\partial t}\right]_{coll}, \tag{1.5}$$

where $f(\underline{x},\underline{u},t)$ is the velocity distribution function (VDF). The velocity distribution function provides the fraction of the molecules with a certain velocity, in a certain physical domain at a specific time in a flowfield [29]. The terms of the equations on the left hand side (LHS) represent the change in time of the velocity distribution function, the convection term and the external forces acting on the molecule, respectively. The right hand side (RHS) of the equation contains the complex collision integral of the Boltzmann equation. It accounts for the rate of increase of number of molecules with a certain velocity as a result of binary collisions. The elastic collisions assumption is required, since the Boltzmann equation accounts for the change in velocity of two molecules when they collide and the probability of the atoms to have certain velocities after collision (see Fig. 1.13). Further, the Boltzmann equation assumes the gas is dilute and only binary encounters occur. The Maxwellian distribution function (Eq. (1.6)), first published in

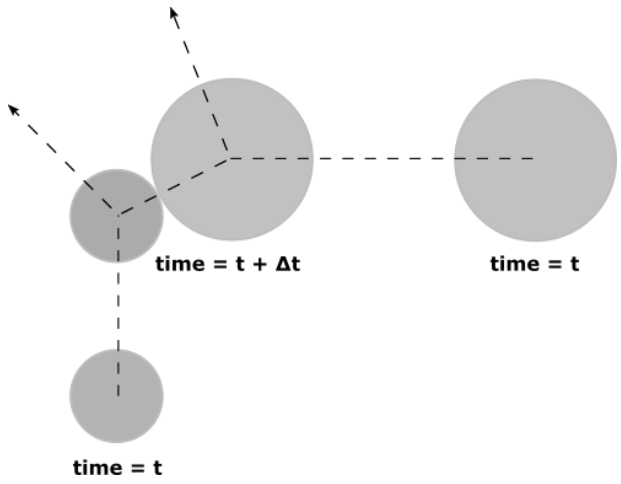

Figure 1.13: Velocity and directional change of two atoms colliding (adapted from Vincenti and Kruger [2])

1860 by Maxwell, provides the velocity distribution function for a gas in equilibrium.

$$f^M(\underline{x},\underline{u},t) = \frac{n}{(2\pi RT)^{\frac{3}{2}}} \exp\left[-\frac{1}{2RT}\Big((u-u_0)^2+(v-v_0)^2+(w-w_0)^2\Big)\right], \tag{1.6}$$

where n is the number density of the flow, R is the specific gas constant, T the gas temperature and $\underline{u}_0$ the macroscopic velocity of the gas. The flow properties are macroscopic averages of the distribution function. They are found by taking statistical moments of $f(\underline{x},\underline{u},t)$ from now on referred to as f for simplicity. The process consists of integrating the velocity distribution function with respect to the three dimensional velocity space for different powers of the velocity. Standard definite integrals are presented in Appendix A [2]. Using these standard integrals, the moments of the Maxwellian distribution function and the procedure for the density (zeroth order moment) integral is demonstrated in Appendix B. The moments of the distribution function and their use is also discussed in Sections 1.3.7 and 1.3.8.

Crucial properties of the Boltzmann equation include the conservation of mass, momentum and energy during collisions, entropy dissipation and collision equilibria. The Boltzmann equation can be extended to flows with multi-monoatomic species by introducing separate distribution functions for each species, create a governing equation for each of these and the formulation of collision terms representing collisions between particles belonging to different species. However, as defined the Boltzmann equation is valid for monoatomic gases and includes only elastic collisions. Extensions of the equations have been derived to include molecules with internal degrees of freedom. The Wang-Chang-Uhlenbeck (WCU) equations [30] include both mechanical and quantised flow modelling. As such WCU are considered semi-classical equations. Molecules at each different internal state are treated as different species. The complexity of the collision term is significantly increased. The computational cost associated with a numerical technique using a direct, deterministic discretization approach makes the Boltzmann equation unfeasible for practical applications. The diatomic extension (Wang-Chang-Uhlenbeck equations) is two orders of magnitude more expensive to simulate numerically than the monoatomic version (Boltzmann equation) [31]. Therefore, for engineering applications alternative methods are to be found. Relaxation model equations have been widely used and are constantly being improved, with the complex collision term significantly simplified and reduced relative to the Boltzmann or WCU equations.

1.3.6 Boltzmann Relaxation Models

The Bhatnagar-Gross-Krook (BGK) relaxation model [32] is the oldest and yet the most widely used kinetic approximation of the Boltzmann equation. It consists of substituting the collision term on the RHS in Eq. (1.5) with the difference between the non-equilibrium and equilibrium velocity distribution function divided by the time required for the flow to relax to this equilibrium, where no external forces are considered (Eq. (1.7)). The BGK is a simplified model of

the Boltzmann equation, but it retains many of the features and the physical significance of the complex collision integral [2].

$$\frac{\partial f}{\partial t} + \underline{u} \cdot \frac{\partial f}{\partial \underline{x}} = \frac{f^{eq} - f}{\tau}, \tag{1.7}$$

where τ is the relaxation time and is expressed by the viscosity coefficient μ and the pressure p of the gas as $\tau = \mu/p$. As such the BGK model is a single relaxation model and the relaxation coefficient is not velocity dependent. Note that since the relaxation coefficient τ depends on macroscopic properties that are positive then $\tau > 0$ is always satisfied.

As discussed in the previous section the equilibrium distribution function is the Maxwellian velocity distribution or $f^{eq} = f^M$. If the gas is in equilibrium then the non-equilibrium distribution function f is equal to f^{eq} and therefore to f^M or $f = f^{eq} = f^M$. The collision term on the RHS of the BGK equation goes to 0 in equilibrium, while on the LHS the non-equilibrium function is substituted with f^M or:

$$\frac{\partial f^M}{\partial t} + \underline{u} \cdot \frac{\partial f^M}{\partial \underline{x}} = \frac{f^M - f^M}{\tau} = 0. \tag{1.8}$$

Taking moments for the collision invariants $\underline{\psi}$ of the BGK model for quasi one-dimensional flow in equilibrium leads to the one-dimensional Euler equations in macroscopic gas dynamics as briefly illustrated here.

$$\iiint_{-\infty}^{+\infty} m\underline{\psi}\left[\frac{\partial f^M}{\partial t} + u\frac{\partial f^M}{\partial x}\right] d\underline{u} = 0, \tag{1.9}$$

where m denotes the molecular mass $\underline{\psi} = [1, u, \frac{1}{2}(u^2+v^2+w^2)]^T$. The moments of the Maxwellian distribution function with respect to the collision invariants are required and are shown for the one-dimensional flow:

$$\iiint_{-\infty}^{+\infty} m f^M d\underline{u} = \rho\,; \qquad \iiint_{-\infty}^{+\infty} um f^M d\underline{u} = \rho u_0 \tag{1.10}$$

$$\iiint_{-\infty}^{+\infty} u^2 m f^M d\underline{u} = \rho\left(\frac{kT}{m}\right) + \rho(u_0)^2\,; \quad \iiint_{-\infty}^{+\infty} v^2 m f^M d\underline{u} = \iiint_{-\infty}^{+\infty} w^2 m f^M d\underline{u} = \rho\left(\frac{kT}{m}\right)$$

$$\iiint_{-\infty}^{+\infty} u^3 m f^M d\underline{u} = 3\rho u_0\left(\frac{kT}{m}\right) + \rho u_0^3\,; \quad \iiint_{-\infty}^{+\infty} uv^2 m f^M d\underline{u} = \iiint_{-\infty}^{+\infty} uw^2 m f^M d\underline{u} = \rho u_0\left(\frac{kT}{m}\right)$$

Switching the differentiation and integration, applying the moments of the Maxwellian distribution function and expressing as a system of equations leads to the well-known Euler equations

in 1D for a monoatomic gas:

$$\frac{\partial}{\partial t}\begin{pmatrix}\rho\\ \rho u_0\\ \rho\left(\frac{3}{2}RT+\frac{1}{2}u_0^2\right)\end{pmatrix}+\frac{\partial}{\partial x}\begin{pmatrix}\rho u_0\\ \rho u_0^2+\rho RT\\ \rho u_0\left(\frac{5}{2}RT+\frac{1}{2}u_0^2\right)\end{pmatrix}=0 \tag{1.11}$$

The shear and normal stresses as well as the heat flux are not present in the macroscopic equations. This is expected since for a flow in thermal equilibrium these effects do not occur.

1.3.7 Chapman-Enskog Expansion

The Chapman-Enskog expansion is a derivation procedure allowing to establish a relationship between the mesoscopic level of modelling (i.e. via the velocity distribution function) and macroscopic level (via the flow variables). It demonstrates the continuum limit and properties of the Boltzmann equation and the Boltzmann relaxation equations. It provides the Navier-Stokes equations and higher orders of the expansion were shown to recover the Burnett and super-Burnett equations. We have limited ourselves to the most common use: the NS equations. Even though the expansion is well-known [2], the detailed procedure is discussed in this section, since it constitutes an important part of the construction and validation of new kinetic models and is used on multiple occasions throughout the thesis.
The Chapman-Enskog expansion is effectively a power series (Eq. (1.12)) of the distribution function for a small deviation from equilibrium.

$$f=f^{(0)}+\varepsilon f^{(1)}+\varepsilon^2 f^{(2)}+\ldots, \tag{1.12}$$

where $\varepsilon \ll 1$ is a small perturbation parameter of the order of the Knudsen number. Expressing the relaxation coefficient as $\tau=\varepsilon\hat{\tau}$ (with $\hat{\tau}$ of order $O(1)$) leads to:

$$\begin{aligned}\frac{\partial f}{\partial t}+\underline{u}\cdot\frac{\partial f}{\partial \underline{x}} &= \frac{1}{\varepsilon\hat{\tau}}(f^{eq}-f)\\ \varepsilon\frac{\partial f}{\partial t}+\varepsilon\underline{u}\cdot\frac{\partial f}{\partial \underline{x}} &= \frac{1}{\hat{\tau}}(f^{eq}-f)\end{aligned} \tag{1.13}$$

Substituting the series expansion from Eq. (1.12) into (Eq. (1.13)) leads to:

$$\varepsilon\frac{\partial f^{(0)}}{\partial t}+\varepsilon^2\frac{\partial f^{(1)}}{\partial t}+\varepsilon\underline{u}\cdot\frac{\partial f^{(0)}}{\partial \underline{x}}+\varepsilon^2\underline{u}\cdot\frac{\partial f^{(1)}}{\partial \underline{x}}=\frac{1}{\hat{\tau}}(f^{eq}-f^{(0)}-\varepsilon f^{(1)}-\varepsilon^2 f^{(2)}), \tag{1.14}$$

up to second order. Matching the powers of ε for the zeroth and first order approximations:

$$\begin{aligned} f^{(0)} &= f^{eq} \\ f^{(1)} &= -\hat{\tau}\Big(\frac{\partial f^{(0)}}{\partial t} + \underline{u}\cdot\frac{\partial f^{(0)}}{\partial \underline{x}}\Big) = -\hat{\tau}\Big(\frac{\partial f^{eq}}{\partial t} + \underline{u}\cdot\frac{\partial f^{eq}}{\partial \underline{x}}\Big) \end{aligned} \tag{1.15}$$

Therefore the expansion of the non-equilibrium distribution function in powers of ε up to and including first order terms leads to:

$$f = f^{eq} - \varepsilon\hat{\tau}\Big(\frac{\partial f^{eq}}{\partial t} + \underline{u}\cdot\frac{\partial f^{eq}}{\partial \underline{x}}\Big) \tag{1.16}$$

This expansion is valid for any target equilibrium distribution function. In the case of the BGK model [32], the target equilibrium distribution function is the Maxwellian VDF and $f^{eq} = f^M = f^{(0)}$. From here onwards the CE expansion proceeds in a one-dimensional form for simplicity. Taking moments of the zeroth-order expansion of the the BGK governing equation (Eq. (1.7)) provides the 1D Euler equations in the continuum limit. When the equilibrium VDF is a Maxwellian VDF the Euler equations are in the form:

$$\frac{\partial}{\partial t}\begin{pmatrix} \rho \\ \rho u_0 \\ \rho\left(\frac{3}{2}\frac{k}{m}T + \frac{1}{2}u_0^2\right) \end{pmatrix} + \frac{\partial}{\partial x}\begin{pmatrix} \rho u_0 \\ \rho u_0^2 + \rho\frac{k}{m}T \\ \rho u_0\left(\frac{5}{2}\frac{k}{m}T + \frac{1}{2}u_0^2\right) \end{pmatrix} = 0 \tag{1.17}$$

Applying the Chapman-Enskog first order expansion (up to ε^1) for monoatomic one-dimensional flow to the familiar BGK model recovers the one-dimensional Navier-Stokes equations in the hydrodynamic limit. The first order expansion requires knowledge of the derivatives of the VDF f w.r.t. time t and space x. However, the VDF is a function of the macroscopic variables density, velocity and temperature, therefore the chain rule is used:

$$\frac{\partial f^{eq}}{\partial t} = \frac{\partial f^{eq}}{\partial \rho}\frac{\partial \rho}{\partial t} + \frac{\partial f^{eq}}{\partial u_0}\frac{\partial u_0}{\partial t} + \frac{\partial f^{eq}}{\partial T}\frac{\partial T}{\partial t} \tag{1.18}$$

$$\frac{\partial f^{eq}}{\partial x} = \frac{\partial f^{eq}}{\partial \rho}\frac{\partial \rho}{\partial x} + \frac{\partial f^{eq}}{\partial u_0}\frac{\partial u_0}{\partial x} + \frac{\partial f^{eq}}{\partial T}\frac{\partial T}{\partial x} \tag{1.19}$$

The time derivatives of the macroscopic variables are expressed from the Euler equations (Eq. (1.17)). The evolution of the equilibrium distribution function when $f^{eq} = f^M$ becomes:

$$\begin{aligned} &\frac{\partial f^{eq}}{\partial t} + u\frac{\partial f^{eq}}{\partial x} = \frac{\partial f^M}{\partial t} + u\frac{\partial f^M}{\partial x} = f^M\Bigg[\Big(m\frac{\left(u-u_0\right)^2 + v^2 + w^2}{2kT^2} - \frac{5}{2T}\Big)\Big\{\left(u-u_0\right)\frac{\partial T}{\partial x}\Big\} \\ &+\frac{m\left(u-u_0\right)}{kT}\Big\{\left(u-u_0\right)\frac{\partial u_0}{\partial x}\Big\} - \Big(m\frac{\left(u-u_0\right)^2 + v^2 + w^2}{3kT}\Big)\Big(\frac{\partial u_0}{\partial x}\Big)\Bigg] \end{aligned} \tag{1.20}$$

Let the expression in square brackets be equal to A for short notation as in $f = f^M(1-\varepsilon\hat{\tau}A) = f^M - \tau f^M A$. Taking the moments of this expression :

$$\iiint_{-\infty}^{+\infty} mf\,d\underline{u} = \iiint_{-\infty}^{+\infty} mf^M\,d\underline{u} - \tau \iiint_{-\infty}^{+\infty} mf^M A\,d\underline{u} = \rho \tag{1.21}$$

$$\iiint_{-\infty}^{+\infty} muf\,d\underline{u} = \iiint_{-\infty}^{+\infty} muf^M\,d\underline{u} - \tau \iiint_{-\infty}^{+\infty} muf^M A\,d\underline{u} = \rho u_0 \tag{1.22}$$

$$\iiint_{-\infty}^{+\infty} mu^2 f\,d\underline{u} = \iiint_{-\infty}^{+\infty} mu^2 f^M\,d\underline{u} - \tau \iiint_{-\infty}^{+\infty} mu^2 f^M A\,d\underline{u} = \rho(\frac{k}{m}T + {u_0}^2) - \frac{4}{3}\tau\rho\frac{k}{m}T\frac{\partial u_0}{\partial x} \tag{1.23}$$

$$\iiint_{-\infty}^{+\infty} mv^2 f\,d\underline{u} = \iiint_{-\infty}^{+\infty} mw^2 f\,d\underline{u} = \iiint_{-\infty}^{+\infty} mv^2 f^M\,d\underline{u} - \tau \iiint_{-\infty}^{+\infty} mv^2 f^M A\,d\underline{u} = \rho\frac{k}{m}T + \frac{2}{3}\tau\rho\frac{k}{m}T\frac{\partial u_0}{\partial x} \tag{1.24}$$

$$\begin{aligned} \iiint_{-\infty}^{+\infty} mu^3 f\,d\underline{u} &= \iiint_{-\infty}^{+\infty} mu^3 f^M\,d\underline{u} - \tau \iiint_{-\infty}^{+\infty} mu^3 f^M A\,d\underline{u} \\ &= \rho u_0(3\frac{k}{m}T + {u_0}^2) - \tau\left(4\rho\frac{k}{m}Tu_0\frac{\partial u_0}{\partial x} + 3\rho\left(\frac{k}{m}\right)^2 T\frac{\partial T}{\partial x}\right) \end{aligned} \tag{1.25}$$

$$\begin{aligned} \iiint_{-\infty}^{+\infty} muv^2 f\,d\underline{u} &= \iiint_{-\infty}^{+\infty} muv^2 f^M\,d\underline{u} - \tau \iiint_{-\infty}^{+\infty} muv^2 f^M A\,d\underline{u} \\ &= \rho\frac{k}{m}Tu_0 - \tau\left(\rho\left(\frac{k}{m}\right)^2 T\frac{\partial T}{\partial x} - \frac{2}{3}\rho\frac{k}{m}Tu_0\frac{\partial u_0}{\partial x}\right) \end{aligned} \tag{1.26}$$

$$\begin{aligned} \iiint_{-\infty}^{+\infty} muw^2 f\,d\underline{u} &= \iiint_{-\infty}^{+\infty} muv^2 f^M\,d\underline{u} - \tau \iiint_{-\infty}^{+\infty} muv^2 f^M A\,d\underline{u} \\ &= \rho\frac{k}{m}Tu_0 - \tau\left(\rho\left(\frac{k}{m}\right)^2 T\frac{\partial T}{\partial x} - \frac{2}{3}\rho\frac{k}{m}Tu_0\frac{\partial u_0}{\partial x}\right) \end{aligned} \tag{1.27}$$

Taking moments of the BGK equation for the collision invariants $\underline{\psi} = [1, u, \frac{1}{2}(u^2+v^2+w^2)]^T$ after substituting the expanded expression for f to the first order leads to the one-dimensional

Navier-Stokes (NS) equations (Eq. (1.28)) for a monoatomic gas:

$$\frac{\partial}{\partial t}\begin{pmatrix}\rho\\ \rho u_0\\ \rho\left(\frac{3}{2}\frac{k}{m}T+\frac{1}{2}u_0^2\right)\end{pmatrix}+\frac{\partial}{\partial x}\begin{pmatrix}\rho u_0\\ \rho u_0^2+\rho\frac{k}{m}T\\ \rho u_0\left(\frac{5}{2}\frac{k}{m}T+\frac{1}{2}u_0^2\right)\end{pmatrix}-\frac{\partial}{\partial x}\begin{pmatrix}0\\ \tau_{xx}\\ -q_x+\tau_{xx}u_0\end{pmatrix}=0, \tag{1.28}$$

where for one dimensional single species monoatomic gas flow the normal stress τ_{xx} and the translational heat flux q_x are the only terms present due to viscosity and thermal conductivity and are in the form:

$$\tau_{xx}=\frac{4}{3}\tau\rho\frac{k}{m}T\frac{\partial u_0}{\partial x}=\frac{4}{3}\mu\frac{\partial u_0}{\partial x} \qquad\qquad q_x=-\frac{5}{2}\tau\rho\left(\frac{k}{m}\right)^2T\frac{\partial T}{\partial x}=-\kappa\frac{\partial T}{\partial x}, \tag{1.29}$$

where the local relaxation time for the BGK model equation is defined as $\tau=\mu/p$. It is a well know disadvantage of the BGK approximation that the Prandtl number in the hydrodynamic limit is $Pr=1$ [2], while for monoatomic gas it should be $Pr=\frac{2}{3}$. We can easily observe this result for the Prandtl number from the above expressions for the viscosity coefficient μ and the heat conduction coefficient κ:

$$Pr=\frac{c_p\mu}{\kappa}=\frac{\frac{5}{2}\frac{k}{m}\tau\rho\frac{k}{m}T}{\frac{5}{2}\tau\rho\left(\frac{k}{m}\right)^2T}=1 \tag{1.30}$$

Corrections to the BGK model for both monoatomic and diatomic gases exists in the literature. For monoatomic cases the Shakhov model [33] regards the heat flux and the Ellipsoidal Statistical (ES) model [34] treats the stress to recover the Prandtl number for a monoatomic gas. Both approximations use a single relaxation time and the changes are in the expression for the equilibrium distribution function. The two models will be demonstrated in the next sections.

1.3.8 Shakhov Model

The BGK relaxation model is the most widely applied, due to its simplicity and reliability. Many models build upon it to change some of its properties and to expand the range of applications. These changes are always on the RHS of the equation and often incorporate a modification of the equilibrium distribution function. The Shakhov kinetic model [33] was first introduced in 1968 and incorporates a change in the equilibrium distribution function (Eq. (1.31)), referred to as f^{Sh} here, that directly alters the heat flux of the solution. Correspondingly , this leads to the correct Prandtl number in the continuum limit.

$$f^{Sh}(\underline{u})=f^{M}(\underline{u})\left\{1+\frac{2\left(1-Pr^*\right)\left(\underline{u}-\underline{u}_0\right)\cdot\underline{q}^{corr}}{5pkT/m}\left[\frac{m}{2kT}\left(\underline{u}-\underline{u}_0\right)^2-\frac{5}{2}\right]\right\}, \tag{1.31}$$

where the pressure $p = nkT$, the heat flux correction is q^{corr} and Pr^* is the target Prandtl number and for single species monoatomic gas $Pr^* = 2/3$. This Shakhov equilibrium function f^{Sh} is inserted in the governing equation (Eq. (1.7)) instead of f^{eq} and the governing equation is in the form:

$$\frac{\partial f}{\partial t} + \underline{u} \cdot \frac{\partial f}{\partial \underline{x}} = \frac{f^{Sh} - f}{\tau}. \tag{1.32}$$

Note only the higher order moments (above 2nd order) are affected by the Shakhov correction. This is expected since only the heat flux should be modified and it appears only in the energy conservation equation, which requires these moments. For one-dimensional flow the modified moments of the Shakhov equilibrium function are in the form:

$$\begin{aligned} \iiint_{-\infty}^{+\infty} u^3 m f^{Sh} d\underline{u} &= 3\rho u_0 \Big(\frac{kT}{m}\Big) + \rho u_0^3 + \frac{6\big(1-Pr^*\big)q_x^{corr}}{5} \\ \iiint_{-\infty}^{+\infty} uv^2 m f^{Sh} d\underline{u} &= \iiint_{-\infty}^{+\infty} uw^2 m f^{Sh} d\underline{u} = \rho u_0 \Big(\frac{kT}{m}\Big) + \frac{2\big(1-Pr^*\big)q_x^{corr}}{5} \end{aligned} \tag{1.33}$$

Following the procedure of the CE expansion for the BGK equation as above, now the Shakhov equilibrium function is substituted. The zeroth order expansion of the non-equilibrium function becomes equal to the new equilibrium function, instead of the Maxwellian equilibrium and $f = f^{(0)} = f^{Sh}$. The first order CE expansion is of order ε and the difference between the Shakhov and Maxwellian equilibrium functions is also of order ε. Therefore, up to order $O(\varepsilon^2)$ the derivatives in the CE expression are of the Maxwellian equilibrium function. The non-equilibrium distribution function in power series of ε is in the form:

$$f = f^{Sh} - \varepsilon \hat{\tau} \Big(\frac{\partial f^M}{\partial t} + \underline{u} \cdot \frac{\partial f^M}{\partial \underline{x}} \Big) + O(\varepsilon^2). \tag{1.34}$$

The correction of the heat flux q^{corr} in the equilibrium function is found as a moment of the non-equilibrium function in the continuum limit as:

$$\begin{aligned} \underline{q}^{corr} &= \iiint_{-\infty}^{\infty} m(\underline{u}-\underline{u}_0)\frac{1}{2}(\underline{u}-\underline{u}_0)^2 f d\underline{u} \\ \underline{q}^{corr} &= \iiint_{-\infty}^{\infty} m(\underline{u}-\underline{u}_0)\frac{1}{2}(\underline{u}-\underline{u}_0)^2 \Big\{ f^{Sh} - \tau \Big(\frac{\partial f^M}{\partial t} + \underline{u}\frac{\partial f^M}{\partial \underline{x}} \Big) \Big\} d\underline{u} + O(\varepsilon^2) \\ \underline{q}^{corr} &= (1-Pr^*)\underline{q}^{corr} - \tau \frac{5}{2} k \frac{nkT}{m} \frac{\partial T}{\partial \underline{x}} + O(\varepsilon^2) \\ \underline{q}^{corr} &= -\tau \frac{1}{Pr^*} \frac{5}{2} k \frac{nkT}{m} \frac{\partial T}{\partial \underline{x}} + O(\varepsilon^2) \end{aligned} \tag{1.35}$$

The continuum limit is acquired with the same procedure as for the BGK model. The goal is to receive the Navier-Stokes equations in macroscopic gas dynamics with the correct Prandtl number in Eq. (1.36).

$$\frac{\partial}{\partial t}\begin{pmatrix}\rho\\ \rho u_0\\ \rho\left(\frac{3}{2}\frac{k}{m}T+\frac{1}{2}u_0^2\right)\end{pmatrix}+\frac{\partial}{\partial x}\begin{pmatrix}\rho u_0\\ \rho u_0^2+\rho\frac{k}{m}T\\ \rho u_0\left(\frac{5}{2}\frac{k}{m}T+\frac{1}{2}u_0^2\right)\end{pmatrix}-\frac{\partial}{\partial x}\begin{pmatrix}0\\ \tau_{xx}\\ -q_x+\tau_{xx}u_0\end{pmatrix}=0, \tag{1.36}$$

where the normal stress stays the same, but the heat flux has an additional term leading to a different thermal conductivity expression and therefore different Prandtl number:

$$\tau_{xx}=\frac{4}{3}\tau\rho\frac{k}{m}T\frac{\partial u_0}{\partial x}=\frac{4}{3}\mu\frac{\partial u_0}{\partial x} \qquad \begin{aligned} q_x &= -\frac{5}{2}\tau\rho\left(\frac{k}{m}\right)^2T\frac{\partial T}{\partial x}+(1-Pr^*)q_x^{corr} \\ q_x &= -\frac{1}{Pr^*}\frac{5}{2}\tau\rho\left(\frac{k}{m}\right)^2T\frac{\partial T}{\partial x}+O(\varepsilon^2) \\ q_x &= -\kappa\frac{\partial T}{\partial x}+O(\varepsilon^2). \end{aligned} \tag{1.37}$$

Inspecting the Prandtl number:

$$Pr=\frac{c_p\mu}{\kappa}=\frac{\frac{5}{2}\frac{k}{m}\tau\rho\frac{k}{m}T}{\frac{1}{Pr^*}\frac{5}{2}\tau\rho\left(\frac{k}{m}\right)^2T}=Pr^*=\frac{2}{3} \tag{1.38}$$

Comparison between the Navier-Stokes equations before and after the Shakhov correction confirms that only the heat flux term in the equation is affected, which is expressed in a change of the energy equation. The correct continuum limit for a single species monoatomic gas is provided by the Shakhov kinetic model.

Notice that if the target Prandtl number set to $Pr^*=1$, the NS equations (Eq. (1.36)) reduce to the familiar form of NS provided by the BGK model (Eq. (1.28)) and Eq. (1.38) leads to $Pr=1$ as for the BGK model. Therefore the Shakhov model is consistent with the BGK model and can be reduced to it. This observation will be used in the thesis when simulations of the BGK model are preformed using the Shakhov model with Pr set to unity.

1.3.9 Ellipsoidal Statistical Model

The Ellipsoidal Statistical model (ES-model) [34] was formulated in 1965 and is an alternative approach to correct the Prandtl number. An anisotropic correction to the equilibrium distribution function f^{eq} modifies the temperature T into a tensor $\underline{\underline{\Lambda}}$, leading to a new ES equilibrium distribution function f^{ES} in the form:

$$f^{ES}(\underline{u}) = \frac{n}{\sqrt{det(2\pi\underline{\underline{\Lambda}})}}\exp\Big[-\frac{1}{2}\left(\underline{u}-\underline{u}_0\right)\cdot\underline{\underline{\Lambda}}^{-1}\cdot\left(\underline{u}-\underline{u}_0\right)\Big], \tag{1.39}$$

with the tensor defined as:

$$\underline{\underline{\Lambda}} = \nu_{ES}\underline{\underline{\Theta}} + \left(1-\nu_{ES}\right)\left(\frac{kT}{m}\right)\underline{\underline{I}} \tag{1.40}$$

where $\underline{\underline{I}}$ is the identity matrix and the tensor $\underline{\underline{\Theta}}$ is based on the velocity $\underline{u}_0$ and in the form:

$$\underline{\underline{\Theta}} = \frac{1}{n}\iiint_{-\infty}^{+\infty}\left(\underline{u}-\underline{u}_0\right)\otimes\left(\underline{u}-\underline{u}_0\right)f\,d\underline{u}. \tag{1.41}$$

The new ES equilibrium function is inserted in the governing equation instead of the Maxwellian VDF and the relaxation coefficient ν_{ES} is also introduced in this equation, modifying the collision term on the RHS:

$$\frac{\partial f}{\partial t}+\underline{u}\cdot\frac{\partial f}{\partial \underline{x}} = \frac{f^{ES}-f}{\tau(1-\nu_{ES})}. \tag{1.42}$$

In comparison to the Shakhov model, more of the moments for the ES model are affected and instead of the temperature in the macroscopic properties the tensor $\underline{\underline{\Lambda}}$ appears. Only moments above the first order w.r.t. velocity are affected in comparison to the Maxwellian VDF and are summarized for one-dimensional formulation as:

$$\begin{aligned}
&\iiint_{-\infty}^{+\infty} u^2 m f^{ES} d\underline{u} = \rho\lambda_{11}+\rho u_0^2; \qquad \iiint_{-\infty}^{+\infty} u^3 m f^{ES} d\underline{u} = 3\rho u_0\lambda_{11}+\rho u_0^3\\
&\iiint_{-\infty}^{+\infty} v^2 m f^{ES} d\underline{u} = \iiint_{-\infty}^{+\infty} w^2 m f^{ES} d\underline{u} = \rho\lambda_{22} = \rho\lambda_{33}\\
&\iiint_{-\infty}^{+\infty} uv^2 m f^{ES} d\underline{u} = \iiint_{-\infty}^{+\infty} uw^2 m f^{ES} d\underline{u} = \rho u_0\lambda_{22} = \rho u_0\lambda_{33},
\end{aligned} \tag{1.43}$$

where λ_{11}, λ_{22} and λ_{33} are the diagonal terms of the tensor $\underline{\underline{\Lambda}}$. The CE expansion proceeds in a similar fashion as the Shakhov model, where the zeroth order in the power series expansion of the non-equilibrium function is expressed by the ES equilibrium function f^{ES} and the higher order moments involve the Maxwellian equilibrium function f^M as:

$$f = f^{ES} - \varepsilon\hat{\tau}(1-\nu_{ES})\left(\frac{\partial f^M}{\partial t}+\underline{u}\cdot\frac{\partial f^M}{\partial \underline{x}}\right)+O(\varepsilon^2). \tag{1.44}$$

For a quasi one-dimensional flow ($u_0 \neq 0, v_0 = 0, w_0 = 0$) the elements of the matrix $\underline{\underline{\Lambda}}$ can be obtained as moments of the CE expanded non-equilibrium function as:

$$\begin{aligned}
\lambda_{11} &= \left(1-\nu_{ES}\right)\left(\frac{kT}{m}\right) + \frac{\nu_{ES}}{n}\iiint_{-\infty}^{+\infty}\left(u-u_0\right)^2 f d\underline{u} = \left(\frac{kT}{m}\right) - \frac{\nu_{ES}}{n}\frac{4}{3}\tau n\frac{kT}{m}\frac{\partial u_0}{\partial x} \\
\lambda_{22} &= \left(1-\nu_{ES}\right)\left(\frac{kT}{m}\right) + \frac{\nu_{ES}}{n}\iiint_{-\infty}^{+\infty} v^2 f d\underline{u} = \left(\frac{kT}{m}\right) + \frac{\nu_{ES}}{n}\frac{2}{3}\tau n\frac{kT}{m}\frac{\partial u_0}{\partial x} \\
\lambda_{33} &= \left(1-\nu_{ES}\right)\left(\frac{kT}{m}\right) + \frac{\nu_{ES}}{n}\iiint_{-\infty}^{+\infty} w^2 f d\underline{u} = \left(\frac{kT}{m}\right) + \frac{\nu_{ES}}{n}\frac{2}{3}\tau n\frac{kT}{m}\frac{\partial u_0}{\partial x}
\end{aligned} \tag{1.45}$$

with all off-diagonal elements equal to zero. The Navier-Stokes equations are formed after the CE expansion and substituting the tensor elements of $\underline{\underline{\Lambda}}$:

$$\frac{\partial}{\partial t}\begin{pmatrix}\rho \\ \rho u_0 \\ \rho\left(\frac{3}{2}\frac{k}{m}T + \frac{1}{2}u_0^2\right)\end{pmatrix} + \frac{\partial}{\partial x}\begin{pmatrix}\rho u_0 \\ \rho u_0^2 + \rho\frac{k}{m}T \\ \rho u_0\left(\frac{5}{2}\frac{k}{m}T + \frac{1}{2}u_0^2\right)\end{pmatrix} - \frac{\partial}{\partial x}\begin{pmatrix}0 \\ \tau_{xx} \\ -q_x + \tau_{xx}u_0\end{pmatrix} = 0, \tag{1.46}$$

where the shear stress and heat flux are in the form:

$$\tau_{xx} = \frac{4}{3}\tau\rho\frac{k}{m}T\frac{\partial u_0}{\partial x} = \frac{4}{3}\mu\frac{\partial u_0}{\partial x} \qquad q_x = -\frac{5}{2}(1-\nu_{ES})\tau\rho\left(\frac{k}{m}\right)^2 T\frac{\partial T}{\partial x} = -\kappa\frac{\partial T}{\partial x} \tag{1.47}$$

Inspecting the Prandtl number:

$$Pr = \frac{c_p\mu}{\kappa} = \frac{\frac{5}{2}\frac{k}{m}\tau\rho\frac{k}{m}T}{\frac{5}{2}(1-\nu_{ES})\tau\rho\left(\frac{k}{m}\right)^2 T} = \frac{1}{1-\nu_{ES}} = Pr^* = \frac{2}{3}, \tag{1.48}$$

where the relaxation coefficient for the ES is bound by the Prandtl number as $Pr = \frac{1}{1-\nu_{ES}}$ and in order to achieve $Pr = 2/3$, it is required $\nu_{ES} = -1/2$ for a monoatomic gas. Comparing with the NS equations resulting from the Shakhov model (Eq. (1.36) and the heat flux expression (Eq. (1.38)), which receive the correct Prandtl number, then $Pr^* = 1/(1-\nu_{ES}) = 2/3$ are target values.

1.3.10 Transport Properties

Transport mechanisms include but are not limited to convective transport and molecular transport [25, 35]. The convection is accounted for in governing equations for flow modelling and is due to the bulk motion of the fluid. Molecular transport refers to the the motion of molecules relative to the bulk motion. It is expressed by gradients in the field and this type of transport

of mass, momentum and energy is described by the transport properties or coefficients of the flow. For typical aerospace applications these non-equilibrium effects are usually described by the viscosity and thermal conductivity. For gas mixtures the diffusion between the two species is also an important quantity. Table 1.1 summarizes the transport coefficients related to the flux of mass and energy in a gas mixtures and the cause of each of these types of molecular transport. What is different in comparison to single species gas is that the mass density gradient can create both mass and energy flux and the temperature gradient can affect both fluxes as well.

	mass gradient	temperature gradient
mass flux	Fick's law (ordinary diffusion)	Soret effect (thermal diffusion)
energy flux	Dufour effect (heat of transport)	Fourier law (thermal conductivity)

Table 1.1: Transport properties (mass and energy flux)

Fick's and Fourier's laws are effects causing mass flux from diffusion and energy flux from thermal conductivity, respectively. For this reason, they are known as direct effects. The Dufour and Soret are coupled effects and reciprocal phenomena for a gas mixture according to Onsager's phenomenological equations.
Furthermore, the viscosity is the resistance of one fluid layer to another layer and is described in a similar style in Table 1.2:

	velocity gradient	temperature difference
momentum flux	Newton's law (viscosity)	bulk viscosity

Table 1.2: Transport properties (momentum flux)

where the bulk viscosity is associated with diatomic and polyatomic gas, but not monoatomic, since it is connected to rotational non-equilibrium. This effect will be further discussed in Chapter 5. It is also important for the discussion of diatomic molecules that the ordinary diffusion, Soret effect (and therefore the Dufour effect) and the viscosity for diatomic and polyatomic molecules have the same expressions as for monoatomic gas [35]. Only the heat flux of the system and the appearance of bulk viscosity are influenced by the presence of internal degrees of freedom.
Note also that all of the transport coefficients are of order $O(\varepsilon)$ in the context of the CE expansion. The study of transport properties is a big and active research area on its own and here we just aim to summarize part of it in a simple way.

1.3.11 Gas Surface Interaction

A normal shock wave is often used through the validation of novel mathematical models for high-speed flows, since it is the simplest form of strong non-equilibrium flow. It is also studied in great detail in this thesis. However, more complex cases: such that include a geometric

body, are of greater interest for practical applications. These cases are more intricate due to the increased dimensionality of the problem, higher computational expense and gas-surface interactions that need to be accounted for. Different collision types are defined corresponding to the molecules' reaction on encountering a wall. According to the type of collision, different boundary conditions can be imposed. If an elastic collision occurs and the incidence angle is equal to the reflection angle, specular reflection is observed as shown in Fig. 1.14. The normal momentum is reversed and no transfer of momentum between the molecule and the wall takes place. After collision the particle will have the same velocity magnitude. No energy exchange takes place due to the fully elastic collision with the wall. A diffuse reflection, also known as

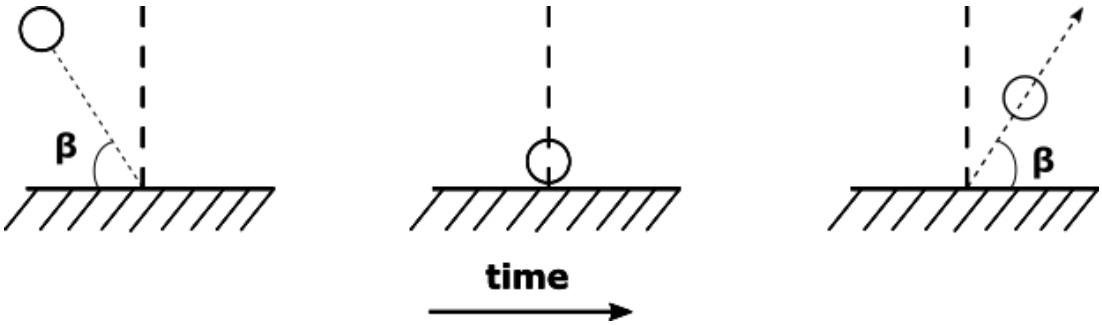

Figure 1.14: Specular reflection (adapted from Cunningham and Williams [4])

absorptive collision [4], is such that momentum transfer is observed between the molecule and the wall. In comparison to the specular reflection, the reflection angle of the emitted molecule is independent of the incidence angle as demonstrated in Fig. 1.15. Assuming an isotropic wall, the reflection of the molecule in all directions has equal probability. Therefore a Maxwellian distribution function is imposed at the wall. This Maxwellian is defined for the imposed wall temperature. An exchange of energy between particle and wall does take place unlike for the specular reflection. The boundary condition, introduced by Maxwell in 1879 [36], combines the

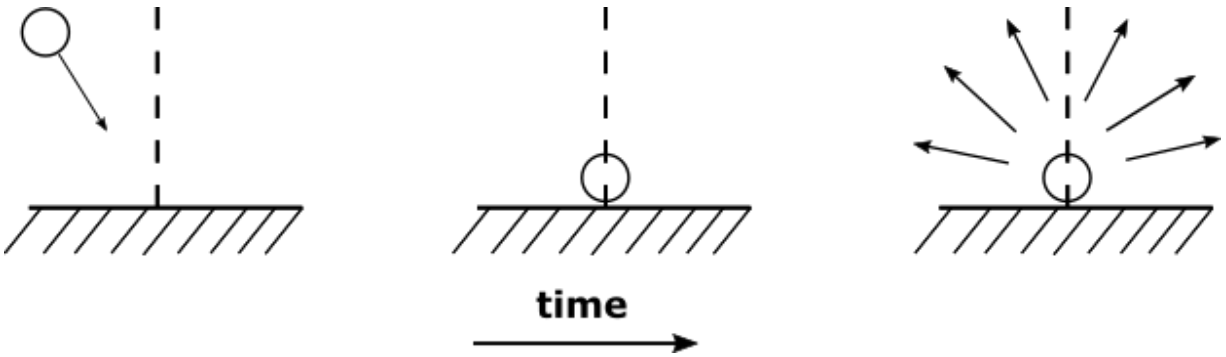

Figure 1.15: Diffuse reflection (adapted from Cunningham and Williams [4])

specular reflection and the diffuse reflection kinetic boundary conditions. The Maxwell model uses an accommodation coefficient, which defines the ratio of specular and diffuse reflection. The Maxwell model is one of the most widely used model with the accommodation coefficient

dependent on multiple factors, including the surface composition and material and the type of gas. A detailed description and numerical comparison between the Maxwell model and more advanced models is available in the recent paper by Wu and Struchtrup [37].
In this thesis fully diffusive wall (Fig. 1.15) is used for all simulations, with an imposed half-Maxwellian boundary condition at local surface temperature. This reflection type is selected due to the simplicity of assuming a perfectly accommodating surface. Clearly, the different conditions will lead to different boundary layers and effectively changing the resulting flow. The effect of the selected reflection type is a separate topic in kinetic modelling and does not comprise part of this thesis.

1.3.12 Numerical Discretisation

The numerical application of the kinetic models requires a numerical discretization of the discussed equations. There are two main routes- statistical (DSMC) and deterministic (i.e. DVM) and we will use the deterministic approach. The numerical discretization consists of finite volume method (FVM) in physical space, the discrete velocity method (DVM) in velocity space and the total variation diminishing scheme (TVD) in time. All three schemes will be summarized and the discretization of the BGK governing equation, independent on the form of the equilibrium function, is shown gradually. From the discretized distribution function by applying the trapezoidal rule, the moments of the VDF are found, which correspond to the macroscopic variables. These discretization choices are selected to ensure a reliable and simple numerical application. There are more advanced approaches available in the literature, but the focus on the thesis is not on numerical improvement, rather on the mathematical development and numerical application.
First, the finite volume method [38] is applied. For the one-dimensional in space single-species BGK model:

$$\frac{\partial f}{\partial t} + u\frac{\partial f}{\partial x} = \frac{f^{eq} - f}{\tau}, \tag{1.49}$$

the finite volume scheme approximation leads to:

$$\begin{aligned} \iiint_V \frac{\partial f}{\partial t} dV + \iiint_V u\frac{\partial f}{\partial x} dV &= \iiint_V \frac{f^{eq} - f}{\tau} dV, \\ \iiint_V \frac{\partial f}{\partial t} dV + u \oiint_S f \cdot \underline{n} dS &= \iiint_V \frac{f^{eq} - f}{\tau} dV. \end{aligned} \tag{1.50}$$

Assuming that in small volumes ΔV, the state does not change in time, which

$$\Delta V \frac{\partial f}{\partial t} + \Delta S u f = \Delta V \frac{f^{eq} - f}{\tau} \tag{1.51}$$

In one-dimensional setup, the surface integral reduces to two fluxes on either side of the cell j:

$$\begin{aligned} \frac{\partial f_j}{\partial t} + \frac{1}{\Delta x} uf \Big|_{j-\frac{1}{2}}^{j+\frac{1}{2}} &= \frac{f_j^{eq} - f_j}{\tau} \\ \frac{\partial f_j}{\partial t} + \frac{1}{\Delta x}(F_{j+\frac{1}{2}} - F_{j-\frac{1}{2}}) &= \frac{f_j^{eq} - f_j}{\tau_j}, \end{aligned} \tag{1.52}$$

where $\underline{n}$ is the unit vector normal to the surface, S is the total surface area on the cell, j is the cell index and $F_{j+\frac{1}{2}}$ and $F_{j-\frac{1}{2}}$ are the fluxes on the left and right faces of the j cell. The distribution function and the fluxes calculation are defined in the next Section.

1.3.13 Discrete Velocity Method

The discrete velocity method (DVM) [39] is a deterministic numerical approach developed to solve the Boltzmann equation and is widely used for applying kinetic models. The name of the method comes from representing the continuous velocity by discrete velocities. Advantage of the methodology are simplicity, the relatively easy computational implementation and accuracy of the results. In this section the procedure of the discrete velocity method (DVM) is detailed. Figure (1.16) demonstrates how the scheme is formulated for a one dimensional flow. In the DVM approach in each cell of the mesh in space, a phase (velocity)-space is defined. Cut-off minimum and maximum velocity bounds are set and the number of discrete velocities represent all possible velocities in these bounds.

In each cell of the space mesh, this velocity-space is used to define discretized non-equilibrium and equilibrium distribution functions. For each of these velocities, the numerical flux of the non-equilibrium distribution function through each cell face is computed to represent the convection part of the kinetic Boltzmann equation. For the fluxes, second order accurate upwinding in velocity space is used on the velocity component normal to the cell face. The second order formulation uses a min-mod limiter to suppress numerical oscillations. The discretized non-equilibrium and equilibrium distribution functions in each cell center are used to evaluate the collision term based on the BGK approximation. Following the discretization of the governing equation from the previous subsection Eq. (1.52) is expressed for each discrete velocity u_m and can be shown as:

$$\frac{\partial f_j}{\partial t}|_m + \frac{1}{\Delta x}(F_{j+\frac{1}{2}}|_m - F_{j-\frac{1}{2}}|_m) = \frac{f_j^{eq}|_m - f_j|_m}{\tau_j}, \tag{1.53}$$

where m is the discrete velocity index. This index will be omitted in further discussions.

In each time step, the convection and collision effects create a modified non-equilibrium distribution function, from which the corresponding continuum quantities are obtained from taking moments in velocity space. Finally, an updated equilibrium distribution function is created based on these continuum quantities in each cell center. Both the number of velocities and

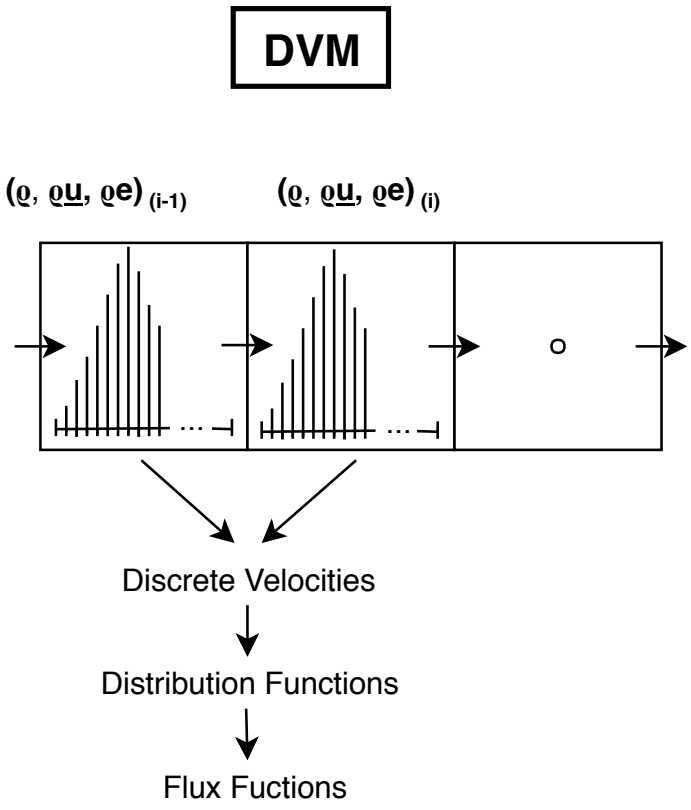

Figure 1.16: Discrete velocity method diagram [5].

the bounds of the velocity space depend on the considered problem. The required number of discrete velocities for which the distribution function is evaluated increases drastically for 2D and 3D problems, such that the DVM approach is not widely used for large-scale 2D and 3D practical applications. Combining the DVM method with a continuum solver creates a practical approach to simulating partially rarefied flows in case effective coupling methods are employed.

1.3.14 Total Variation Diminishing

The physical and velocity space are discretized. Next step concerns the time derivative in the governing equation. The time marching method used is a second order total variation diminishing scheme (TVD), described here. The TVD is chosen for its capability to accurately capture extreme changes in variables without the need of a very fine mesh [40], unlike other difference schemes. The TVD was first introduced by Harten [41]. The discretized governing equation becomes:

$$\frac{f_j^{n+1} - f_j^n}{\Delta t} + \frac{1}{\Delta x}(F_{j+\frac{1}{2}} - F_{j-\frac{1}{2}}) = \frac{f_j^{eq} - f_j}{\tau_j}, \tag{1.54}$$

where f^n is the solution at time step n. The second order TVD [42] discretises the time derivative of the BGK model as:

$$\begin{aligned} L(f^n) &= \Big[-\frac{1}{\Delta x}(F^n_{j+\frac{1}{2}} - F^n_{j-\frac{1}{2}}) + \frac{f^n_{eq} - f^n}{\tau} \Big] \\ f^{(1)} &= f^n + \Delta t L(f^n) \\ f^{n+1} &= \frac{1}{2} f^n + \frac{1}{2} f^{(1)} + \frac{1}{2} \Delta t L(f^{n+1}), \end{aligned} \tag{1.55}$$

where $f^{(1)}$ is an intermediate solution between time level n and $n+1$. The two-step update as shown in Eq. (1.55) is implemented in the DVM solver, requiring only one intermediate solution to be stored. The added accuracy and numerical stability of this TVD scheme relative to a single-step Euler-forward method justifies the extra storage requirement due to this intermediate solution.

1.3.15 Gas Kinetic Scheme

The gas kinetic scheme (GKS) [6,43] based on the BGK was first introduced by Xu and Prendergast [44,45] as a finite volume CFD solution method. It provides an alternative solution methodology as compared to more conventional approximate Riemann-solver based finite-volume CFD methods, with the key difference in the flux computation. The approach taken in the gas kinetic scheme (GKS) is completely different than the DVM and is described here. A key difference is that in the GKS a finite volume method (FVM) for the continuum variables is constructed, while the DVM discussed previously directly discretizes the kinetic equation. In the GKS, the kinetic-level modelling appears only in the formulation and evaluation of the numerical fluxes used in this finite volume method. This will be summarized in the following paragraphs.
The macroscopic variables update is found from the value of the variable on the previous time step and the flux of the variable. The update of the conservative variables from time step n to $(n+1)$ is then defined as:

$$\underline{W}^{n+1}_j = \underline{W}^n_j + \frac{1}{\Delta x} \int_{t^n}^{t^{n+1}} \Big(\underline{F}_{j-1/2}(t) - \underline{F}_{j+1/2}(t) \Big) dt, \tag{1.56}$$

where $\underline{W}_j$ is the vector containing the conservative variables, which for a single-species monoatomic one-dimensional flow is expressed as:

$$\underline{W}_j = \begin{pmatrix} \rho \\ \rho u_0 \\ \frac{3}{2} nkT + \frac{1}{2} \rho u_0^2 \end{pmatrix}_j \tag{1.57}$$

and the time-dependent flux $\underline{F}_{j+\frac{1}{2}}$ across the cell-face $j+\frac{1}{2}$ in the x-direction (and similarly for the other face $\underline{F}_{j-\frac{1}{2}}$) is defined as:

$$\underline{F}_{j+\frac{1}{2}} = \iiint_{-\infty}^{\infty} um\underline{\Psi} f(x_{j+1/2},t,u)d\underline{u} \tag{1.58}$$

where $\underline{\Psi} = (1,u,\frac{1}{2}(u^2+v^2+w^2))^T$ and the detailed derivation of the expression for distribution function at the cell face $f(x_{j+1/2},t,u)$, dependent on the equilibrium distribution function g as defined by the kinetic model and the initial distribution function at the beginning of the time step f_0 (see Fig. 1.17), is shown by Xu in [6,43]. The flux in Eq. (1.58) is not numerically evaluated

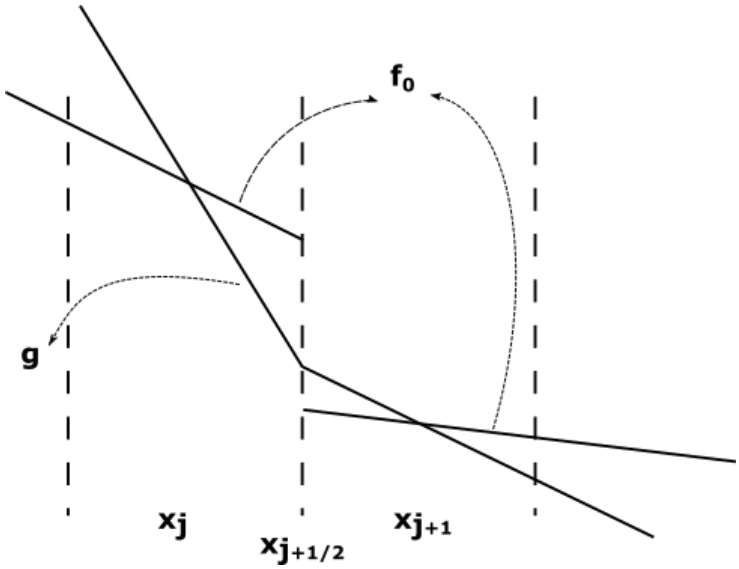

Figure 1.17: Cell face distribution function reconstruction in a gas- kinetic scheme (adapted from Xu [6])

in the solver, but the moments are computed analytically and then inserted in the solver as dependent on the macroscopic variables. The analytical flux expression is directly related to the GKS solver resemblance to a continuum solver in its structure and also in its computational expense. To make this process clearer we have visualised the process in Fig. 1.18. The red box drawn around the considered cell face represents this reconstructed kinetic solution $f(x_{j+1/2},t,u)$. The kinetic solution is not actually stored and the moments of the locally-constructed kinetic solution are evaluated analytically by Eq. (1.58) on the basis of the CE expansion of the non-equilibrium distribution function f. Note also that different to the UGKS [15] and DUGKS [16], which are described in more detail later, the distribution function is not stored locally on the cell face and the fluxes are not numerical moments of the non-equilibrium distribution function in the GKS. The UGKS and DUGKS are extensions of the original GKS method that do involve storing and updating a discretized distribution function - this extends their applicability to larger Kn, at an increased computational cost.

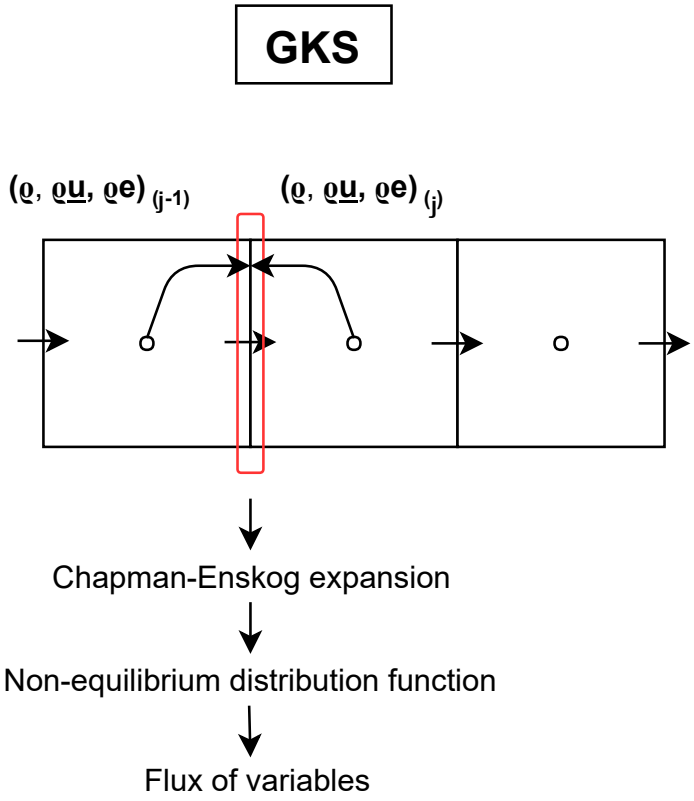

Figure 1.18: Gas kinetic scheme diagram [5]

A limiting case of the presented gas-kinetic scheme is when the flow region is well-resolved. The well-resolved scheme is achieved at a mesh that is fine enough so that the reconstructed conservative variables in two neighbouring cells have similar values. It follows that the equilibrium function g on the left and right side of the cell face has equal values and in Fig. 1.17 it becomes approximately a straight line. Similarly, the spatial and temporal derivatives on the two sides of the face become equal. It follows that f_0 in Fig. 1.17 is not discontinued any longer and is approximately a straight line. These simplifying assumptions lead to definition of the non-equilibrium distribution function at the cell face $f(x_{j+1/2},t,u)$, which depends only on the equilibrium distribution function and the CE expansion of it at the cell face. In this thesis, we will use the well-resolved gas-kinetic scheme to resolve a number of high-speed non-equilibrium flows.

1.4 Literature Review

After a detailed background into the theory required for this research, this literature survey focuses on relevant works and innovation in the sphere of kinetic models. This section also creates a bridge between the discussed theory and the novelty of the thesis.

1.4.1 Monoatomic Kinetic Models

The Boltzmann equation [24] is a fundamental equation of gas dynamics as detailed previously. The relaxation models try to replicate its fidelity, while simplifying the complex collision integral. Therefore, the models resemble the structure of the Boltzmann equation and can be related back to it. The tree diagram in Fig. 1.19 demonstrates the connection between the Boltzmann equation and the BGK model as well as the improvements based on it for single species gases. Consequently, the complex collision integral of the Boltzmann equation is substituted by the

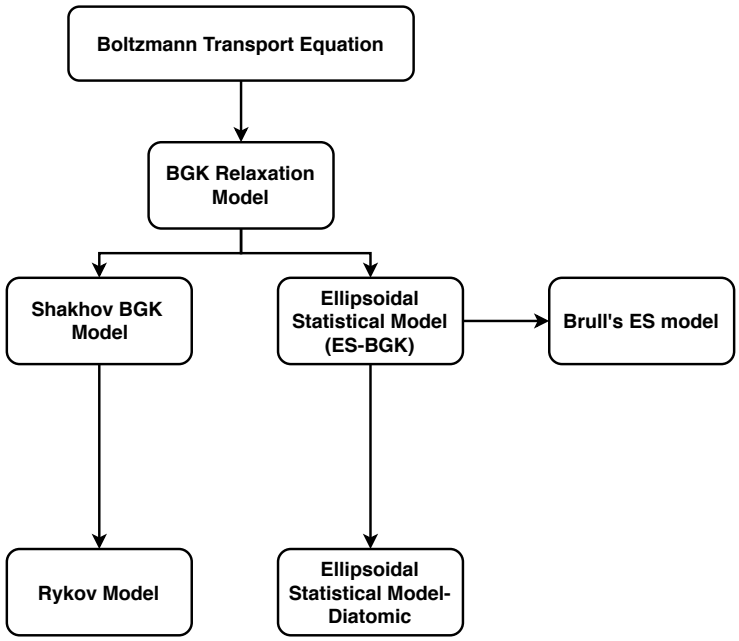

Figure 1.19: Single-species BGK-type models for monoatomic gas (BGK, Shakhov and ES) and diatomic extensions (Rykov and ES diatomic) tree diagram.

BGK relaxation model [32], which preserves the most important mathematical and physical characteristics of the full equation close to equilibrium. This model has a simplified mathematical form and is widely applied in numerical simulations, e.g. [6, 46]. However, the BGK model cannot concurrently determine the correct viscous and heat transfer coefficients in the hydrodynamic limit and thus the Prandtl number is not correct.

For monoatomic gas, the issue has been addressed in two ways- the Shakhov BGK model [33] and the Ellipsoidal Statistical (ES) BGK model [34] (Fig. 1.19). These corrections were detailed in earlier sections. Both models modify the Maxwellian distribution function in the original BGK model to receive a new target equilibrium function to rectify Prandtl number. Both corrections behave well in the asymptotic continuum limit and the Navier-Stokes equations can be derived through the Chapman-Enskog expansion. The Shakhov model has shown to be more reliable for strong non-equilibrium conditions [47], while the ES-BGK has been investigated more thoroughly mathematically to confirm non-negativity of the distribution function and the macroscopic fields [48–50].

The extension of the kinetic model equations to gas mixtures is not trivial and resorting to relaxation models presents a substantial difficulty. There is momentum and energy exchange between species and therefore the conservation equations are for the whole system. The hydrodynamic limit involves species diffusion and the number of transport coefficients for monoatomic binary mixtures increases to five - Fick, Soret, Dufour, Fourier and viscosity coefficients. Besides, the simplified collision term can lead to non-physical effects such as a negative distribution function and negative density or temperature regions. Mixture BGK-type approximation for a Maxwellian potential [51–54] and later on for an arbitrary potential [55] have been developed and confirm the obstacles mentioned. A common weakness of these models is the breakdown of the indifferentiability principle, which has been defined and overcome for an arbitrary potential [56], however reintroducing the negativity problem.

Andries et al. [57] formulated a consistent BGK mixture model, preserving positive continuum fields and distributions, complying with the indifferentiability principle and considering entropy decay. This model was a big step forward for kinetic modelling and despite its limitations, it is still a widely-used approach for numerical applications [58, 59]. There are two types of Boltzmann derived models for mixtures in regard to the formulation of the collision term of the transport equation. The AAP model [57] is a single-relaxation based model, treating self- and cross-collisions with one operator on the right-hand side of the equation. Another possible approach is to have a sum of collision operators, similar to the full Boltzmann equation and model each collision type individually [60, 61]. A detailed comparison of the mathematical properties of the two types of models is presented by Klingenberg et al. [62] and Bobylev et al. [63]. The multi-relaxation models allow treating self- and cross-collisions with different relaxation rates, while the collisions of the single-relaxation models are treated with the same relaxation rate. This suggests multi-relaxation models are advantageous for the modelling of multi-species gases, specifically when the species differ significantly from each other, e.g. high mass ratio. However, important advantages the single-relaxation models provide are the reduced complexity and higher computational efficiency. For this reason, in this work we focus our attention on studying single-relaxation models and evaluating their capabilities. We will add to the single-species figure (Fig. 1.19), the development of the mixture kinetic models, based on a single-relaxation coefficient in Fig. 1.20 and will refer to this tree diagram as we introduce the most recent mixture models.

The number of correctly fitted transport properties is a great challenge for BGK-type models for gas mixtures. Table 1.3 is used to present an overview of the properties of the single-relaxation mixture models, which are described in greater detail here. A similar formulation to the AAP model is defined by Groppi et al. [64]. Both AAP and Groppi et al. models introduce modified species velocity and temperature in the equilibrium distribution function that differ from the species mean velocity and temperature. These modified quantities recover the correct total momentum and energy of the system and are directly related to the species mean variables. An

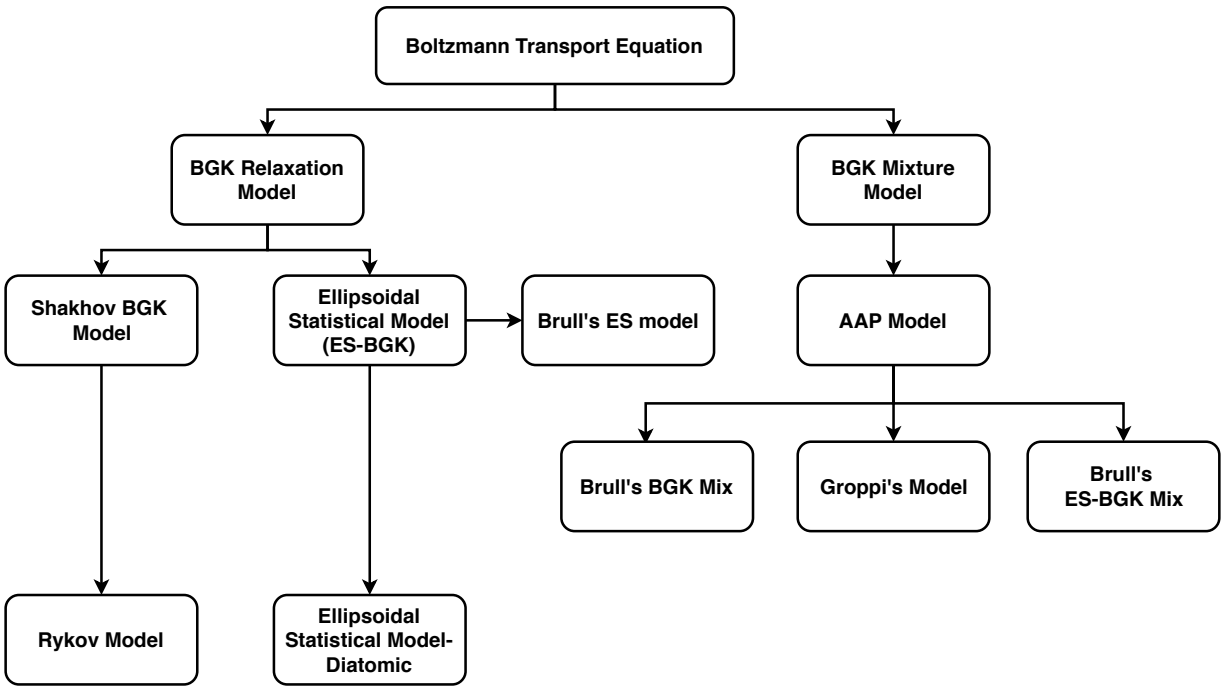

Figure 1.20: Single-species and mixture kinetic models for monoatomic gas tree diagram.

advantage of the model by Groppi et al. is that it contains two relaxation coefficients, capable of fitting two of the transport coefficients correctly, leading to true diffusion and viscosity as summarized in Table 1.3. The model also guarantees positive macroscopic fields. The novel kinetic models introduced in this thesis are based on the Groppi et al. model and for this reason the Groppi et al. model is described in greater detail in the next chapter. Similarly, Brull's BGK mixture model [65] also has species mean velocity in the equilibrium velocity distribution function. The model targets the fit of the diffusion and viscosity coefficients, but requires further work to have a correct Prandtl number. The latest ES-BGK mixture model by Brull [66] has a common mixture velocity in the species distribution function. Two relaxation coefficients recover the exact viscosity and heat flux of the system. However, as outlined in the paper, the value of the Fick coefficient is calculated according to the new model, but remains incorrect (see Table 1.3). A new consistent BGK mixture model was introduced recently [63]. Both Maxwellian and arbitrary potential molecules are considered in the presented model. For an arbitrary number of species, this model was shown to fulfil all consistency requirements concerning conservation laws, equilibria and H-theorem. The number of correctly fitted transport coefficients is not detailed in this work.

In this thesis two new kinetic models are presented that are more advanced than other models currently available in the literature. Key advantages of the new models include accurate modelling of binary mixture of monoatomic gases, accounting for species-specific macroscopic properties, velocity diffusion and the correct definition of all three transport properties, summarized in Table 1.3. Their detailed description and comparison with previous works is the basis

Table 1.3: Transport properties difference between kinetic mixture models

	AAP	**Brull's BGK**	**Groppi's Model**	**Brull's ES-BGK**
Ordinary Diffusion (Fick)		✓	✓	
Viscosity (Newton)	✓	✓	✓	✓
Thermal Conductivity (Fourier)				✓
H-theorem	✓	✓	✓	✓

for Chapter 2.

1.4.2 Numerical Evaluation

The numerical modelling of the Boltzmann and the kinetic relaxation models consists of two separate research areas. The first area is the implementation and validation of the model equations for different applications and conducting a comparison with established results. It usually consists of a new theoretical model, applied by a well-known and reliable numerical method. It is the initial step of numerical tests and explores the limitations and accuracy of the mathematical models. The second research area focuses on numerical efficiency and explores different numerical representations. A well-established theory is applied with a new numerical method with the goal of improving result accuracy or ordinarily for computational efficiency.

Gas mixtures extend further the complexity and the computational expense of this research. However, accounting for the species diffusion in gas mixture flows is essential when strong species gradients and temperature gradients occur. An example application where modelling the flow as a gas mixture is important includes gas separation in order to create multiple products or purify a single product [67, 68].

In this thesis both research questions will be approached. The new kinetic models are first applied with a well-established numerical scheme, validated and compared with known results for a variety of test cases. Then, one of the models will be applied with a numerically efficient scheme with the purpose to reduce the computational expense.

To start with the most widely used computational methods for gas mixtures applying both the Boltzmann and the relaxation equations will be discussed here. Further their main properties are detailed in Table 1.4. Current techniques focused on high-speed gas mixture flows include statistical and deterministic approaches. The direct simulation Monte Carlo (DSMC) method [23, 69, 70] is widely studied and statistically approximates solutions to the Boltzmann equation. It is a particle based method that is most commonly used in modelling flows under rarefied conditions. Each DSMC simulator particle represents a large number of real molecules/atoms and are moved ballistically, while collision events are treated stochastically after the movement step. This makes the DSMC a widely used and reliable algorithm, par-

Mathematical model	Numerical model	Characteristic and Problem
Boltzmann eq.	DSMC	- statistical method - excessive noise & expensive in the transitional regime
Boltzmann eq.	FSM	- deterministic method - computationally very expensive
Kinetic models	DVM	- deterministic method - large memory overhead - unfeasable for most practical applications
AAP	UGKS	- combines GKS and DVM: large memory overhead - capable of modeling variety of levels of rarefaction - matches only 1 transport coefficient in the continuum
AAP	DUGKS	- less expensive than UGKS - capable of modeling variety of levels of rarefaction - matches only 1 transport coefficient in the continuum limit
McCormack	DUGKS	- less expensive than UGKS - valid close to equilibrium - matches all transport coefficient in the continuum limit

Table 1.4: Numerical methods based on mixture models for monoatomic gases.

ticularly in the high Knudsen flows. The limitations of the method occur when the flow is approaching continuum regime, lower speeds or trace gas in a mixture, where challenges arise using DSMC due to large number of particles and long sampling times required. Therefore, there are important applications in which a deterministic solution of the kinetic equations (such as DVM) is desirable. The discrete velocity method (DVM), but also the Unified Gas Kinetic Scheme (UGKS) [58] and Discrete Unified Gas Kinetic Scheme (DUGKS) [59] schemes are deterministic numerical methods, which apply kinetic models. Zhang et al. [71] presented a DUGKS method for a binary mixture based on the McCormack model with a key benefit- correct transport properties and Prandtl number. For microchannel flows, Lorenzani [72] showed semi-analytical solutions for a linearized BGK mixture model. Without this linearization, such semi-analytical solutions cannot be obtained and in the present work the DVM approach is used instead. In comparison to the Monte Carlo method, typical characteristics of deterministic methods include larger memory overhead and computational time than DSMC. This limits the range of applications of DVM. However, there are no statistical sampling errors allowing modelling of flows in regimes that represent a challenge for DSMC.

In this thesis a detailed numerical testing and validation of the new Shakhov-based and ES-based kinetic models for binary gas mixtures is conducted using the DVM for numerical application. Previously, from the single-relaxation models for gas mixtures, the AAP model [57] has been

numerically studied in different schemes, e.g. [58,59,73]. However, as described earlier only one transport coefficient is recovered with this model. In these works, the authors specify that some of the inaccuracies of the results are probably caused by the underlying kinetic model, rather than the numerical scheme itself. It is suggested that more advanced schemes will benefit the solution of the physical problem. Even though improved mixture kinetic models, e.g. [64–66], are available in the literature, they have not been tested numerically yet. Therefore application and validation of more advanced gas mixture models is required. This issue will be addressed in this thesis.

A benchmark test case for validation of new models is the profile of a normal shock wave, since it is the simplest form of high speed non-equilibrium flow. It is a simple step flow between two different equilibrium states and does not involve any boundary layer or wall interactions. Moreover, it is well-inspected for binary mixtures of monoatomic gases, e.g experimentally [74, 75] and numerically [58, 59, 76–78], where all numerical papers validate their results against the results from the full Boltzmann equation [9]. The normal shock wave is an important first step in the numerical validation and evaluation of the capabilities of the new kinetic models. More complex geometries, based on the DVM, have been inspected for high-speed flows of single species gas, e.g. [79], but not many results are available for a mixture of monoatomic gases.

1.4.3 Numerical Schemes

The discrete velocity methods (DVM) [39] require significant computational resources and for the vast majority of aerospace applications, involving hypersonic and rarefied flows, are not feasible. The DSMC method, in comparison, loses efficiency and potentially also accuracy for reduced mean speeds in the considered flow as well as for increasing densities. Therefore, for flows in the transitional regime between rarefied and continuum, particular challenges exist for CFD methods.

The gas kinetic scheme (GKS) based on BGK relaxation models [44, 45] attempts to address these issues by providing an alternative numerical method for applying BGK-based kinetic models and recovering the Navier-Stokes equations in the continuum limit. As originally introduced, GKS methods were Navier-Stokes solvers, and more recently the GKS approach has been extended by a number of authors, e.g. [6, 46, 80], with a capability to resolve thermal non-equilibrium and flow rarefaction effects. The strength of the gas-kinetic scheme lies in its capability to include the effect of collisions introducing a multi-scale effect which is missing in more commonly-used Navier-Stokes schemes. Moreover, due to their nature, gas-kinetic schemes can predict flow fields with a certain degree of rarefaction, enabling the computational analysis of a wide range of high-speed flows from the continuum to the rarefied regime without having to rely on different numerical methods.

For simulation of flows covering a wide range of rarefaction, Xu and co-workers introduced the unified gas kinetic scheme (UGKS) method [15, 81], more recently extended to diatomic gas

flows with rotational relaxation [82] and vibrational and rotational relaxation [83]. The computational overhead of the UGKS is however similar to that of a DVM approach and therefore, despite the capabilities of the UGKS methodology, further work in the development of more computationally efficient methods is still an active line of research, e.g. [16, 80, 84].
Xu introduced a multicomponent gas kinetic scheme [85] based on an inviscid gas kinetic BGK scheme with common mean velocity and temperature. This model was extended to a chemically reacting mixture [86] and more recently to a fourth order multi-species GKS [87] in order to overcome the numerical dissipation caused by the lower order method. A unified gas-kinetic scheme [58] has been constructed for a gas mixture, based on the single-BGK-operator model [57], capable of recovering one transport coefficient correctly. Wang and Xu [58] validate the scheme by inspecting a shock structure under different conditions and the micro channel problem and suggest that some of the discrepancies in the results are due to the selected mixture kinetic model. Most recently a discrete unified gas kinetic scheme (DUGKS) for a binary mixture [59] has been developed, again based on the single-BGK-operator model [57]. The DUGKS possesses all the advantages and shows excellent agreement with the UGKS, while being computationally more efficient. As outlined in that paper, a limitation in both UGKS and DUGKS is connected with the chosen kinetic model that has only one correct transport coefficient in the continuum limit. Very recently the McCormack method was applied with the DUGKS [71] in order to overcome this disadvantage. All transport coefficients are correctly fitted, but the method itself introduces a restriction on the level of non-equilibrium in the flow.
Clearly, there is a need for further improvements and investigation on numerical schemes based on more advanced kinetic models for gas mixtures. Detail level of flow modelling combined with numerical efficiency is key to designing the next generation of high-speed aircrafts.

1.4.4 Diatomic Kinetic Models

Most practical application include flows involving gas mixtures and in the vast majority of cases these are not noble gases. Monatomic mixture models represent an active research area [57, 60–66, 88]. Diatomic molecules present a further modelling challenge due to the internal degrees of freedom (DoF). Molecules, unlike atoms, are known to have rotational and vibrational DoF. These extra degrees of freedom and the corresponding flow-field variables associated with the internal DoF differ for each species in a diatomic gas mixture, which makes the modelling of a mixture of gases with internal degrees of freedom a complex task. At the same time, diatomic gas mixtures are particularly important for aerospace applications such that in cases without chemistry, a binary mixture of nitrogen and oxygen needs to be considered (when ignoring small concentration of argon). Relevant engineering problems include the hypersonic rarefied gas flows, chemical reacting flows and plasmas [1, 25] and other applications in a variety of industries, discussed in the beginning of this chapter. Clearly, a flowfield comprised of a mixture of gases with internal degrees of freedom is of practical interest for numerous domains. In this

section, the focus is on reviewing excising diatomic models and their characteristic features.
The simplest and most widely used simplification of the Boltzmann equation is the Bhatnagar-Gross-Krook (BGK) model [32] for a single-species monoatomic gases. We will focus on the extensions of the BGK model to a model for diatomic molecules, which is to include the internal energy of the gas, and we will consider the different level of detail of each model. Then, we will introduce a new binary mixture model for diatomic gases. Most initial models for polyatomic gases include the internal DoF, where the rotational and vibrational components are not separated, but represent a part of the internal energy. This kind of formalisation is demonstrated in the works by Morse [89], where the internal energy is quantised, and Andries et al. [48], where an alternative approach is used and the internal energy is continuously distributed. Notice that the relationship between the first polyatomic relaxation model shown by Morse [89] to the more detailed and complex WCU [30] is similar to the BGK model [32] and the Boltzmann equation [24] for the monoatomic gas.
The monoatomic BGK model is modified by the Shakhov [33] and Ellipsoidal Statistical (ES) [34] models to have a correct Prandtl number in the continuum limit. Similar extensions for a polyatomic gas with a correct Prandtl number were introduced by the Rykov [90] (defined with a continuously distributed internal energy) and ES [34] polyatomic models (as introduced by Holway with quantum energy levels), which are extensions of the Shakhov model and the monoatomic ES model, respectively. The 4 diatomic models, with the exception of the Andries et al.'s model [48], have a multi-relaxation approach. Their collision term of the right-hand-side (RHS) of the governing equation consists of two stages, splitting the process in elastic and inelastic relaxation, while Andries et al.'s model has a single-relaxation approach. The single-relaxation allows for a more simple formulation, but the multi-step approach better represents the slower excitation of the internal modes. All of the models introduce translational and internal temperatures as separate flow properties, since it is well-known that in flows with strong non-equilibrium effects the single-temperature model is insufficient [1, 25, 91]. Notice that from the four models only the Morse kinetic model [89] does not have a Prandtl correction. A different approach to derive Andries et al.'s model [48] was detailed by Brull and Schneider [50], leading to the same expressions.
More recently the model by Andries et al. [48] was further generalized with a model by Kosuge et al. [92] extending it from a calorically perfect gas to thermally perfect gas by introducing temperature-dependent specific heat. The model inherits an ellipsoidal statistical (ES) correction for the Prandtl number and the continuous distribution of the internal energy. A kinetic model, introduced by Wu et al. [93], presents a model with continuous rotational energy and quantum vibrational energy. The authors build upon a model previously presented by two of them [94] that has continuously distributed energy by coupling it with the model by Morse [89], which contributes to the quantisation of the vibrational energy. The model has a three-step relaxation process and separate translational, rotational and vibrational temperatures. The paper also

features an initial numerical evaluation of the model and shows good comparison with results obtained with DSMC for the selected initial conditions. Titarev and Frolova [95] generalize the Rykov [90] and the polyatomic ES models [48] to take vibrational energy into account. The two extensions have three-step relaxation process for the translational, rotational and vibrational relaxation. The Prandtl number correction is present, but the vibrational heat flux in the continuum limit is not accurately modelled, according to the authors. Nevertheless, the model is comprehensive, has good mathematical properties and is validated with DSMC results. Another recent model is presented by Mathiaud and Mieussens [96]. The model has a single relaxation time to a Maxwellian distribution function, which is based on a single equilibrium temperature. The internal DoF include continuous rotational distribution and discrete vibrational energy. It allows for calorically imperfect gases to be considered. The continuum limit and H-theorem are shown. The simplicity of this model and the detailed description allow us to extend it to a multi-relaxation model for gas mixtures in this article. The original model [96] will be further discussed in the next section.

Modelling the flow as a mixture with separate species-dependent macroscopic properties in the flow-field is important for practical applications. Even though there is a lot of work in the literature on creating models for monoatomic gas mixtures, such models for polyatomic gases (and more specifically diatomic gases) are a less explored area. The model by Mathiaud and Mieussens [96] is said to be extended to a mixture model in the work by Baranger et al. [97]. However, this mixture model has a single Maxwellian distribution for both species (in particular nitrogen and oxygen mixture is discussed due to their small mass ratio) and no species-specific variables or relationships are modelled. As such, the model is lacking detail, e.g. in describing different levels vibrational excitation in the gases. A recent model, introduced by Klingenberg, Pirner and Puppo [98] , is capable of modelling a binary gas mixture with internal degrees of freedom. It demonstrates an extension from a single-species diatomic model [99], which has a separate rotational relaxation applied to the macroscopic variables rather than the RHS of the governing equation. The two gases in the mixture in Klingenberg et al. [98] have individual species-specific self- and cross- collisions, which is consistent with previous monoatomic models from the same authors [60, 62]. An ellipsoidal correction (ES) is also demonstrated in the paper, which corrects the Prandtl number in the continuum limit. Other ES-based models for polyatomic gas mixtures have been detailed with particular focus on chemically-reactive gases [100–102]. However, these models do not model the internal energy in detail, e.g. with a multi-relaxation collision term or separate translational, rotational and vibrational variables. Therefore, even though these models have extended capabilities beyond inert mixtures, they do not possess some of the features of recent models for non-reactive gas mixtures. A model focusing on a mixture of polyatomic and monoatomic gases or two polyatomic gases with different discrete internal energy levels was presented by Bisi and Travaglini [103]. The model is yet to separate the effects of the rotational and vibrational DoF and to introduce multi-relaxation

approach.

Computational results based on the single-species diatomic models have been demonstrated for a variety of test cases and conditions, starting with the work by Huang et al. [104] using the Morse model [89] as early as 1973. Numerous numerical applications based on the polyatomic ES model [48] were performed by Tantos et al. [105, 106]. The model by Rykov has also been extensively tested by Larina et al. [107], Titarev et al. [108], the unified gas-kinetic scheme (UGKS) [82], Colonia et al. [80], etc. The papers presenting more recent kinetic models [92, 93, 97] have shown results for the flow past a cylinder or the profile of a normal shock within the same paper. Validation of these models is limited. In contrast to the models created through extension of previous monoatomic models, a more practical approach is taken by Xu and co-workers [83, 109, 110] in order to simulate a two or three step multi-relaxation process. A more phenomenological approach is taken rather then a detailed mathematical derivation of a new kinetic model. The benefit of this approach is the simplicity of the modelling procedure and the broad variety of test cases.

There are not many results for binary mixture of non-reacting diatomic gases in the literature based on kinetic modelling. Agarwal et al. [31] shows detailed results for the profile of a normal shock wave for a binary mixture of oxygen and nitrogen and also for a mixture of nitrogen and argon. The model used for the simulations is the Generalized Boltzmann equations (GBE), which is identical to the Wang- Chang- Uhlenbeck equations (WCU).

It is clear from the discussion that there is a need for a detailed kinetic model for diatomic gas mixtures and numerical testing to show the model's applicability.

1.5 Summary of Findings

The survey shows that kinetic models for gas mixtures are of practical interest and an active research area. However, developing a model with good mathematical properties and numerically proven capabilities is a challenging task.

Since the introduction of the first Boltzmann relaxation model, many new models and improvements were demonstrated. Monoatomic mixture models in the literature can model species properties and diffusion, while preserving the model compatibility and conservation of mass, momentum and energy. Difficulty occurs when trying to correctly fit more than two transport coefficients in the continuum limit. As a result, the Prandtl number is also incorrect. Furthermore, the most recent models, which demonstrate the best mathematical advantage, are not applied numerically and therefore their capabilities are not inspected beyond the theoretical point. Consequently, more efficient numerical schemes, which allow for complex geometries and varied engineering applications, rely on less advanced models.

Diatomic mixture models present a greater difficulty and in comparison to the monoatomic mixture models less work is conducted. The level of detail of the modelling is insufficient and

accurate representation of the physics of the flow is missing. Standard features of mixture models, e.g. separate species variables, are unaccounted for. The lack of mathematical development leads to lack of numerical testing and evaluation.
This thesis will address the issues summarised here and the next section provides details of the approach taken.

1.6 Aim & Objectives of the Thesis

The aim of the thesis is to derive and analyse a new kinetic model for a binary mixture of gases with internal degrees of freedom for high-speed rarefied flows with improved fidelity over existing models. The model is to be validated and evaluated mathematically and numerically.
The objectives of the thesis are as follows:

1. To analyse the existing models for mixtures of monoatomic gases and identify their limitations.

2. To address the limitations by developing two new kinetic models for binary mixture of monoatomic gases [88]. The goal is to demonstrate models with three correct transport coefficients in the continuum limit and the correct Prandtl number recovery, while accurately modelling species diffusion.

3. To implement the new models in a discrete velocity solver (DVM solver) and evaluate them.

4. To compare with existing results in the literature to validate the models [111, 112]. To demonstrate the changes introduced by the two models and discuss the results.

5. Moreover, to assess the models against results obtained with direct simulation Monte Carlo (DSMC) for challenging high-speed flows.

6. After the models are evaluated with the discrete velocity method, to address the need for higher numerical efficiency. Following the approach of the gas-kinetic scheme to derive one of the kinetic mixture models in a gas-kinetic framework [5]. The purpose is to achieve a numerically efficient scheme for a monoatomic gas mixture, while preserving as much as possible the accuracy demonstrated by the kinetic model.

7. Building on the foundation of the monoatomic mixture models, to develop a binary mixture model for diatomic gases [113]. The model is to have a species translational, species rotational and species vibrational temperatures. A multi-relaxation approach is to be utilised to accommodate for the difference in relaxation times between translation and rotation and rotation and vibration.

8. To model the species velocities and diffusion consistently with the monoatomic version.
9. To obtain transport properties in the continuum limit through the Chapman-Enskog (CE) type expansion.
10. Finally, to numerically evaluate the diatomic mixture model for a gas mixture of nitrogen and oxygen [113].
11. To validate the model against Monte Carlo results for the profile of a normal shock.
12. To consider more complex geometry,e.g. the flow past a circular cylinder.
13. To demonstrate the variation in flow properties through a parametric study with different Mach numbers, vibrational collision numbers and concentration.
14. To investigate the importance of modelling the flow as a mixture by studying the effect of the different levels of vibrational excitation in the different species.

1.7 Outline of the Thesis

The structure of the thesis is as follows:
Chapter 1 presents the motivation and the background of the thesis. A detailed literature survey covers the development of kinetic models and their numerical applications. Limitation and challenges in the field are identified, as well as available solutions.
Chapter 2 presents two new kinetic model: Shakhov-based and ES-based models for a gas mixture of monoatomic gases. The mathematical properties of the new model are demonstrated. The diffusion behaviour between species and the transport properties in the continuum limit are detailed.
Chapter 3 numerically evaluates the new kinetic models for monoatomic mixtures with different mass ratios. The results are validated for a variety of test cases for the profile of a normal shock and the flowfield around a circular cylinder.
Chapter 4 presents a numerically efficient gas-kinetic scheme (GKS) applying the novel Shakhov-based mixture model. The GKS is evaluated against results acquired with the same kinetic model applied with the more computationally expensive but accurate discrete velocity method (DVM) as benchmark results. The computational benefits and limitations of the scheme are discussed.
Chapter 5 presents a new model for a gas mixture of diatomic gases with rotational and vibrational degrees of freedom and three step relaxation process. The chapter contains the derivation of the model, the continuum limit, transport properties and diffusion behaviour of the species.
Chapter 6 evaluates numerically the newly-introduced diatomic mixture model for a mixture of nitrogen and oxygen gases. The results are compared with DSMC acquired results. Physics of

the flow are inspected for a variety ot test condition and different cases.
Chapter 7 is the final chapter of the thesis. It contains contains conclusions and future work.

Chapter 2

Monoatomic Mixture Kinetic Models *

Gas mixtures are important for many practical applications. Extending kinetic model equations of the Bhatnagar-Gross-Krook (BGK) type from a single-species gas to a multi-species gas mixture presents a number of significant challenges. First, obtaining the correct species diffusions, viscous stresses as well as heat conduction in the continuum limit requires a careful design of the collision terms in the kinetic equations. Secondly, the derived model collision terms need to guarantee positivity of the macroscopic fields and distribution functions.

In this chapter, two new kinetic models are introduced and compared: an approach based on the Shakhov kinetic model and an approach involving an anisotropic Gaussian equilibrium function. The models are based on the work by Groppi et al. [64] with new equilibrium distribution functions by incorporating Shakhov-type and ES-type corrections, respectively. The two new models are capable of modelling a binary mixture of monoatomic gases, with updated definitions for the relaxation parameters and target species velocities and temperature. Both methods account for separate species-mean velocity such that the species diffusion and velocity drift are accurately represented. The Chapman-Enskog procedure is followed to derive the asymptotic hydrodynamic limit and provide expressions for viscosity, thermal conductivity and diffusion coefficients.

The novelty of the two newly-introduced models lies in the capability to capture one extra transport property and a correct Prandtl number in the continuum limit for binary mixtures of chemically inert gases in comparison to the existing kinetic mixture models, e.g. [64–66]. The extensions of the two models provide an extra relaxation parameter that allows for the correct fit of the three transport coefficients: Fick, Newton and Fourier laws in the continuum limit. This is a significant improvement. The models enjoy good mathematical properties, including conservation of mass, momentum and energy, indifferentiability condition and more specifically for the ES-based model the H-theorem and the equilibrium state at maximum entropy are shown.

This chapter details the new kinetic models for binary mixtures of monoatomic gases, their proof and comparison in the continuum limit and the closure of the models with the transport

*Published in European Journal of Mechanics - B/Fluids

coefficients definitions.

2.1 Kinetic Mixture Models

The standard properties described in this section are common between different kinetic mixture models. They are inherent to the Boltzmann equation and provide consistency between the full equation and the simplified relaxation models. For a binary gas mixture the governing equation is defined per species $s = 1,2$ (Eq. (2.1)) and the simplified collision operator Q_s involves a target equilibrium distribution function F_s and the non-equilibrium distribution function f_s. Single-relaxation models are defined by a common collision rate ν for all collision types. The evolution of the species-specific distribution function is governed by the BGK-type relaxation equation:

$$\frac{\partial f_s}{\partial t} + \underline{u} \cdot \nabla_{\underline{x}} f_s = Q_s\left[f_1, f_2\right] \quad ; \quad Q_s = \nu\left(F_s - f_s\right); \quad ; \quad s = 1,2, \tag{2.1}$$

with collision terms $Q_s\left[f_1, f_2\right]$ and $\underline{u}$ the particle velocity. The common collision rate is defined by the gas mixture properties: the pressure p and viscosity μ based on the mixture temperature T, such that $\nu = p/\mu$ and $\underline{u}$ is the particle velocity. The simplification of the kinetic equations lies in the substitution of the complex collision integral of the Boltzmann equation with the relaxation term $Q_s\left[f_1, f_2\right]$, expressed by the relaxation rate of the difference between the equilibrium and non-equilibrium state. The target equilibrium function F_s varies between kinetic models and determines most of the main properties. However, a necessary condition for all models is that the collision term preserves mass, momentum and energy. Note that since the gas is a chemically inert mixture, mass conservation is per species, while momentum and energy can be exchanged between them and it is only the sum over all species that needs to be conserved. Therefore, the following constraints on the collision operator are imposed:

$$\begin{aligned}
&\iiint_{-\infty}^{\infty} Q_s d\underline{u} = 0 \quad ; \quad s = 1,2, \\
&\sum_{s=1}^{2} \iiint_{-\infty}^{\infty} m_s \underline{u} Q_s d\underline{u} = 0, \\
&\sum_{s=1}^{2} \iiint_{-\infty}^{\infty} \frac{1}{2} m_s |\underline{u}|^2 Q_s d\underline{u} = 0,
\end{aligned} \tag{2.2}$$

where $d\underline{u} = dudvdw$. We denote with n_s, ρ_s, u_s and T_s the species macroscopic quantities: number density, density, mean velocity and temperature of a species s. They are found as moments

of the nonequilibrium distribution function f_s:

$$\begin{aligned} n_s &= \iiint_{-\infty}^{\infty} f_s d\underline{u}, \\ n_s \underline{u}_s &= \iiint_{-\infty}^{\infty} \underline{u} f_s d\underline{u}, \\ \frac{3}{2} n_s k T_s &= \frac{m_s}{2} \iiint_{-\infty}^{\infty} (\underline{u} - \underline{u}_s)^2 f_s d\underline{u}, \end{aligned} \tag{2.3}$$

where k is the Boltzmann constant and the species density is $\rho_s = m_s n_s$. From the species macroscopic variables, the overall gas mixture properties n, ρ, $\underline{u}_0$ and T are obtained:

$$\begin{aligned} n = \sum_{s=1}^{2} n_s \;\; ; \;\; \rho = \sum_{s=1}^{2} \rho_s \;\; ; \;\; \underline{u}_0 = \frac{1}{\rho} \sum_{s=1}^{2} \rho_s \underline{u}_s \;\; ; \\ \sum_{s=1}^{2} \rho_s \left(\underline{u}_s - \underline{u}_0\right)^2 = \sum_{s=1}^{2} \rho_s |\underline{u}_s|^2 - \rho |\underline{u}_0|^2 \; ; \end{aligned} \tag{2.4}$$

$$\frac{3}{2} n k T = \sum_{s=1}^{2} \frac{3}{2} n_s k T_s + \frac{1}{2} \sum_{s=1}^{2} \rho_s \left(\underline{u}_s - \underline{u}_0\right)^2. \tag{2.5}$$

The equilibrium solution is defined by the Maxwellian distributions as functions of common macroscopic velocity ($\underline{u}_0$) and gas temperature (T), and number densities n_s for each species:

$$f_s^M(\underline{u}) = n_s \left(\frac{m_s}{2\pi k T}\right)^{3/2} \exp\left[- \frac{m_s}{2kT} \left(\underline{u} - \underline{u}_0\right)^2 \right]. \tag{2.6}$$

These properties are standard for all single-relaxation mixture models and are used by the Groppi et al. model [64] and the new Shakhov-based and ES-based kinetic models. A main difference between kinetic models begins with the introduction of a different target equilibrium distribution function F_s in the collision term on the RHS of Eq. (2.1). The full derivation and description of the models follows in this chapter.

2.2 Groppi, Monica and Spiga's Model

The two new kinetic models introduced build upon the work by Groppi et al. [64]. This section summarises their work and allows for a comparison of the key features of the models, including definitions of the distribution function, target species velocity and temperature.

The collision term involves a common relaxation rate ν as a standard single relaxation model, but the equilibrium distribution function f_s^M is substituted with the modified distribution function

G_s, leading to the following expression for Q_s:

$$Q_s = \nu\big(G_s - f_s\big) \quad ; \quad s = 1,2. \tag{2.7}$$

The modified function allows for species drift velocities $\underline{u}_s^{(g)}$ and common modified temperature $\hat{T}$ that are different from the local gas mixture velocity and temperature. The modified distribution function G_s is then defined as:

$$G_s(\underline{u}) \;=\; n_s\left(\frac{m_s}{2\pi k\hat{T}}\right)^{3/2}\exp\left[-\frac{m_s}{2k\hat{T}}\left(\underline{u}-\underline{u}_s^{(g)}\right)^2\right]. \tag{2.8}$$

The main advantage of Groppi et al's model [64] is the introduction of a second relaxation parameter η, which sets a constraint on the species drift velocity equalisation:

$$\frac{1}{n_1}\iiint_{-\infty}^{\infty}\underline{u}Q_1 d\underline{u} - \frac{1}{n_2}\iiint_{-\infty}^{\infty}\underline{u}Q_2 d\underline{u} = -\eta\left(\underline{u}_1 - \underline{u}_2\right). \tag{2.9}$$

The drift velocity coefficient η was introduced to control the diffusion between species, which in itself is a macroscopic quantity. The coefficient will be used to define the target velocity and temperature and consequently the new target equilibrium distrubution function. The expression for this coefficient is defined in section 2.7.2.

Evaluating the integrals in Eq. (2.9) and following the momentum conservation equation, the species target velocity in G_s is expressed from the local species velocity and the average gas mixture velocity:

$$\underline{u}_s^{(g)} = \Big(1-\frac{\eta}{\nu}\Big)\underline{u}_s + \frac{\eta}{\nu}\underline{u}_0 \quad ; \quad s = 1,2. \tag{2.10}$$

The same principle is applied with the energy conservation equation to express the modified temperature in the equilibrium functions G_s:

$$\hat{T} \;=\; T - \frac{1}{3nk}\sum_{s=1}^{2}\rho_s\big(\underline{u}_s^{(g)} - \underline{u}_0\big)^2 = T - \frac{1}{3nk}\Big(1-\frac{\eta}{\nu}\Big)^2\sum_{s=1}^{2}\rho_s\big(\underline{u}_s - \underline{u}_0\big)^2. \tag{2.11}$$

As demonstrated in the original paper [64] the relaxation ratio is limited in the bounds $0 \leq \eta/\nu \leq 2$ to ensure positive temperature fields. The second relaxation coefficient allows for two transport coefficients to be recovered correctly in the hydrodynamic limit: the Fick and viscosity coefficients. Building upon the discussed model, we aim to fit three transport coefficients with two different approaches, discussed in the next sections.

2.3 Shakhov-based Mixture Model

A Shakhov-type correction is applied to extend the kinetic model in order to correct the Prandtl number. The Prandtl number of a binary mixture has previously been examined [7, 114, 115]. The values it takes depend on the mass ratio between species and the concentration levels as shown in Fig. 2.1.

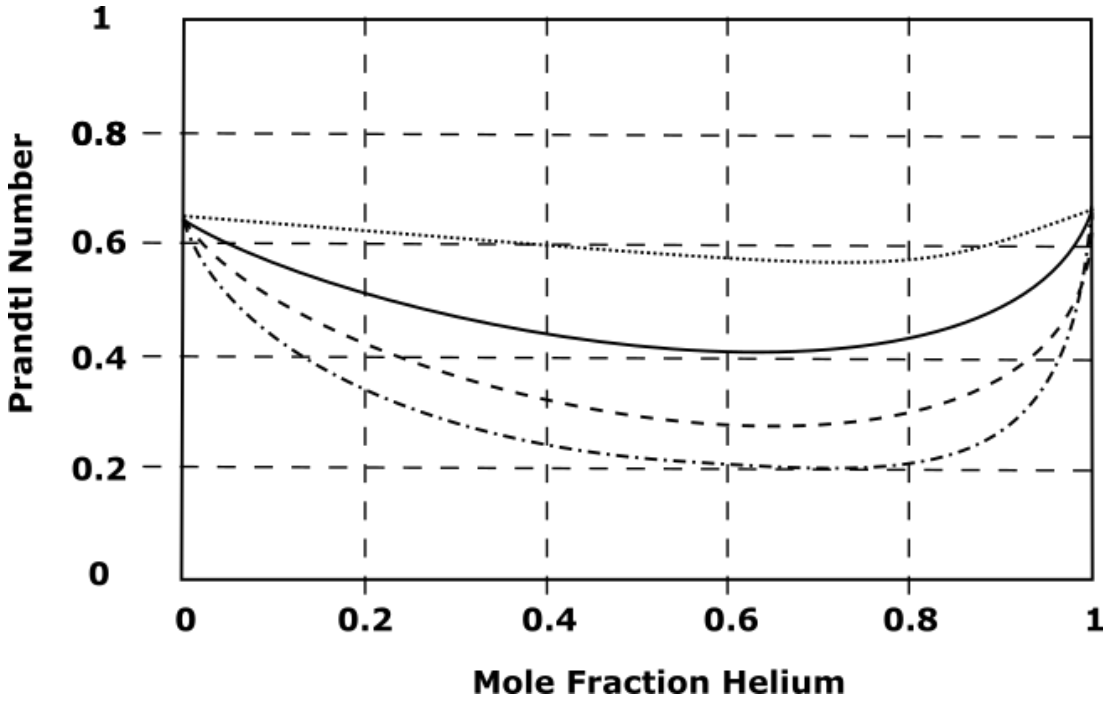

Figure 2.1: Prandtl number variation with concentration and mass ratio between species at 1 atm pressure and 300 K temperature. Helium-Neon (dotted), Helium-Argon (solid), Helium-Krypton (dashed), Helium- Xenon (dot dash). (adapted from Belcher at al. [7])

For high mass ratios (e.g helium-krypton mix with mass ratio of 21) and equal species concentration, the Prandtl number can drop to values as low as $Pr_{mix} = 1/5$, while the maximum values for a monoatomic gas are reached when the gas is pure/simple (i.e. when the mixture consists of 100% of one of the species), leading to $Pr_{mix} = Pr = 2/3$. This creates a 'bucket' type of shape of the Prandtl number plot in Fig. 2.1 with maximums at both ends at $2/3$. In theory increasing the mass ratio further will lead the Prandtl number close to 0 and therefore the limits of the Pr_{mix} for monoatomic gases are $Pr_{mix} \in (0,\ 2/3]$. The expression for the mixture Prandtl number is discussed further in Section 2.6.

The Shakhov model [33] modifies the Maxwellian distribution function by introducing a heat flux correction. Similarly, expanding the described extended Gaussian distribution (Eq. (2.8)), a

new equilibrium distribution function is introduced:

$$G_s^{Sh}(\underline{u}) = \underbrace{n_s\left(\frac{m_s}{2\pi k\hat{T}}\right)^{3/2}\exp\left[-\frac{m_s}{2k\hat{T}}\left(\underline{u}-\underline{u}_s^{(g)}\right)^2\right]}_{G_s(\underline{u})} * \left\{1+\frac{2\left(1-Pr\right)\left(\underline{u}-\underline{u}_s^{(g)}\right)\cdot\underline{q}_s^{corr}}{5p_sk\hat{T}/m_s}\left[\frac{m_s}{2k\hat{T}}\left(\underline{u}-\underline{u}_s^{(g)}\right)^2-\frac{5}{2}\right]\right\}, \quad (2.12)$$

with species pressure p_s defined as $p_s=\rho_sk\hat{T}/m_s=n_sk\hat{T}$ and Pr is a target Prandtl number. The moments of the quasi one-dimensional Shakhov-based mixture model are detailed:

$$\iiint_{-\infty}^{\infty} G_s^{Sh}d\underline{u}=n_s \;\; ; \;\; \iiint_{-\infty}^{\infty}\underline{u}G_s^{Sh}d\underline{u}=n_s\underline{u}_s^{(g)}$$

$$\iiint_{-\infty}^{\infty} u^2G_s^{Sh}d\underline{u}=n_s\left(\frac{k\hat{T}}{m_s}\right)+n_s(u_s^{(g)})^2 \;\; ; \;\; \iiint_{-\infty}^{\infty} v^2G_s^{Sh}d\underline{u}=\iiint_{-\infty}^{\infty} w^2G_s^{Sh}d\underline{u}=n_s\left(\frac{k\hat{T}}{m_s}\right)$$

$$\iiint_{-\infty}^{\infty} u^3G_s^{Sh}d\underline{u}=3n_su_s^{(g)}\left(\frac{k\hat{T}}{m_s}\right)+n_s(u_s^{(g)})^3+\frac{6\left(1-Pr\right)q_{x_s}^{corr}}{5m_s}$$

$$\iiint_{-\infty}^{\infty} uv^2G_s^{Sh}d\underline{u}=\iiint_{-\infty}^{\infty} uw^2G_s^{Sh}d\underline{u}=n_su_s^{(g)}\left(\frac{k\hat{T}}{m_s}\right)+\frac{2\left(1-Pr\right)q_{x_s}^{corr}}{5m_s} \quad (2.13)$$

In the single species Shakhov model, the heat flux correction $\underline{q}^{corr}$, which goes into the distribution function, is the full heat flux. This represents the Fourier conduction effect. The heat flux correction for two or more species is defined for each species individually and only affects the conduction part of the heat flux. For single-species, it is computed by taking the moment of the non-equilibrium distribution function f^{ε} (expanded by the Chapman-Enskog expansion as described in Chapter 1 Eq. (1.16)) with respect to the mean gas velocity $\frac{1}{2}m(\underline{u}-\underline{u}_0)(\underline{u}-\underline{u}_0)^2$ as:

$$\underline{q}^{corr}=\iiint_{-\infty}^{\infty}\frac{1}{2}m(\underline{u}-\underline{u}_0)(\underline{u}-\underline{u}_0)^2f^{\varepsilon}d\underline{u}. \quad (2.14)$$

For a mixture of gases, the heat flux of the gas comprises of energy flux based on the temperature gradient (thermal conductivity) and the mass gradient (the Dufour effect). However, the introduced Shakhov correction is not affected by the coupled effect, but only from the direct effect of energy flux dependent on the temperature gradient (Fourier effect). To achieve a heat flux correction $\underline{q}_s^{corr}$ that involves only the Fourier effect, the moments of the non-equilibrium

distribution function f_s^ε are taken with respect to the species mean velocity: $\frac{1}{2}m_s(\underline{u}-\underline{u}_s)(\underline{u}-\underline{u}_s)^2$ as:

$$\underline{q}_s^{corr} = \iiint_{-\infty}^{\infty} \frac{1}{2} m_s(\underline{u}-\underline{u}_s)(\underline{u}-\underline{u}_s)^2 f_s^\varepsilon d\underline{u}. \tag{2.15}$$

The expression for f_s^ε comes from the Chapman-Enskog expansion up to $O(\varepsilon^2)$ order (see Eq. (2.48) and Eq. (2.49)). The heat flux correction is found from:

$$\iiint_{-\infty}^{\infty} m_s(\underline{u}-\underline{u}_s)\frac{1}{2}(\underline{u}-\underline{u}_s)^2 f_s^\varepsilon d\underline{u} = \iiint_{-\infty}^{\infty} m_s(\underline{u}-\underline{u}_s)\frac{1}{2}(\underline{u}-\underline{u}_s)^2\Big\{G_s^{Sh} - \frac{\varepsilon}{\nu}\Big(\frac{\partial f_s^M}{\partial t} + \underline{u}\frac{\partial f_s^M}{\partial \underline{x}}\Big)\Big\} d\underline{u} + O(\varepsilon^2). \tag{2.16}$$

In the continuum limit the integration yields:

$$\iiint_{-\infty}^{\infty} m_s(\underline{u}-\underline{u}_s)\frac{1}{2}(\underline{u}-\underline{u}_s)^2 G_s^{Sh} d\underline{u} = \frac{5}{2} n_s kT\left(\underline{u}_s^{(g)} - \underline{u}_s\right) + (1-Pr)\underline{q}_s^{corr} + O(\varepsilon^2)$$

$$\iiint_{-\infty}^{\infty} m_s(\underline{u}-\underline{u}_s)\frac{1}{2}(\underline{u}-\underline{u}_s)^2\Big\{-\frac{\varepsilon}{\nu}\Big(\frac{\partial f_s^M}{\partial t} + \underline{u}\frac{\partial f_s^M}{\partial \underline{x}}\Big)\Big\} d\underline{u} = \frac{\eta}{\nu}\frac{5}{2} n_s kT(\underline{u}_s - \underline{u}_0) - \frac{\varepsilon}{\nu}\frac{5}{2}k\frac{n_s kT}{m_s}\frac{\partial T}{\partial \underline{x}} + O(\varepsilon^2), \tag{2.17}$$

where ε represents a small parameter, corresponding to the Knudsen number, used in the Chapman-Enskog expansion (see Appendix C). Combining the two parts of the integration and substituting the expression for $u_s^{(g)}$ (Eq. (2.19)) leads to the expression for the heat flux correction.

$$\begin{aligned} \underline{q}_s^{corr} &= -\frac{\varepsilon}{\nu}\frac{5}{2}k\frac{n_s kT}{m_s}\frac{\partial T}{\partial \underline{x}} + (1-Pr)\underline{q}_s^{corr} + O(\varepsilon^2) \\ \underline{q}_s^{corr} &= -\frac{\varepsilon}{\nu}\frac{5}{2}\frac{k}{Pr}\frac{n_s kT}{m_s}\frac{\partial T}{\partial \underline{x}} + O(\varepsilon^2) \end{aligned} \tag{2.18}$$

The moments of the extended distribution function G_s^{Sh} are unchanged up to and including second order in molecular velocity in comparison to Groppi et al.'s model [64]. As expected from a Shakhov-type correction, only the third order moments are affected with a correction on the heat flux with the Prandtl number (see Eq. (2.13)). Therefore, the expressions for $\underline{u}_s^{(g)}$ and $\hat{T}$ are unchanged in comparison to the original model (Eq. (2.10) and Eq. (2.11)):

$$\underline{u}_s^{(g)} = \Big(1-\frac{\eta}{\nu}\Big)\underline{u}_s + \frac{\eta}{\nu}\underline{u}_0 \quad ; \quad s = 1,2. \tag{2.19}$$

From the energy conservation, the modified temperature in the distribution function G_s^{Sh} is expressed:

$$\hat{T} = T - \frac{1}{3nk}\sum_{s=1}^{2}\rho_s\left(\underline{u}_s^{(g)} - \underline{u}_0\right)^2 = T - \frac{1}{3nk}\left(1-\frac{\eta}{\nu}\right)^2\sum_{s=1}^{2}\rho_s\left(\underline{u}_s - \underline{u}_0\right)^2, \tag{2.20}$$

$$nk\hat{T} = \sum_{s=1}^{2} n_s k T_s + \frac{1}{3}\left[\frac{\eta}{\nu}\left(2-\frac{\eta}{\nu}\right)\sum_{s=1}^{2}\rho_s\left(\underline{u}_s - \underline{u}_0\right)^2\right]. \tag{2.21}$$

To preserve positive temperature fields the ratio of relaxation parameters η/ν needs inspection. The collision rate is defined by strictly positive quantities: viscosity μ and pressure p and therefore $\nu > 0$. The second relaxation coefficient η, defined in section 2.7.2, has the same constraint $\eta > 0$, as imposed by the Groppi et al. [64]. Therefore, the lower bound of the ratio is $\eta/\nu > 0$. In Eq. (2.21) for $T_s > 0$, the $\hat{T} > 0$ is guaranteed for $\left(2-\frac{\eta}{\nu}\right) \geq 0$, leading to the upper bound $\frac{\eta}{\nu} \leq 2$. The limits of the ratio of relaxation coefficients are then $0 < \eta/\nu \leq 2$. The relaxation ratio is with the same limits for preserving positive temperature fields as the original mixture model.

Clearly the ratio η/ν is an important part of the definition of the model and is bound by limits defined above. It is discussed in detail for both the Shakhov- and ES-based models in section 2.7.

2.4 ES-based Mixture Model

Starting from the same original distribution function (Eq. (2.8)), an anisotropic modification is formulated, following the approach used for the single species ES model [34] . The new distribution function is defined as:

$$G_s^{ES}(\underline{u}) = \frac{n_s}{\sqrt{det(2\pi\underline{\underline{\Lambda}}_s)}}\exp\Big[-\frac{1}{2}\left(\underline{u}-\underline{u}_s^{(g)}\right)\cdot\underline{\underline{\Lambda}}_s^{-1}\cdot\left(\underline{u}-\underline{u}_s^{(g)}\right)\Big]. \tag{2.22}$$

The separate drift velocity $\underline{u}_s^{(g)}$ for each species is kept as in the isotropic Gaussian, while the tensor $\underline{\underline{\Lambda}}_s$ is introduced by the temperature $\hat{T}$ and the ES relaxation parameter ν_{ES}:

$$\underline{\underline{\Lambda}}_s = \nu_{ES}\underline{\underline{\Theta}}_s + \left(1-\nu_{ES}\right)\left(\frac{k\hat{T}}{m_s}\right)\underline{\underline{I}}, \tag{2.23}$$

where the tensor $\underline{\underline{\Theta}}_s$ is also based on the species drift velocity $\underline{u}_s^{(g)}$ as:

$$\underline{\underline{\Theta}}_s = \frac{1}{n_s}\iiint_{-\infty}^{\infty}\left(\underline{u}-\underline{u}_s^{(g)}\right)\otimes\left(\underline{u}-\underline{u}_s^{(g)}\right)f_s d\underline{u}. \tag{2.24}$$

For a quasi one-dimensional flow ($u_0 \neq 0, v_0 = 0, w_0 = 0$) the elements of the matrix $\underline{\underline{\Lambda}}_s$ can be obtained as:

$$\begin{aligned}
\lambda_{11}^s &= \left(1-\nu_{ES}\right)\left(\frac{k\hat{T}}{m_s}\right)+\frac{\nu_{ES}}{n_s}\iiint_{-\infty}^{\infty}\left(u-u_s^{(g)}\right)^2 f_s^{\varepsilon} d\underline{u}\\
\lambda_{22}^s &= \left(1-\nu_{ES}\right)\left(\frac{k\hat{T}}{m_s}\right)+\frac{\nu_{ES}}{n_s}\iiint_{-\infty}^{\infty} v^2 f_s^{\varepsilon} d\underline{u}\\
\lambda_{33}^s &= \left(1-\nu_{ES}\right)\left(\frac{k\hat{T}}{m_s}\right)+\frac{\nu_{ES}}{n_s}\iiint_{-\infty}^{\infty} w^2 f_s^{\varepsilon} d\underline{u}
\end{aligned} \tag{2.25}$$

with all off-diagonal elements equal to zero. In the continuum limit after substituting the 1st-order CE expansion for f_s^{ε} the tensor elements become:

$$\begin{aligned}
\lambda_{11}^s = \left(1-\nu_{ES}\right)\left(\frac{k\hat{T}}{m_s}\right)+\frac{\nu_{ES}}{n_s}\iiint_{-\infty}^{\infty}\left(u-u_s^{(g)}\right)^2 G_s^{ES} d\underline{u} - \frac{\nu_{ES}}{n_s}\frac{\varepsilon\left(1-\nu_{ES}\right)}{\nu}\iiint_{-\infty}^{\infty}\Big\{\left(u-u_0\right)^2\\
-2\left(u-u_0\right)\left(u_0-u_s^{(g)}\right)+\left(u_0-u_s^{(g)}\right)^2\Big\}\Big(\frac{\partial f_s^M}{\partial t}+u\frac{\partial f_s^M}{\partial x}+v\frac{\partial f_s^M}{\partial y}\Big)d\underline{u}\\
\Rightarrow \lambda_{11}^s = \left(\frac{k\hat{T}}{m_s}\right)-\nu_{ES}\frac{\varepsilon}{\nu}\frac{kT}{m_s}\frac{4}{3}\frac{\partial u_0}{\partial x}+O(\varepsilon^2)
\end{aligned} \tag{2.26}$$

and for λ_{22}^s and λ_{33}^s:

$$\begin{aligned}
\lambda_{22}^s = \left(1-\nu_{ES}\right)\left(\frac{k\hat{T}}{m_s}\right)+\frac{\nu_{ES}}{n_s}\iiint_{-\infty}^{\infty} v^2 G_s^{ES} d\underline{u}\\
-\frac{\nu_{ES}}{n_s}\frac{\varepsilon\left(1-\nu_{ES}\right)}{\nu}\iiint_{-\infty}^{\infty} v^2\Big(\frac{\partial f_s^M}{\partial t}+u\frac{\partial f_s^M}{\partial x}+v\frac{\partial f_s^M}{\partial y}\Big)d\underline{u}\\
\Rightarrow \lambda_{22}^s = \left(\frac{k\hat{T}}{m_s}\right)+\nu_{ES}\frac{\varepsilon}{\nu}\frac{kT}{m_s}\frac{2}{3}\frac{\partial u_0}{\partial x} \quad ; \qquad \lambda_{33}^s = \left(\frac{k\hat{T}}{m_s}\right)+\nu_{ES}\frac{\varepsilon}{\nu}\frac{kT}{m_s}\frac{2}{3}\frac{\partial u_0}{\partial x}
\end{aligned} \tag{2.27}$$

The collision operator is also altered with the relaxation parameter ν_{ES} and is in the form:

$$Q_s = \frac{\nu}{1-\nu_{ES}}\left(G_s - f_s\right) \quad ; \quad s = 1,2, \tag{2.28}$$

where the expression for ν_{ES} is bound by the Prandtl number and $Pr = \frac{1}{1-\nu_{ES}}$ as in [48]. For monoatomic gases the parameter $Pr = 2/3$, which leads to $\nu_{ES} = -1/2$. This value assures the mixture Prandtl number Pr_{mix} has a correct behavior in the limit of a pure monoatomic gas for the ES-based model, as will be demonstrated in Section 2.6. Therefore, following the relaxation between velocities, introduced by Groppi and co-workers [64] (Eq. (2.9)):

$$\frac{1}{n_1}\iiint_{-\infty}^{\infty} \underline{u} Q_1 d\underline{u} - \frac{1}{n_2}\iiint_{-\infty}^{\infty} \underline{u} Q_2 d\underline{u} = -\eta\left(\underline{u}_1 - \underline{u}_2\right) \tag{2.29}$$

leads to a modified relaxation of the mean species velocities:

$$\begin{aligned} \frac{\nu}{1-\nu_{ES}}\left[\left(\underline{u}_1^{(g)} - \underline{u}_1\right) - \left(\underline{u}_2^{(g)} - \underline{u}_2\right)\right] &= -\eta\left(\underline{u}_1 - \underline{u}_2\right) \\ \Rightarrow \underline{u}_1^{(g)} - \underline{u}_2^{(g)} &= \left(1 - \frac{\eta}{\nu}(1-\nu_{ES})\right)\left(\underline{u}_1 - \underline{u}_2\right). \end{aligned} \tag{2.30}$$

To finalise the definition of the new kinetic model, we examine the expressions for the species modified velocity and temperature. The formulation of $\underline{u}_s^{(g)}$ is now changed to accommodate for the relaxation parameter, characteristic for the ES model ν_{ES}:

$$\underline{u}_s^{(g)} = \left(1 - \frac{\eta}{\nu}(1-\nu_{ES})\right)\underline{u}_s + \frac{\eta}{\nu}(1-\nu_{ES})\underline{u}_0 \quad ; \quad s = 1,2. \tag{2.31}$$

The common target temperature $\hat{T}$ is also required to change to provide an energy conserving model:

$$\hat{T} = T - \frac{1}{3nk(1-\nu_{ES})}\left[\sum_{s=1}^{2}\rho_s\left(\underline{u}_s^{(g)} - \underline{u}_0\right)^2 - \nu_{ES}\sum_{s=1}^{2}\rho_s\left(\underline{u}_s - \underline{u}_0\right)^2 + \nu_{ES}\sum_{s=1}^{2}\rho_s\left(\underline{u}_s^{(g)} - \underline{u}_s\right)^2\right]. \tag{2.32}$$

The expression for $\hat{T}$ as a function of the mean species and gas velocities is obtained by substituting $\underline{u}_s^{(g)}$ from equation (2.31) into (2.32):

$$\hat{T} = T - \frac{1}{3nk}\left[\left(1 - \frac{\eta}{\nu}(1-\nu_{ES})\right)^2\sum_{s=1}^{2}\rho_s\left(\underline{u}_s - \underline{u}_0\right)^2\right]. \tag{2.33}$$

A comparison with the original expression for $\hat{T}$ (Eq. (2.11)) shows that the additional term comes from the relaxation change ν_{ES} introduced by the ES correction. Setting $\nu_{ES} = 0$ will eliminate the difference and the equations will reduce to Groppi et al.'s model [64]. This is also true for the Shakhov-based model when $Pr = 1$. Notice that when the gas equilibrium temperature is substituted with:

$$\frac{3}{2}nkT = \frac{3}{2}\sum_{s=1}^{2}n_s k T_s + \frac{1}{2}\sum_{s=1}^{2}\rho_s(\underline{u}_s - \underline{u}_0)^2 \tag{2.34}$$

Eq. (2.33) becomes:

$$nk\hat{T} = \sum_{s=1}^{2} n_s k T_s + \frac{1}{3}\left[\frac{\eta}{\nu}(1-\nu_{ES})\left(2-\frac{\eta}{\nu}(1-\nu_{ES})\right)\sum_{s=1}^{2}\rho_s\left(\underline{u}_s-\underline{u}_0\right)^2\right]. \quad (2.35)$$

To guarantee a positive temperature, the fraction η/ν is in the limits $0 \leq \eta/\nu \leq 2/(1-\nu_{ES})$. In comparison to the Groppi model the possible range for the relaxation parameter η is more restrictive due to the introduction of ν_{ES} with maximum value of $\eta/\nu = 4/3$ when the maximum for $\nu_{ES} = -1/2$ for a monoatomic binary mixture is reached.

2.5 Properties

The fundamental properties derived for the Boltzmann model need to be satisfied by the kinetic models. For a gas mixture, these include the H-theorem, the equilibrium state, indifferentiability principle, collision invariants and continuum limit and are discussed in this and the following sections.

2.5.1 H-functional

The entropy of a system increases constantly until it reaches its maximum at the equilibrium level. The H-theorem is an a priori statement that guarantees the second law of thermodynamics is preserved, where the connection between H and the entropy S was indicated by Boltzmann in 1872 [24] and relates with an opposite sign and constant as $S = -kH$. This means that for maximum entropy S, H is minimised.
The H-theorem is shown for the ES-based model in this section. For a binary gas mixture:

$$H = \sum_{s=1}^{2}\iiint_{-\infty}^{\infty}(f_s ln f_s - f_s)d\underline{u}. \quad (2.36)$$

We will prove that:

$$\frac{\partial H}{\partial t} = \frac{\partial}{\partial t}\sum_{s=1}^{2}\iiint_{-\infty}^{\infty}(f_s ln f_s - f_s)d\underline{u} \leq 0. \quad (2.37)$$

The LHS of Eq. (2.37) can be simplified as:

$$\frac{\partial}{\partial t}\sum_{s=1}^{2}\iiint_{-\infty}^{\infty}(f_s ln f_s - f_s)d\underline{u} = \sum_{s=1}^{2}\iiint_{-\infty}^{\infty}\frac{\partial}{\partial t}(f_s ln f_s - f_s)d\underline{u} = \sum_{s=1}^{2}\iiint_{-\infty}^{\infty}\frac{\partial f_s}{\partial t} ln f_s d\underline{u}\,. \quad (2.38)$$

The governing equation for the ES-based model for a spatially homogeneous problem allows to express the derivative of f_s:

$$\frac{\partial f_s}{\partial t} = \frac{\nu}{1-\nu_{ES}}(G_s^{ES} - f_s) \;\; ; \;\; s = 1,2, \tag{2.39}$$

$$\frac{\partial}{\partial t}\sum_{s=1}^{2}\iiint_{-\infty}^{\infty}(f_s ln f_s - f_s)d\underline{u} \;\; = \;\; \sum_{s=1}^{2}\iiint_{-\infty}^{\infty}\frac{\nu}{1-\nu_{ES}}(G_s^{ES} - f_s)ln f_s d\underline{u}. \tag{2.40}$$

Since $y(x) = xlnx - x$ is a strictly convex function for $x > 0$ and $y'(x) = lnx$ it follows that for $x = f_s$:

$$\sum_{s=1}^{2}\iiint_{-\infty}^{\infty}(G_s^{ES} - f_s)ln f_s d\underline{u} \;\; \leq \;\; H(G_s^{ES}) - H(f_s). \tag{2.41}$$

It is sufficient to prove that $H(G_s^{ES}) \leq H(f_s)$. This is a challenging derivation and it is better to consider the following process $H(G_s^{ES}) \leq H(G_s^{\underline{\underline{\Theta}}_s}) \leq H(G_s) \leq H(f_s)$.
The first two inequalities are deduced by analogy with the formal derivation of the ES-BGK model [48], where the velocity is $u_s^{(g)}$, the temperature: $\hat{T}$, $\underline{\underline{\Lambda}}_s$ and $\underline{\underline{\Theta}}_s$ are functions of $u_s^{(g)}$ and $\hat{T}$. The distribution functions G_s^{ES} and G_s are defined as before (see Eq. (2.22) and Eq. (2.8) respectively) and $G_s^{\underline{\underline{\Theta}}_s}$ expressed from the tensor $\underline{\underline{\Theta}}_s$ for $\nu_{ES} = 1$ as:

$$G_s^{\underline{\underline{\Theta}}_s} \;\; = \;\; \frac{n_s}{\sqrt{det(2\pi\underline{\underline{\Theta}}_s)}}\exp\Big[-\frac{1}{2}\big(\underline{u} - \underline{u}_s^{(g)}\big)\cdot\underline{\underline{\Theta}}_s^{-1}\cdot\big(\underline{u} - \underline{u}_s^{(g)}\big)\Big]. \tag{2.42}$$

Following [48]:

$$H(G_s^{ES}) - H(G_s^{\underline{\underline{\Theta}}_s}) = \frac{1}{2}\sum_{s=1}^{2} n_s ln\frac{det\ \underline{\underline{\Theta}}_s}{det\ \underline{\underline{\Lambda}}_s}. \tag{2.43}$$

If the RHS of Eq. (2.43) is negative, $H(G_s^{ES}) \leq H(G_s^{\underline{\underline{\Theta}}_s})$ follows. This is achieved only if $det\ \underline{\underline{\Lambda}}_s \geq det\ \underline{\underline{\Theta}}_s$, the detailed derivation of which is described by Andries et al. [48, 116]. Andries and Perthame [116] and the reference therein state the classical result that the entropy at a given velocity, number density and pressure tensor ($\underline{\underline{\Theta}}_s$) is minimised for the Gaussian defined by that pressure tensor and therefore $H(G_s^{\underline{\underline{\Theta}}_s}) \leq H(G_s)$.
The final inequality ($H(G_s) \leq H(f_s)$) follows the proof of the H function of the original model [64], but with the new definition of $u_s^{(g)}$ and the allowed range of the relaxation parameter $0 < \eta < 2\nu/(1-\nu_{ES})$. This is done by the direct evaluation of $H(G_s)$ and $H(f_s)$, where the entropy evaluated at the local Maxwellian (f_s^{LocM}) with the same variables of the non-equilibrium

f_s (u_s, n_s and T_s) is $H(f_s^{LocM})$ and is less than the entropy $H(f_s)$.

$$\begin{aligned} H(G_s) &= \sum_{s=1}^{2} n_s \left(ln(n_s) + \frac{3}{2} ln\left(\frac{m_s}{2\pi k \hat{T}} \right) \right) - n, \\ H(f_s) \geq H(f_s^{LocM}) &= \sum_{s=1}^{2} n_s \left(ln(n_s) + \frac{3}{2} ln\left(\frac{m_s}{2\pi k T_s} \right) \right) - n \\ &\Rightarrow \quad H(G_s) - H(f_s) \leq \sum_{s=1}^{2} \frac{3}{2} n_s ln\left(\frac{T_s}{\hat{T}} \right) \leq \frac{3}{2\hat{T}} \left(\sum_{s=1}^{2} n_s T_s - n\hat{T} \right). \end{aligned} \tag{2.44}$$

The last inequality is due to the second order Taylor expansion for lnT_s, centered at $\hat{T}$: ($lnT_s \leq ln\hat{T} + (T_s - \hat{T})/\hat{T}$). From Eq. (2.33) and for the allowed range of η, it follows that $n\hat{T} \geq \sum_{s=1}^{2} n_s T_s$ and therefore $H(G_s) \leq H(f_s)$.
Since $H(G_s^{ES}) \leq H(G_s^{\underline{\underline{\Theta}}_s}) \leq H(G_s) \leq H(f_s)$ then $H(G_s^{ES}) - H(f_s) \leq 0$:

$$\begin{aligned} \frac{\partial}{\partial t} \sum_{s=1}^{2} \iiint_{-\infty}^{\infty} (f_s ln f_s - f_s) d\underline{u} &\leq \frac{\nu}{1 - \nu_{ES}} (H(G_s^{ES}) - H(f_s)) \leq 0 \\ &\Longrightarrow \quad \frac{\partial H}{\partial t} \leq 0 \,. \end{aligned} \tag{2.45}$$

With the H function minimised, the proof is completed.

2.5.2 Equilibrium

The entropy of a gas increases with time and reaches maximum at equilibrium. To achieve the equality of the H-functional, a necessary condition is $(H(G_s^{ES}) - H(f_s^{LocM})) = 0$, which can be expanded as:

$$\underbrace{H(G_s^{ES}) - H(G_s)}_{} + \underbrace{H(G_s) - H(f_s^{LocM})}_{} = 0, \tag{2.46}$$

where f_s^{LocM} is the local Maxwellian defined with species variables n_s, u_s and T_s as described previously. We know from the previous section that both expressions within the brackets are non-positive. Therefore, in order to satisfy the equation, each one needs to be 0. It follows that $H(G_s^{ES}) - H(G_s) = 0$ and $H(G_s) - H(f_s^M) = 0$ or $H(G_s^{ES}) = H(G_s)$ and $H(G_s) = H(f_s^M)$. The first equality is based on $H(G_s^{ES}) = H(G_s^{\underline{\underline{\Theta}}_s}) = H(G_s)$, following the single species Ellipsoidal statistical model [48]. The entropies $H(G_s^{ES}) = H(G_s^{\underline{\underline{\Theta}}_s})$ are equal only if $det\ \underline{\underline{\Lambda}}_s = det\ \underline{\underline{\Theta}}_s$ according to Eq. (2.43), from which the eigenvalues expression follows: $\lambda_1^s = \lambda_2^s = \lambda_3^s = \frac{k}{m_s}\hat{T}$. The entropies $H(G_s^{\underline{\underline{\Theta}}_s}) = H(G_s)$ are equal when G_s is expressed from the Gaussian structure and equal to $G_s^{\underline{\underline{\Theta}}_s}$. Substituting $\underline{\underline{\Theta}}_s = \frac{k}{m_s}\hat{T}\underline{\underline{I}}$ into Eq. (2.42) leads to the known expression for G_s (Eq. (2.8)).
The equality $H(G_s) = H(f_s^{LocM})$ is inspected by comparing the difference in the entropy expres-

sion in Eq. (2.44) and holds only if $n\hat{T} = \sum_{s=1}^{2} n_s T_s$. Substituting this into Eq. (2.33), it follows that $u_s = u_0$, which leads to $u_s = u_0 = u_s^{(g)}$ and $\hat{T} = T$. Under these constrains the distribution function G_s is equivalent to the isotropic Maxwellian or $G_s \equiv f_s^M$ and $H(G_s) = H(f_s^M) = H(f_s^{LocM})$:

$$\frac{\partial H}{\partial t} = 0 \Longleftrightarrow G_s^{ES} = f_s^M. \tag{2.47}$$

Therefore the equality of the H-functional is achieved at equilibrium and both species have a Maxwellian isotropic distribution. The species target equilibrium temperature and velocities are equal to the mean properties of the mixture.

2.5.3 Indifferentiability principle

The indifferentiability principle, described by Garzo et al. [56], requires the ES-BGK model for two species to reduce to a single species ES-BGK model when the species are identical. To test this principle the species masses are set equal (for a binary mixture this means $m_1 = m_2$) and the distribution function: $\mathbf{G} = \sum_{s=1}^{2} G_s^{ES}$ should satisfy the ES monospecies kinetic model. A necessary assumption [66] is that $u_s = u_0$ for all species s, which leads to $u_s^{(g)} = u_0$ and $\hat{T} = T$. With equal species mass and velocity, the distribution functions differ only by number density n_s and can easily be added up to the distribution function $\mathbf{G}(n, m, u_0, \hat{T})$, which satisfies the indifferentiability principle. Note that under these conditions the principle is also valid for the Shakhov-based model.

2.6 Continuum Limit

In this section the continuum limit of the kinetic models leading to the mass, momentum and energy equations is examined and Groppi et al.'s [64], Shakhov-based and ES-based models are compared using the Chapman-Enskog expansion. This is performed in order to achieve the asymptotic limit, but also to emphasize the difference between the models and how and where the two proposed models make corrections. In the near-continuum regime, the Knudsen number can be used as a small perturbation parameter $\varepsilon \ll 1$ to perform a Chapman-Enskog expansion up to $O(\varepsilon^2)$ order, where f_s^ε is of order $O(1)$ after rescaling with ε (see Eq. (2.48)), as described in Chapter 1:

$$\varepsilon\Big(\frac{\partial f_s^\varepsilon}{\partial t} + \underline{u}\cdot\nabla_{\underline{x}} f_s^\varepsilon\Big) \;=\; \nu\Big(F_s\big[f_1^\varepsilon, f_2^\varepsilon\big] - f_s^\varepsilon\Big) \;\;;\;\; s = 1,2, \tag{2.48}$$

where F_s=G_s, G_s^{Sh}, G_s^{ES} for the corresponding model, $\nu = \frac{\nu}{1-\nu_{ES}}$ for the ES model and f_s^ε is expanded in powers of ε. At zeroth order $F_s\big[f_1^0, f_2^0\big] = f_s^M$, as given by Eq. (2.6) and expressing

the non-equilibrium distribution function from Eq. (2.48) leads to:

$$f_s^{\varepsilon}(\underline{u}) = F_s\left[f_1^{\varepsilon}, f_2^{\varepsilon}\right](\underline{u}) - \frac{\varepsilon}{\nu}\Big(\frac{\partial f_s^M}{\partial t} + \underline{u}\cdot\nabla_{\underline{x}} f_s^M\Big) + O(\varepsilon^2). \tag{2.49}$$

For simplicity the quasi one-dimensional flow is considered from here onwards. The evolution of the Maxwellian distribution can be derived and after substituting the time derivatives with the spatial gradients from the unexpanded conserved moments leads to:

$$\begin{aligned}
&\frac{\partial f_s^M}{\partial t} + u\frac{\partial f_s^M}{\partial x} = f_s^M\Bigg[\frac{1}{n_s}\big(u-u_0\big)\Big\{\frac{\partial n_s}{\partial x} - \frac{\rho_s}{\rho}\frac{\partial n}{\partial x}\Big\} \\
&+\Big(m_s\frac{\big(u-u_0\big)^2+v^2+w^2}{2kT^2} - \frac{m_s n}{\rho T} - \frac{3}{2T}\Big)\Big\{\big(u-u_0\big)\frac{\partial T}{\partial x}\Big\} \\
&+\frac{m_s\big(u-u_0\big)}{kT}\Big\{\big(u-u_0\big)\frac{\partial u_0}{\partial x}\Big\} - \Big(m_s\frac{\big(u-u_0\big)^2+v^2+w^2}{3kT}\Big)\Big(\frac{\partial u_0}{\partial x}\Big)\Bigg].
\end{aligned} \tag{2.50}$$

A key aspect of the kinetic model for the binary mixture is the velocity drift of the species relative to the mean gas mixture. For the velocity component in $x-$direction, the following moments involving molecular velocity u in $x-$direction can be used,where as before F_s=G_s, G_s^{Sh}, G_s^{ES} for the corresponding model and $\nu = \frac{\nu}{1-\nu_{ES}}$ for the ES model.

$$\begin{aligned}
n_s u_s^{\varepsilon} &= \iiint_{-\infty}^{\infty} u\Big[F_s - \frac{\varepsilon}{\nu}\Big(\frac{\partial f_s^M}{\partial t} + u\frac{\partial f_s^M}{\partial x}\Big)\Big]d\underline{u} \\
&= n_s u_s^{(g)} - \frac{kT\varepsilon}{\nu}\Big[\frac{1}{m_s}\frac{\partial n_s}{\partial x} - \frac{n_s}{\rho}\frac{\partial n}{\partial x} + \frac{n_s}{T}\Big(\frac{1}{m_s} - \frac{n}{\rho}\Big)\frac{\partial T}{\partial x}\Big].
\end{aligned} \tag{2.51}$$

Inserting the expression for $u_s^{(g)}$ for each model, the species velocity in the $x-$ direction up to 1st-order in ε is:

$$u_s^{\varepsilon} = u_0 - \frac{\varepsilon kT}{n_s\eta}\Big[\frac{1}{m_s}\frac{\partial n_s}{\partial x} - \frac{n_s}{\rho}\frac{\partial n}{\partial x} + \frac{n_s}{T}\Big(\frac{1}{m_s} - \frac{n}{\rho}\Big)\frac{\partial T}{\partial x}\Big]. \tag{2.52}$$

Total mass, momentum and energy of the system need to be conserved. The mass and momentum equations for the three models in the continuum limit up to $O(\varepsilon^2)$ order are recovered (Eq. (2.53) and Eq. (2.54)), after substituting the expression for $u_s^{(g)}$, $\hat{T}$ and for the ES-based model - the matrix elements λ_s as described in more detail in Appendix C: CE limit. Mass conservation equation:

$$\frac{\partial n_s}{\partial t} + \frac{\partial}{\partial x}\Big\{n_s u_0 - \varepsilon\frac{kT}{\eta}\Big[\frac{1}{m_s}\frac{\partial n_s}{\partial x} - \frac{n_s}{\rho}\frac{\partial n}{\partial x} + \frac{n_s}{T}\Big(\frac{1}{m_s} - \frac{n}{\rho}\Big)\frac{\partial T}{\partial x}\Big]\Big\} = 0. \tag{2.53}$$

From the Chapman-Enskog expansion we find for the mixture momentum equation:

$$\frac{\partial \rho u_0}{\partial t} + \frac{\partial}{\partial x}\Big\{ nkT + \rho u_0^2 - \frac{\varepsilon}{\nu} nkT \frac{4}{3}\frac{\partial u_0}{\partial x} \Big\} = 0,$$

which for the ES-based mixture model is in the same form but with a difference of the ν coefficient:

$$\frac{\partial \rho u_0}{\partial t} + \frac{\partial}{\partial x}\Big\{ nkT + \rho u_0^2 - (1-\nu_{ES})\frac{\varepsilon}{\nu} nkT \frac{4}{3}\frac{\partial u_0}{\partial x} \Big\} = 0,$$

The momentum equation in the Navier-Stokes equations for a compressible one-dimensional flow is most commonly expressed as:

$$\frac{\partial \rho u_0}{\partial t} + \frac{\partial}{\partial x}\Big\{ nkT + \rho u_0^2 - \mu \frac{4}{3}\frac{\partial u_0}{\partial x} \Big\} = 0. \tag{2.54}$$

From which it follows that the viscosity coefficient μ is expressed as $\mu = \frac{\varepsilon}{\nu} nkT$. This is concluded since the viscosity coefficient is the expression expected in front of the velocity derivative $\frac{\partial u_0}{\partial x}$ in the momentum flux. Note again, that for the ES-based model ν represents $\nu = \nu/(1-\nu_{ES})$ and the viscosity coefficient expression is actually $\mu = (1-\nu_{ES})\frac{\varepsilon}{\nu} nkT$.

The corrections in the new models affect the limit of the energy equation and the following three equations demonstrate the introduced change, found in the underbraced temperature gradient term. Since $Pr = \frac{1}{1-\nu_{ES}}$ [48], the Shakhov and ES corrections lead to the same expression for the energy equation. Moreover, when $Pr = 1$ or $\nu_{ES} = 0$ the limit reduces to the original model. This is a desired result and shows theoretical consistency between all models. Note that by examining problems with $Pr = 1$ and $\nu_{ES} = 0$, numerical consistency will also be demonstrated. For the Groppi et al's model the energy equation is:

$$\frac{\partial}{\partial t}\Big[\frac{3}{2}nkT + \frac{1}{2}\rho_0 u_0^2\Big] + \frac{\partial}{\partial x}\Bigg\{ \sum_{s=1}^{2} m_s n_s \Big[\frac{5}{2}\frac{kT}{m_s}u_0 + \frac{1}{2}u_0^3 + \Big\{\frac{5}{2}\frac{kT}{m_s} + \frac{3}{2}u_0^2\Big\}\big(u_0 - u_s\big)\Big] - \varepsilon\frac{kT}{\nu}\sum_{s=1}^{2}\Big[\frac{4}{3}n_s u_0 \frac{\partial u_0}{\partial x} + \underbrace{\frac{5}{2}n_s\Big(\frac{k}{m_s}\Big)\frac{\partial T}{\partial x}}\Big]\Bigg\} = 0. \tag{2.55}$$

The Shakhov correction shows a dependency on Pr :

$$\frac{\partial}{\partial t}\Big[\frac{3}{2}nkT + \frac{1}{2}\rho_0 u_0^2\Big] + \frac{\partial}{\partial x}\Bigg\{ \sum_{s=1}^{2} m_s n_s \Big[\frac{5}{2}\frac{kT}{m_s}u_0 + \frac{1}{2}u_0^3 + \Big\{\frac{5}{2}\frac{kT}{m_s} + \frac{3}{2}u_0^2\Big\}\big(u_0 - u_s\big)\Big] - \varepsilon\frac{kT}{\nu}\sum_{s=1}^{2}\Big[\frac{4}{3}n_s u_0 \frac{\partial u_0}{\partial x} + \underbrace{\frac{1}{Pr}\frac{5}{2}n_s\Big(\frac{k}{m_s}\Big)\frac{\partial T}{\partial x}}\Big]\Bigg\} = 0. \tag{2.56}$$

The ES-based model energy equation:

$$\frac{\partial}{\partial t}\Big[\frac{3}{2}nkT+\frac{1}{2}\rho_0 u_0^2\Big]+\frac{\partial}{\partial x}\Bigg\{\sum_{s=1}^{2}m_s n_s\Big[\frac{5}{2}\frac{kT}{m_s}u_0+\frac{1}{2}u_0^3+\Big\{\frac{5}{2}\frac{kT}{m_s}+\frac{3}{2}u_0^2\Big\}\big(u_0-u_s\big)\Big] -\varepsilon\frac{kT}{\nu}\sum_{s=1}^{2}\Big[\frac{4}{3}n_s u_0\frac{\partial u_0}{\partial x}+\underbrace{(1-\nu_{ES})\frac{5}{2}n_s\Big(\frac{k}{m_s}\Big)\frac{\partial T}{\partial x}}\Big]\Bigg\}=0. \tag{2.57}$$

2.7 Transport Properties

To define the transport coefficients, the flux vectors in the hydrodynamic limit of the kinetic equations need to be studied. It should be noted that the same assumption for a dilute gas mixture as in the Boltzmann equation is made and the gas is considered with low enough density so that the three-body collisions can be ignored.

In this section the expression for transport coefficients known from the literature are compared against the expressions from the Groppi et al. [64], Shakhov-based and ES-based kinetic mixture models. The relaxation coefficients allow to match the received transport properties with the correct values. For this reason we say the relaxation coefficients allow us to "correctly fit" the transport coefficients and the Prandtl number of the kinetic mixture models in the continuum limit.

2.7.1 Diffusion

The mass flux vector in the species conservation equations, excluding the external forces, is caused by gradients of concentration, pressure and temperature. The mass flux equation is taken from Hirschfelder's book [35] as a standard expression and has the following form for species s:

$$\underline{j}_s = n_s m_s \underline{\overline{V}}_s = \frac{n^2}{\rho}m_s m_r \mathscr{D}_{sr}\underline{d}_r - D_s^T\frac{\partial\, lnT}{\partial x}, \tag{2.58}$$

where $\mathscr{D}_{sr}=\mathscr{D}_{rs}$ is the binary diffusion coefficient and is single valued, $r\in\{1,2\}$ and $r\neq s$, $\underline{d}_r$ is such that:

$$\underline{d}_r = \frac{\partial}{\partial \underline{x}}\left(\frac{n_r}{n}\right)+\left(\frac{n_r}{n}-\frac{n_r m_r}{\rho}\right)\frac{\partial\, lnp}{\partial \underline{x}}. \tag{2.59}$$

Splitting the pressure gradient into concentration and temperature expressions and considering only the ordinary diffusion part, provides an expression for the mass flux based on the binary diffusion coefficient $\mathscr{D}_{sr}$:

$$\underline{j}_s = -\frac{n}{\rho}m_s m_r \mathscr{D}_{sr}\left(\frac{\partial n_s}{\partial \underline{x}}-\frac{\rho_s}{\rho}\frac{\partial n}{\partial \underline{x}}\right). \tag{2.60}$$

The binary diffusion coefficient is expressed from the comparison between the mass flux from the CE expansion from Eq. (2.53), shown explicitly in Eq. (2.61) and the above expression provided by Hirschfelder (Eq. (2.60)):

$$\underline{j}_s = -\frac{\varepsilon kT}{\eta}\left(\frac{\partial n_s}{\partial \underline{x}} - \frac{\rho_s}{\rho}\frac{\partial n}{\partial \underline{x}}\right), \tag{2.61}$$

leading to an expression for the coefficient:

$$\mathscr{D}_{sr} = \frac{\varepsilon kT\rho}{\eta n m_s m_r}. \tag{2.62}$$

2.7.2 Viscosity

The viscosity coefficient for the mixture is shown in Section 2.6 (Eq. (2.54)) to be in the form:

$$\mu = \frac{\varepsilon}{\nu} nkT. \tag{2.63}$$

For a binary mixture the diffusion and viscosity coefficients are closely connected [35]:

$$\mu = \frac{5}{3}\frac{m_1 m_2}{(m_1+m_2)}\frac{n\mathscr{D}_{12}}{A^*_{12}}, \tag{2.64}$$

where A^*_{12} is a non-dimensional coefficient, defined by the ratio of collision integrals and is in general a function of the gas temperature and the force law between molecules. However, the variation of A^*_{12} is limited and after inspection of the values of noble mixtures presented in the Weissmann and Mason paper [117], a good approximation for A^*_{12} is $A^*_{12} = 1.11$. Now there is a platform to express the relaxation ratio $\frac{\eta}{\nu}$, required for the computation of the species target velocity $u_s^{(g)}$ and the modified temperature $\hat{T}$:

$$\frac{\eta}{\nu} = \frac{5}{3}\frac{1}{(m_1+m_2)A^*_{12}}\frac{\rho}{n}. \tag{2.65}$$

It is clear that the relaxation ratio will vary only in the regions where strong non-equilibrium effects and large gradients occur and this effect will be amplified for higher mass ratios.
Moreover, it is easy to check that it is within the defined limits for the above expression (Eq. (2.65)) for the Shakhov-based model. A positive density leads to $\eta/\nu > 0$. The upper bound requires considering part of the expression:

$$\frac{1}{m_1+m_2}\frac{\rho}{n} = \frac{1}{m_1+m_2}\frac{n_1m_1+n_2m_2}{n_1+n_2} = \frac{n_1m_1+n_2m_2}{n_1m_1+n_2m_2+n_1m_2+n_2m_1} < 1, \tag{2.66}$$

which is always less than 1 and therefore $\frac{\eta}{\nu} < \frac{5}{3A^*_{12}}$, which in turn leads to $\frac{\eta}{\nu} < 2$ for all ρ, m_1,m_2, etc. This means that the temperature field is always positive for every possible species mass or

density for the Shakhov mixture model.
For the ES-based model, the $\nu_{ES} = -1/2$ corresponds to the typical value for the Prandtl number of a pure monoatomic gas ($Pr = 2/3$), which is the maximum value of the Prandtl number for a gas mixture. A similar study to the Shakhov-based model of the relaxation ratio confirms it is always positive or $\eta/\nu > 0$ for all variables in Eq. (2.65). For $\nu_{ES} = -1/2$, the upper bound is limited to $\eta/\nu \leq 4/3$, which means a necessary condition is:

$$\frac{5}{3}\frac{1}{(m_1+m_2)A_{12}^*}\frac{\rho}{n} \leq \frac{4}{3} \;\rightarrow\; \frac{1}{m_1+m_2}\frac{\rho}{n} \leq 0.888, \tag{2.67}$$

which limits the possible species densities and masses. Note that this condition is for a strict guarantee of positivity, while in practical applications positivity of $\hat{T}$ occurs for a wider range of ratios η/ν. For the test cases considered with the ES-based model within this thesis, the values of $\hat{T}$ were always found to be positive.

2.7.3 Heat Flux

The model introduced by Groppi et al. [64] can recover correctly the diffusion and the viscous coefficients due to the introduction of a second relaxation parameter. The velocity equalisation coefficient η and together with the standard BGK relaxation coefficient ν allows for a maximum of two transport coefficients to be set. The Shakhov and ES-based extensions of this model instigate a third variable- the Prandtl number Pr and the corresponding anisotropic model variable - ν_{ES}. The goal is to recover the thermal conductivity and have a system with three correct transport coefficients. We inspect the thermal conductivity k_s in the expression for the heat flux, found by a standard integration with respect to the mean gas mixture velocity u_0. The non-equilibrium part is common for all models and yields:

$$\begin{aligned}\iiint_{-\infty}^{\infty} m_s(\underline{u}-\underline{u}_0)\frac{1}{2}\big((\underline{u}-\underline{u}_0)^2\big)\Big\{-\frac{\varepsilon}{\nu}\Big(\frac{\partial f_s^M}{\partial t}+\underline{u}\frac{\partial f_s^M}{\partial \underline{x}}\Big)\Big\}d\underline{u} \\ = \frac{\eta}{\nu}\frac{5}{2}n_s kT(\underline{u}_s-\underline{u}_0) - \frac{\varepsilon}{\nu}\frac{5}{2}k\frac{n_s kT}{m_s}\frac{\partial T}{\partial \underline{x}} + O(\varepsilon^2),\end{aligned} \tag{2.68}$$

where as before, for the ES-based model in the above expression $\nu = \frac{\nu}{1-\nu_{ES}}$. The moments with respect to the equilibrium distribution functions are expressed as:

$$\iiint_{-\infty}^{\infty} m_s(\underline{u}-\underline{u}_0)\frac{1}{2}\big((\underline{u}-\underline{u}_0)^2\big)G_s^{Sh} = \Big(1-\frac{\eta}{\nu}\Big)\frac{5}{2}n_s kT(\underline{u}_s-\underline{u}_0) + (1-Pr)\underline{q}_s^{corr} + O(\varepsilon^2), \tag{2.69}$$

$$\iiint_{-\infty}^{\infty} m_s(\underline{u}-\underline{u}_0)\frac{1}{2}\big((\underline{u}-\underline{u}_0)^2\big)G_s^{ES} = \Big(1-\frac{\eta}{\nu}(1-\nu_{ES})\Big)(\underline{u}_s-\underline{u}_0)\Big(\frac{5}{2}n_skT-\nu_{ES}\frac{\varepsilon}{\nu}n_skT\frac{4}{3}\frac{\partial u_0}{\partial x}\Big)+O(\varepsilon^2). \quad (2.70)$$

Combining the moment of the Shakhov and ES-based model with the corresponding CE expansion, provides the heat flux q_s for each model.

$$\begin{aligned}\underline{q}_s^{Sh} &= \frac{5}{2}n_skT(\underline{u}_s-\underline{u}_0)-\frac{\varepsilon}{\nu}\frac{5}{2}k\frac{n_skT}{m_s}\frac{\partial T}{\partial \underline{x}}+(1-Pr)\underline{q}_s^{corr}+O(\varepsilon^2),\\ \underline{q}_s^{ES} &= \frac{5}{2}n_skT(\underline{u}_s-\underline{u}_0)-\frac{\varepsilon(1-\nu_{ES})}{\nu}\frac{5}{2}k\frac{n_skT}{m_s}\frac{\partial T}{\partial \underline{x}}+O(\varepsilon^2).\end{aligned} \quad (2.71)$$

Substituting the previously derived expression for $\underline{q}_s^{corr}$ - Eq. (2.19) for the Shakhov model:

$$\underline{q}_s^{Sh} = \frac{5}{2}n_skT(\underline{u}_s-\underline{u}_0)-\frac{\varepsilon}{\nu}\frac{5}{2}\frac{k}{Pr}\frac{n_skT}{m_s}\frac{\partial T}{\partial \underline{x}}+O(\varepsilon^2). \quad (2.72)$$

Again, we observe consistency between the models when $(1-\nu_{ES})=1/Pr$. The species heat flux is determined by the combination of Fourier law (term involving the temperature gradient) and Dufour effect (term based on the diffusion effect). It is important to remember that only the mixture energy is conserved, while species energy equations would contain a source term due to the exchange of energy between the species. Note that if the species have the same mass, the difference between $\underline{u}_s$ and $\underline{u}_0$ will vanish and the Dufour effect will not contribute to the heat flux.

The main advantage of the proposed models lies in the definition of the Fourier part of the heat flux. The thermal conductivity is qualitatively and quantitatively reproduced and the thermal conductivity coefficient κ_s is recovered for both models as:

$$\kappa_s = \frac{\varepsilon}{\nu}\frac{5}{2}\frac{k}{Pr}\frac{n_skT}{m_s} = \frac{\varepsilon(1-\nu_{ES})}{\nu}\frac{5}{2}k\frac{n_skT}{m_s}. \quad (2.73)$$

2.7.4 Prandtl number

The Prandtl number for a gas mixture Pr_{mix} is evaluated from the gas mixture properties as: $Pr_{mix}=c_p\mu/\kappa$, where $c_p=\frac{5}{2}\frac{k}{m}$ is evaluated with the mixture mass $m=\rho/n$, μ is the mixture viscosity (Eq. (2.63)) and κ is the mixture thermal conductivity coefficient in front of the temperature gradient, received from summing the heat flux expressions (Eq. (2.71) for the ES-based model and Eq. (2.72) for the Shakhov-based model) over all species s.

$$Pr_{mix} = \frac{c_p\mu}{\kappa} = \frac{\frac{5}{2}\frac{k}{m}\frac{\varepsilon}{\nu}nkT}{\frac{\varepsilon}{\nu}\frac{5}{2}\frac{k}{Pr}kT\sum_s\frac{n_s}{m_s}} = \frac{Pr}{\sum_s\frac{n_s}{n}\frac{m}{m_s}}, \quad (2.74)$$

where $Pr = 1/(1-\nu_{ES})$ for the ES-based model. The Prandtl number for a gas mixture is known to vary with the mass and concentration of each species and the same conclusion is observed in the expression for the Pr_{mix}. The maximum value of Pr_{mix} is found in the limiting case when the gas mixture reduces to a pure gas and $Pr_{mix} = Pr$.

2.8 Summary of Findings

Two new kinetic models for binary gas mixtures of monoatomic gases were introduced. The development of the two models was detailed. Both models were compared with an established mixture model. The models were shown to have good mathematical properties and more specifically:

- The Shakhov single-species and ES single-species models that address the Prandtl number problem in the single-species BGK models are well understood. However, so far these approaches had not been applied to gas mixtures. In this chapter the Shakhov- and ES-based extensions were detailed correcting the Prandtl number for a binary mixture kinetic model.

- The equilibrium functions in the collision term for the new mixture models were shown, as well as the new target velocity and temperature values.

- The new models were shown to be consistent with previous work on mixture models. They were shown to reduce to the initial mixture model for Prandtl number of 1.

- The models were shown to reduce to their single species Shakhov and ES models for indifferentiable species.

- The H-theorem was proved for the ES-based mixture model.

- Conservation of mass per species, mixture momentum and mixture energy were demonstrated for all models.

- The continuum limit for the uncorrected mixture model, the Shakhov-based mixture model and the ES-based mixture models was derived and compared. The effect of the Prandtl correction in the continuum limit was clearly identified.

- Species diffusion was accounted for with a relaxation parameter allowing the two species velocities to separate.

- A third relaxation coefficient was introduced in both models to allow for the correct fit of the thermal conductivity coefficient.

- The three relaxation coefficients, the correctly fitted transport coefficients, as well as the correct Prandtl number were defined and derived.
- The Shakhov-based mixture model and the ES-based mixture model were derived with different equilibrium functions and target velocity and temperature expressions, but reduced to the same continuum limit.

Chapter 3

Numerical Evaluation of Mixture Kinetic Models *

The goal of this chapter is to numerically validate the two new kinetic models introduced in Chapter 2 for a range of high-speed flows and demonstrate their capabilities and limitations. The mixture models are first shown to reduce to single species models for identical species and are validated with known results. The indifferentiability principle is demonstrated numerically in this chapter. The models are then validated against known numerical results for normal shocks from the full Boltzmann equation, showing good agreement for species density and temperature profiles. Moreover, the Shakhov- and ES-based models are compared with each other and with the Groppi et al. model, showing the improvement of the shock profile caused by an extra correct transport coefficient. Furthermore, the importance of the Prandtl number correction is also demonstrated with the evaluation of the heat flux. A parametric study demonstrates the variation in flow properties for different mass ratios between species and for different Mach numbers. Finally, the models are evaluated for the more complex flow around a circular cylinder. A parametric study shows the change in the flow-field when the temperature of the wall is varied and when the mass ratio between species is increased. A detailed comparison of the results, acquired with a DSMC solver, demonstrates promising results from both kinetic models.
To summarise, the novelty of the work presented in this chapter lies in the numerical application of the two new kinetic models for gas mixtures, which are validated with well-established test cases and assessed in detail for varied flow conditions.

3.1 Numerical Method

The two kinetic models are validated and tested for the profile of a normal shock wave and the flow around a circular cylinder. The problem and solver setup are defined in this section, together with the used non-dimensionalisation.

*Published in Physics of Fluids and the European Journal of Mechanics - B/Fluids.

3.1.1 Discrete Velocity Method

The results of the kinetic models are obtained using the discrete-velocity method [39] within the Multi Physics Code (MΦC) [80, 118] in-house framework. The method is chosen for its relative simplicity, accuracy and deterministic nature (i.e. avoiding sampling errors). Possible molecular velocities are uniformly spaced in a defined velocity domain. The domain varies according to the initial conditions and is highly dependent on the Mach number. The number of molecular velocities in the domain varies with Mach number and mass ratio between species. For the profile of the normal shock wave 100 uniformly spaced discrete velocities are used, unless stated otherwise (e.g. for mass ratios of 10 and more), while the number of discrete velocities increases drastically for the two-dimensional cylinder case and is specified in the cylinder section for each case. For two- and three-dimensional cases code parallelisation is necessary and for the presented cylinder case the code is parallelised in both space and velocity phase space.
The distribution function and the fluxes are evaluated for each of the velocities in every cell. The moments of the distribution functions (macroscopic variables) are found by applying the trapezoidal rule. A finite-volume scheme and a second order Total Variation Diminishing (TVD) time marching method [41, 42] are used to numerically discretise the models' governing equation. Note that in contrast to a continuum solver, which stores only the macroscopic variables in each cell, the two kinetic solvers, based on the DVM, require much more computational time and memory. The difference in CPU time will be discussed in detail in the Chapter 4.

3.1.2 Problems Setup

All shock profile simulations are set with the same uniform spatial domain, where $x \in [-75L_{ref}, 75L_{ref}]$, which is discretised by 1200 cells in the x-direction. Note the domain is selected to avoid the disturbances, downstream of the shock during the simulation, to reflect on the downstream boundary and affect the shock structure.
The setup of the problem is as follows: a flow with initial conditions undergoes strong non-equilibrium changes through a normal shock wave to arrive at a different equilibrium state. The state to state change is initialised with the Rankine-Hugoniot conditions for the macroscopic variables and Maxwellian distributions are set at the two different initial equilibrium states.
To evaluate the models' capability for two-dimensional flows, a high-speed flow past a cylinder is presented. The flow is initialised with initial Mach number, species concentration, mass ratio between species, rarefaction level and fixed wall temperature. Note the rarefaction level is defined by a Knudsen number, based on the radius of the cylinder, where the radius has length $1L_{ref}$, where L_{ref} depends on the reference time and reference velocity as shown in the following subsections. Note that this is standard for kinetic modelling and it differs from the Knudsen number definition based on the mean free path as in molecular modelling [119]. These differences are taken into account when comparison between the kinetic models and the Monte Carlo

method is conducted. The Knudsen number is equalised between the two modelling approaches and it is quoted based on the kinetic definition. The used geometry is a quarter of a cylinder with a symmetry condition on the stagnation streamline as shown in Fig. 3.1. The spatial grid consists of 36 blocks and 27864 cells for the Shakhov- and ES-based models. The DSMC setup is described in the corresponding section.
Validation for the normal shock is performed by comparing with numerical results from the full Boltzmann equation available in the literature. The validation and comparison of the flow past a cylinder is through a comparison with solutions acquired through DSMC with the number of particles and samples specified for each condition.

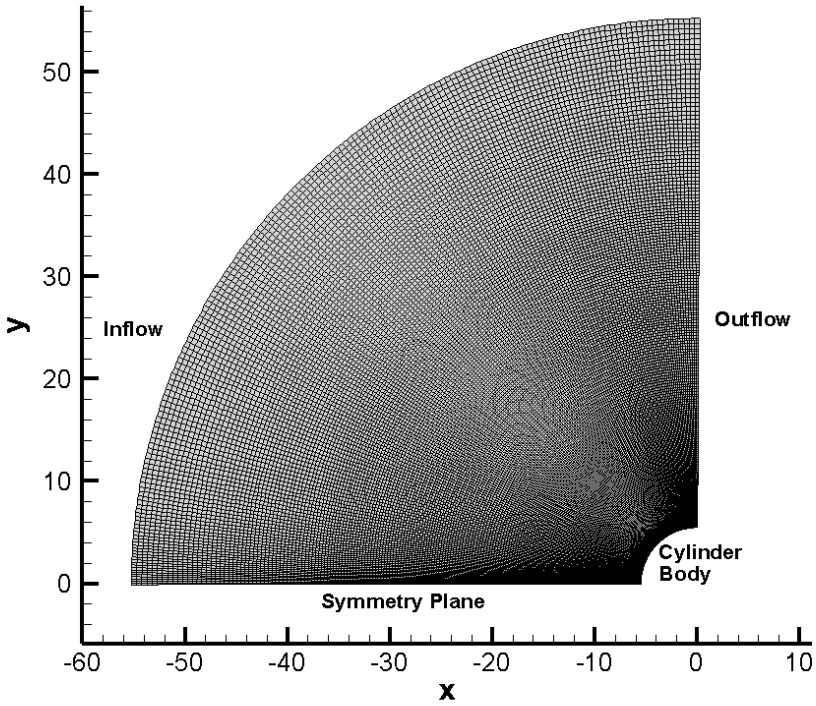

Figure 3.1: Mesh of cylinder and imposed boundary conditions.

3.1.3 Dimensional Reduction

In the one-dimensional formulation, the distribution functions are dimensionally reduced to functions defined in one-dimensional velocity space to reduce computational cost [120]. Since the mean velocities v_0, w_0 in the y and z-directions are zero, the species distribution function f_s reduces to translational g_s and thermal h_s energy component, as demonstrated in Eq. (3.1). The

macroscopic variables are then found by taking moments of the reduced distribution functions:

$$\begin{aligned} g_s &= \iint_{-\infty}^{\infty} f_s \, dvdw, \\ h_s &= \iint_{-\infty}^{\infty} (v^2+w^2) f_s \, dvdw. \end{aligned} \tag{3.1}$$

Therefore the solver uses four velocity distribution functions: two for each species to define the flowfield. Note the dimensional reduction for the cylinder follows the same procedure but for two-dimensional reduced functions by integrating out only the z-direction. This also leads to four velocity distribution functions.

The macroscopic variables. found as moments of the reduced distribution functions, are then in the form:

$$\begin{aligned} n_s &= \int_{-\infty}^{\infty} g_s du, \\ n_s u_s &= \int_{-\infty}^{\infty} u g_s du, \\ \frac{3}{2} n_s k T_s &= \frac{m_s}{2} \left[\int_{-\infty}^{\infty} u^2 g_s du + \int_{-\infty}^{\infty} h_s du \right] - \frac{1}{2} \rho_s u_s^2, \end{aligned} \tag{3.2}$$

3.1.4 Dimensionless Form

The macroscopic variables are non-dimensionalised and the reference values are described in this subsection. The lighter species and its mass m_1 are taken as reference at free-stream conditions. All velocities are non-dimensionalised with the most probable speed u_{ref} of the light species. Elements of the anisotropic tensor for the ES-based model λ_r^s are scaled per species to preserve the scaling of the ES distribution functions the same as the distribution functions in the Shakhov-based model - f_r, g_r, h_r. Note the non-dimensionalisation presented is for the one-dimensional flow formulation. The constant $\beta = m_2/m_1$ is the mass ratio in the expressions for the distribution functions of the heavy gas and the reference values for non-dimensionalisation

are:

$$
\begin{aligned}
&u_{ref} = \sqrt{2kT_r/m_1}, \\
&\rho_r = n_r m_1, \\
&\lambda_r^s = R_s T_r = \frac{kT_r}{m_s}, \\
&f_r = \frac{n_r}{u_{ref}^3} = \frac{n_r}{\left(2kT_r/m_1\right)^{3/2}}, \\
&g_r = \frac{n_r}{u_{ref}} = \frac{n_r}{\sqrt{2kT_r/m_1}}, \\
&h_r = n_r u_{ref} = n_r\sqrt{2kT_r/m_1}, \\
&\beta = m_2/m_1, \\
&q_r = \frac{1}{2} n_r m_1 u_{ref}^3 = n_r kT_r\sqrt{\frac{2kT_r}{m_1}}, \\
&L_{ref} = \frac{u_{ref}}{t_{ref}} = \frac{u_{ref}}{\tau_{ref}} = \frac{u_{ref}\mu_{ref}}{p_{ref}}.
\end{aligned}
\tag{3.3}
$$

In the kinetic model, the reference length L_{ref} is defined by reference time and velocity, where the $t_{ref} = \tau_{ref}$ - the collision time, expressed from the mixture pressure and viscosity at reference conditions. The reference viscosity is taken for a variable cross-section hard sphere model (VHS), which depends on the molecular potential ω and the mean free path for a VHS model, as described in [119] and by Eq. (3.4) :

$$
\mu_{ref} = \frac{15}{2}\lambda_{ref}\rho\sqrt{\frac{2\pi kT}{m_{mix}}}\frac{1}{(7-2\omega)(5-2\omega)}, \tag{3.4}
$$

where the mass of the mixture $m_{mix} = \rho/n$. Note that for a hard sphere model, the molecular potential is $\omega = 0.5$, which reduces the expression for the viscosity to:

$$
\mu_{ref} = \frac{5}{16}\lambda_{ref}\rho\sqrt{\frac{2\pi kT}{m_{mix}}}. \tag{3.5}
$$

This allows for comparison with a variety of models, where the mean free path λ_{ref} is taken as a reference length. Note that in the following section the hard sphere model and Eq. (3.5) are used for a comparison with the Boltzmann solution [9] for the normal shock wave simulations and the variable hard sphere model and Eq. (3.4) are used for the validation with DSMC for the flow around a cylinder. The resultant reference length is:

$$
\begin{aligned}
L_{ref} &= \frac{\sqrt{\frac{2kT}{m_1}}\frac{15}{2}\lambda_{ref}\rho\sqrt{\frac{2\pi kT}{m_{mix}}}\frac{1}{(7-2\omega)(5-2\omega)}}{nkT} = \frac{15\sqrt{\pi}}{(7-2\omega)(5-2\omega)}\lambda_{ref}\sqrt{\frac{m_{mix}}{m_1}}, \qquad (3.6)\\
L_{ref} &= \frac{15\sqrt{\pi}}{(7-2\omega)(5-2\omega)}\lambda_{ref}\sqrt{\frac{n_1 m_1 + n_2 m_2}{m_1(n_1+n_2)}}.
\end{aligned}
$$

The ratio of the two reference lengths L_{ref} for the kinetic models and λ_{ref} for the validation models is the required scaling factor with all variables taken at free-stream conditions:

$$\frac{L_{ref}}{\lambda_{ref}} = \frac{15\sqrt{\pi}}{(7-2\omega)(5-2\omega)}\sqrt{\frac{n_1+\beta n_2}{n_1+n_2}}. \tag{3.7}$$

3.1.5 Normalised Values

The macroscopic quantities presented for the shock wave are normalised following Kosuge's approach [9], where y is the macroscopic variable, Y_- is the pre-shock value of y and Y_+ is post-shock:

$$\tilde{y} = \frac{y-Y_-}{Y_+-Y_-}. \tag{3.8}$$

Note that the tilde is omitted from here on for simplicity. Also, the origin of the plots ($X = 0$) is defined at the location where the total number density is exactly half of the sum of the pre-shock and post-shock values.

3.2 Normal Shock Wave

3.2.1 Single Species Recovery

The numerical evaluation of the models begins with an investigation of the structure of a normal shock wave. The first step is to demonstrate that the two models collapse to a single-species model not only theoretically as in Chapter 2, but also numerically. This means that for the same properties of the two species, the binary-mixture model satisfies the indifferentiability principle and recovers the single-species Shakhov-model and ES-model respectively. We will show that the single-species models are recovered and we will validate the results by a comparison with the solution for a single-species normal shock wave.

There are two main points to be made here. First, a mixture of two gases with the same mass, initial velocity and temperature is inspected. Each gas is at 50% concentration. Numerically there is nothing to push the two gases to separate and we expect to observe equal species macroscopic properties through the shock, e.g. $n_1 = n_2$, $u_1 = u_2$, $T_1 = T_2$, etc.

In Fig. 3.2 (a) and (b) the Shakhov- and ES-based solvers respectively are tested to confirm that the species variables will collapse into one. The species number densities, species velocities and species temperature are plotted with a solid line for species 1 and dashed line for species 2. The results between species 1 and 2 match exactly for each solver, confirming that for identical species masses, the species do not separate from each other.

The second proof is to compare the total macroscopic properties of the gas ρ, u_0, T and validate the results against single species results. This test case is well-studied and there are suitable experimental, e.g [121], and numerical results, e.g [8, 78, 122]. As described earlier, the power

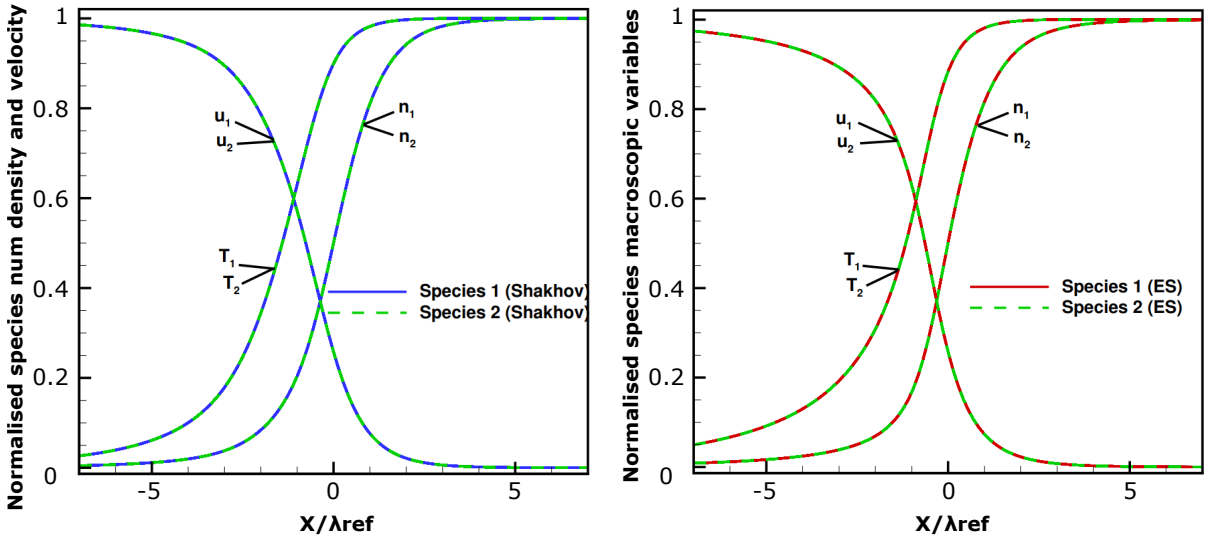

(a) Shakhov-based results (b) ES-based results

Figure 3.2: Profile of a normal shock wave with a free-stream Mach number 3.0, a mass ratio between species $\beta = 1$ and equal concentration between the species of 50%.Comparison of species macroscopic variables. Results for the Shakhov-based model shown in (a), with results for ES-based model in (b).

law for the viscosity is used in the Shakhov- and ES-based solvers with a molecular potential ω. The results from Ohwada are for a hard-sphere and therefore, $\omega = 0.5$, while the Sutherland law is found most suitable to compare against Alsmeyer's results. In Fig. 3.3 the results of the Shakhov-based and ES-based models in blue and green are validated with the results from Ohwada [8] (red elements) for flow with free-stream Mach number $M_\infty = 3$. This also allows for a comparison between the two kinetic models. The mixture density ρ and velocity u_0 follow closely the results from Ohwada. The Shakhov- and ES-based results have a longer upstream tail, as can be expected in results of BGK-type models. This effect can also be observed in the early decrease of the mixture velocity u_0 of the models in comparison to the mixture velocity from Ohwada. It is further pronounced in the higher moments of the distribution function: the mixture temperature T, where the variation is more significant. The Shakhov-based model preserves the profile of the shock better than the ES-based model for a single species gas, which has been observed previously [47]. The main goal of the investigation in this section was to demonstrate numerically that the mixture Shakhov- and ES-based kinetic models have the capability to reduce to single-species models. Indeed, the results show that for identical molecular mass of the species the single-species Shakhov and ES models are recovered.

3.2.2 Normal Shock of a Gas Mixture

The numerical evaluation of the mixture models continues with an investigation of the structure of a normal shock wave for a binary gas mixture comprised of two distinguishable gases. The profile of the shock wave is studied for gases with different mass and with mean species veloc-

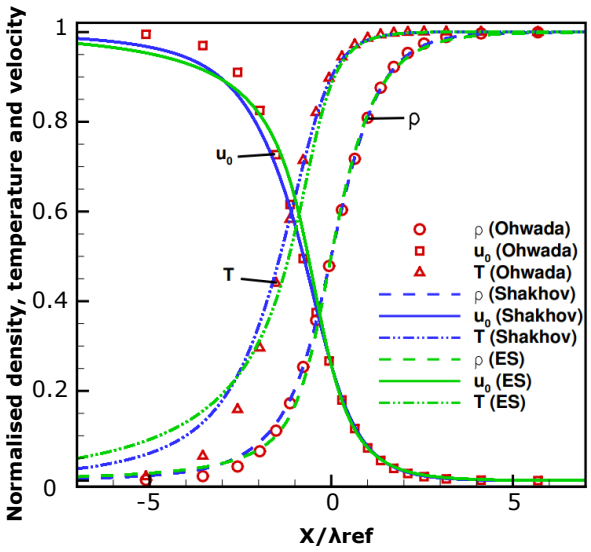

Figure 3.3: Profile of a normal shock wave with a free-stream Mach number 3.0, a mass ratio between species $\beta = 1$ and equal concentration between the species of 50%. Comparison of total mixture variables with the single-species full Boltzmann equation [8].

ities and temperatures that are allowed to deviate. The goal is to inspect the effect of different free stream conditions (Mach number, ratio of masses and concentration ratio) on the profile of the shock. A viscosity law with $\omega = 0.5$ is used for a hard-sphere mixture model, except for one case where the variable hard sphere with $\omega = 0.72$ is used to inspect the effect of the molecular potential on the shock. Test case conditions are summarised in Table 3.1.

M_∞	m_2/m_1	n_1/n	ω
1.5	2	0.9	0.5
1.5	4	0.9	0.5
1.5	4	0.9	0.72
1.5	2	0.5	0.5
3	2	0.9	0.5
3	2	0.5	0.5

Table 3.1: Test case conditions for a normal shock wave (DVM)

Figures 3.4 and 3.5 show the results obtained by the Shakhov-based model in blue and ES-based model in green, while the Groppi et al.'s model is presented with black lines. For the three kinetic models the light gas macroscopic variables are presented with solid lines (species 1) and the heavy gas variables are with dashed lines (species 2). We validate against the results from the full Boltzmann equation [9], which are presented by the red elements- squares for species 1 and triangles for species 2.

Figures 3.4 and 3.5 show the normalised number density and temperature for each species through the shock profile under the specified conditions. Figures 3.4 (a) and (c) focus on comparing the Shakhov and ES-based models with Kosuge's full Boltzmann model for two different free-stream Mach numbers: $M_\infty = 1.5$ and $M_\infty = 3$. Combining the higher velocities with a gas

having predominantly the light component leads to an overshoot of the heavy species' temperature, which is a known numerical result [23]. The results from the new BGK-type models follow closely the full Boltzmann results and match well with each other. For normal shocks at higher Mach numbers, longer upstream tails for the species temperatures are observed. This is a known disadvantage of all BGK-type models and the introduced corrections in the two kinetic models cannot target this drawback. This result is also observed for the uncorrected model in figure 3.4 (b) and (d). Comparing the results of the two new models, we can see that the upstream tail is more pronounced in the ES model than in the Shakhov-based model, consistent with observations for single-species simulations based on ES and Shakhov models [47]. The Shakhov model with Prandtl number $Pr = 1$ eliminates the introduced correction (Fig. 3.4 (b)) and the same happens when the ES-based model is simulated with $\nu_{ES} = 0$ (Fig. 3.4 (d)). These conditions allow to demonstrate the results that can be obtained by the original Groppi et al. model [64]. The original model follows the results of the full Boltzmann equation, but clearly reveals the changes the new models introduce. The difference is emphasised for more extreme conditions. For a higher Mach number (Fig. 3.4 (c) and (d)) Groppi et al.'s model moves further away from the target solution, while the Shakhov- and ES-based models preserve the structure of the shock wave more closely.

Further validation and parametric study show the change of the flow with the increase of the mass ratio from 2 to 4 on figure 3.5 (a). An example setup of a mixture of noble gases with these mass ratios are the mixtures of neon and argon and neon and krypton correspondingly. The shock thickness increases and the shock front is more gradual with an increasing mass ratio between species. The solutions demonstrate that increasing the mass ratio leads to changes in the flow further upstream in the flow, since the lighter gas's faster reaction to the shock is enhanced in comparison to the heavy gas. This phenomenon has previously been confirmed for monoatomic and diatomic gas mixtures with the generalised Boltzmann equation [123].

All simulations until now were performed for a hard sphere model in order to compare with the Boltzmann solution. The effect of molecular model is inspected by comparing at the same free-stream conditions and changing the viscosity power law - see figures 3.5 (a)-hard-sphere model ($\omega = 0.5$) with (b)-variable hard-sphere model ($\omega = 0.72$). The changes in the shock profile from introducing the different molecular potential are small in comparison to the change caused by the Prandtl number correction, which is the desired result.

Two more cases with 50% concentration for each component and mass ratio of 2, but under different Mach numbers ($M_\infty = 1.5, 3$) allow to solely examine the effect of the ratio of light to heavy species in the flow (Fig. 3.5 (c) and (d)). The figures show that the shock thickness reduces with the increase of heavy species in the flow and the structure becomes steeper overall, which corresponds to the properties of the heavy species observed until now.

Note that for any pure monoatomic gas the Prandtl number is $2/3$, while it is known that for a binary mixture of monoatomic gases it is reduced, according to the mass ratio and species con-

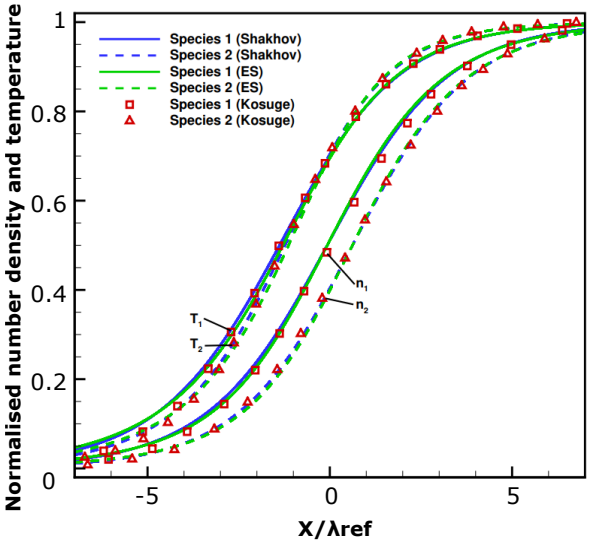

(a) $M = 1.5;\ m_2/m_1 = 2;\ n_1/n = 0.9$

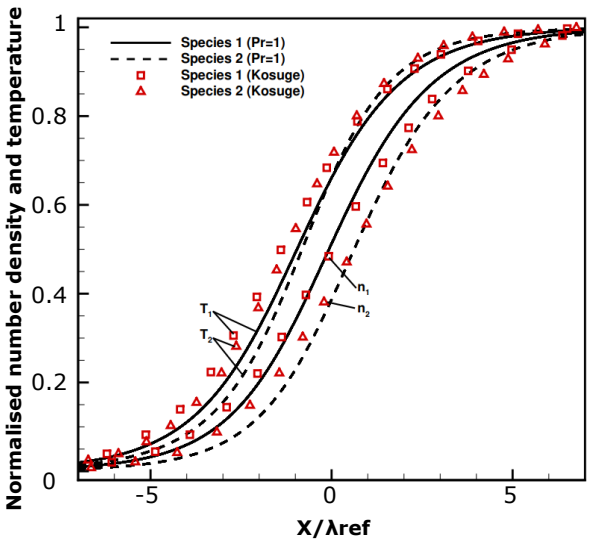

(b) $M = 1.5;\ m_2/m_1 = 2;\ n_1/n = 0.9;\ Pr = 1$

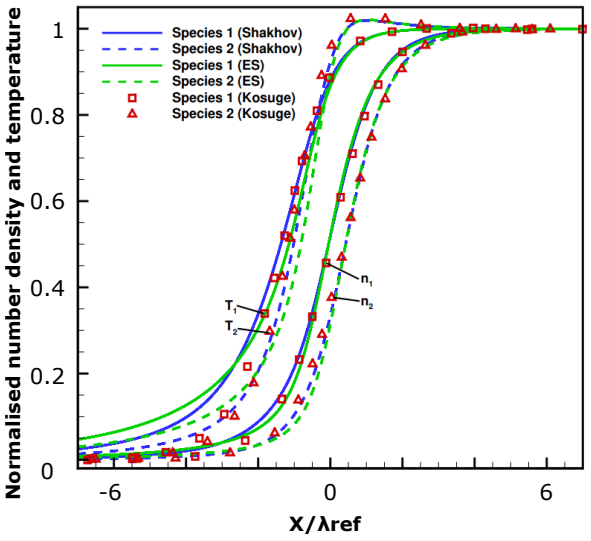

(c) $M = 3;\ m_2/m_1 = 2;\ n_1/n = 0.9$

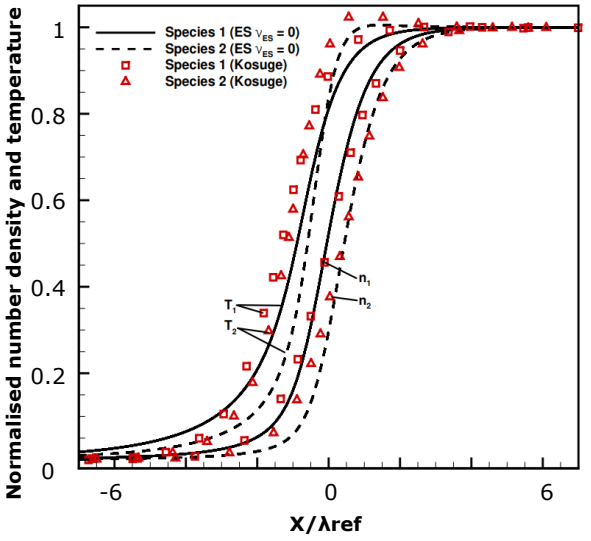

(d) $M = 3;\ m_2/m_1 = 2;\ n_1/n = 0.9;\ \nu_{ES} = 0$

Figure 3.4: Validation and comparison of the Shakhov and ES-based models with Kosuge's full Boltzmann model [9] and without the added corrections for flow conditions: (a) $M = 1.5;\ m_2/m_1 = 2;\ n_1/n = 0.9$ (b) $M = 1.5;\ m_2/m_1 = 2;\ n_1/n = 0.9;\ Pr = 1$. (c) $M = 3;\ m_2/m_1 = 2;\ n_1/n = 0.9$ (d) $M = 3;\ m_2/m_1 = 2;\ n_1/n = 0.9;\ \nu_{ES} = 0$.

centration [114, 115]. For 90% concentration of the lighter species, the mixture Prandtl number remains close to the target Prandtl number (Pr = 2/3), i.e. the resultant mixture Prandtl number is $Pr_{mix} = 0.638$, however for $n_1/n = 50\%$ and $m_2/m_1 = 2$ it reduces to $Pr_{mix} = 0.593$. Increasing the mass ratio to $m_2/m_1 = 10$, e.g. for a helium-argon mixture can decrease the mixture Prandtl number to ≈ 0.22 , making the Shakhov and ES-based corrections further pronounced. Characteristic features of the problem are observed, including the lighter species (species 1) reacting faster to the shock, while the temperature rise of the heavy species T_2 is steeper and crosses T_1. Species mean velocities and number densities also react at different rate but unlike

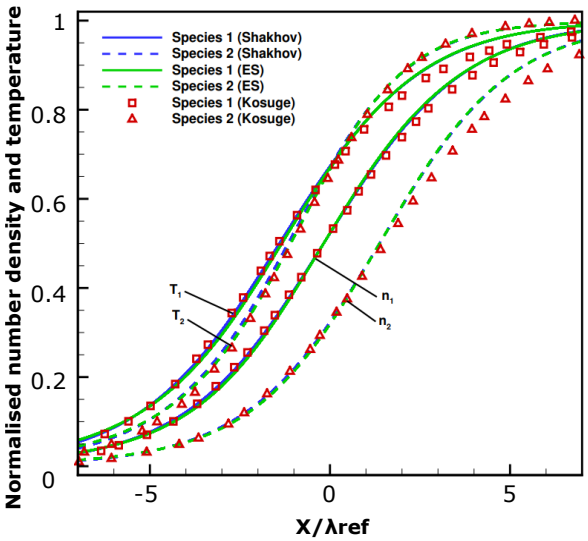

(a) $M = 1.5;\ m_2/m_1 = 4;\ n_1/n = 0.9$

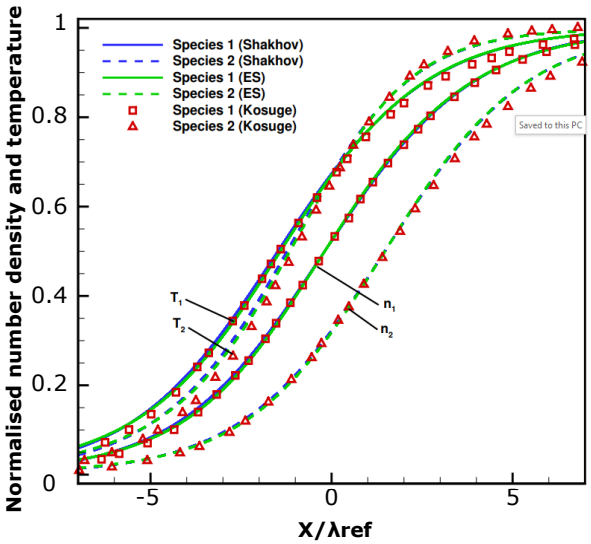

(b) $M = 1.5;\ m_2/m_1 = 4;\ n_1/n = 0.9;\ \omega = 0.72$

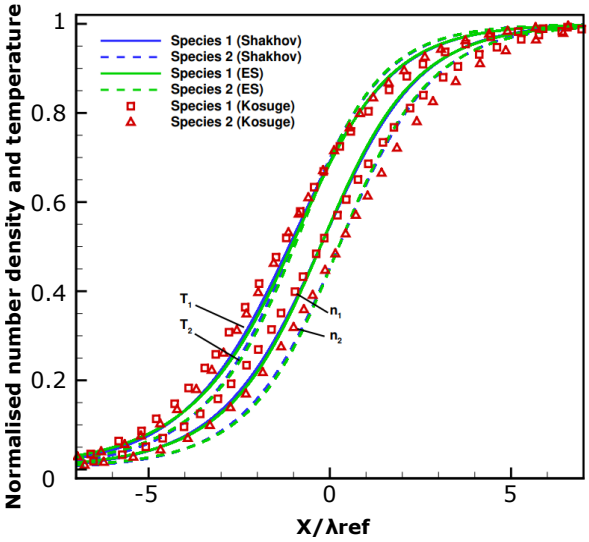

(c) $M = 1.5;\ m_2/m_1 = 2;\ n_1/n = 0.5$

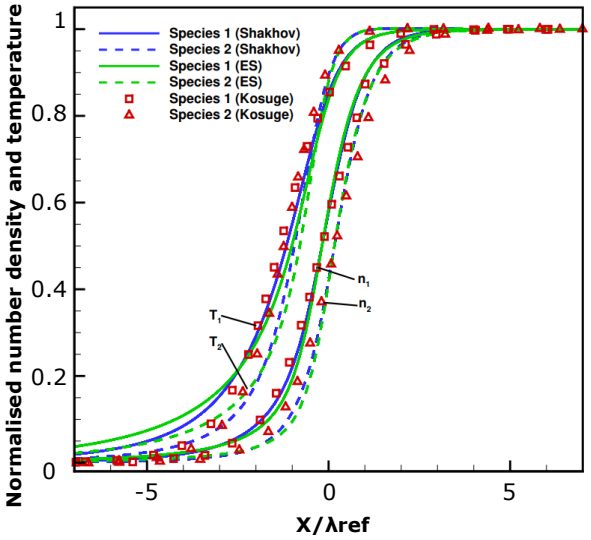

(d) $M = 3;\ m_2/m_1 = 2;\ n_1/n = 0.5$

Figure 3.5: Validation of the Shakhov and ES-based models with Kosuge's full Boltzmann model [9] for flow conditions: (a) $M = 1.5;\ m_2/m_1 = 4;\ n_1/n = 0.9$ (b) $M = 1.5;\ m_2/m_1 = 4;\ n_1/n = 0.9;\ \omega = 0.72$. (c) $M = 1.5;\ m_2/m_1 = 2;\ n_1/n = 0.5$ (d) $M = 3;\ m_2/m_1 = 2;\ n_1/n = 0.5$.

the temperatures do not intersect at any point. Based on the validation and parametric study shown, a good agreement with the results by Kosuge et al. [9] is evident. Note that the findings in this section are verified with the more detailed results of the full Boltzmann model and are consistent with the trends of other BGK-based models [58, 59]. From the results for the normal shock waves, the Shakhov-based model shows a slightly better behavior upstream of the shock wave in comparison to the ES-based model. Given the fact that the numerical complexity for this model is also lower, this model is the preferred choice for normal shock wave simulations. The relative merit for both models will be further assessed for a cylinder later in this chapter and

for a wider range of test cases in future studies.

3.2.3 Heat Flux

The two models introduce changes that provide a correct third transport coefficient: the thermal conductivity in the continuum limit, leading to a correct Prandtl number for the gas mixture. This affects all variables, defining the flow, but mostly the heat flux. In the present work the difference of the heat flux prediction is demonstrated for the Groppi et al.'s [64], Shakhov-based and ES-based models through the normal shock. Moreover, the results are evaluated against the results from the full Boltzmann equation [9]. Figure 3.6 inspects the total heat flux variation through a normal shock wave of the same test cases: for free-stream Mach numbers 1.5 and 3, mass ratio of 2 and 90 percent light species concentration. On the plot we see the variation of the non-dimensionalised heat flux through the normal shock, defined as:

$$\tilde{q} = -\frac{q(x)}{p_r \sqrt{\frac{2kT_r}{m_2}}}, \tag{3.9}$$

where here $q(x)$ is the dimensional heat flux through the shock and the $\tilde{q}$ the heat flux non-dimensionalised as in the results provided by the full Boltzmann equation [9] and the tilde is omitted as we proceed. The reference pre-shock pressure and temperature are p_r and T_r with m_2- the heavy species mass. This non-dimensionalisation is done to match with the results of

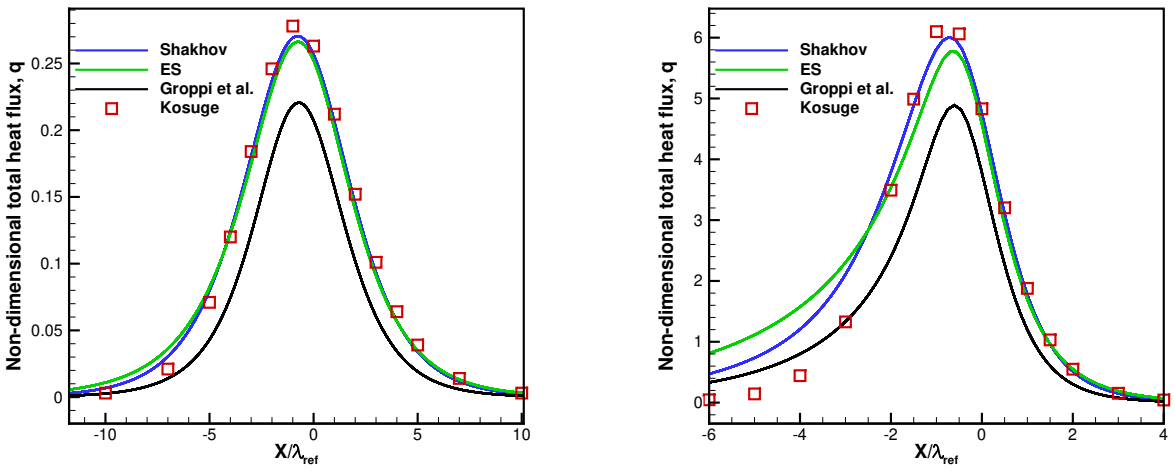

(a) $M_\infty = 1.5$ (b) $M_\infty = 3$

Figure 3.6: Non-dimensional total heat flux for the gas mixture q for the Shakhov-based, ES-based and Groppi et al. models through a normal shock wave with free stream Mach numbers 1.5 (shown in (a)) and 3 (shown in (b)), mass ratio $\beta = 2$ and light-species concentration 90%. Results are evaluated against gas heat flux result from the full Boltzmann equation, provided to us by the authors of the paper showing normal shock wave results with the Boltzmann equation [9].

the full Boltzmann equation, provided by the authors of the paper showing normal shock wave results with the Boltzmann equation [9], shown with red elements in Fig. 3.6. Note that heat flux is a combined effect between the thermal conduction and the Dufour effect. Our models fix only the thermal conductivity coefficient and the Dufour effect is not correctly fitted, which will offset the results for the total heat flux. However, for the described cases, this offset is small since the thermal effect is much stronger than the diffusion effect in the flow and is dominating the heat flux.

The heat flux, which is a macroscopic variable corresponding to a higher order moment, vary over a more spread-out region, covering approximately 60% larger number of mean free paths. We observe a difference between the two new models of 4.1%, while the Shakhov-based and Groppi et al.'s models differ by a total of 20.5%. This emphasises the importance of fitting correctly the transport coefficients and in particular the thermal conductivity.

Comparing with results from the full Boltzmann equation, the results for the heat flux from the Shakhov- and ES-based models demonstrate the capability of the two models to capture the heat flux correctly through the shock and it's maximum. Recovering the heat flux is a key advantage of the two new kinetic models.

When comparing the accuracy of the models, the same longer tail, inherent to BGK-style models, is evident through the shock as in the species temperature profile. This is an expected feature due to the relationship between the translational temperature and the heat flux. Note that the ES-based model has an even longer upstream tail, which is further pronounced with the higher Mach number. In Fig. 3.6 we observe that the Shakhov-based model shows good agreement with the benchmark results, preserving the maximum and downstream tail of the heat flux.

Previously, we observed that the Shakhov-based model is matching the results for the single-species high speed flow through a normal shock more closely than the ES-based model. Furthermore, for both gas mixture cases, the Shakhov-based model performs better than the ES-based model. Therefore, the parametric study on the species mass variation and Mach number variation in the next sections will be performed with the Shakhov-based model.

3.2.4 Species Mass Ratio Variation

In this section a parametric study is conducted for a varying mass ratio between species. The Shakhov-based model is used to investigate the effect. The number of discrete velocities is 100 for the smaller mass ratios, but increases to 200 for mass ratios $\beta = 10, 20$ and 32.8 for better resolution of the velocity space. The solver is initialised at the same Mach number $M_\infty = 1.5$, concentration of light species gas 90% and varied mass ratio. The velocity is defined from a fixed Mach number, but the speed of sound a is defined with the mass of the gas mixture. Therefore, $u_s = M_\infty a = M_\infty \sqrt{\gamma \frac{k}{m_{mix}} T}$, where $m_{mix} = \rho/n$. After non-dimensionalisation the direct relationship between the velocity and the mass ratio β is clear. The velocity is initialised from the set Mach number and the initial macroscopic variables and the non-dimensional initial

velocity is in the form:

$$u_s = M_\infty \sqrt{\frac{\gamma}{2}\frac{n_1+n_2}{n_1+\beta n_2}T}; \quad s = 1,2, \tag{3.10}$$

where $\gamma = 5/3$ for a monoatomic gas. Therefore, for a fixed Mach number and increasing mass ratio β, the initial velocity reduces. Note if the velocity is fixed instead, the Mach number will change for each mass ratio.

Increasing the mass ratio between the two species would lead to a bigger difference between their velocities and temperatures due to different behavior of atoms with a mass difference. However, the initial velocity reduces due to the mass ratio increase and creates a counter-effect. In Fig. 3.7 the velocity variation u_{diff} through the shock is presented, where $u_{diff} = u_2 - u_1$. For the initial increase of mass ratio, the variation between the species increases as expected for species with bigger difference between their masses. However, the difference between the species velocity increases until it reaches its limit between mass ratios $\beta = 4$ and $\beta = 10$. The lower initial velocity begins to counter this effect and for bigger and bigger mass ratios of 20 or 32.8 the velocity reduction is the dominating effect. Note that a simple substitution in Eq. 3.10 shows that the initial velocity at the specified conditions for $\beta = 32.8$ is close to half of the initial velocity for $\beta = 2$, due to the speed of sound change. Notice also that even though the peak of the

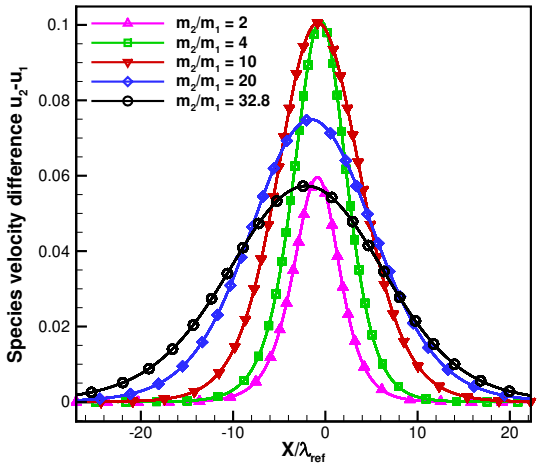

Figure 3.7: Non-dimensional species velocity difference $u_2 - u_1$ through a normal shock wave with free stream Mach number 1.5, light species gas 90% and varied mass ratio from 2 to 32.8 between species.

difference between the species velocity decreases for a higher mass ratio, the number of mean free paths (using reference conditions) required for the velocities to become in equilibrium with each other increases. The difference between velocities is 0 at the far upstream and downstream, while when the flow approaches the shock this $u_2 - u_1$ increases and it decrease back to 0 post shock. In Fig. 3.7 the shock wave with the mass ratio of 2 has difference in species velocities for approximately 24 mean free paths, while for a mass ratio of 32.8 the distance increases to 75

mean free paths for the velocities to equalise again to the gas mixture velocity behind the shock. This demonstrates that the flow non-equilibrium caused by the higher mass ratio between species is governing an extended region.

3.2.5 Mach Number Variation

The variation between species velocity and species temperature is tested in this section for different Mach numbers. Using the Shakhov-based model a parametric study is conducted based on a flow with light-species concentration 90% , mass ratio between species $\beta = 2$. In Fig. 3.8 the species velocity and temperature differences are plotted for Mach numbers $M_\infty = 1.5, 3$ and 6. The light species reacts first to the shock (i.e. furthest upstream of the centre of the shock)

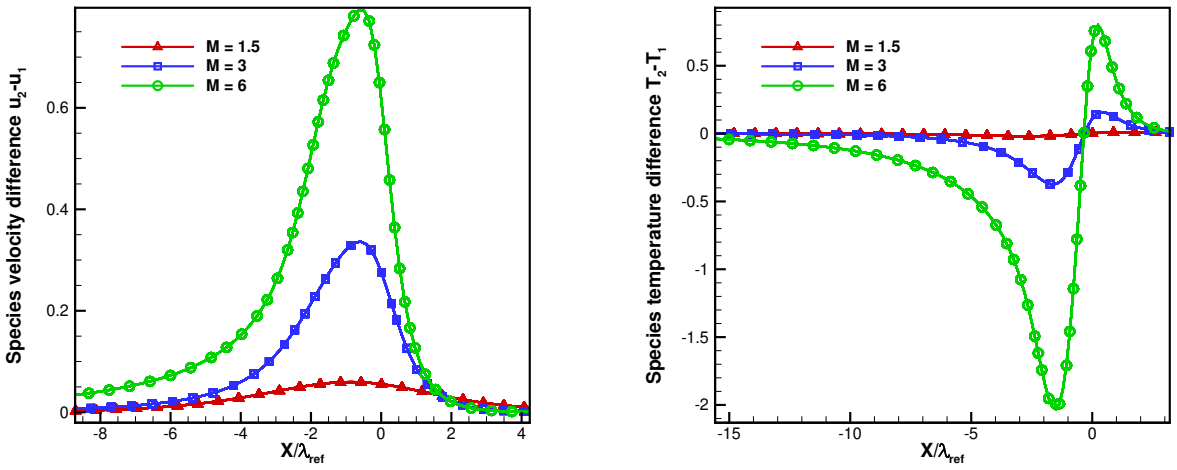

(a) Species velocity difference

(b) Species temperature difference

Figure 3.8: Non-dimensional species velocity difference $u_2 - u_1$ (in (a)) and species temperature difference $T_2 - T_1$ (in (b)) through a normal shock wave for a varied free stream Mach number of 1.5, 3 and 6, mass ratio between species $\beta = 2$ and light-species concentration 90%.

and u_1 decreases first, creating the difference between the two velocities. The species velocity difference increases with the increase of Mach number and for $M_\infty = 6$ it is represented by a sharp spike. Moreover, the highest Mach number creates a difference between the velocities in the flow for a bigger range of mean free paths, due to the light gas reacting to the shock wave very early to the shock. Meanwhile, the shock with $M_\infty = 1.5$ is spread out and gradual rather than steep. When the difference between velocities is normalised by the gas mixture velocity u_0 for each Mach number, the peak value of $M_\infty = 6$ is approximately 4.8 times the peak value of $M_\infty = 1.5$ test case, while $M_\infty = 3$ is approximately 3.7 times the peak value of $M_\infty = 1.5$ test case.

The temperature difference $T_{diff} = T_2 - T_1$ is presented in Fig. 3.8 (b). The relative variation in the temperature is bigger than the velocity. The lighter gas reacts quicker to the shock and the

light species temperature T_1 increases first creating a negative $T_2 - T_1$ difference. The increase of the heavy gas is steep and the difference between $T_2 - T_1$ changes sign through the shock and becomes positive. The difference between temperatures is evident for the $M_\infty = 1.5$ test case, but quite small in comparison to the difference created by $M_\infty = 6$ test case. We confirm that increasing the Mach number has a significant effect on the species properties. Therefore, for higher velocities, the importance of modelling of the flow as a gas mixture is further emphasised.
In the next section, a more complex two-dimensional flow at Mach $M_\infty = 3.0$ is investigated.

3.3 Cylinder

3.3.1 Flow Past a Cylinder

A more complex test case - a two-dimensional flow over a circular cylinder with 48×48 and 64×64 (for the higher mass ratio) uniformly spaced discrete velocity meshes, is investigated. The Shakhov-based model is used to simulate the flow around the cylinder in this first section, while in the next section the two kinetic models are validated and compared. In Fig. 3.9 and 3.10 a flow with free-stream Mach number 3, Knudsen number 0.1, based on the radius of the cylinder and the reference length at free-stream conditions with light species concentration 90 percent of the gas is presented. The formed bow shock is well-resolved on the used mesh (27864 cells), i.e. with on average 25 cells covering the width of the shock. Fully-accommodating diffuse wall boundary conditions are used for the solid wall. We know from previous simulations that the largest differences between species occur in regions with strong non-equilibrium effects. We also know that the lighter species (species 1) reacts faster to those changes and then the heavier gas (species 2) has to catch up until they find a balance. In Fig. 3.9 the variation between species mean velocity is shown, while Fig. 3.10 focuses on the variation between species temperature. In the vicinity of the shock, the velocity of the lighter gas u_1 starts decreasing first and the difference between the two species $u_2 - u_1$ increases, until species 2 catches up post shock. Unlike the velocities, the heavy species temperature has a steeper slope, increases faster and crosses the lighter species temperature in the shock wave. This we can clearly observe in the plots. Temperature T_1 increases first, creating a negative T_2-T_1 difference in blue and then T_2 catches up and surpasses T_1 leading to a positive temperature difference T_2- T_1 in red.
Each figure contains three plots with varied conditions. In Fig. 3.9 (a) and (b) and Fig. 3.10 (a) and (b) the mass ratio between species is 2 and the assigned wall temperature is changed from $T_{wall} = 1.5T_\infty$ in (a) to $T_{wall} = 2.5T_\infty$ in (b) to inspect the sensitivity of the flow field with respect to the imposed wall temperature. The non-equilibrium effect in the flow through the bow shock, expressed by the difference in species velocities and temperatures, is not affected by the changes of the wall temperature. For the considered wall temperatures, the shock stand-off distance is

not significantly changed.

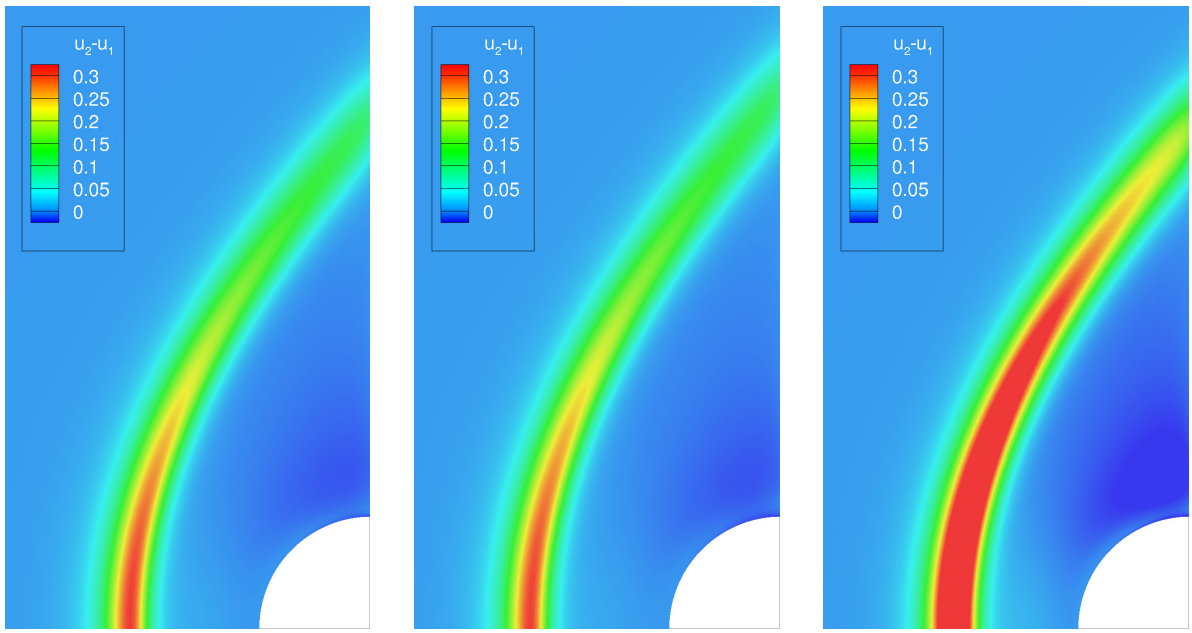

(a) $m_2/m_1 = 2$, $T_{wall} = 1.5T_\infty$ (b) $m_2/m_1 = 2$, $T_{wall} = 2.5T_\infty$ (c) $m_2/m_1 = 4$, $T_{wall} = 1.5T_\infty$

Figure 3.9: Non-dimensional species velocity drift $u_2 - u_1$ in a binary mixture flow over a cylinder (velocity is non-dimensionalised with the most probable speed of the lighter gas) with initial Mach number 3, mass ratio between species $\beta = 2$ and 4, light-species concentration 90%, Knudsen number $Kn = 0.1$ and wall temperature $T_{wall} = 1.5$ and 2.5. Results were obtained with the Shakhov-based model. (a) $m_2/m_1 = 2$, $T_{wall} = 1.5T_\infty$, (b) $m_2/m_1 = 2$, $T_{wall} = 2.5T_\infty$, (c) $m_2/m_1 = 4$, $T_{wall} = 1.5T_\infty$.

Changing the mass ratio between species to 4, however, affects the species mean velocities and temperatures significantly, as we can see in Fig. 3.9 (c) and 3.10 (c). For the higher mass ratio, the non-equilibrium effects and species differences are stronger. The same is observed for the species temperature drift. This is consistent with the behaviour observed previously for the normal shock simulations.

3.3.2 Validation with DSMC Simulations

Until now we were focused on emphasising the difference between species mean properties as a way of establishing the non-equilibrium of the flow. The discussed results were obtained with the Shakhov-based kinetic model. We now consider the stagnation streamline (the streamline on which the stagnation point lies) for the same two flows past the circular cylinder with free-stream Mach number 3, Knudsen number 0.1 and a mass ratio of 2 and 4. The goal of this study is to compare the Shakhov- and the ES-based models with DSMC results. The DSMC solver used in this work is dsmcFoam+ [124] and results were provided by Dr. Craig White. To remain consistent with the kinetic models the Mach number ($M_\infty = 3$) is based on the gas constant of the mixture and the Knudsen number is defined as for the kinetic models, as described in detail

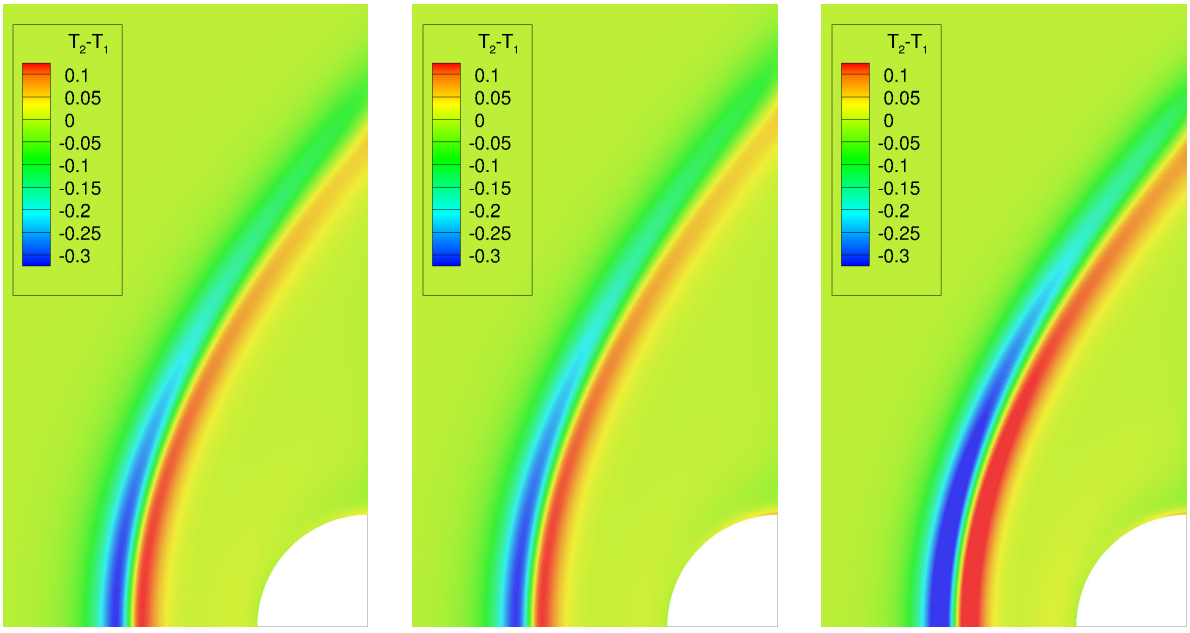

(a) $m_2/m_1 = 2$, $T_{wall} = 1.5T_\infty$ (b) $m_2/m_1 = 2$, $T_{wall} = 2.5T_\infty$ (c) $m_2/m_1 = 4$, $T_{wall} = 1.5T_\infty$

Figure 3.10: Non-dimensional species temperature drift $T_2 - T_1$ in a binary mixture flow over a cylinder with initial Mach number 3, mass ratio between species $\beta = 2$ and 4, light-species concentration 90%, Knudsen number $Kn = 0.1$ and wall temperature $T_{wall} = 1.5$ and 2.5. Results were obtained with the Shakhov-based model. (a) $m_2/m_1 = 2$, $T_{wall} = 1.5T_\infty$, (b) $m_2/m_1 = 2$, $T_{wall} = 2.5T_\infty$, (c) $m_2/m_1 = 4$, $T_{wall} = 1.5T_\infty$.

in Section 3.1.2. In both cases, the light species is neon, with argon and krypton being used for the mass ratios of 2 and 4, respectively. Note that the molecular mass of krypton was slightly modified to get an exact ratio of 4. The variable hard sphere collision model is used ($\omega = 0.72$), with fully diffusive reflections considered for the cylinder surface interactions. As before, the cylinder wall temperature is held constant at $1.5T_\infty$. The DSMC simulation is set up as described. The numerical meshes consist of 40000 cells that are smaller near the stagnation point in order to ensure that all cells are smaller than the local mean free path. The total freestream number density is $3.11\text{x}10^{19} m^{-3}$, which consists of 90% neon and 10% argon for the first test case at $\beta = 2$. A viscosity coefficient of 0.72 and a reference temperature of $273K$ is used for both species to maintain consistency with the kinetic models developed in this work. The variable hard sphere mean free path of the mixture is $8.54\text{x}10^{-2} m$. A freestream temperature of 300 K is used and a velocity of $1299.8 m/s$ to give a Mach number of 3. A time step of $5\text{x}10^{-6} s$ is used and 274000 samples were taken after steady state was reached to reduce the numerical scatter in the results. There are 70 DSMC particles per cell in the free-stream and approximately $3.04\text{x}10^6$ particles in the simulation at steady state. All gas-surface interactions are considered to be fully diffusive with a wall temperature of 450 K. The described test setup is identical for the two mass ratios. The DSMC results are shown in black lines, while the Shakhov-based and ES-based solutions are in blue and green respectively. We plot the non-dimensional number densities and temperatures through the shock and until the solid is reached at $x/R = -1$, where R is the radius

of the cylinder ($x = 0$ at the cylinder centre).

In Fig. 3.11 the non-dimensionalized total number density n and the heavy gas number density n_2 are shown. Physically, the gas undergoes a compression effect through the shock and then towards the stagnation point of the cylinder, demonstrated by the increase in number density. Figure 3.11 shows good agreement in the stagnation streamline density profiles predicted by

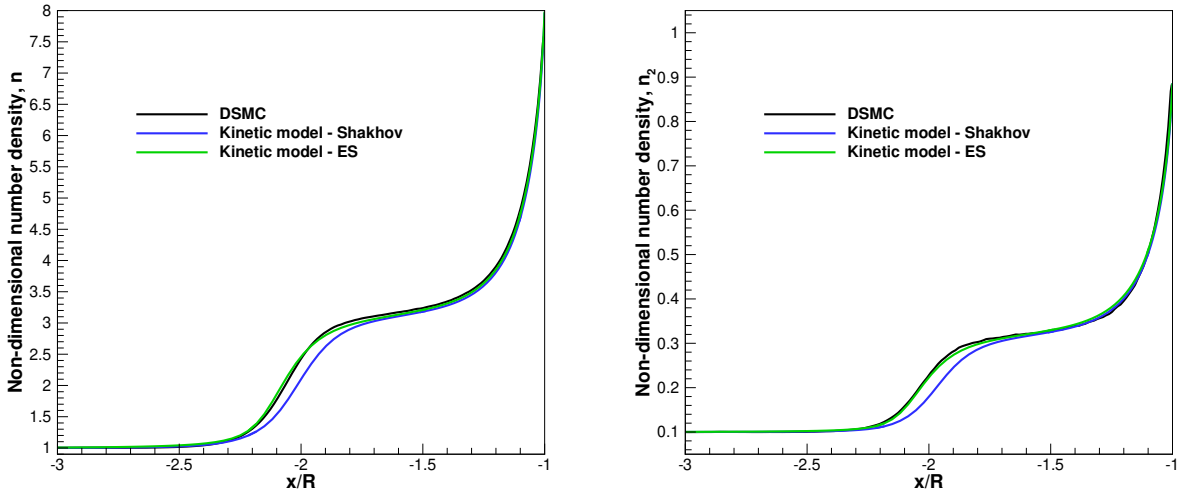

(a) Total number density

(b) Heavier-species number density

Figure 3.11: Comparison of the total number density (in (a)) and heavy species number density (in (b)) for the Shakhov and ES kinetic models with DSMC results for Mach number 3, mass ratio $\beta = 2$, light species concentration 90%, Knudsen number $Kn = 0.1$ and $T_{wall} = 1.5T_{\infty}$.

dsmcFoam+ and the kinetic models, with the ES-based model slightly closer to the DSMC than the Shakhov-based model for the total number density, while the heavy gas number density's profile is also matching closely with the ES-based model. Notice that the number density for both kinetic models reaches a maximum value of approximately 8 times the free-stream number density in the center of the cell neighbouring the wall of the cylinder, while DSMC predicts approximately 7.55 times the free-stream value. A possible explanation for this effect is the better flow resolution in the near-wall region in the kinetic simulations, originating from the finer mesh used in this region as compared to the DSMC mesh.

The mixture temperature is shown on Fig. 3.12 (a). The temperature jump is caused by the shock and later on relaxes, going into the boundary layer of the cylinder towards the prescribed wall temperature $T_{wall} = 1.5T_{\infty}$. The figure shows a reasonable agreement in the stagnation streamline temperature profile for the gas mixture. The longer tail upstream of the shock appears for both models in comparison to DSMC, with a more pronounced effect in the solution by the ES-based model. In this first region of the bow shock the Shakhov-based model solution matches closer to the solution by DSMC. However, the peak of temperature provided by the ES-based model predicts the DSMC results better than the Shakhov-based model. Near to the solid wall the gas mixture temperature of the kinetic models closely approaches the fixed wall temperature

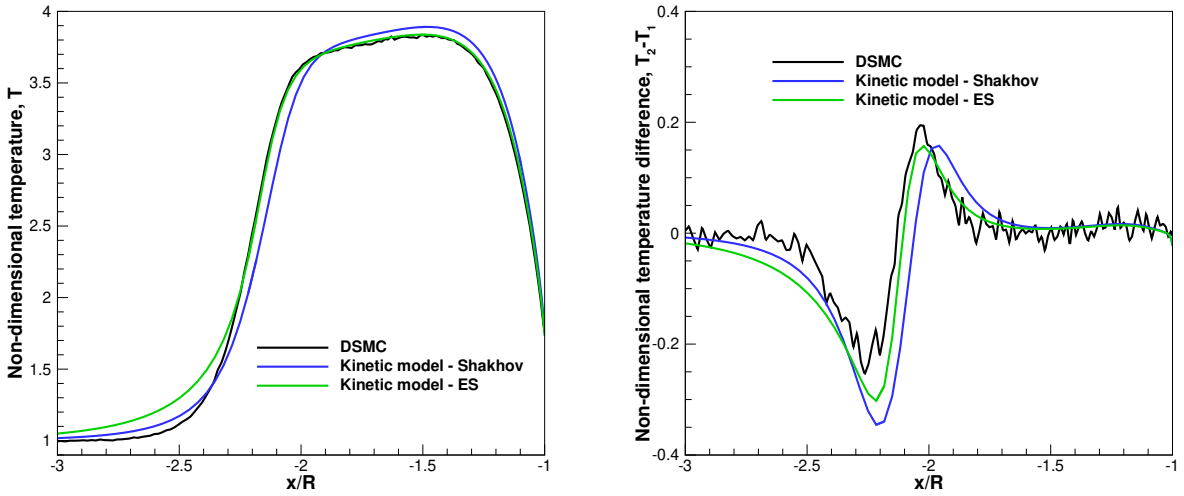

(a) Mixture temperature (b) Species-temperature difference

Figure 3.12: Comparison of the mixture temperature (in (a)) and the species temperature drift (in (b)) for the Shakhov and ES kinetic models with DSMC results for Mach number 3, mass ratio $\beta = 2$, light species concentration 90%, Knudsen number $Kn = 0.1$ and $T_{wall} = 1.5T_\infty$.

$T_{wall} = 1.5T_\infty$ in the first cell above the wall in the stagnation point for the two kinetic models ($T = 1.75T_\infty$) and so does the DSMC solution ($T = 1.77T_\infty$).

It is very interesting to observe the variation between species temperature $T_2 - T_1$ (Fig. 3.12 (b)). As in the normal shock study, the increase in T_1 is faster and therefore negative difference between the temperatures $T_2 - T_1$ is seen in the first part of the shock. Then a steeper growth of the heavy species temperature, creates a positive $T_2 - T_1$ difference, until we reach equilibrium, where the species temperatures are equalised. The kinetic models follow qualitatively the results by DSMC, but the increase of the temperature of the light species is larger. The DSMC results display some statistical scatter, since the heavy gas species is only 10% of the gas mixture and therefore a trace species in the DSMC simulation. This means the number of particles for the heavy species is only 10% of the total number of particles at the imposed boundary condition in the free-stream. This makes reducing the statistical scatter challenging with the use of constant particle weighting factors. Here we observe one of the benefits and motivations of kinetic modelling with DVM - the lack of statistical scatter for these type of flows with small concentrations of one of the species, of course at a large memory overhead.

Considering the higher mass ratio $\beta = 4$, a gas mixture of neon and krypton is simulated by DSMC. The setup closely resembles the neon-argon mixture. Again, the total free-stream number density is $3.11\text{x}10^{19} m^{-3}$, which consists of 90% neon and 10% krypton. The variable hard sphere mean free path of the mixture is $8.31\text{x}10^{-2} m$. The freestream velocity to achieve Mach number 3 is $1194.51 m/s$ with this gas mixture. Note that for the same Mach number and different mass ratios, the freestream velocity has decreased. This is consistent with the findings from the normal shock wave results in the previous section. All other simulation parameters are the

same as for the neon-argon mixture described above. Figure 3.13 shows very good agreement in the stagnation streamline density profiles predicted by dsmcFoam+ and the kinetic models.

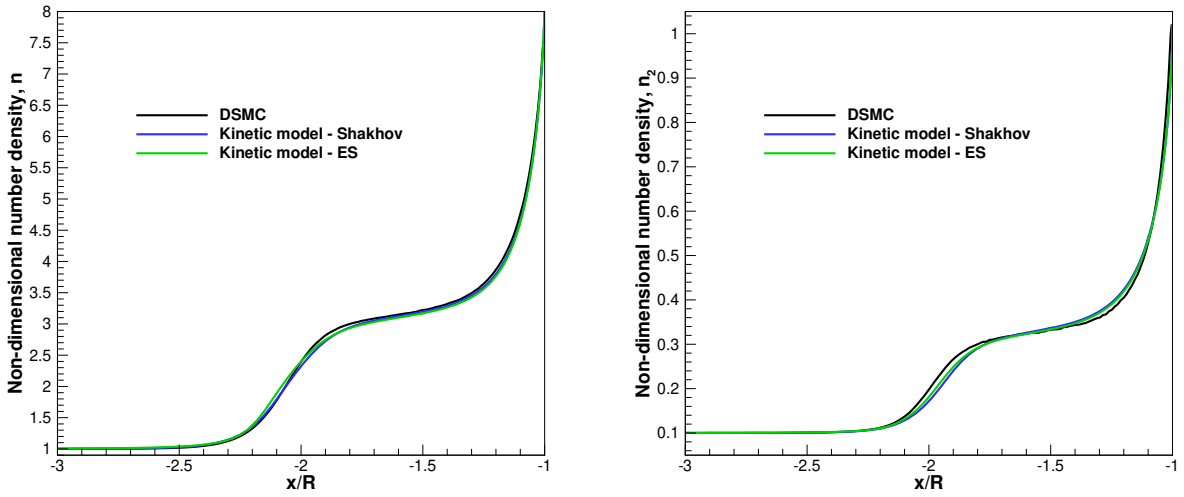

(a) Total number density

(b) Heavier-species number density

Figure 3.13: Comparison of the total number density (in (a)) and heavy species number density (in (b)) for the Shakhov and ES kinetic models with DSMC results for Mach number 3, mass ratio $\beta = 4$, light species concentration 90%, Knudsen number $Kn = 0.1$ and $T_{wall} = 1.5T_{\infty}$.

Figure 3.14 (a) shows good agreement in the stagnation streamline temperature profile for the gas mixture. The shock stand-off distances of the two kinetic models are similar to each other and to the DSMC results. The peak temperature is also lower in the DSMC results than for the kinetic models, while the Shakhov-based model is closer to the DSMC prediction.

The difference between species temperatures in Fig. 3.14 (b) is well captured by the kinetic models and DSMC in its decrease, while the increase predicted by dsmcFoam+ has a significantly greater peak temperature difference than the kinetic models. The DSMC results do not exhibit as much scatter as the lower mass ratio, because the non-dimensional temperature differences between the species are greater at the higher mass ratio. For the higher mass ratio, the two kinetic models are fairly close to each other, while the Shakhov-based model matches DSMC slightly better than the ES-based model in first part of the bow shock region.

Even though the differences between DSMC and the kinetic models are discussed in detail, they are very small and we consider the validation of the kinetic models with DSMC successful. Overall, the comparison between Shakhov-based, ES-based and DSMC shows good agreement and further inspection of different parameters like Mach number and concentration are considered part of future work.

3.3.3 Surface Heat Flux and Pressure

The heat flux and pressure along the surface of the cylinder are of particular interest for industrial applications. Two cases are investigated for the same conditions as in the previous section

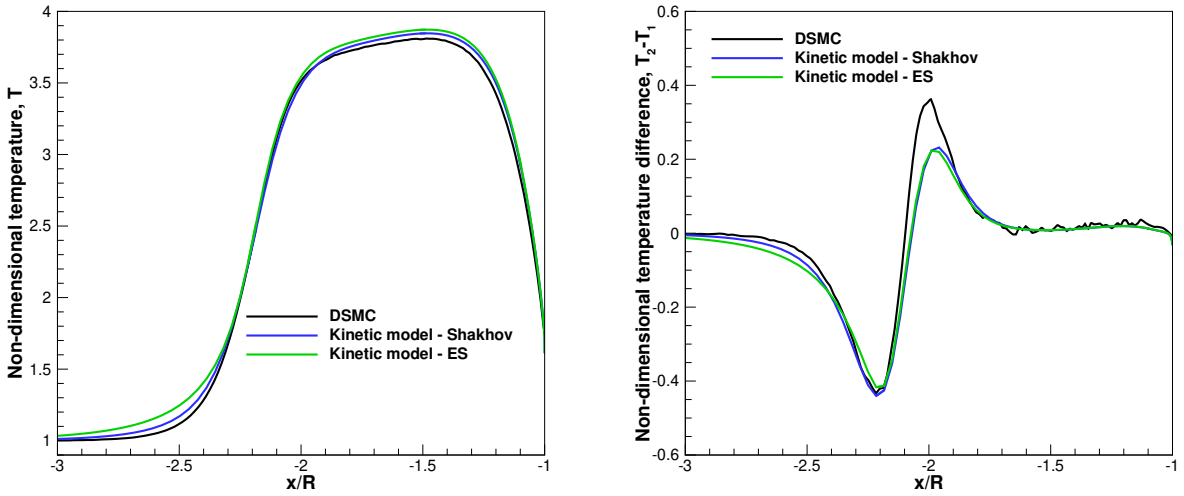

(a) Mixture temperature (b) Species-temperature difference

Figure 3.14: Comparison of the mixture temperature (in (a)) and the species temperature drift (in (b)) for the Shakhov and ES kinetic models with DSMC results for Mach number 3, mass ratio $\beta = 4$, light species concentration 90%, Knudsen number $Kn = 0.1$ and $T_{wall} = 1.5T_{\infty}$.

and the results from the Shakhov-based mixture model and the DSMC method are compared. The kinetic model is presented by red elements and DSMC with black elements for both heat flux (Fig. 3.15) and pressure (Fig. 3.16) results. Note that the heat flux non-dimensionalisation is consistent with Kosuge's [9] approach and is described in Section 3.2.3, while pressure is scaled with the free-stream pressure. In the figures the heat flux and pressure are plotted on the ordinate, while the abscissa shows the cylinder angle as measured from the center ($X = 0.0$), where the stagnation streamline is in line with 0 degrees and 90 degrees is the point where the cylinder surface is parallel to the free-stream.

The results from the DVM show good agreement with results from DSMC. The value of the non-dimensional heat flux at the stagnation point is greater for the larger mass ratio. The peak of the heat flux is at the stagnation point where the difference between DVM and DSMC results is 0.73% for $\beta = 2$ and 1.85% for $\beta = 4$. The difference between the results from the kinetic model and DSMC decreases along the cylinder surface. At the top of the cylinder ($90deg$) the non-dimensional heat flux has values under 1 (for $\beta = 2$, $q = 0.86$) and just above 1 (for $\beta = 4$, $q = 1.12$), as observed in Fig. 3.15 (a) and (b). Some discrepancies are observed in the last few cells, most likely due to the imposed boundary conditions. For DVM the extrapolation boundary condition is applied on the outflow boundary face. Meanwhile, the vacuum boundary condition imposed for DSMC is only strictly accurate for Mach number $>> 1$. Close to the cylinder surface, the flow is subsonic and therefore both boundary conditions are not strictly valid, although both are widely used for this kind of cylinder test cases. This is further pronounced in the results for the pressure on the cylinder surface and discussed in more detail below.

The gas mixture pressure along the cylinder surface for the two mass ratios is shown in

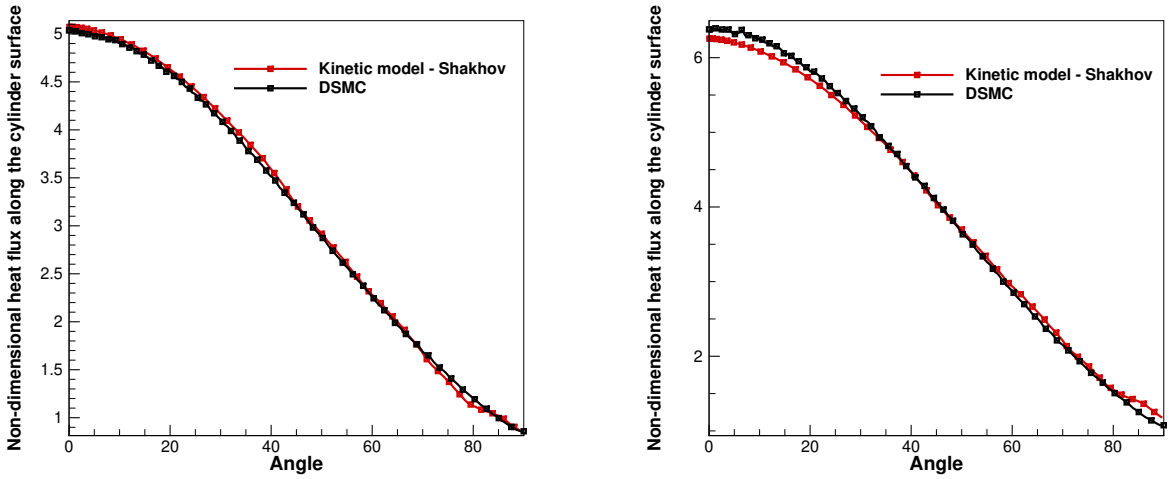

(a) Heat flux at $\beta = 2$ (b) Heat flux at $\beta = 4$

Figure 3.15: Comparison of the surface heat flux along the cylinder for the Shakhov-based kinetic model with DSMC results for Mach number 3, mass ratio $\beta = 2$ (in (a)) and $\beta = 4$ (in (b)), light species concentration 90%, Knudsen number $Kn = 0.1$ and $T_{wall} = 1.5T_{\infty}$.

Fig. 3.16 (a) and (b). There is a good comparison between the kinetic model and DSMC from the

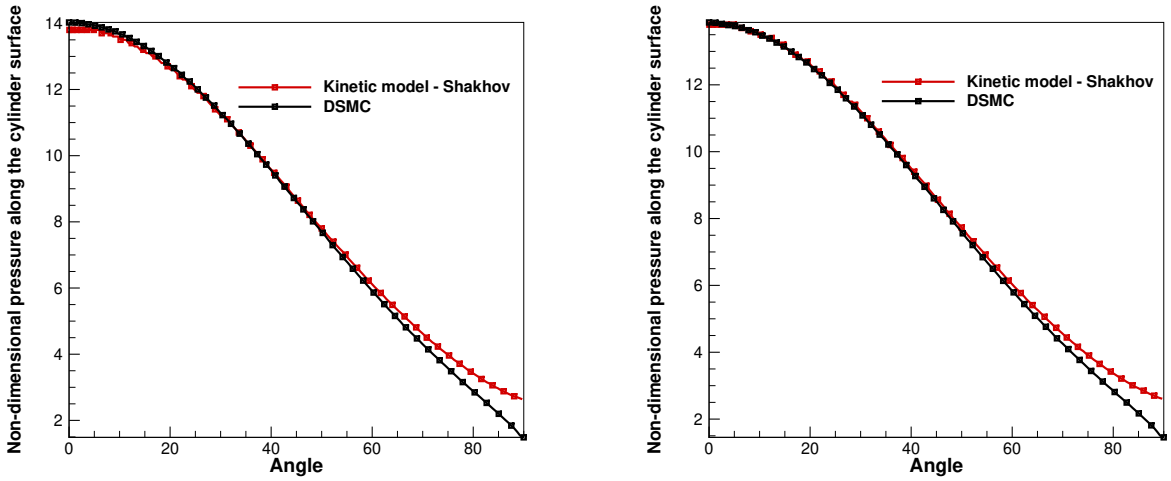

(a) Pressure at $\beta = 2$ (b) Pressure at $\beta = 4$

Figure 3.16: Comparison of the surface pressure along the cylinder for the Shakhov-based kinetic model with DSMC results for Mach number 3, mass ratio $\beta = 2$ (in (a)) and $\beta = 4$ (in (b)), light species concentration 90%, Knudsen number $Kn = 0.1$ and $T_{wall} = 1.5T_{\infty}$.

stagnation line to approximately $70deg$. Beyond that, for both mass ratios the surface pressure predicted by the kinetic model is higher than the DSMC prediction. Most likely this is due to the outflow boundary conditions imposed by the two solvers for a flow that is not supersonic in this region.

3.4 Summary of Findings

The two newly introduced kinetic models for binary gas mixtures were tested and evaluated through simulations examining the structure of a normal shock wave and the high speed flow over a cylinder. Results show:

- Indifferentiability principle was demonstrated numerically, showing the two species collapse into one under the same conditions.
- The single species profile of a normal shock wave was inspected and results for the macroscopic variables were validated with known results in the literature.
- A detailed evaluation of the profile of a normal shock for a gas mixture with different masses was conducted for varied free-stream conditions.
- Previously, detailed numerical tests were not conducted in such detail in the literature for single-relaxation mixture kinetic models with two or more correct transport coefficients. In this Chapter, results acquired by the Shakhov-based, ES-based and the Groppi et al. (with $Pr = 1$) mixture models were presented for varied free-stream conditions.
- A detailed evaluation of the three mixture model showed the correction of the third transport coefficient and the Prandtl number advantage and good agreement between the two mixture models and the Boltzmann results was observed.
- The results for the total heat flux through the shock for the two corrected models and the uncorrected model compared with the Boltzmann results further emphasized the importance of a correct Prandtl number. While a significant difference occurred in the Groppi et al. model, both the Shakhov-based and the ES-based model were close to the full Boltzmann results.
- A parametric study based on the Shakhov-based mixture model for a wide range of mass ratios and Mach numbers was conducted, which further demonstrated the importance of modelling a flow as a gas mixture.
- A parametric study varying the Mach number and the wall temperature was conducted for a flow past a cylinder. The non-equilibrium region of the shock was clearly shown to depend on the mass ratio between the species.
- The same mass ratio variation for both the Shakhov-based and ES-based models was compared with results acquired by DSMC, where a good agreement was observed in the number densities and temperatures on the stagnation streamline.
- The surface heat flux and pressure on the cylinder are important aerodynamic quantities and were also shown using the Shakhov-based mixture models and compared with DSMC.

- The Shakhov-based mixture model generally demonstrated higher accuracy than the ES-based model for both the single-species and multi-species flows considered here. It will therefore be used in the future gas kinetic study as the underlying kinetic model.

The comparisons with the benchmark results for the full Boltzmann equation and DSMC respectively, showed promising results from both new mixture kinetic models for a range of free-stream conditions. Even though future tests will be beneficial, at this stage the models are considered validated for mixtures of noble gases.

Chapter 4

Comparison of DVM and GKS for Gas Mixtures *

The formulation of computationally efficient methods describing gas mixtures at kinetic level suitable for demanding aerospace applications presents significant challenges. In the previous chapters new kinetic models were derived, theoretically validated and also numerically tested and validated using the discrete velocity method. A range of demanding high-speed flows were shown to be well-described at the kinetic level, however the computational expense of the used numerical method makes it unfeasible for large-scale aerospace applications. A more efficient method to model similar level of detail is required.

In this chapter, a gas-kinetic scheme for binary gas mixtures is derived in which the kinetic model is capable of recovering, in the continuum limit, the correct heat transfer, mixture viscosity as well as species diffusion. This gas-kinetic scheme is based on the Shakhov-based mixture model, introduced and detailed in previous chapters. The model accounts for separate species-mean velocity such that the species diffusion and velocity drift are accurately represented and this property is transferred to the gas-kinetic scheme.

The chapter begins with the GKS method development and its formulation. For the binary mixture kinetic model, a number of sample solutions, obtained using the discrete velocity method (DVM) and the new GKS methods are presented. The derivation of the GKS involves using a CE expansion, which limits the scheme to flows close to equilibrium. A detailed comparison is shown where the DVM results represent a benchmark for the GKS and assist in establishing the extent to which GKS provides accurate results. Supersonic flows with varying species mass ratios, concentrations and Knudsen number are investigated. The complex flow physics occurring in a normal shock in a binary mixture is considered to highlight the species diffusion and velocity drift effects and their dependencies on the species atomic mass ratios and concentration. A two-dimensional flow over a flat plate is also studied for different flow conditions, where strong non-equilibrium effects of interest occur particularly around the leading edge of the plate. The

*Published in Journal of Thermophysics and Heat Transfer.

key advantage of the GKS is the computational efficiency of the scheme, which is discussed in detail for the presented baseline test cases. The limitations of the GKS for different flows and different levels of thermodynamic non-equilibrium are examined.

4.1 Development of a Gas-kinetic Scheme

4.1.1 Governing Equations

In this section, the gas-kinetic scheme for a well-resolved flow (defined in Chapter 1) is presented, based on the newly developed Shakhov-based mixture model [88], presented in Chapter 2, and the original gas-kinetic BGK scheme [6,44,45]. It is important to note that unlike a single species gas, momentum and energy are conserved only for the gas mixture. This means that the species momentum equations will return a source term S_s. The source term is created due to the difference between species velocities, which is of order $O(\varepsilon)$ (where ε is a small number of the order of the Knudsen number). The presented GKS is derived for viscous flow based on the first order CE expansion so that $O(\varepsilon)$ terms are included. Separate species momentum equations are used which include sources as defined previously. The species conservation follows from the CE analysis as:

$$\frac{\partial n_s}{\partial t}+\frac{\partial}{\partial x}\left\{n_s u_0-\varepsilon\frac{kT}{\eta}\left[\frac{1}{m_s}\frac{\partial n_s}{\partial x}-\frac{n_s}{\rho}\frac{\partial n}{\partial x}+\frac{n_s}{T}\left(\frac{1}{m_s}-\frac{n}{\rho}\right)\frac{\partial T}{\partial x}\right]\right\}=0, \tag{4.1}$$

where the second term within curly brackets represents the velocity drift between species mean velocity u_s and the mixture mean velocity u_0, caused by diffusion in case of different molecular masses of the species. The species momentum equation is:

$$\frac{\partial\left(\rho_s u_s\right)}{\partial t}+\frac{\partial}{\partial x}\left[n_s k\hat{T}+\rho_s u_0^2-2\rho_s u_0\left(u_0-u_s\right)+\left(1-\frac{\eta}{\nu}\right)^2\left(u_0-u_s\right)^2-\mu\left(\frac{4}{3}\frac{\partial u_0}{\partial x}\right)\right] = \nu\rho_s\left(\frac{\eta}{\nu}\right)\left(u_0-u_s\right), \tag{4.2}$$

with viscosity coefficient $\mu=(\varepsilon/\nu)nkT$. As expected, the right-hand side of Eq. (4.2) results in a source term S_s for each species. The summation of the source terms over all species goes to zero, which confirms that momentum is conserved for the mixture. The energy equation for the gas mixture is in the form:

$$\frac{\partial}{\partial t}\left[\frac{3}{2}nkT+\frac{1}{2}\rho u_0^2\right]+\frac{\partial}{\partial x}\left\{\sum_{s=1}^{2}m_s n_s\left[\frac{5}{2}\frac{kT}{m_s}u_0+\frac{1}{2}u_0^3+\left\{\frac{5}{2}\frac{kT}{m_s}+\frac{3}{2}u_0^2\right\}\left(u_0-u_s\right)\right] -\varepsilon\frac{kT}{\nu}\sum_{s=1}^{2}\left[\frac{4}{3}n_s u_0\frac{\partial u_0}{\partial x}+\frac{1}{Pr}\frac{5}{2}n_s\left(\frac{k}{m_s}\right)\frac{\partial T}{\partial x}\right]\right\}=0. \tag{4.3}$$

4.1.2 Cell Face Distribution Function

The mathematical development of the GKS concerns with the evolution of the species distribution function at a cell face. Here, we initially follow the derivation as introduced by Xu in [6,43] as adapted to include the Shakhov-based mixture model. We also introduce the assumption for a well-resolved scheme, similar to Xu. In the last step, following the work introduced by Colonia et al. [80] for the Rykov GKS, we use cell-centered data of the two cells around the cell face to calculate the flux, which will be detailed in this section.

In the following, a quasi-1D flow is considered. Starting from the BGK-type equation for a gas mixture with species s and mixture collision rate ν, the GKS for the mixture is detailed. The numerical fluxes for a cell face $(j+1/2)$ between cell j (left) and cell $j+1$ (right) can be obtained from the time dependent distribution function (Eq. (4.4)) around the interface $x_{j+1/2}$.

$$f_s(x_{j+1/2},t,u) = \nu \int_0^t f_s^{eq}(x',t',u)\exp\big(-\nu(t-t')\big)dt' + \exp\big(-\nu t\big) f_s^0(x_{j+1/2}-ut,0,u), \quad (4.4)$$

with $x' = x_{j+1/2} - u(t-t')$ - the particle trajectory during the time-step considered and u is the particle velocity in the x-direction. A characteristic of the GKS method is that the inviscid and viscous fluxes are obtained simultaneously, since the distribution function comprises of equilibrium and non-equilibrium contributions. The initial distribution function f_s^0 around the interface is based on a CE expansion as:

$$f_s^0(x,0,u) \;=\; G_s^{Sh}(x,0) - \frac{1}{\nu}\left(\frac{\partial f_s^M}{\partial t} + u\frac{\partial f_s^M}{\partial x}\right), \quad (4.5)$$

where $G_s^{Sh}(x,0)$ is the modified Maxwellian in the mixture kinetic model evaluated for the conditions in position x at time $t=0$, while f_s^M are the unmodified Maxwellian distribution function. Assuming a linear variation of the distribution function within the cells, the expression is expanded as:

$$\begin{aligned} f_s^0(x,0,u) \;&=\; G_s^{Sh}(x_{j+1/2},0) + \left.\frac{\partial G_s^{Sh}}{\partial x}\right|_{x_{j+1}/2}\big(x-x_{j+1/2}\big) \\ &\quad -\frac{1}{\nu}\left(\frac{\partial f_s^M}{\partial t} + u\frac{\partial f_s^M}{\partial x}\right)\bigg|_{x_{j+1/2}} - \frac{1}{\nu}\left(\frac{\partial^2 f_s^M}{\partial t\partial x} + u\frac{\partial^2 f_s^M}{\partial x^2}\right)\bigg|_{x_{j+1/2}}\big(x-x_{j+1/2}\big), \\ f_s^0(x,0,u) \;&\approx\; G_s^{Sh}(x_{j+1/2},0) + f_s^M\Big[a\big(x-x_{j+1/2}\big) - \frac{1}{\nu}\Big(ua+A\Big)\Big], \end{aligned} \quad (4.6)$$

where a and A represent spatial and temporal derivatives as:

$$a = \frac{1}{f_s^M}\frac{\partial f_s^M}{\partial x} \;\;;\;\; \frac{\partial f_s^M}{\partial x} \approx \frac{\partial G_s^{Sh}}{\partial x} \;\;;\;\; A = \frac{1}{f_s^M}\frac{\partial f_s^M}{\partial t}, \quad (4.7)$$

where the derivatives are evaluated at $x_{j+1/2}$ and the assumption is made that the derivative of G_s^{Sh} can be approximated by the derivative of f_s^M for the order of accuracy in ν and space considered. The equilibrium distribution f_s^{eq} around the cell interface is also approximated using a second-order accurate in space Taylor series expansion:

$$f_s^{eq}(x,t,u) = G_s^{Sh}(x_{j+1/2},0) + f_s^M\Big[a\big(x-x_{j+1/2}\big)+At\Big]. \tag{4.8}$$

Unlike the initial non-equilibrium function f_s^0, which is independent in time, the equilibrium function varies within a time-step due to the fact that particle collisions are considered along with particle convection. Using Eq. (4.8), the integral on the right-hand side of Eq. (4.4) becomes:

$$\begin{aligned}\nu\int_0^t f_s^{eq}(x',t',u)\exp\big(-\nu(t-t')\big)dt' &= \nu G_s^{Sh}(x_{j+1/2},0)\int_0^t \exp\big(-\nu(t-t')\big)dt' \\ &\quad + \nu f_s^M\int_0^t\Big[-ua(t-t')+At'\Big]\exp\big(-\nu(t-t')\big)dt' \\ = \Big[1-\exp\big(-\nu t\big)\Big]G_s^{Sh}(x_{j+1/2},0) &+ f_s^M\Bigg[-au\frac{1}{\nu}+au\Big(t+\frac{1}{\nu}\Big)\exp\big(-\nu t\big) \\ &\quad + At-\frac{1}{\nu}\Big[1-\exp\big(-\nu t\big)\Big]A\Bigg].\end{aligned} \tag{4.9}$$

Using Eq. (4.6), the second term on the right-hand side of Eq. (4.4) becomes:

$$\exp\big(-\nu t\big)f_s^0(x_{j+1/2},0,u) = G_s^{Sh}(x_{j+1/2},0)\exp\big(-\nu t\big) + f_s^M\Big[-aut-\frac{1}{\nu}\big(ua+A\big)\Big]\exp\big(-\nu t\big). \tag{4.10}$$

Combining Eq. (4.9) and (4.10), for a well-revolved flow, Eq. (4.4) becomes the time-dependent gas distribution function on the cell face, from which the flux of macroscopic variables can be expressed:

$$\begin{aligned}f_s(x_{j+1/2},t,u) &= G_s^{Sh}(x_{j+1/2},0) - \Big[\frac{1}{\nu}\Big(au+A\Big)-At\Big]f_s^M \\ &= G_s^{Sh}(x_{j+1/2},0) - \frac{1}{\nu}\left(\frac{\partial f_s^M}{\partial t}+u\frac{\partial f_s^M}{\partial x}\right)+t\frac{\partial f_s^M}{\partial t}.\end{aligned} \tag{4.11}$$

The time-derivative in the Maxwellian is ignored in our implementation, since extensive examination for the single-species GKS showed that neglecting this term has a negligible effect on flow solution [80]. Following Xu, the time-dependent numerical fluxes across the cell face should be evaluated by taking moments of the time-dependent distribution function on the cell face:

$$\underline{F}_{j+\frac{1}{2}} = \sum_{s=1}^{2}\iiint_{-\infty}^{+\infty} u\underline{\Psi}_s f_s(x_{j+1/2},t,u)d\underline{u}, \tag{4.12}$$

where $\underline{\Psi}_1 = (1,0,m_1u,0,\frac{1}{2}m_1(u^2+v^2+w^2))^T$ and $\underline{\Psi}_2 = (0,1,0,m_2u,\frac{1}{2}m_2(u^2+v^2+w^2))^T$. However, following the work on the Rykov GKS by Colonia, Steijl and Barakos [80] spatial reconstruction towards cell-face data is not carried out, but rather the cell-centred data is used to calculate the right and left state of the equilibrium distribution function and the spatial and temporal derivatives around the $j+1/2$ face. It follows:

$$f_s(x_j,t,u) = G_s^{Sh}(x_j,0) - \frac{1}{\nu}\left(\frac{\partial f_s^M}{\partial t} + u\frac{\partial f_s^M}{\partial x}\right), \tag{4.13}$$

is the left state calculated in cell center j and similar calculation is done for the right state in cell center $j+1$ for $f_s(x_{j+1},t,u)$. The flux $\underline{F}_{j+\frac{1}{2}}$ on the cell face is calculated by summing the two half-spaced integrals over of all positive molecular velocities u going from left to right and all negative velocities coming from right to left. Eq. (4.12) then becomes:

$$\underline{F}_{j+\frac{1}{2}} = \sum_{s=1}^{2}\left[\iiint_{-\infty}^{+\infty}\int_{0}^{+\infty} u\underline{\Psi}_s f_s(x_j,t,u)dudvdw + \iiint_{-\infty}^{+\infty}\int_{-\infty}^{0} u\underline{\Psi}_s f_s(x_{j+1},t,u)dudvdw\right], \tag{4.14}$$

where $\underline{\Psi}_1 = (1,0,m_1u,0,\frac{1}{2}m_1(u^2+v^2+w^2))^T$ and $\underline{\Psi}_2 = (0,1,0,m_2u,\frac{1}{2}m_2(u^2+v^2+w^2))^T$. Compared to Xu's formulation for well-resolved flow, our implementation adds as a small amount of additional numerical dissipation and robustness, at the price of a reduction in the order of accuracy in space. As a benefit, the used version is less complicated to implement, i.e. no need for limiters. For the cases considered, the meshes were selected to lead to well-revolved flows, supporting the assumptions made in the current GKS solver implementation. The conserved macroscopic variables $\underline{W}_j$ (Eq. (4.15)) are the variables the GKS method stores in the cell centers and which are integrated in time:

$$\underline{W}_j = \begin{pmatrix} n_1 \\ n_2 \\ \rho u_1 \\ \rho u_2 \\ \frac{3}{2}nkT + \frac{1}{2}\rho u_0^2 \end{pmatrix}_j . \tag{4.15}$$

The update of the conservative variables from time step n to $(n+1)$ is then defined as:

$$\underline{W}_j^{n+1} = \underline{W}_j^n + \frac{1}{\Delta x}\int_{t^n}^{t^{n+1}}\Big(\underline{F}_{j-1/2}(t) - \underline{F}_{j+1/2}(t)\Big)dt + \Delta t(0,0,S_1,S_2,0)^T, \tag{4.16}$$

where the source term is defined as shown in Eq. (4.17):

$$S_s = \nu\rho_s\left(\frac{\eta}{\nu}\right)(u_0 - u_s) \quad ; \quad s = 1,2. \tag{4.17}$$

The GKS model described above for quasi one-dimensional flows was further derived for two-dimensional flows on a curvilinear mesh. In the two-dimensional formulation, a direction-cosine approach is followed and the cell-face normal direction replaces the x-direction in the discussion above for 1D flows. The velocity-space integrals were worked out analytically to provide the main efficiency gain of a GKS approach relative to the DVM method.

4.2 Numerical Evaluation

The newly developed GKS scheme is tested in the next sections and compared to DVM solutions for the same kinetic model as shown in Fig. 4.1. Two different test cases, e.g. the flow through

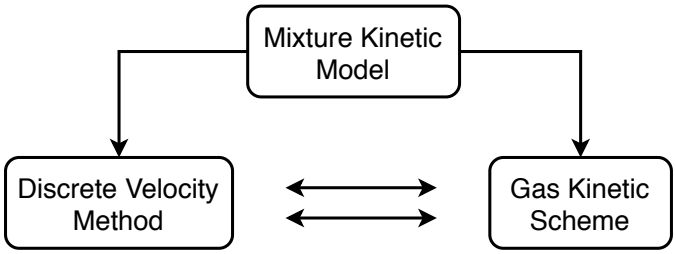

Figure 4.1: The DVM and GKS apply the same Shakhov-based mixture kinetic model and are compared.

a normal shock wave and the rarefied supersonic flow over a flat plate, are considered. The normal shock test case represents the simplest problem that involves strong gradients and non-equilibrium flow and is also well documented. The focus is on the effect of treating the gas as a mixture, inspecting the diffusion effect and species properties. The change in the flow is demonstrated for different Knudsen numbers and species mass ratios. The kinetic model is implemented with the discrete velocity method (DVM) and the gas kinetic scheme (GKS). DVM allows for strong non-equilibrium flows, since there are no underlying assumptions for small deviations as in the CE expansion, required for the GKS. The high computational expense of the DVM is feasible for one and two-dimensional cases, but the extension to vehicles of practical application will require an alternative approach, e.g. the GKS method or a hybrid GKS/DVM approach. The solutions provided by the GKS and DVM methods are compared, based on the same kinetic model. Ideally, the results from the GKS will be as close as possible to the results of the DVM. The computational cost of both numerical approaches is also detailed.

4.3 Normal Shock Wave

A classical problem for rarefied flows is the study of a normal shock wave for single as well as multi-species gases. Monoatomic binary mixtures have been investigated extensively, experimentally [74, 75] and numerically [9], providing a dataset for validation.

Table 4.1: Test case conditions for a normal shock wave (DVM vs GKS)

M_∞	m_2/m_1	n_1/n	ω
1.5	2	0.9	0.5
1.5	2	0.5	0.5
1.5	4	0.9	0.5
1.5	4	0.9	0.72

In this section the profile of a normal shock wave is studied for a binary mixture of gases with different molecular masses. Test case conditions are summarised in Table 4.1. Here M_∞ is the free-stream Mach number, m_2/m_1 defines the heavy to light gas mass ratio, n_1/n is the concentration of light gas in the flow. The $\omega = 0.5$ refers to a hard-sphere molecular potential and $\omega = 0.72$ to a variable hard-sphere potential. The goal is to analyse the effect of different free stream conditions (ratio of masses, concentration ratio and molecular potential) on the macroscopic flow variables.

Figure 4.2 shows the normalised number density for each species and the mixture temperature through the shock under the specified conditions, starting with free stream Mach number of 1.5 and varying the concentration (50% and 90% light species) and mass (m_2/m_1= 2; 4) ratios (Fig. 4.2 (a)-(d)). These flow-conditions are chosen to allow for a numerical comparison with the results from Kosuge et. al [9] for a normal shock using the full Boltzmann equation, represented by the red elements. The DVM results are in blue and the GKS results are in green. It is important to stress that the model in Kosuge's work is not a single-relaxation time BGK model and therefore the DVM results for Shakhov-derived binary mixture model will also deviate from those results. The reference length of the problem is defined as:

$$L_{ref} = \frac{u_{ref}}{t_{ref}} = \frac{u_{ref}}{\tau_{ref}} = \frac{u_{ref}\mu_{ref}}{p_{ref}}, \tag{4.18}$$

where the reference viscosity is defined as in Eq. (4.19) and τ_{ref} is a reference relaxation time where $\tau = 1/\nu$. The reference viscosity μ_{ref} is taken for a smooth, rigid, elastic sphere [24] with diameter d and mass of the mixture $m_{mix} = \rho/n$ as:

$$\mu_{ref} = \frac{5}{16d^2}\sqrt{\frac{km_{mix}T}{\pi}}. \tag{4.19}$$

The mean free path is defined as $\lambda_{ref} = 1/(\sqrt{2}\pi d^2 n)$ in the solution of the full Boltzmann equation [9]. We use the ratio between the reference length L_{ref} and the mean free path λ_{ref} as a scaling factor:

$$\frac{L_{ref}}{\lambda_{ref}} = \frac{5\sqrt{\pi}}{8}\sqrt{\frac{n_1+\beta n_2}{n_1+n_2}}, \tag{4.20}$$

where the constant $\beta = m_2/m_1$ is the mass ratio. For increasing levels of thermodynamic non-

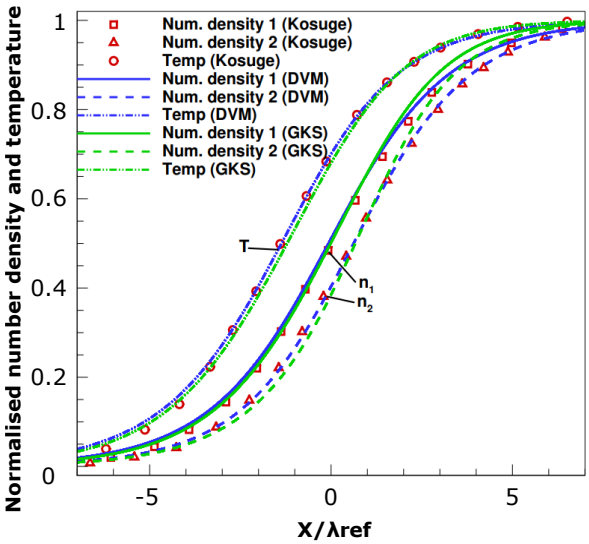

(a) $M_\infty = 1.5;\ m_2/m_1 = 2;\ n_1/n = 0.9$

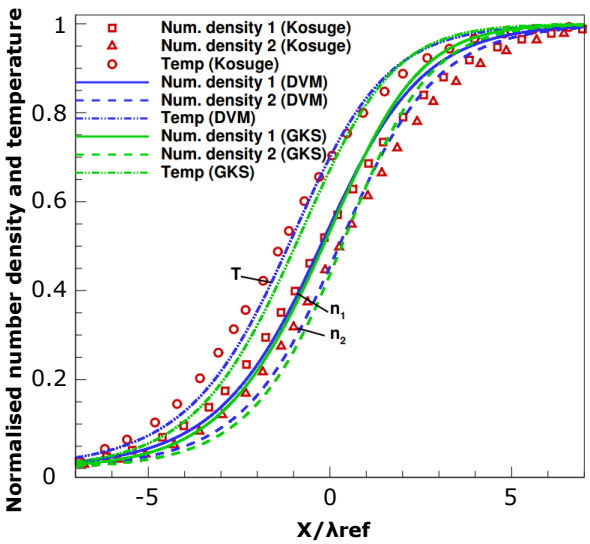

(b) $M_\infty = 1.5;\ m_2/m_1 = 2;\ n_1/n = 0.5.$

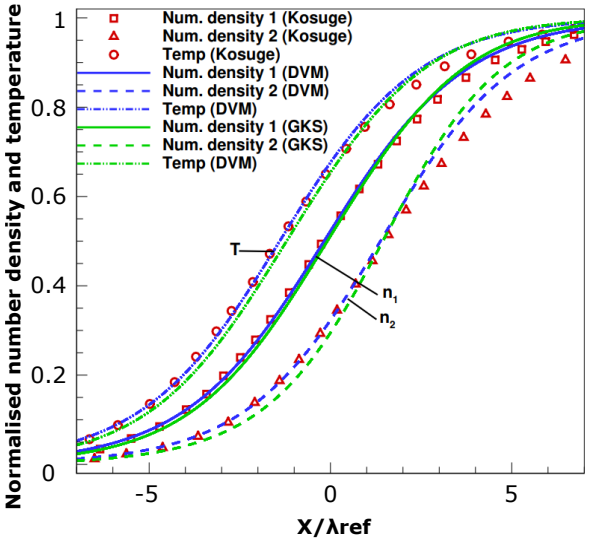

(c) $M_\infty = 1.5;\ m_2/m_1 = 4;\ n_1/n = 0.9$

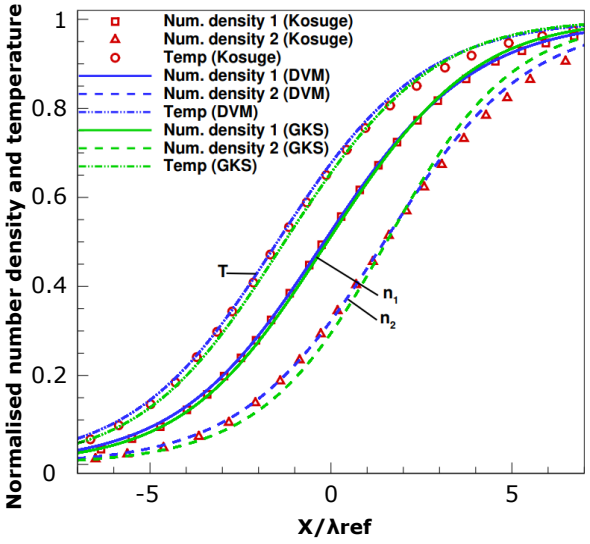

(d) $M_\infty = 1.5;\ m_2/m_1 = 4;\ n_1/n = 0.9;$ $\omega = 0.72.$

Figure 4.2: Profile of species number densities and mixture temperature of a binary gas mixture through a normal shock wave for Mach number 1.5 and varied inflow conditions: $m_2/m_1 = 2;\ n_1/n = 0.9$ in (a), $m_2/m_1 = 2;\ n_1/n = 0.5.$ in (b), $m_2/m_1 = 4;\ n_1/n = 0.9$ in (c) and $m_2/m_1 = 4;\ n_1/n = 0.9;\ \omega = 0.72.$ in (d).

equilibrium this difference in the used kinetic models will be more pronounced. A key aspect of the comparison between our DVM and GKS results (both based on the same kinetic model [88]) is to assess for what level of thermodynamic non-equilibrium the GKS approach can be employed.

Characteristic features of the problem include the lighter species (Species 1) reacting faster to the shock than the heavy species (Species 2). This becomes more evident for higher concentration of light species and with increasing mass ratios, as can be seen in Fig. 4.2. The observed GKS solutions for the number densities and the mixture temperature match closely with the solutions

from the DVM under different flow conditions. The number density of the heavy gas (n_2), which acts as a trace gas where the concentration of light gas is 90%, deviates more from the Boltzmann solution for both the DVM and GKS than the number density of the lighter gas (n_1). The shock profile predicted by the GKS scheme versus the DVM is slightly steeper and as a consequence the shock is thinner in comparison to the DVM results. This thinner shock is in line with expectations based on single-species GKS results [80]. This effect will be more pronounced for higher Mach numbers. At the same time, the well-known disadvantage of the BGK-based kinetic models, i.e. the longer upstream tail, will be reduced with the steeper profile of the GKS solutions.

The GKS presented in this chapter is derived from the Shakhov-based mixture model, introduced in Chapter2. A characteristic feature of the underlying kinetic model for this GKS is that it recovers three correct transport coefficients. Compared to the established GKS mixture work [85–87], the species mean velocities and temperatures are allowed to deviate from each other and from the gas mixture means. Figure 4.3 shows the normalised species velocity profiles u_2 and u_1 through the shock wave. The difference between the velocities and their change under varied conditions demonstrates the importance of modelling the species velocities separately. This important limitation of most existing GKS methods for gas mixtures is overcome with the current scheme. As with the number densities, the lighter species velocity reacts faster to the shock than the heavy gas. Focusing on the differences between Fig. 4.3 (a),(b) and (c),(d), it is easy to notice that the higher the mass ratio, the bigger the difference between the velocities, as can be expected since a stronger non-equilibrium effect will occur. The GKS provides a good match with the DVM for the solution of the species velocities. As before the shock wave profile is slightly steeper and results for the gas with bigger concentration (species 1) are in better agreement.

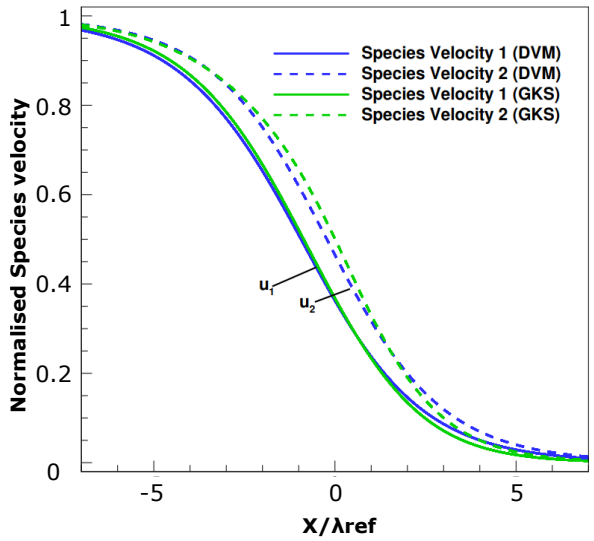

(a) $M_\infty = 1.5;\ m_2/m_1 = 2;\ n_1/n = 0.9$

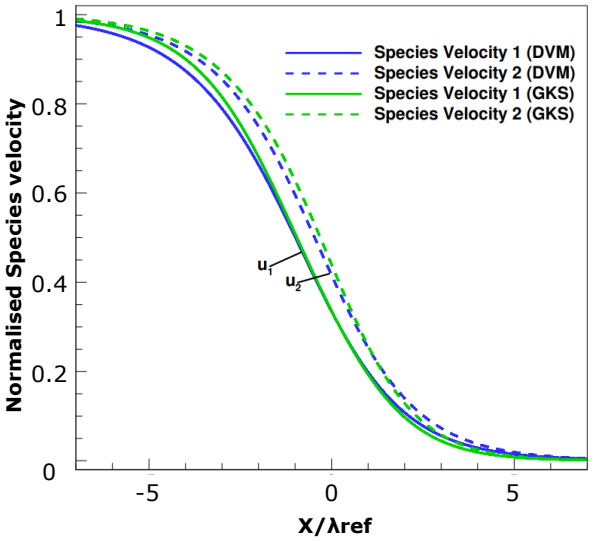

(b) $M_\infty = 1.5;\ m_2/m_1 = 2;\ n_1/n = 0.5.$

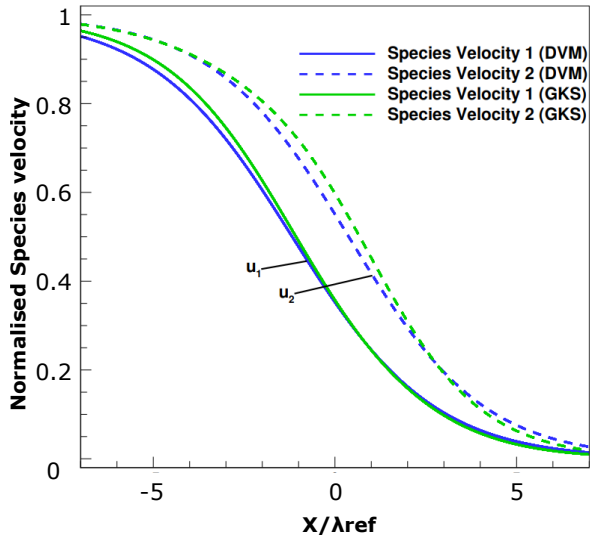

(c) $M_\infty = 1.5;\ m_2/m_1 = 4;\ n_1/n = 0.9$

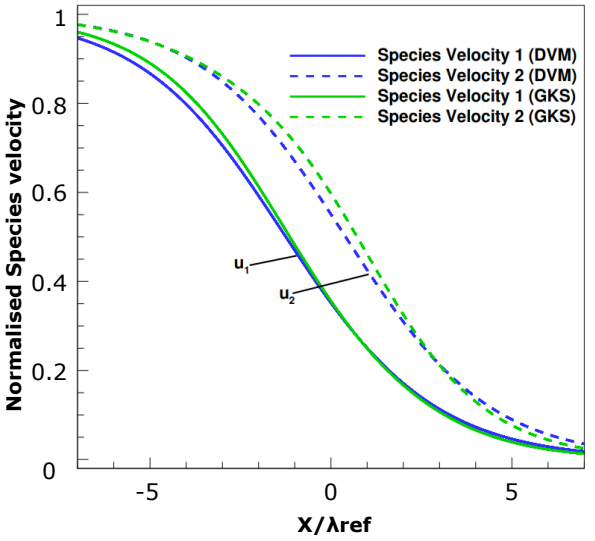

(d) $M_\infty = 1.5;\ m_2/m_1 = 4;\ n_1/n = 0.9;$ $\omega = 0.72.$

Figure 4.3: Profile of species velocities of a binary gas mixture through a normal shock wave for Mach number 1.5 and varied inflow conditions: $m_2/m_1 = 2;\ n_1/n = 0.9$ in (a), $m_2/m_1 = 2;\ n_1/n = 0.5.$ in (b), $m_2/m_1 = 4;\ n_1/n = 0.9$ in (c) and $m_2/m_1 = 4;\ n_1/n = 0.9;\ \omega = 0.72.$ in (d).

4.4 Flat Plate

A second test case considered is a supersonic rarefied flow over a flat plate. This test case is challenging due to the complex non-equilibrium boundary layer, with velocity slip as well as a jump in temperature between the wall and the gas in the immediate vicinity for the rarefied cases considered here. The grid is shown in Fig. 4.4 together with the boundary conditions. The changes of the flow are examined for varied species mass ratio, rarefication level and wall temperature. The DVM and GKS solutions are compared. The baseline test case is taken at

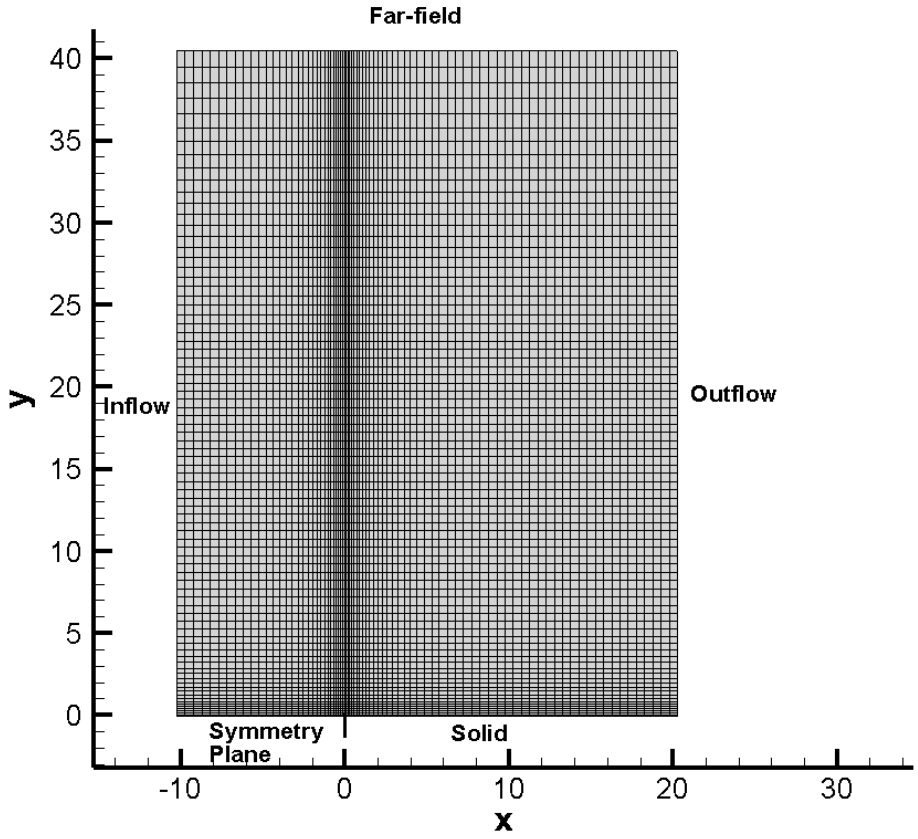

Figure 4.4: Mesh of cylinder and imposed boundary conditions.

$M_\infty = 1.5$, mass ratio of 2, Knudsen number 0.05. Note that the Knudsen number is based on the reference length, calculated as in Eq. (4.18). The scaling factor is not required since we can compare the DVM and GKS based on the same reference length. This is also reference length is used for the 2D mesh. The temperature of the wall is fixed at 1.5 times the free-stream temperature, while a fully accommodating diffuse wall is assumed. The free-stream conditions for all cases involve a concentration of 90% for the light species and 10% heavy species. All test case conditions are summarised in the Table 4.2.

Table 4.2: Test case conditions for a flow over a flat plate (DVM vs GKS)

M_∞	m_2/m_1	Kn	T_{wall}
1.5	2	0.05	$1.5T_\infty$
1.5	2	0.025	$1.5T_\infty$
1.5	4	0.05	$1.5T_\infty$
1.5	2	0.05	$1.0T_\infty$

The solutions for the flow variables for the DVM and GKS matched closely as seen from the

normal shock wave results. For the same Mach number 1.5, the shock at the flat plate is weaker, which leads to even better agreement between the two numerical schemes for the macroscopic variables. In Fig. 4.5 the Mach number and the mixture temperature contours for the baseline test case are presented. The results demonstrate a good comparison between the DVM and GKS. We want to investigate the differences between them. Therefore, we will next focus our atten-

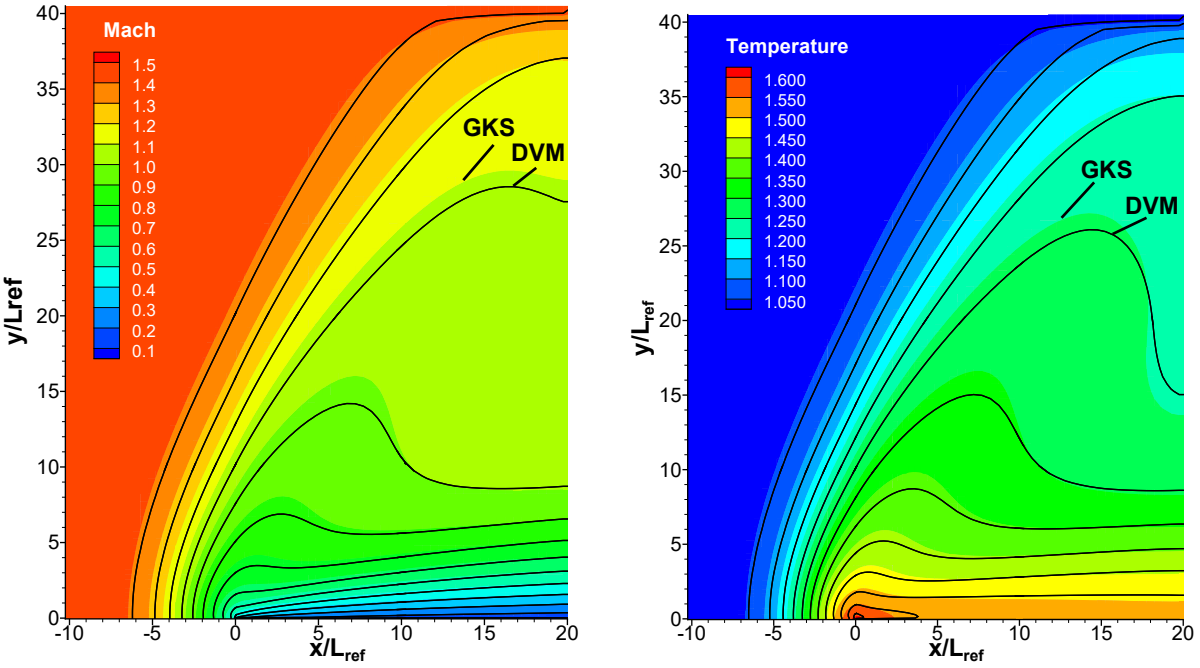

(a) Mach number (b) Mixture temperature

Figure 4.5: Mach number and mixture temperature variation of the baseline test case for a binary mixture flow over a flat plate for Mach number $M_\infty = 1.5$, mass ratio $m_2/m_1 = 2$, Knudsen number $Kn = 0.05$ and $T_{wall} = 1.5T_\infty$.

tion on the diffusion effects, in particular the concentration variation of the light species in the mixture (Fig. 4.6) and the species velocity difference $u_2 - u_1$ (Fig. 4.7). Note that these are very detailed plots and seemingly large variations between the GKS (in color flood) and the DVM (black lines) are of the order of less than 1% for the concentrations and $3-4\%$ for the difference in velocities.

To highlight the effect of the Knudsen number, two different length-scales were considered in the presented numerical results. The lower-Knudsen number case involves a flat plate length of 40 reference lengths of the flow at free-stream conditions, while the higher-Knudsen number case involves a plate length of 20 reference lengths. The ratio of the species molecular masses is also varied. A further aspect investigated is the imposed wall temperature, i.e. a lower wall temperature will lead to thinner boundary layer and a somewhat weaker displacement effect. Fig. 4.6 and Fig. 4.7 show the variation of concentration of the light species and the difference between the species velocities, respectively. The strongest non-equilibrium effects will occur close to the leading edge of the plate, where the largest gradients in the flow occur. This is evident in all the

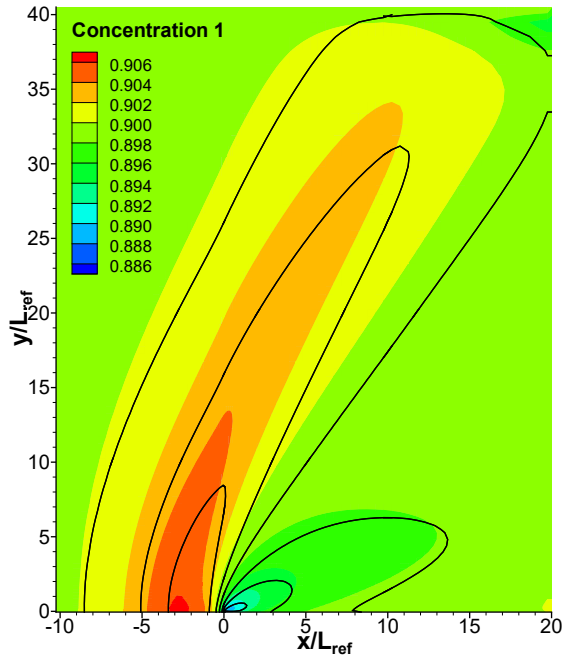

(a) $m_2/m_1 = 2$; $Kn = 0.05$; $T_{wall} = 1.5T_\infty$

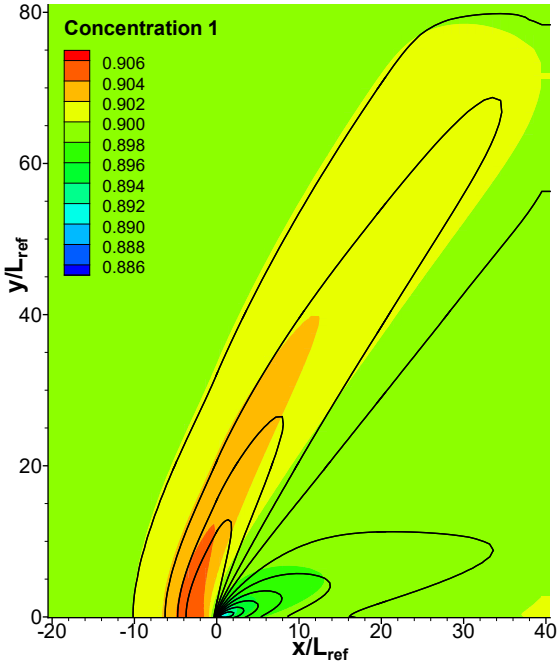

(b) $m_2/m_1 = 2$; $Kn = 0.025$; $T_{wall} = 1.5T_\infty$

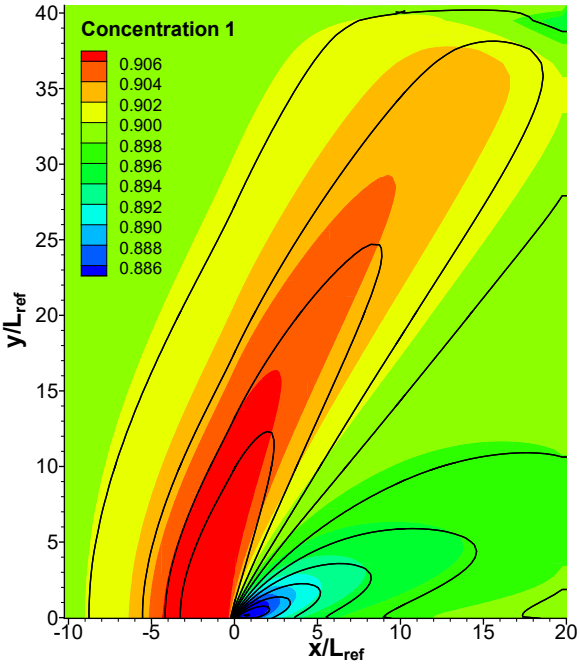

(c) $m_2/m_1 = 4$; $Kn = 0.05$; $T_{wall} = 1.5T_\infty$

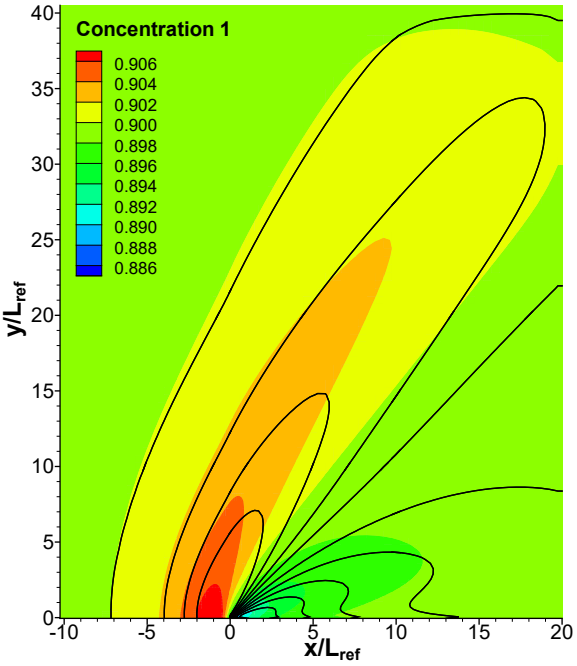

(d) $m_2/m_1 = 2$; $Kn = 0.05$; $T_{wall} = 1.0T_\infty$

Figure 4.6: Light species concentration variation in a binary mixture flow over a flat plate for Mach number $M_\infty = 1.5$ and varied inflow conditions: $m_2/m_1 = 2$; $Kn = 0.05$; $T_{wall} = 1.5T_\infty$ in (a), $m_2/m_1 = 2$; $Kn = 0.025$; $T_{wall} = 1.5T_\infty$ in (b), $m_2/m_1 = 4$; $Kn = 0.05$; $T_{wall} = 1.5T_\infty$ in (c) and $m_2/m_1 = 2$; $Kn = 0.05$; $T_{wall} = 1.0T_\infty$ in (d).

results shown in the figures. In Fig. 4.6 it can be seen that even for the considered flows without chemistry, the non-equilibrium effects give rise to a change in species concentration, caused

by diffusion of the species. As expected the lower level of rarefaction in the $Kn = 0.025$ case leads to a slightly smaller change in concentration as compared to the baseline $Kn = 0.050$ case. Clearly, for a larger ratio of molecular masses, the velocity drift is more pronounced, leading to larger concentration changes, as can be seen in Fig. 4.6(c). The effect of the lower wall temperature can be seen by comparing Fig. 4.6(d) with the result in Fig. 4.6(a). For this relatively low Mach number, it can be seen that the effect is limited, however not insignificant. Comparing the GKS and DVM results, overall a good agreement can be observed, considering the level of detail highlighted. It is important to note that the GKS solver represents concentration changes that compare well with DVM, showing that this important non-equilibrium effect is captured.

A similar comparison for the different cases and for the DVM and GKS is shown in Fig. 4.7. The non-equilibrium effect shown here is the occurrence of velocity drift, represented by the difference between the non-dimensional species $u-$velocities. The extent of non-equilibrium effects follows the pattern of that in the concentration changes, i.e. with more pronounced effects for larger Kn and mass ratio, mainly focussed in the immediate vicinity of the plate leading edge. Comparing Fig. 4.7(a) and Fig. 4.7(c), it shows that the maximum and the region of the difference between the species velocities are bigger for the larger mass ratio case.

In order to explore the limitations of the gas-kinetic scheme, we focus on the shear stress at the wall of the flat plate. The biggest variation between the DVM and the GKS is at the leading edge of the flat plate and in the cells just above it. Three test cases are considered with fixed Mach number 1.5, mass ratio 2 and light species concentration 90%, while the Knudsen number is varied. Starting at the baseline test case at $Kn = 0.05$ (in blue), we consider a more rarefied flow at $Kn = 0.075$ (in green) and a more continuum flow at $Kn = 0.0125$ (in red). In Fig. 4.8(a) the shear stress along the flat plate is presented. As expected the biggest variation between the DVM (square symbols) and GKS(delta symbols) solutions is at the leading edge of the flat plate. The most rarefied case with $Kn = 0.075$ shows the biggest difference between the DVM and GKS in the result for the shear stress. As the flow becomes more continuum towards Knudsen number of 0.05 and 0.0125 this difference decreases. Since the GKS is based on the Chapman-Enskog and as demonstrated in this plot, the results will keep improving as $Kn \to 0$ (in the hydrodynamic limit).

Focusing on the peak value of the shear stress along the flat plate, the velocity profile for the different Knudsen numbers is plotted at that point in Fig. 4.8(b). The velocity profile is well-captured, but the difference between the two schemes at the plate propagates up through the whole profile. It should be noted that the more rarefied cases seem to match the two gas mixture velocities better, but this is only due to the scaling of the problem. The same location on the y-axis on Fig. 4.8(b), e.g. $y = 20L_{ref}$, when compared to each flat plate length of $80L_{ref}(Kn = 0.0125), 20L_{ref}(Kn = 0.05), 13.3L_{ref}(Kn = 0.075)$ refers to a different location at the downstream farfield of each case. Therefore, the velocity of the most rarefied case $(Kn = 0.075)$ in fact takes the longest to converge to the same value.

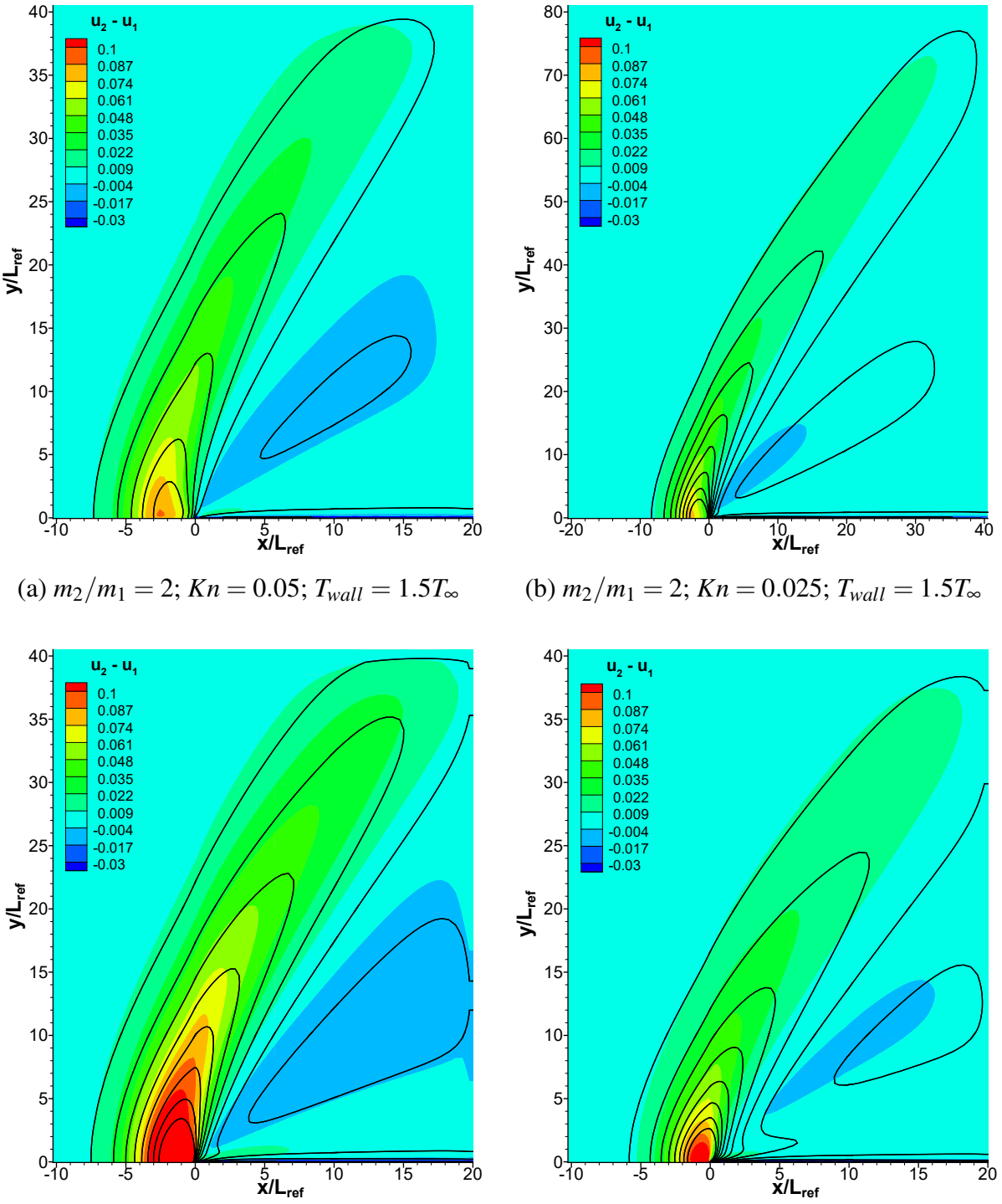

(a) $m_2/m_1 = 2$; $Kn = 0.05$; $T_{wall} = 1.5T_\infty$

(b) $m_2/m_1 = 2$; $Kn = 0.025$; $T_{wall} = 1.5T_\infty$

(c) $m_2/m_1 = 4$; $Kn = 0.05$; $T_{wall} = 1.5T_\infty$

(d) $m_2/m_1 = 2$; $Kn = 0.05$; $T_{wall} = 1.0T_\infty$

Figure 4.7: Non-dimensional species mean velocity difference $u_2 - u_1$ in a binary mixture flow over a flat plate for Mach number $M_\infty = 1.5$ and varied inflow conditions: $m_2/m_1 = 2$; $Kn = 0.05$; $T_{wall} = 1.5T_\infty$ in (a), $m_2/m_1 = 2$; $Kn = 0.025$; $T_{wall} = 1.5T_\infty$ in (b), $m_2/m_1 = 4$; $Kn = 0.05$; $T_{wall} = 1.5T_\infty$ in (c) and $m_2/m_1 = 2$; $Kn = 0.05$; $T_{wall} = 1.0T_\infty$ in (d).

The profile of the shear stress is plotted at two different points. One is at the peak of the stress along the plate on Fig. 4.8(b) and the other is further downstream: at a quarter of each plate's

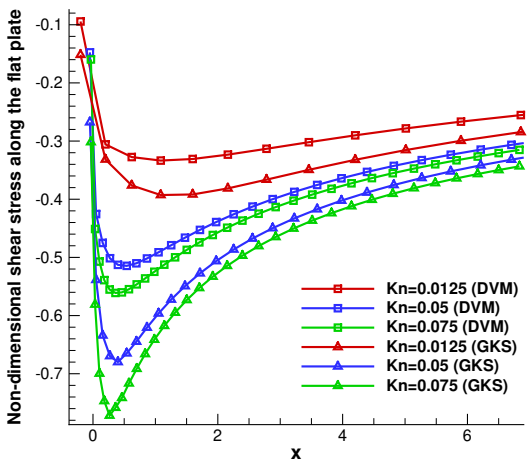

(a) Shear stress along the flat plate

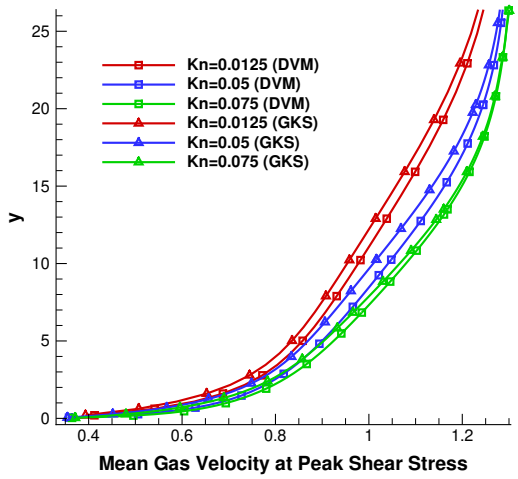

(b) Velocity profile at peak shear stress

Figure 4.8: Comparison of DVM and GKS results for the shear stress along the flat plate (in (a)) and velocity profile at peak shear stress at the flat plate (in (b)) for Mach number $M_\infty = 1.5$, mass ratio $m_2/m_1 = 2$ and varied Knudsen number $Kn = 0.0125$; $Kn = 0.05$; $Kn = 0.075$.

length - on Fig. 4.9(b) to establish how the flow develops. At the peak shear stress location the variation between the DVM (square) and GKS (delta) values of the shear stress in the first few cells is significant. The biggest difference is for the most rarefied case, where the GKS overpredicts the value of the shear stress in the vicinity of the wall. The difference propagates in the farfield but reduces quickly. The match between profiles of the shear stress at the downstream location from the GKS and DVM is much better as shown on Fig. 4.9(b). The most rarefied test case shows good agreement between the schemes, while the test case at $(Kn = 0.0125)$ demonstrates the convergence of the GKS when the flow goes towards the continuum limit.

From these results and the shown comparison between DVM and GKS it follows that despite the relatively large Knudsen numbers considered for this flat plate case, the GKS performs relatively well. Partly this can be explained by the Mach number of 1.5. For higher Mach numbers, stronger non-equilibrium will occur and bigger deviations can be expected. It should be noted that currently the GKS is limited at Mach number of 1.5 and Knudsen numbers up to 0.05 due to stability issues discussed in Section 6 of this chapter. For this reason they have been extensively investigated in this chapter. It was also found that Mach number of 2 and Kn=0.1 are critical for the GKS at concentration of 90%. A more detailed investigation of this aspect forms part of future work.

In the next section the main advantage of the GKS - the computational efficiency - is discussed.

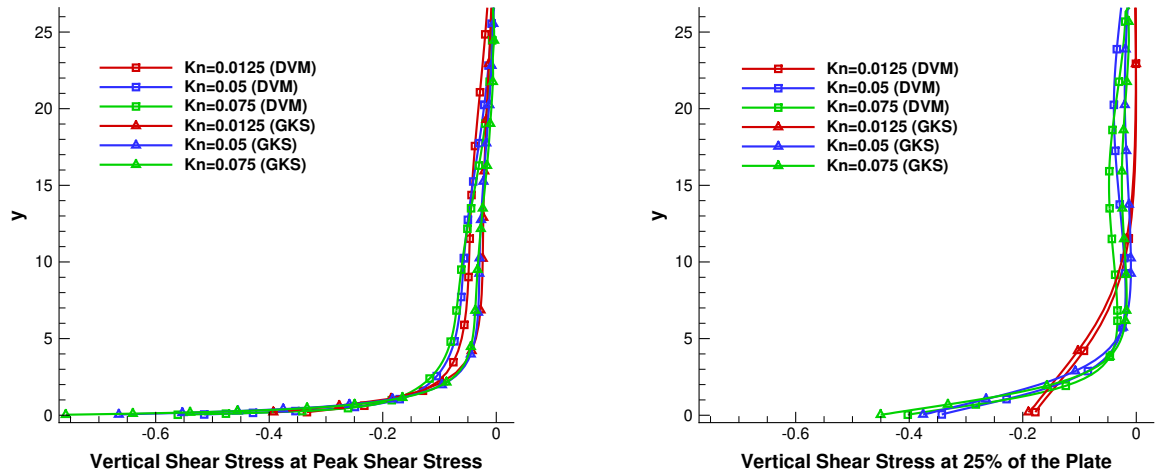

(a) Shear stress profile at the peak shear

(b) Shear stress at a quarter of the plates' lengths

Figure 4.9: Comparison of the DVM and GKS results for the vertical shear stress profile at two locations: at the peak in (a) and at a quarter of the plates' lengths in (b) for Mach number $M_\infty = 1.5$, mass ratio $m_2/m_1 = 2$ and varied Knudsen number $Kn = 0.0125$; $Kn = 0.05$; $Kn = 0.075$.

4.5 Computational Efficiency

The described results were achieved by implementing the new mixture kinetic model with a DVM and a GKS scheme. The distribution functions are per species and vary with the mass of the each gas. For higher mass ratios m_2/m_1 for the DVM the number of discrete velocities needs to be increased in order to correctly resolve the velocity distribution functions. This is also true for an increase in the Mach number. While for a one-dimensional test the increase of velocities is possible, it becomes computationally highly expensive to achieve the same resolution in higher dimensions. The main goal for constructing the gas-kinetic scheme is achieving numerical efficiency, which will allow for more complex cases and aerospace vehicles to be investigated. The results for a normal shock and the supersonic flow over a flat plate under different conditions demonstrated that the GKS is capable of preserving the physical details of the flow. There is a good agreement between the solutions from the discrete velocity method and the gas-kinetic scheme based on the same kinetic model for the cases considered. The shock wave grid has 1200 cells in the x-direction for the DVM and GKS simulations. Two-dimensional formulations were used for the flat plate simulations. The flat plate's grid is three-dimensional and has 19200 cells, but no computational effort is used in the third dimension. By comparing the computational requirements for the shock wave and flat plate problems, we observe the effect of higher dimensionality for both the DVM and GKS simulations. For the shock wave DVM test case 100 uniformly spaced discrete velocity are sufficient, while for the flat plate DVM $32 \times 32 = 1024$ discrete velocities were used. Note the number of discrete velocities for the flat plate are limited and provide a relatively course velocity grid. Notice if we have used the same number of dis-

crete velocities as for the shock wave but in two dimensions, the flat plate test case would run with $100 \times 100 = 10000$, which would increase the CPU time for the DVM significantly. The simulations were run on a quad-core Intel®Xeon®3.30 GHz computer. Table 4.3 demonstrates the CPU time required for every 1000 steps for the DVM and the GKS for the two baseline test cases: $M_\infty = 1.5$, $m_2/m_1 = 2$, $n_1/n = 0.9$ and for the flat plate also $Kn = 0.05$, $T_{wall} = 1.5T_\infty$. The times quoted are those for simulations running on a single core. The orders of magnitude

Table 4.3: CPU time per 1000 steps (DVM vs GKS)

	Shock Wave (1D)	Flat Plate (2D)
DVM	64 min	376 min
GKS	22.7 sec	1 min 15 sec
Speed-up	169	301

difference between the CPU time of the DVM and the GKS methods is significant. The differences between the relative speed-ups for the shock wave and the flat-plate cases are due to the fact that in the flat-plate DVM a two-dimensional velocity-space discretisation was used, while for the DVM simulations of the shock wave, a one-dimensional discretisation was employed. The CPU time difference for the GKS shock wave and flat plate simulations is directly the result of the larger mesh for the flat-plate case, while the difference between the DVM simulations results from both the larger mesh and the increased number of discrete velocities. For a larger Mach number or species mass ratio, the DVM approach requires an increased number of discrete velocities, leading to significantly larger CPU times, while the CPU time for the GKS remains the same. Overall, the GKS method shows a significant computational advantage and promising numerical results.

4.6 GKS vs DVM Performance

Since the gas-kinetic scheme is based on the first-order in Knudsen number Chapman-Enskog expansion, only small to moderate levels of rarefaction can be modelled. This was demonstrated by the numerical results with increase of the Knudsen number. The first order expansion also means that the current scheme reduces to the Navier-Stokes equations of hydrodynamic limit. At the same time the scheme allows to model beyond the capabilities of a continuum solver in regions of thermodynamic non-equilibrium and provides a method to connect microscopic behaviour to macroscopic quantities. This summarises the theoretical part of the limitation of the GKS. After comparing the numerical results from implementing the new kinetic mixture model with both the DVM and GKS and discussing in detail the numerical accuracy and efficiency of both schemes,a summary of the findings is provided in Table 4.4. The strong non-equilibrium created by high Mach numbers and high Knudsen numbers is found to be unsuitable for the mixture GKS. As a conclusion, GKS for mixture of gases is showing promising results in terms

Table 4.4: Comparison of DVM and GKS

DVM	GKS
Accurate results	Good accuracy
Accurate for high Mach numbers	Limited to lower Mach numbers
Accurate for higher Knudsen numbers	Limited to moderate levels of rarefaction
Computationally expensive	Inexpensive
Memory overhead	No memory restrictions
2D and 3D cases need parallel simulations	Runs on a single PC (CPU time similar to NS)

of accuracy in comparison to the detailed, but expensive DVM method. This accuracy is demonstrated close to continuum flow and for high Mach numbers and Knudsen numbers, the solutions deviate from the desired results in the regions of strong non-equilibrium.
It should be noted that DVM in cases close to continuum tend to create artificial dissipation. Therefore, differences with GKS are to be expected. However, the GKS is compared with DVM in this chapter since the underlying kinetic model is identical,i.e. the Shakhov-based mixture model.

4.7 Summary of Findings

- A new gas-kinetic scheme was introduced for a binary mixture of monoatomic gases based on a new kinetic model. This model is more advanced and detailed than the kinetic models previously used as the basis for GKS methods.
- The derivation of the gas-kinetic scheme was detailed.
- The new GKS has species velocity and the correct transport properties in the continuum limit, i.e. recovering the correct viscosity, heat flux and diffusion coefficients and the correct Prandtl number.
- The GKS was implemented numerically and results from high-speed flows were presented.
- A detailed comparison was presented between the results provided by the gas-kinetic scheme and a discrete velocity method using the same underlying kinetic model as the GKS.
- The GKS method agreed well with the DVM method for the cases of a shock wave and a flow past a flat plate.
- The limitations of the GKS were explored. The shear stress along the flat plate computed with GKS and DVM demonstrated that increasing the Knudsen number leads to bigger discrepancies in the results.

- In further work, the limitations of the GKS in terms of Kn for a wider range of test cases needs to be investigated. Here, it needs to be remarked that for a comparison with DVM, the computational cost of the limiting factor in terms of mesh sizes that can be used. In particular for lower Knudsen cases, this DVM cost factor also limits the extent to which a detailed mesh dependency study can be performed.

- The main advantage of the GKS is the computational efficiency and the speed-up of the CPU time, shown for the shock wave and the flat plate, was significant.

- The good comparison with DVM results, together with the computational efficiency, make this GKS scheme a viable alternative for supersonic mixture flows in the moderately rarefied regime.

Chapter 5

Diatomic Model for Gas Mixtures *

Extending kinetic model equations of the Bhatnagar-Gross-Krook (BGK) type from a single-species gas to multi-species gas mixtures presents a number of important challenges, as discussed in detail in Chapter 2. This challenge is further pronounced when diatomic gas mixtures are considered due to the addition of internal energy modes.

In this chapter a diatomic binary mixture with separate translational, rotational and vibrational temperatures is derived and the emphasis is on the procedure of deriving the model and the additional information each temperature provides. This derivation is demonstrated as a logical build-up with a multi-step approach from a well-described diatomic model known in the literature [96]. More specifically the changes in the collision term on the RHS of the equation and the target equilibrium function or functions are detailed. First, starting from the existing single species, single-temperature model, a two- temperature model with common translational and rotational temperatures is introduced. The vibrational temperature is allowed to deviate from the common translation-rotational temperature. Second, this model is extended to a three-temperature model with separate translational, rotational and vibrational temperatures. All three models' continuum limit is obtained through the Chapman-Enskog expansion and the effect of each additional temperature is examined in the corresponding Navier-Stokes equations.

Finally, we extend the three-temperature model with the capability to describe a mixture of two diatomic gases. Common translational temperature between the species is assumed, while the rotational and vibrational temperatures are defined separately for each species. Species velocity and diffusion effects are accounted for. Transport properties in the continuum limit are obtained through the Chapman-Enskog type expansion. The diatomic mixture model is demonstrated to reduce to a well-known mixture monoatomic model [64], which has two correct transport coefficients in the continuum limit and to reduce to the known single-species single-temperature model [96].

*Published in AIP Advances.

5.1 Single-Temperature to Three-Temperature Model

In this section we will build up a three-temperature model with translational, rotational and vibrational degrees of freedom and separate temperatures. Notice the emphasis here is on three different single-species models. The goal is to observe the changes each additional temperature provides and examine the continuum limit for all three models. The limit will differ solely due to the different process of temperature relaxation, since these are all single-species models and therefore no velocity relaxation occurs through this process. We will later observe that this is a characteristic valid only for the single-species models and not for the mixture model, where species diffusion effects can be modelled at different levels of accuracy in different models.

5.1.1 Single Temperature Model

This section summarises the work by Mathiaud, Mieussens and co-workers on a BGK model for diatomic gases, presented in [96, 97]. The model is well-defined and proved theoretically to be mathematically consistent. Furthermore, numerical tests for moderately rarefied gas flows (Knudsen $Kn = 0.01$) demonstrate good agreement in comparison to results obtained by a compressible-flow Navier-Stokes solver [97].

The BGK model includes rotational and vibrational degrees of freedom, where rotation is considered fully excited and similar to the translational energy: continuous, while vibrational energy is partially excited and has quantised levels. The distribution functions and the governing equation are presented for each quantised level i, but for brevity the subscript i is omitted, e.g the distribution function f_i is written as f. The model contains a single temperature T and gas velocity u_0. The governing equation is in the form:

$$\frac{\partial f}{\partial t} + \underline{u} \cdot \frac{\partial f}{\partial \underline{x}} = \frac{1}{\tau}(m^{eq} - f), \tag{5.1}$$

where the collision term on the RHS of the equation is denoted Q with $Q = \frac{1}{\tau}(m^{eq} - f)$ and τ is the relaxation time. The equilibrium distribution function is in the form:

$$m^{eq} = \frac{\rho}{(2\pi(k/m)T)^{3/2}} \exp\left(-\frac{m(\underline{u}-\underline{u}_0)^2}{2kT}\right) \frac{m}{kT} \exp\left(-\frac{mI}{kT}\right) \times \left(1 - \exp\left(-\frac{\theta_v}{T}\right)\right) \exp\left(-\frac{i\theta_v}{T}\right), \tag{5.2}$$

where T is the equilibrium temperature, I is the rotational energy, θ_v is the characteristic temperature for vibrational excitation, m is the molecular mass and i is the considered quantised level. The distribution function is defined at each quantised level, which is a very detailed modelling approach. However, the complexity of the model is reduced by summing over all quantised levels i up to infinity, where Boltzmann distribution of the vibrational states is assumed, lead-

ing to the removal of discrete vibrational levels and a reduced form of the distribution function m^{eq} [96] to two distributions M_{eq}^{tran} and M_{eq}^{vib}. In practical applications, only a finite number of vibrational quantum states need to be considered and this number may be different for different diatomic species.

$$\begin{aligned} M_{eq}^{tran} &= \sum_{i=0}^{\infty} m^{eq} = \frac{\rho}{(2\pi(k/m)T)^{3/2}} \exp\left(-\frac{m(\underline{u}-\underline{u}_0)^2}{2kT}\right) \frac{m}{kT} \exp\left(-\frac{mI}{kT}\right), \\ M_{eq}^{vib} &= \sum_{i=0}^{\infty} i\frac{k}{m}\theta_v m^{eq} = \frac{\delta(T)}{2}\frac{k}{m}T \frac{\rho}{(2\pi(k/m)T)^{3/2}} \exp\left(-\frac{m(\underline{u}-\underline{u}_0)^2}{2kT}\right) \frac{m}{kT} \exp\left(-\frac{mI}{kT}\right). \end{aligned} \tag{5.3}$$

Furthermore, the distribution function can be reduced with respect to the rotational energy I and also the z- direction in velocity for a two-dimensional problem. This form of the equations is a standard procedure to reduce complexity and computational expense in kinetic modelling and it was also used in Chapter 2. It will be extensively used throughout this chapter and next chapter but it will not be detailed for each kinetic model for single-species gas. We will refer back to the reduced form after introducing the diatomic mixture model and will carefully detail each reduced distribution function and the resulting governing equation. This is done for the mixture model since it is the focus of this study. Furthermore, the dimensionally-reduced form of the equation is implemented in the MΦC solver, extending the previously-implemented discrete-velocity method for the new diatomic mixture model. The reduced distribution functions together with the numerical results of the study will be part of the next chapter.

Returning back to the description of the single-species single-temperature model, following the procedure detailed in Chapter 1, the first order Chapman-Enskog expansion provides an expression for the non-equilibrium distribution function:

$$f = m^{eq} - \varepsilon\hat{\tau}\Big(\frac{\partial m^{eq}}{\partial t} + \underline{u}\cdot\frac{\partial m^{eq}}{\partial \underline{x}}\Big), \tag{5.4}$$

where as before the collision parameter τ is equal to $\tau = \varepsilon\hat{\tau}$.

Note that the internal energy for the single-species single-temperature model is in the form:

$$e = \frac{5+\delta(T)}{2}RT, \tag{5.5}$$

where $R = k/m$ and $\delta(T)$ is the number of excited vibrational degrees of freedom and for the harmonic oscillator is expressed as:

$$\delta(T) = \frac{2\Theta_v/T}{exp(\Theta_v/T)-1}. \tag{5.6}$$

The harmonic oscillator, which was described in detail in Chapter 1, is one of the simplest and most widely used methods for modelling intermolecular forces for the considered non-reactive

flows. Notice that if the kinetic models presented in this chapter are extended to involve chemistry then the more advanced and realistic anharmonic oscillator should be considered. The limits of the vibrational degrees of freedom $\delta(T)$, as defined in Eq. (5.6), for low temperatures with respect to θ_v is approaching 0, while for high temperatures it approaches 2 (fully excited state). The expression for the internal energy e based on the degrees of freedom and the corresponding temperatures will change with the introduction of multiple temperatures, but will always be equal to the expression based on the equilibrium temperature T as shown in Eq. (5.5). The continuum limit as well as the H-theorem are shown in the papers [96, 97] by Mathiaud and Mieussens. This is a well-defined single temperature model including rotational and vibrational degrees of freedom. We will build on it to extend the level of accuracy, physical detail and applications. The continuum limit is shown and further discussed in the next section of this Chapter.

5.1.2 Two Temperature Model

The described single temperature model accounts for variable degrees of freedom, but has a distinct disadvantage: the different types of internal energy are all based on one temperature, which is the equilibrium temperature. This is an approximation, which shows that presenting a flow in non-equilibrium with one (translational) temperature leads to significant deviation (for the case in which the gas is compressed, e.g. in the presence of a shock, the deviation is overestimation) of the actual value of the gas temperature [25, 91] (see Chapter 1, Fig. 1.9). Park [91] discusses this issue and provides a model for the reaction rates and equilibrium coefficients in the Navier-Stokes equations. This model has two distinct temperatures: one governing the translation and rotation and a second one for the vibration and electron degrees of freedom. This approach groups temperatures with closer values and allows the deviation of the slowly reacting vibrational and electron temperatures.

We use a similar approach in the extension of the single-temperature kinetic model. Here we present a two-temperature kinetic model for a diatomic gas. The model contains a single translational and rotational temperature T_{tr} and a separate vibrational temperature T_v and gas velocity u_0. The typical for BGK relaxation from non-equilibrium to equilibrium state, i.e $f \to m^{eq}$, now has an extra step. The relaxation is in the form $f \to m_2 \to m^{eq}$, where m_2 is an intermediate equilibrium distribution function in which the temperatures T_{tr} and T_v are separate, while the final equilibrium function m_{eq} stays the same and has a common equilibrium temperature T. The two-step relaxation process is not uniform and the time for the non-equilibrium function f to relax to the first (intermediate) equilibrium function m_2 is τ as before, while it takes longer for the vibration to relax to the translation and effectively to equilibrium, represented by a longer relaxation time $Z_v\tau$ between m_2 to m^{eq} ($Z_v > 1$). Typical values of the Z_v coefficient are in the

tens to hundreds and in some cases in the thousands. The governing equation is in the form:

$$\frac{\partial f}{\partial t} + \underline{u} \cdot \frac{\partial f}{\partial \underline{x}} = \frac{1}{\tau}(m_2 - f) + \frac{1}{Z_v \tau}(m^{eq} - m_2), \tag{5.7}$$

where the collision integral is $Q = \frac{1}{\tau}(m_2 - f) + \frac{1}{Z_v \tau}(m^{eq} - m_2)$ and the non-equilibrium function f and the equilibrium distribution functions are for each quantised level i, as in the previous model. The intermediate distribution function is in the form:

$$m_2 = \frac{\rho}{(2\pi(k/m)T_{tr})^{3/2}} \exp\left(-\frac{m(\underline{u} - \underline{u}_0)^2}{2kT_{tr}}\right) \frac{m}{kT_{tr}} \exp\left(-\frac{mI}{kT_{tr}}\right) \times \left(1 - \exp\left(-\frac{\theta_v}{T_v}\right)\right) \exp\left(-\frac{i\theta_v}{T_v}\right), \tag{5.8}$$

while the equilibrium distribution function is in the form:

$$m^{eq} = \frac{\rho}{(2\pi(k/m)T)^{3/2}} \exp\left(-\frac{m(\underline{u} - \underline{u}_0)^2}{2kT}\right) \frac{m}{kT} \exp\left(-\frac{mI}{kT}\right) \times \left(1 - \exp\left(-\frac{\theta_v}{T}\right)\right) \exp\left(-\frac{i\theta_v}{T}\right). \tag{5.9}$$

Following the expansion of the non-equilibrium distribution function procedure in powers of ε (with ε a small parameter of the order of the Knudsen number Kn) and utilising the assumption that the difference between m^{eq} and m_2 is of order $O(\varepsilon)$ and therefore:

$$\varepsilon\hat{\tau}\left(\frac{\partial m_2}{\partial t} + \underline{u} \cdot \frac{\partial m_2}{\partial \underline{x}}\right) = \varepsilon\hat{\tau}\left(\frac{\partial m^{eq}}{\partial t} + \underline{u} \cdot \frac{\partial m^{eq}}{\partial \underline{x}}\right) + O(\varepsilon^2) \tag{5.10}$$

leads to the expression for the non-equilibrium distribution function up to and including first order terms in ε for the two-temperature model :

$$f = m_2 + \frac{1}{Z_v}(m^{eq} - m_2) - \varepsilon\hat{\tau}\left(\frac{\partial m^{eq}}{\partial t} + \underline{u} \cdot \frac{\partial m^{eq}}{\partial \underline{x}}\right). \tag{5.11}$$

In comparison to the single-temperature model (Eq. (5.4)), the 0th- order expansion is the intermediate equilibrium function m_2, while also the difference to the 'Maxwellian' equilibrium m^{eq} is accounted for with the relaxation coefficient Z_v also involved.

5.1.3 Three-Temperature Model

Building upon the two-temperature model, a three-temperature model for a diatomic gas is introduced. The next step of this process is to split the common T_{tr} temperature into a separate translational and rotational temperature, while preserving the separate vibrational temperature.

This allows for each different type of energy to be calculated based on the corresponding temperature. It will also assist in solving problems with high levels of non-equilibrium where all three internal degrees of freedom are excited at different levels and differ significantly between each other, due to the difference in characteristic relaxation rate for translation, rotation and vibration.

The new relaxation process is a three-step approach and follows the process: $f \rightarrow m_1 \rightarrow m_2 \rightarrow m^{eq}$, where m_1 is the first intermediate equilibrium function and is a function of all three temperatures, m_2 is the second intermediate equilibrium function and is in the same form as before (two temperatures) and m^{eq} is the final equilibrium function with one temperature. The three-temperature model contains a translational $\hat{T}$, rotational T_r and a vibrational temperature T_v. The gas velocity is u_0. Notice that T_t would have been a logical notation for the translational temperature. However, $\hat{T}$ is legacy notation for the translational temperature from the monoatomic gas mixture model, presented in Chapter 2. It will allow for consistency and easier comparison between the monoatomic and diatomic models. Furthermore, it will be used in the diatomic mixture model within this chapter to represent the target translational temperature of the gas and will therefore be used in the current model. The governing equation is in the form:

$$\frac{\partial f}{\partial t} + \underline{u} \cdot \frac{\partial f}{\partial \underline{x}} = \frac{1}{\tau}(m_1 - f) + \frac{1}{Z_r \tau}(m_2 - m_1) + \frac{1}{Z_v \tau}(m^{eq} - m_2), \tag{5.12}$$

where the collision term is $Q = \frac{1}{\tau}(m_1 - f) + \frac{1}{Z_r \tau}(m_2 - m_1) + \frac{1}{Z_v \tau}(m^{eq} - m_2)$. The three-step relaxation process is not uniform and the delay of rotational to translational equilibration is via the rotational collision number Z_r, while to vibration is via the vibrational collision number Z_v ($Z_v > Z_r > 1$). These coefficients are temperature dependent and the ratio of the two coefficients of rotation and vibration with respect to τ is typically 1:5:100 [31], with Z_v at least one order of magnitude higher than the other two (with values of hundreds and thousands). Here, for simplicity, Z_r and Z_v are taken as constants, i.e. assumed to be independent of temperatures and therefore fixed throughout the considered flow domain.

The first intermediate distribution function is in the form:

$$m_1 = \frac{\rho}{\left(2\pi(k/m)\hat{T}\right)^{3/2}} \exp\left(-\frac{m(\underline{u}-\underline{u}_0)^2}{2k\hat{T}}\right) \frac{m}{kT_r} \exp\left(-\frac{m_s I}{kT_r}\right) \times \left(1 - \exp\left(-\frac{\theta_v}{T_v}\right)\right) \exp\left(-\frac{i\theta_v}{T_v}\right) \tag{5.13}$$

The second intermediate distribution function is in the form:

$$m_2 = \frac{\rho}{\left(2\pi(k/m)T_{tr}\right)^{3/2}} \exp\left(-\frac{m(\underline{u}-\underline{u}_0)^2}{2kT_{tr}}\right) \frac{m}{kT_{tr}} \exp\left(-\frac{m_s I}{kT_{tr}}\right) \times \left(1 - \exp\left(-\frac{\theta_v}{T_v}\right)\right) \exp\left(-\frac{i\theta_v}{T_v}\right), \tag{5.14}$$

while the equilibrium distribution function is in the form:

$$m^{eq} = \frac{\rho}{(2\pi(k/m)T)^{3/2}} \exp\left(-\frac{m(\underline{u}-\underline{u}_0)^2}{2kT}\right) \frac{m}{kT} \exp\left(-\frac{m_s I}{kT}\right) \times \left(1-\exp\left(-\frac{\theta_v}{T}\right)\right) \exp\left(-\frac{i\theta_v}{T}\right). \quad (5.15)$$

Therefore the expansion of the non-equilibrium distribution function in powers of ε where m_1 is the 0th-order expansion and the same property as in Eq. (5.10) for the difference between two equilibrium functions leads to:

$$f = m_1 + \frac{1}{Z_r}(m_2 - m_1) + \frac{1}{Z_v}(m^{eq} - m_2) - \varepsilon\hat{\tau}\left(\frac{\partial m^{eq}}{\partial t} + \underline{u}\cdot\frac{\partial m^{eq}}{\partial \underline{x}}\right) + O(\varepsilon^2) \quad (5.16)$$

$$\implies f = \left(1-\frac{1}{Z_r}\right)m_1 + \left(\frac{1}{Z_r}-\frac{1}{Z_v}\right)m_2 + \frac{1}{Z_v}m^{eq} - \varepsilon\hat{\tau}\left(\frac{\partial m^{eq}}{\partial t} + \underline{u}\cdot\frac{\partial m^{eq}}{\partial \underline{x}}\right) + O(\varepsilon^2)$$

For the three-temperature model both collision numbers are involved and we notice that they are present in the first order expansion, which means they will directly influence the transport properties (which are of order $O(\varepsilon)$).

Splitting the collision term in three different relaxation processes is a widely used approach and the above kinetic model is very similar to the UGKS three-temperature model [83] in terms of the definition of the equilibrium functions and the governing equation formulation. Furthermore, if vibrational excitation is not considered, the model will have only two relaxation processes (without the Z_v), which is similar to the UGKS with translational and rotational non-equilibrium, presented in [82]. Another two-step approach is demonstrated by the Rykov model [90], but the formulation is classified as a heat-flux correction for diatomic gas as an alternative to the Shakhov correction for monoatomic gas. This shows that this multistep build-up from the single temperature model to the three temperature model is consistent with models previously published in the literature.

To visualize the main difference in the three models, Fig. 5.1 demonstrates the different temperatures for each model and their relaxation process. The comparison between the three models and their expansion will proceed when the continuum limit is discussed next.

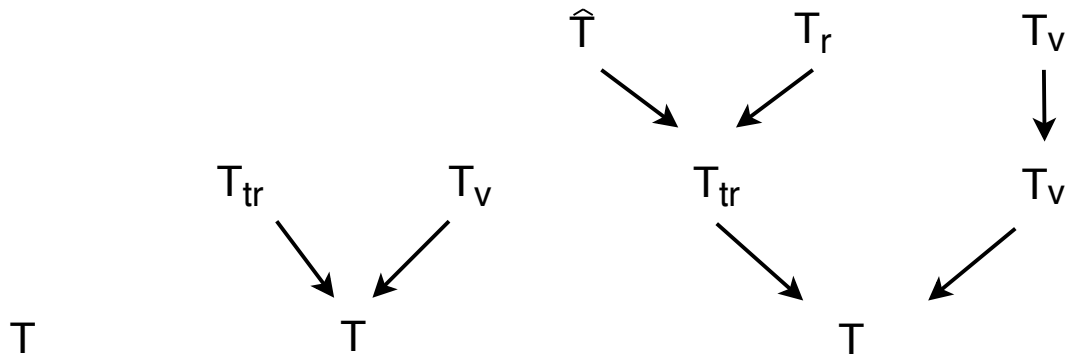

(a) Single temperature (b) Two temperature (c) Three temperature model

Figure 5.1: Temperature relaxation process for the single-, two- and three-temperature models for diatomic single-species.

5.2 Continuum Limit

This section demonstrates the continuum limit of the presented diatomic kinetic models and compares the single-, two- and three-temperature mass, momentum and energy conservation equations. The Chapman-Enskog expansion upto first order of the non-equilibrium functions f, detailed in the previous section, for the diatomic gas consists of summation over all vibration levels i, integration over all positive rotational energies I and similarly to the monoatomic gas: integration in the three velocity directions and is performed as:

$$\frac{\partial}{\partial t}\iiint_{-\infty}^{\infty}\int_{0}^{\infty}\sum_{i=0}^{\infty}\underline{\psi} f dI\, d\underline{u} + \frac{\partial}{\partial \underline{x}}\iiint_{-\infty}^{\infty}\int_{0}^{\infty}\sum_{i=0}^{\infty}\underline{u}\underline{\psi} f dI\, d\underline{u} = 0, \tag{5.17}$$

where $\underline{\psi}$ is the collision invariant and is in the form $\underline{\psi} = [1, \underline{u}, \frac{1}{2}(u^2+v^2+w^2)+I+i\frac{k_B}{m}\theta_v]^T$.
We observe that the mass conservation equation is the same for all models:

$$\frac{\partial}{\partial t}\iiint_{-\infty}^{\infty}\int_{0}^{\infty}\sum_{i=0}^{\infty} f dI\, d\underline{u} + \frac{\partial}{\partial x}\iiint_{-\infty}^{\infty}\int_{0}^{\infty}\sum_{i=0}^{\infty} u f dI\, d\underline{u} = 0, \tag{5.18}$$

where from here onwards we consider the Chapman- Enskog expansion only in the one-dimensional formulation leading to:

$$\frac{\partial}{\partial t}\rho + \frac{\partial}{\partial x}(\rho u_0) = 0 \tag{5.19}$$

Since only the temperatures are changed, the mass conservation of the system is not affected. Notice also that in comparison to the monoatomic gas (Chapter 1 Eq. (1.28)) no additional terms are present.
The flux in the momentum equation is different for the one-, two- and three-temperature models as:

Single Temperature:

$$\begin{aligned}\frac{\partial}{\partial t}(\rho u_0) &+ \frac{\partial}{\partial x}\Big(\rho u_0^2+\rho\frac{k_B}{m}T\Big)\\ &- \varepsilon\hat{\tau}\frac{\partial}{\partial x}\Big[2\rho\frac{k_B}{m}T\frac{\partial u_0}{\partial x}-\rho\frac{k_B}{m}\frac{T}{\Big(\frac{5}{2}+\frac{\delta^2(T)}{4}\exp\Big(\frac{\theta_v}{T}\Big)\Big)}\frac{\partial u_0}{\partial x}\Big]=0\end{aligned} \tag{5.20}$$

Two Temperature:

$$\begin{aligned}\frac{\partial}{\partial t}(\rho u_0) &+ \frac{\partial}{\partial x}\Big(\rho u_0^2+\rho\frac{k_B}{m}T_{tr}\overbrace{-\frac{1}{Z_v}\rho\frac{k_B}{m}\Big(T_{tr}-T\Big)}\Big)\\ &- \varepsilon\hat{\tau}\frac{\partial}{\partial x}\Big[2\rho\frac{k_B}{m}T\frac{\partial u_0}{\partial x}-\rho\frac{k_B}{m}\frac{T}{\Big(\frac{5}{2}+\frac{\delta^2(T)}{4}\exp\Big(\frac{\theta_v}{T}\Big)\Big)}\frac{\partial u_0}{\partial x}\Big]=0\end{aligned} \tag{5.21}$$

Three Temperature:

$$\begin{aligned}\frac{\partial}{\partial t}\rho u_0 &+ \frac{\partial}{\partial x}\Big(\rho u_0^2+\rho\frac{k_B}{m}\hat{T}\overbrace{-\frac{1}{Z_r}\rho\frac{k_B}{m}(\hat{T}-T_{tr})-\frac{1}{Z_v}\rho\frac{k_B}{m}(T_{tr}-T)}\Big)\\ &- \varepsilon\hat{\tau}\frac{\partial}{\partial x}\Big[2\rho\frac{k_B}{m}T\frac{\partial u_0}{\partial x}-\rho\frac{k_B}{m}\frac{T}{\Big(\frac{5}{2}+\frac{\delta^2(T)}{4}\exp\Big(\frac{\theta_v}{T}\Big)\Big)}\frac{\partial u_0}{\partial x}\Big]=0\end{aligned} \tag{5.22}$$

We observe that all three models lead to different momentum equations. The single-temperature model is matching the continuum limit presented by the model from Mieussens and co-workers [96, 97]. The two- and three- temperature models have extra terms that are highlighted with a bracket on top. It is easy to see that if for the two-temperature model $T_{tr} = T$ then it collapses to the expression of the single-temperature model. Again, for the three-temperature model if $\hat{T} = T_{tr}$, we recover the two-temperature model and if we set them equal to T as $\hat{T} = T_{tr} = T$, the single-temperature expression in the continuum is recovered. This shows consistency between the models with the additional terms involving temperature differences that are of order $O(\varepsilon)$ and contribute to the bulk viscosity in the gas. The transport properties will be further discussed in the following section.

Unlike the momentum equation, the energy equations are modified in both the time and space derivative terms when changing from single-temperature to two- and three-temperature models. Note that the considered energy equation governs the conservation of total energy of the gas, while for the two- and three-temperature model, separate equations for rotational and vibrational energy can be derived (which correspondingly will include a source term on the RHS). The total energy conservation for the three models is:

Single Temperature:

$$\frac{\partial}{\partial t}\left[\frac{1}{2}\rho u_0^2+\frac{5}{2}\rho\frac{k_B}{m}T+\frac{\delta(T)}{2}\rho\frac{k_B}{m}T\right]+\frac{\partial}{\partial x}\left[\frac{1}{2}\rho u_0^3+\frac{7}{2}\rho u_0\frac{k_B}{m}T+\frac{\delta(T)}{2}\rho u_0\frac{k_B}{m}T\right]$$
$$-\varepsilon\hat{\tau}\frac{\partial}{\partial x}\left[\left(2-\frac{1}{\left(\frac{5}{2}+\frac{\delta^2(T)}{4}\exp\left(\frac{\theta_v}{T}\right)\right)}\right)\rho u_0\frac{k_B}{m}T\frac{\partial u_0}{\partial x}\right.$$
$$\left.+\left(\frac{7}{2}+\frac{\delta(T)^2}{4}\exp\left(\frac{\theta_v}{T}\right)\right)\rho\frac{k_B^2}{m^2}T\frac{\partial T}{\partial x}\right]=0 \qquad (5.23)$$

Two Temperature:

$$\frac{\partial}{\partial t}\left[\frac{1}{2}\rho u_0^2+\frac{5}{2}\rho\frac{k_B}{m}T_{tr}+\frac{\delta(T_v)}{2}\rho\frac{k_B}{m}T_v\right.$$
$$\left.\overbrace{-\frac{1}{Z_v}\left(\frac{5}{2}\rho\frac{k_B}{m}T_{tr}-\frac{5}{2}\rho\frac{k_B}{m}T+\frac{\delta(T_v)}{2}\rho\frac{k_B}{m}T_v-\frac{\delta(T)}{2}\rho\frac{k_B}{m}T\right)}^{(1)}\right]$$
$$+\frac{\partial}{\partial x}\left[\frac{1}{2}\rho u_0^3+\frac{7}{2}\rho u_0\frac{k_B}{m}T_{tr}+\frac{\delta(T_v)}{2}\rho u_0\frac{k_B}{m}T_v\right.$$
$$\left.\overbrace{-\frac{1}{Z_v}\left(\frac{7}{2}\rho u_0\frac{k_B}{m}T_{tr}-\frac{7}{2}\rho u_0\frac{k_B}{m}T+\frac{\delta(T_v)}{2}\rho u_0\frac{k_B}{m}T_v-\frac{\delta(T)}{2}\rho u_0\frac{k_B}{m}T\right)}^{(2)}\right]$$
$$-\varepsilon\hat{\tau}\frac{\partial}{\partial x}\left[\left(2-\frac{1}{\left(\frac{5}{2}+\frac{\delta^2(T)}{4}\exp\left(\frac{\theta_v}{T}\right)\right)}\right)\rho u_0\frac{k_B}{m}T\frac{\partial u_0}{\partial x}+\left(\frac{7}{2}+\frac{\delta(T)^2}{4}\exp\left(\frac{\theta_v}{T}\right)\right)\rho\frac{k_B^2}{m^2}T\frac{\partial T}{\partial x}\right]$$
$$=0 \qquad (5.24)$$

Three Temperature:

$$\frac{\partial}{\partial t}\Bigg[\frac{1}{2}\rho u_0^2+\frac{3}{2}\rho\frac{k_B}{m}\hat{T}+\rho\frac{k_B}{m}T_r+\frac{\delta(T_v)}{2}\rho\frac{k_B}{m}T_v\overbrace{-\frac{1}{Z_r}\Big(\frac{3}{2}\rho\frac{k_B}{m}\hat{T}-\frac{5}{2}\rho\frac{k_B}{m}T_{tr}+\rho\frac{k_B}{m}T_r\Big)}^{(3)}$$
$$\overbrace{-\frac{1}{Z_v}\Big(\frac{5}{2}\rho\frac{k_B}{m}T_{tr}-\frac{5}{2}\rho\frac{k_B}{m}T+\frac{\delta(T_v)}{2}\rho\frac{k_B}{m}T_v-\frac{\delta(T)}{2}\rho\frac{k_B}{m}T\Big)}^{(4)}\Bigg]$$
$$+\frac{\partial}{\partial x}\Bigg[\frac{1}{2}\rho u_0^3+\frac{5}{2}\rho u_0\frac{k_B}{m}\hat{T}+\rho u_0\frac{k_B}{m}T_r+\frac{\delta(T_v)}{2}\rho u_0\frac{k_B}{m}T_v$$
$$\overbrace{-\frac{1}{Z_r}\Big(\frac{5}{2}\rho u_0\frac{k_B}{m}\hat{T}-\frac{7}{2}\rho u_0\frac{k_B}{m}T_{tr}+\rho u_0\frac{k_B}{m}T_r\Big)}^{(5)}$$
$$\overbrace{-\frac{1}{Z_v}\Big(\frac{7}{2}\rho u_0\frac{k_B}{m}T_{tr}-\frac{7}{2}\rho u_0\frac{k_B}{m}T+\frac{\delta(T_v)}{2}\rho u_0\frac{k_B}{m}T_v-\frac{\delta(T)}{2}\rho u_0\frac{k_B}{m}T\Big)}^{(6)}\Bigg]$$
$$-\varepsilon\hat{\tau}\frac{\partial}{\partial x}\Bigg[\Bigg(2-\frac{1}{\Big(\frac{5}{2}+\frac{\delta^2(T)}{4}\exp\Big(\frac{\theta_v}{T}\Big)\Big)}\Bigg)\rho u_0\frac{k_B}{m}T\frac{\partial u_0}{\partial x}+\Big(\frac{7}{2}+\frac{\delta(T)^2}{4}\exp\Big(\frac{\theta_v}{T}\Big)\Big)\rho\frac{k_B^2}{m^2}T\frac{\partial T}{\partial x}\Bigg]$$
$$=0 \qquad (5.25)$$

Notice that in the time-derivative term, the expressions that are highlighted with the top bracket ((1), (3) and (4)) are outside the well-known total energy expression. Since this is a total energy conservation, we do not expect these extra terms. When discussing each of these terms in the next section, we will prove the "extra" expressions to be equal to 0, which in turn will lead to a consistent energy conservation for all there models. Furthermore, expression (5) is also 0 and expressions (2) and (6) in the space-derivative terms will be partially reduced as well.

Moreover, observing the consistency property of the three models, equalisation of the temperatures leads to reduction of the model from three- to two- and then from two- to one-temperature model. A similar process in the reduction is followed as in the momentum equations. However, a distinct difference is the appearance of the rotational temperature T_r in the energy equation of the three temperature model. The energy equation is the first continuum equation in which the three initial temperatures $\hat{T}$, T_r and T_v are all present. Therefore to reduce to the two-temperature model first the translational and rotational temperatures equilibrate to the common translation-rotation temperature or $\hat{T}=T_r=T_{tr}$. This leads the first terms in the time- and space-derivatives with an overbrace and multiplier $1/Z_r$ (i.e. expressions (3) and (5)) to 0. Logically, the next step to reduce to the single-temperature model will be to equalise $T_{tr}=T_v=T$, which will make the brackets multiplied with $1/Z_v$ (i.e. expressions (4) and (6)) also 0.

We can clearly see the effect of additional temperatures and relaxation ratios in the kinetic mod-

els lead to changes in the continuum limit. The additional information facilitates a more detailed level of modelling.

5.3 Transport Properties

The Chapman-Enskog [24] expansion is widely used in the kinetic gas theory and it was established and derived specifically for monoatomic gases, while it is also often used for diatomic models. Monoatomic kinetic models utilise the expansion to demonstrate the continuum limit and show the corresponding closure of the Navier-Stokes equations. The derived continuum limit allows for the transport coefficients to be evaluated and with the help of relaxation coefficients to be correctly fitted, as shown in Chapter 2. Therefore the full derivation and numerical application of kinetic models is not possible without the evaluation of the transport properties, which are the focus on this section. Furthermore, this section will proceed to discuss the additional level of detail provided by the models with different number of temperatures, while focusing on the transport properties and how they are affected.

The transport properties for a single-species monoatomic gas are viscosity and thermal conductivity. As previously discussed, more transport effects occur for a gas mixture (see Chapter 1.4.11). Similarly, for diatomic and polyatomic gases additional transport properties are present. When the CE is applied to a polyatomic model, a volume viscosity component and extra thermal conductivity terms occur, due to the internal degrees of freedom [125]. The volume (bulk) viscosity for a monoatomic gas is zero as are the extra thermal conductivity terms as well. Comparing the continuum equations of a monoatomic single-species gas and diatomic single-species gas will highlight these properties. Considering the equations in the previous section and comparing with the Navier-Stokes for a monoatomic model (shown in Chapter 1), the change in transport coefficients moving from monoatomic to diatomic single temperature model and then to two- and three- temperature models is examined. First, the mass conservation equations are inspected.

Monoatomic Mass Conservation:

$$\frac{\partial}{\partial t}\rho + \frac{\partial}{\partial x}(\rho u_0) = 0 \tag{5.26}$$

Diatomic Mass Conservation:

$$\frac{\partial}{\partial t}\rho + \frac{\partial}{\partial x}(\rho u_0) = 0 \tag{5.27}$$

In the previous section, it was shown that for all three models the mass equation does not change. Furthermore, the continuity equation is not affected, i.e. there is no difference between the expressions for monoatomic or diatomic mass conservation, as shown in Eq. (5.26) and Eq. (5.27).

5.3.1 Bulk Viscosity

As expected we observe changes in the momentum equation. If we compare the monoatomic and diatomic momentum equations, an additional term appears. That additional term is known as the bulk viscosity. The literature specifies the bulk viscosity for a diatomic gas is due to presence of internal degrees of freedom. It can be regarded as a relaxation phenomenon [24]. Furthermore, the difference of relaxation times between translational, rotational and vibrational degrees of freedom contribute to the definition of this transport term. Due to this difference, the work done by the pressure on the gas affects the mechanical (translational) energy faster than the thermal (by inelastic collisions) energy which then gives rise to the bulk viscosity [24, 126]. Examples of flows where the bulk viscosity becomes important include flow where the velocity divergence is large, e.g. inside a shock wave, when fluid is compressed and expanded in multiple cycles (e.g sound wave) or when the atmosphere consists of a gas with large bulk viscosity e.g. CO_2 in the atmosphere of Mars [2, 126]. Even though it is a viscosity coefficient and has viscosity units, the bulk viscosity does not represent a momentum transfer, but an energy transfer [127].
The momentum equation in the x-direction for the monoatomic gas is shown in Eq. (5.28). Splitting the viscous term in diatomic momentum equation (Eq. (5.20)) into a normal stress that matches the monoatomic gas momentum in Eq. (5.28) and examining the remaining terms leads to the bulk viscosity, consisting of the last two terms in Eq. (5.29), which are emphasised with an underbracket. This is possible since we know that the ordinary viscosity does not differ for a monoatomic and diatomic gas [35].
Monoatomic Momentum Conservation:

$$\frac{\partial}{\partial t}(\rho u_0) + \frac{\partial}{\partial x}\left(\rho u_0^2 + \rho\frac{k_B}{m}T\right) - \varepsilon\hat{\tau}\frac{\partial}{\partial x}\left[\frac{4}{3}\rho\frac{k_B}{m}T\frac{\partial u_0}{\partial x}\right] = 0, \tag{5.28}$$

Single Temperature Momentum Conservation:

$$\begin{aligned}&\frac{\partial}{\partial t}(\rho u_0) + \frac{\partial}{\partial x}\left(\rho u_0^2 + \rho\frac{k_B}{m}T\right)\\ &-\varepsilon\hat{\tau}\frac{\partial}{\partial x}\Big[\frac{4}{3}\rho\frac{k_B}{m}T\frac{\partial u_0}{\partial x} + \underbrace{\frac{2}{3}\rho\frac{k_B}{m}T\frac{\partial u_0}{\partial x} - \rho\frac{k_B}{m}\frac{T}{\left(\frac{5}{2}+\frac{\delta^2(T)}{4}\exp\left(\frac{\theta_v}{T}\right)\right)}\frac{\partial u_0}{\partial x}}\Big] = 0,\end{aligned} \tag{5.29}$$

where the ordinary viscosity μ for the monoatomic model and all diatomic models is:

$$\mu = \tau\rho\frac{k_B}{m}T. \tag{5.30}$$

Therefore the contribution to the normal stress from the bulk viscosity for the single temperature model is in the form:

$$\sigma(\mu_B) = \frac{2}{3}\tau\rho\frac{k_B}{m}T\frac{\partial u_0}{\partial x} - \tau\rho\frac{k_B}{m}\frac{T}{\left(\frac{5}{2}+\frac{\delta^2(T)}{4}\exp\left(\frac{\theta_v}{T}\right)\right)}\frac{\partial u_0}{\partial x}. \tag{5.31}$$

Notice that in the limit of $\delta(T) \to 0$, where no vibrational energy is present, the classical result [128] for the stress due to bulk viscosity appears:

$$\sigma(\mu_B) = \frac{2}{3}\tau\rho\frac{k_B}{m}T\frac{\partial u_0}{\partial x} - \frac{2}{5}\tau\rho\frac{k_B}{m}T\frac{\partial u_0}{\partial x} = \frac{4}{15}\tau\rho\frac{k_B}{m}T\frac{\partial u_0}{\partial x}, \tag{5.32}$$

where in the absence of vibrational energy, this bulk viscosity is solely due to the rotation of the molecules in the gas.

The two-temperature model has a common translational and rotational temperature and a separate vibrational temperature. The same comparison is used for the model with two relaxation times. Extra terms of order $O(\varepsilon)$ appear in the first space-derivative term and have been moved into the second space-derivative bracket with the other order $O(\varepsilon)$ terms.

Two Temperature Momentum Conservation:

$$\begin{aligned}&\frac{\partial}{\partial t}(\rho u_0) + \frac{\partial}{\partial x}\left(\rho u_0^2 + \rho\frac{k_B}{m}T_{tr}\right) - \varepsilon\hat{\tau}\frac{\partial}{\partial x}\Big[\frac{4}{3}\rho\frac{k_B}{m}T\frac{\partial u_0}{\partial x} \\ &+ \frac{1}{\varepsilon Z_v\hat{\tau}}\left(\rho\frac{k_B}{m}T_{tr} - \rho\frac{k_B}{m}T\right) + \frac{2}{3}\rho\frac{k_B}{m}T\frac{\partial u_0}{\partial x} - \rho\frac{k_B}{m}\frac{T}{\left(\frac{5}{2}+\frac{\delta^2(T)}{4}\exp\left(\frac{\theta_v}{T}\right)\right)}\frac{\partial u_0}{\partial x}\Big] = 0\end{aligned} \tag{5.33}$$

Therefore the normal stress caused by the bulk viscosity for the two temperature model is now modified and can be expressed in the form:

$$\sigma(\mu_B) = \frac{1}{Z_v}\left(\rho\frac{k_B}{m}T_{tr} - \rho\frac{k_B}{m}T\right) + \frac{2}{3}\tau\rho\frac{k_B}{m}T\frac{\partial u_0}{\partial x} - \tau\rho\frac{k_B}{m}\frac{T}{\left(\frac{5}{2}+\frac{\delta^2(T)}{4}\exp\left(\frac{\theta_v}{T}\right)\right)}\frac{\partial u_0}{\partial x} \tag{5.34}$$

Notice that relative to the one-temperature model the modification of the expression is a temperature difference and not based on a velocity gradient. The Chapman-Enskog expansion based on the Maxwellian leads to a distinct advantage at this stage that we have noticed after comparing with an expansion that is based on the intermediate equilibrium function. The bulk viscosity is identified after the exact same expression for the ordinary viscosity, based on the equilibrium temperature T, as in the monoatomic gas is in the continuum limit of the diatomic gas. Note that if we are to expand with the intermediate distribution function the ordinary viscosity will be expressed with the combined translational and rotational temperatures T_{tr} and is not identical to the one from the monoatomic gas. Therefore, no straightforward conclusions would be possible for the bulk viscosity, while now we have the capability to assess the bulk viscosity transport

property. Of course, at the same time both expansions are valid alternatives based on the order of ε considered here.

Furthermore, performing the same analysis for the limit of $\delta(T) \to 0$ in order to inspect the bulk viscosity stress in the limit of no vibrational excitation leads to:

$$\sigma(\mu_B) = \frac{1}{Z_v}\left(\rho\frac{k_B}{m}T_{tr} - \rho\frac{k_B}{m}T\right) + \frac{4}{15}\tau\rho\frac{k_B}{m}T\frac{\partial u_0}{\partial x}. \tag{5.35}$$

At first, this expressions differs from the well-known expression shown in Eq. (5.32). However, for the assumed condition of no vibrational excitation the difference between the common translation-rotational temperature T_{tr} and the equilibrium temperature T will be 0, which then in turn reduces to the bulk viscosity stress expression to the expected value as in Eq. (5.32).

Following the same procedure in the expression of the momentum equation for the three temperature model provides an expression for the modified stress due to bulk viscosity for the model.

Three-Temperature Momentum Conservation:

$$\underbrace{\begin{aligned}&\frac{\partial}{\partial t}\rho u_0 + \frac{\partial}{\partial x}\left(\rho u_0^2 + \rho\frac{k_B}{m}\hat{T}\right) - \varepsilon\hat{\tau}\frac{\partial}{\partial x}\Big[\frac{4}{3}\rho\frac{k_B}{m}T\frac{\partial u_0}{\partial x}\\ &+\frac{1}{\varepsilon Z_r\hat{\tau}}\rho\frac{k_B}{m}(\hat{T}-T_{tr}) + \frac{1}{\varepsilon Z_v\hat{\tau}}\rho\frac{k_B}{m}(T_{tr}-T) + \frac{2}{3}\rho\frac{k_B}{m}T\frac{\partial u_0}{\partial x} - \rho\frac{k_B}{m}\frac{T}{\left(\frac{5}{2}+\frac{\delta^2(T)}{4}\exp\left(\frac{\theta_v}{T}\right)\right)}\frac{\partial u_0}{\partial x}\Big]\end{aligned}}_{=0}, \tag{5.36}$$

therefore the expression for normal stress based on the bulk viscosity is:

$$\sigma(\mu_B) = \frac{1}{Z_r}\rho\frac{k_B}{m}(\hat{T}-T_{tr}) + \frac{1}{Z_v}\rho\frac{k_B}{m}(T_{tr}-T) + \frac{2}{3}\tau\rho\frac{k_B}{m}T\frac{\partial u_0}{\partial x} - \tau\rho\frac{k_B}{m}\frac{T}{\left(\frac{5}{2}+\frac{\delta^2(T)}{4}\exp\left(\frac{\theta_v}{T}\right)\right)}\frac{\partial u_0}{\partial x}, \tag{5.37}$$

where additionally to the two-temperature model modification based on T_{tr} and T with a collision number Z_v, further change is introduced with the difference between temperatures $\hat{T}$ and T_{tr} with collision number Z_r. All three temperatures of the model contribute directly to the expression for bulk viscosity. Similarly to the two-temperature model, it is easy to observe the expression for the stress due to bulk viscosity with no vibrational excitation reducing as in Eq. (5.32) and Eq. (5.35). As in the two-temperature model, further to the limit of the vibrational degrees of freedom $\delta(T) \to 0$, the temperatures T_{tr} and T are non-distinguishable or $T_{tr} = T$. Therefore:

$$\sigma(\mu_B) = \frac{1}{Z_r}\rho\frac{k_B}{m}(\hat{T}-T) + \frac{4}{15}\tau\rho\frac{k_B}{m}T\frac{\partial u_0}{\partial x}. \tag{5.38}$$

In contrast to the other two models in which the translational and rotational temperatures are in equilibrium, in the three-temperature model (in the limit of no vibrational excitation) the difference between the translational and equilibrium temperature (which can differ due to the separate rotational temperature in the gas) creates an extra term even in the reduced bulk viscosity ex-

pression.

Furthermore, with the additional assumption of equal translational and rotational temperatures or $T_{tr} = \hat{T} = T_r$, we again receive the result for the stress due to bulk viscosity of the single-temperature model as in Eq. (5.32).

5.3.2 Heat Flux

The second extra term that appears in the continuum limit of a diatomic model in comparison to the monoatomic model is the additional heat flux based on the rotational and vibrational molecular motion. Equations (5.23), (5.24), (5.25) showed the continuum limit as derived from the moments for the energy equation. Notice that in the two and three temperature models terms of order $O(\varepsilon)$ appear even in the time derivative term. Using the internal energy definition, we observe that these terms are eliminated, since:

$$e = \frac{5}{2}RT_{tr} + \frac{\delta(T_v)}{2}RT_v = \frac{5+\delta(T)}{2}RT \tag{5.39}$$

is the definition based on the separate temperatures for the two-temperature model and:

$$e = \frac{3}{2}R\hat{T} + RT_r + \frac{\delta(T_v)}{2}RT_v = \frac{5}{2}RT_{tr} + \frac{\delta(T_v)}{2}RT_v = \frac{5+\delta(T)}{2}RT \tag{5.40}$$

is the definition based on the separate temperatures for the three-temperature model. Using these definitions and inserting the terms of order $O(\varepsilon)$ into the second space derivative bracket similar to the momentum equations, the new expressions for the energy equation of the two and three temperature models are compared with the monoatomic and single temperature diatomic models.

Monoatomic Energy Conservation:

$$\frac{\partial}{\partial t}\left[\frac{1}{2}\rho u_0^2 + \frac{3}{2}\rho\frac{k_B}{m}T\right] + \frac{\partial}{\partial x}\left[\frac{1}{2}\rho u_0^3 + \frac{5}{2}\rho u_0\frac{k_B}{m}T\right] - \varepsilon\hat{\tau}\frac{\partial}{\partial x}\left[\frac{4}{3}\rho u_0\frac{k_B}{m}T\frac{\partial u_0}{\partial x} + \frac{5}{2}\rho\frac{k_B^2}{m^2}T\frac{\partial T}{\partial x}\right] = 0. \tag{5.41}$$

The total energy conservation for diatomic gas will differ due to the extra degrees of freedom due to the molecular rotation and vibration. The temporal and zeroth order of $O(\varepsilon)$ spatial derivative will be in a similar format to the monoatomic gas but differ in the coefficient specifying the contribution due to the DoF. From the standard form of the Navier-Stokes equations the order $O(\varepsilon)$ term in the space derivative will consist of the normal stress multiplied by the gas velocity and the heat flux. By knowing the ordinary and bulk viscosities contributions to the normal stress, we can isolate the heat flux contribution.

Single Temperature Energy Conservation:

$$\frac{\partial}{\partial t}\left[\frac{1}{2}\rho u_0^2+\frac{5}{2}\rho\frac{k_B}{m}T+\frac{\delta(T)}{2}\rho\frac{k_B}{m}T\right]+\frac{\partial}{\partial x}\left[\frac{1}{2}\rho u_0^3+\frac{7}{2}\rho u_0\frac{k_B}{m}T+\frac{\delta(T)}{2}\rho u_0\frac{k_B}{m}T\right]$$
$$-\varepsilon\hat{\tau}\frac{\partial}{\partial x}\Bigg[\Big(\frac{4}{3}\rho\frac{k_B}{m}T\frac{\partial u_0}{\partial x}+\frac{2}{3}\rho\frac{k_B}{m}T\frac{\partial u_0}{\partial x}-\rho\frac{k_B}{m}\frac{T}{\left(\frac{5}{2}+\frac{\delta^2(T)}{4}\exp\left(\frac{\theta_v}{T}\right)\right)}\frac{\partial u_0}{\partial x}\Big)u_0$$
$$+\underbrace{\Big(\frac{5}{2}+\frac{2}{2}+\frac{\delta(T)^2}{4}\exp\Big(\frac{\theta_v}{T}\Big)\Big)\rho\frac{k_B^2}{m^2}T\frac{\partial T}{\partial x}}\Bigg]=0 \tag{5.42}$$

Therefore the heat flux due to translation, rotational and vibrational DoF is in the form:

$$q=-\Big(\frac{5}{2}+\frac{2}{2}+\frac{\delta(T)^2}{4}\exp\Big(\frac{\theta_v}{T}\Big)\Big)\tau\rho\frac{k_B^2}{m^2}T\frac{\partial T}{\partial x}, \tag{5.43}$$

where when compared with the monoatomic energy equation, the translational heat flux is shown to have preserved the same form, as it was expected [35], and the separate contributions to the heat flux from the translational, rotational and vibration DoF are:

$$q^{tran}=-\frac{5}{2}\tau\rho\frac{k_B^2}{m^2}T\frac{\partial T}{\partial x},\qquad q^{rot}=-\frac{2}{2}\tau\rho\frac{k_B^2}{m^2}T\frac{\partial T}{\partial x},\qquad q^{vib}=-\frac{\delta(T)^2}{4}\exp\Big(\frac{\theta_v}{T}\Big)\tau\rho\frac{k_B^2}{m^2}T\frac{\partial T}{\partial x}. \tag{5.44}$$

After simplifying the two-temperature energy equation with the definition of energy, the equation is in the form:

Two-Temperature Energy Conservation:

$$\frac{\partial}{\partial t}\left[\frac{1}{2}\rho u_0^2+\frac{5}{2}\rho\frac{k_B}{m}T_{tr}+\frac{\delta(T_v)}{2}\rho\frac{k_B}{m}T_v\right]+\frac{\partial}{\partial x}\left[\frac{1}{2}\rho u_0^3+\frac{7}{2}\rho u_0\frac{k_B}{m}T_{tr}+\frac{\delta(T_v)}{2}\rho u_0\frac{k_B}{m}T_v\right]$$
$$-\varepsilon\hat{\tau}\frac{\partial}{\partial x}\Bigg[\Big(\frac{4}{3}\rho\frac{k_B}{m}T\frac{\partial u_0}{\partial x}+\frac{1}{\varepsilon Z_v\hat{\tau}}\Big(\rho\frac{k_B}{m}T_{tr}-\rho\frac{k_B}{m}T\Big)+\frac{2}{3}\rho\frac{k_B}{m}T\frac{\partial u_0}{\partial x}$$
$$-\rho\frac{k_B}{m}\frac{T}{\left(\frac{5}{2}+\frac{\delta^2(T)}{4}\exp\left(\frac{\theta_v}{T}\right)\right)}\frac{\partial u_0}{\partial x}\Big)u_0+\underbrace{\Big(\frac{5}{2}+\frac{2}{2}+\frac{\delta(T)^2}{4}\exp\Big(\frac{\theta_v}{T}\Big)\Big)\rho\frac{k_B^2}{m^2}T\frac{\partial T}{\partial x}}\Bigg]=0$$

Therefore, for the two-temperature model the heat flux is in the same form as for the single-temperature model and is expressed with the equilibrium temperature T.

$$q=-\Big(\frac{5}{2}+\frac{2}{2}+\frac{\delta(T)^2}{4}\exp\Big(\frac{\theta_v}{T}\Big)\Big)\tau\rho\frac{k_B^2}{m^2}T\frac{\partial T}{\partial x}. \tag{5.45}$$

No corrections to the heat flux expression is observed up to order $O(\varepsilon)$ from introducing the second temperature. Further, the individual heat flux contribution are also the same as in Eq. (5.44). This is a result of using the equilibrium (Maxwellian) distribution function as the basis for the

CE expansion. Notice that the energy equation overall is still modified due to the work done by the normal stress based on the bulk viscosity.

Three-Temperature Energy Conservation:

$$\begin{aligned}
&\frac{\partial}{\partial t}\left[\frac{1}{2}\rho u_0^2+\frac{3}{2}\rho\frac{k_B}{m}\hat{T}+\rho\frac{k_B}{m}T_r+\frac{\delta(T_v)}{2}\rho\frac{k_B}{m}T_v\right] \\
&+\frac{\partial}{\partial x}\left[\frac{1}{2}\rho u_0^3+\frac{5}{2}\rho u_0\frac{k_B}{m}\hat{T}+\rho u_0\frac{k_B}{m}T_r+\frac{\delta(T_v)}{2}\rho u_0\frac{k_B}{m}T_v\right] \\
&-\varepsilon\hat{\tau}\frac{\partial}{\partial x}\Bigg[\Big(\frac{4}{3}\rho\frac{k_B}{m}T\frac{\partial u_0}{\partial x}+\frac{1}{\varepsilon Z_r\hat{\tau}}\rho\frac{k_B}{m}(\hat{T}-T_{tr})+\frac{1}{\varepsilon Z_v\hat{\tau}}\rho\frac{k_B}{m}(T_{tr}-T)+\frac{2}{3}\rho\frac{k_B}{m}T\frac{\partial u_0}{\partial x} \\
&-\rho\frac{k_B}{m}\frac{T}{\left(\frac{5}{2}+\frac{\delta^2(T)}{4}\exp\left(\frac{\theta_v}{T}\right)\right)}\frac{\partial u_0}{\partial x}\Big)u_0+\underbrace{\Big(\frac{5}{2}+\frac{2}{2}+\frac{\delta(T)^2}{4}\exp\Big(\frac{\theta_v}{T}\Big)\Big)\rho\frac{k_B^2}{m^2}T\frac{\partial T}{\partial x}}\Bigg]=0.
\end{aligned} \tag{5.46}$$

Similar to the two-temperature model, the total heat flux and the individual heat flux contributions from the translation, rotational and vibration are unchanged in comparison to the single-temperature diatomic model. Again, this is a result of the CE expansion based on the Maxwellian distribution function. The total heat flux expression is based on the equilibrium temperature T and is in the form:

$$q=-\Big(\frac{5}{2}+\frac{2}{2}+\frac{\delta(T)^2}{4}\exp\Big(\frac{\theta_v}{T}\Big)\Big)\tau\rho\frac{k_B^2}{m^2}T\frac{\partial T}{\partial x}, \tag{5.47}$$

while the different contributions are as in Eq. (5.44) or:

$$q^{tran}=-\frac{5}{2}\tau\rho\frac{k_B^2}{m^2}T\frac{\partial T}{\partial x},\qquad q^{rot}=-\frac{2}{2}\tau\rho\frac{k_B^2}{m^2}T\frac{\partial T}{\partial x},\qquad q^{vib}=-\frac{\delta(T)^2}{4}\exp\Big(\frac{\theta_v}{T}\Big)\tau\rho\frac{k_B^2}{m^2}T\frac{\partial T}{\partial x}. \tag{5.48}$$

Equations (5.48) will be compared with the heat flux contributions for the diatomic mixture model with three temperatures presented in the next section.

5.4 Diatomic Mixture with Three Temperatures

After building up a diatomic model from a single-temperature model, available in the literature [96, 97], to a three-temperature model, which can model separately translation, rotation and vibration, we focus our attention to expand this model to a diatomic mixture model. Note that we have defined the model for a binary mixture, similar to the monoatomic mixture models. In this section, a diatomic mixture model with separate species velocities is presented. A species target velocity is also introduced similar to the monoatomic mixture models discussed in Chapter 2. Furthermore, the model features three temperatures per species and has a common translational target temperature (used in the equilibrium distribution function), consistent with the monoatomic mixture model. The properties established with the derivations of the

monoatomic mixture model (e.g diffusion coefficients and ordinary viscosity coefficient) and the single-species three temperature model (e.g relaxation process, bulk viscosity, etc.) are found in this new model and are discussed in detail.

The governing equation for a diatomic mixture is per species s, while the rotational and vibrational collision numbers Z_r and Z_v are kept constant for all species. The characteristic temperature θ_{v_s} is also per species s, which allows for specific gases with different levels of vibrational excitation to be considered. This is one of the key benefits of this model. The governing equation per species for the diatomic kinetic model is:

$$\frac{\partial f_s}{\partial t} + \underline{u} \cdot \frac{\partial f_s}{\partial \underline{x}} = \frac{1}{\tau}(m_{s_1} - f_s) + \frac{1}{Z_r \tau}(m_{s_2} - m_{s_1}) + \frac{1}{Z_v \tau}(m_s^{eq} - m_{s_2}) \quad ; \quad s = 1, 2, \tag{5.49}$$

where f_s is the non-equilibrium function, m_{s_1} is the initial (or first) intermediate equilibrium function, m_{s_2} is the second intermediate equilibrium and m_s^{eq} is the final equilibrium function, resembling a Maxwellian distribution. All distribution functions follow the same notation as before, but are per species s. Similarly, the governing equation as well as the distribution functions describing it are quantised (for the vibrational energy levels) as in the single-species multi-temperature approach. Note that in general for different diatomic gases, different number of quantised levels need to be considered.

The first equilibrium function m_{s_1} that the non-equilibrium function f_s relaxes to, is in the form:

$$m_{s_1} = \frac{\rho_s}{\left(2\pi(k_B/m_s)\hat{T}\right)^{3/2}} \exp\left(-\frac{m_s(\underline{u} - \underline{u}_s^{(g)})^2}{2k_B\hat{T}}\right) \frac{m_s}{k_B T_{r_s}} \exp\left(-\frac{m_s I}{k_B T_{r_s}}\right) \times \left(1 - \exp\left(-\frac{\theta_{v_s}}{T_{v_s}}\right)\right) \exp\left(-\frac{i\theta_{v_s}}{T_{v_s}}\right), \tag{5.50}$$

where the target translational temperature is common for both species and is $\hat{T}$. Furthermore, the target species velocity is $u_s^{(g)}$. Both of these variables are consistent with the monoatomic binary mixture model by Groppi et al. [64] and the two models presented in Chapter 2 and in [88]. The relationships between the target temperature $\hat{T}$ and the species translational temperatures T_{tran_s} and between the target species velocities $u_s^{(g)}$ and the species velocities u_s and gas velocity u_0 will be discussed in detail. They are important for compatibility of the model but also to model the diffusion behaviour of the two gases in the mixture. More terms specific for this equilibrium function are the species rotational temperatures T_{r_s} and the species vibrational temperatures T_{v_s}. Notice that since this is the first or initial equilibrium function, the gas is furthest away from equilibrium in the considered relaxation process. This is the reason all temperatures differ from each other.

In the next relaxation step the first intermediate equilibrium function m_{s_1} relaxes to the second intermediate equilibrium function m_{s_2} with relaxation time Z_r times longer than the initial relaxation. At the stage of the relaxation process represented by this equilibrium function, the species

translational and species rotational temperatures should be in equilibrium leading to a species translation-rotation temperature T_{tr_s}. However, in the time of having translational and rotational temperatures equalize, the species translational temperature will be common for both species and similarly the species rotational temperature will be common as well or $T_{r_1} = T_{r_2}$. Therefore, having species translation-rotation temperature T_{tr_s} is unnecessary and a common temperature T_{tr} is used, where $\hat{T} = T_{r_1} = T_{r_2} = T_{tr}$. Note that this can be justified for the common binary gas mixture for aerospace application (air) consisting of nitrogen and oxygen,where the collision number Z_r for N_2 is very close to the collision number Z_r for O_2. Considering modelling different methods for Z_r as a function of temperature [129, 130] and the fact that the species rotational temperatures have similar values, having a value for Z_r common between the two species is a reasonable assumption. The second intermediate equilibrium function becomes:

$$m_{s_2} = \frac{\rho_s}{\left(2\pi(k_B/m_s)T_{tr}\right)^{3/2}} \exp\left(-\frac{m_s(\underline{u}-\underline{u}_0)^2}{2k_BT_{tr}}\right) \frac{m_s}{k_BT_{tr}} \exp\left(-\frac{m_sI}{k_BT_{tr}}\right) \times \left(1-\exp\left(-\frac{\theta_{v_s}}{T_{v_s}}\right)\right) \exp\left(-\frac{i\theta_{v_s}}{T_{v_s}}\right), \quad (5.51)$$

where two species vibrational temperatures T_{v_s} represent the fact that the vibrational temperatures have not equilibrated yet with the other temperatures. Important to notice in Eq. (5.51) is the velocity, which has relaxed from species target velocity $u_s^{(g)}$ to the common mixture velocity u_0 of the gas. There are two possible relaxation routes for the velocity, which is not directly related to the Z_r and Z_v collision numbers. It is considered that the velocity equilibration occurs with the quicker initial relaxation rather than the slower relaxation. For this reason the m_{s_2} distribution function is defined with the gas velocity u_0.

Finally, the last equilibrium distribution function is defined with the equilibrium temperature T and the gas mixture velocity u_0 as:

$$m_s^{eq} = \frac{\rho_s}{\left(2\pi(k_B/m_s)T\right)^{3/2}} \exp\left(-\frac{m_s(\underline{u}-\underline{u}_0)^2}{2k_BT}\right) \frac{m_s}{k_BT} \exp\left(-\frac{m_sI}{k_BT}\right) \times \left(1-\exp\left(-\frac{\theta_{v_s}}{T}\right)\right) \exp\left(-\frac{i\theta_{v_s}}{T}\right). \quad (5.52)$$

At this last stage all temperatures are in equilibrium, which makes this distribution function to resemble a species Maxwellian distribution function for a diatomic gas.

The relaxation process of the distribution function is as $f_s \rightarrow m_{s_1} \rightarrow m_{s_2} \rightarrow m_s^{eq}$. To visualize the temperature relaxation, the temperature reduction stages are shown for the mixture model in Fig. 5.2, similar to the comparison between the single-, two- and three-temperature single-species diatomic models before. The red temperatures and dashed lines are stages in the temperature equalization that are omitted in the modelling process. Despite being omitted, species-specific translational temperatures can still be obtained from taking moments of the non-

equilibrium distribution function f_s. However, these temperatures play no role in the definition of the current model. These red steps are justified through the representation of the model in this section. The equilibration process begins with five temperatures for the two-species model: $\hat{T}$,

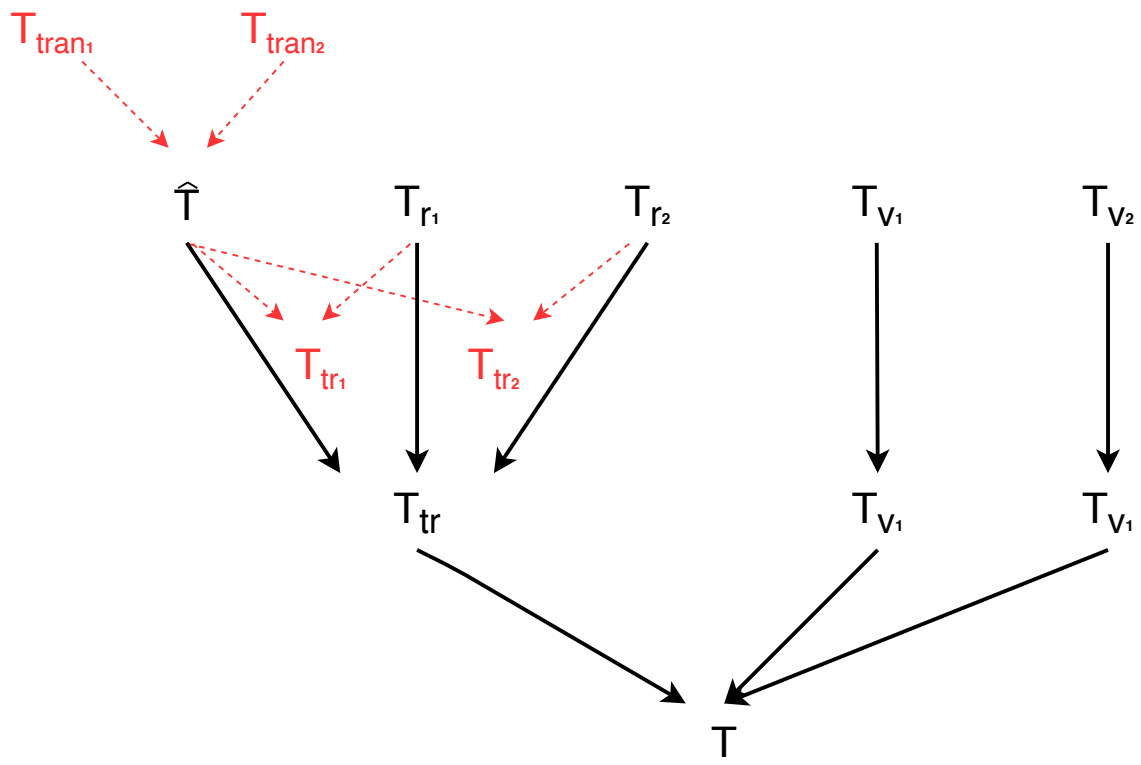

Figure 5.2: Temperature relaxation process for the diatomic mixture model.

T_{r_1}, T_{r_2}, T_{v_1}, T_{v_2}. In the next step, the translational and rotational temperatures have a common T_{tr} temperature, while T_{v_1} and T_{v_2} are still in the process of relaxation. In the final step all temperatures are equal to each other and to the gas temperature T.

Reduction to a single-temperature single-species model

We will now demonstrate the reduction of the mixture diatomic model to the original single-species single-temperature model [96] and the conditions required to achieve it. That model does not have a separate rotational or vibrational relaxation. Therefore, to reduce to the original model, we inspect the case where $Z_r = Z_v = 1$, resulting in the additional equilibrium functions cancelling out as:

$$\begin{aligned} &\frac{\partial f_s}{\partial t} + \underline{u} \cdot \frac{\partial f_s}{\partial \underline{x}} = \frac{1}{\tau}(m_{s_1} - f_s) + \frac{1}{\tau}(m_{s_2} - m_{s_1}) + \frac{1}{\tau}(m_s^{eq} - m_{s_2}), \\ &\implies \frac{\partial f_s}{\partial t} + \underline{u} \cdot \frac{\partial f_s}{\partial \underline{x}} = \frac{1}{\tau}(m_s^{eq} - f_s), \end{aligned} \tag{5.53}$$

where the equilibrium distribution function is dependent on the gas mixture velocity u_0 and the equilibrium temperature. Other macroscopic properties discussed during the mixture model

introduction like the target velocity $u_s^{(g)}$ and the temperatures $\hat{T}, T_{r_s}, T_{v_s}, T_{tr}$ no longer participate in the required set of equations. The equilibrium function is in the form:

$$m_s^{eq} = \frac{\rho_s}{\left(2\pi(k_B/m_s)T\right)^{3/2}} \exp\left(-\frac{m_s(\underline{u}-\underline{u}_0)^2}{2k_BT}\right) \frac{m_s}{k_BT} \exp\left(-\frac{m_s I}{k_BT}\right) \times \left(1-\exp\left(-\frac{\theta_{v_s}}{T}\right)\right) \exp\left(-\frac{i\theta_{v_s}}{T}\right). \quad (5.54)$$

Next, we consider that the original model is not defined for a gas mixture. Therefore, the final step is to reduce out the species specific properties: $\rho_s = \rho$, $m_s = m$ and $\theta_{v_s} = \theta_v$. The governing equation is for the distribution function f for the gas:

$$\frac{\partial f}{\partial t} + \underline{u} \cdot \frac{\partial f}{\partial \underline{x}} = \frac{1}{\tau}(m^{eq} - f), \quad (5.55)$$

and the equilibrium function goes to:

$$m^{eq} = \frac{\rho}{\left(2\pi(k_B/m)T\right)^{3/2}} \exp\left(-\frac{m(\underline{u}-\underline{u}_0)^2}{2k_BT}\right) \frac{m}{k_BT} \exp\left(-\frac{mI}{k_BT}\right) \times \left(1-\exp\left(-\frac{\theta_v}{T}\right)\right) \exp\left(-\frac{i\theta_v}{T}\right). \quad (5.56)$$

We recover the single-species model with one equilibrium temperature and one gas velocity, demonstrating the consistency of the diatomic mixture model. This property is discussed mathematically, but in the next chapter will be shown numerically.

Reduction to monoatomic gas mixture

To reduce to the monoatomic gas mixture, we consider the case when there is no energy exchange between the translational and internal energies. The rotational and vibrational relaxation effects are so much slower than the translation relaxation that they never really begin to propagate and Therefore, the collision numbers $Z_r \to \infty$ and $Z_v \to \infty$. In the limit of infinity it follows that $1/Z_r = 0$ and $1/Z_v = 0$, which reduces the governing equation of the diatomic mixture kinetic model to:

$$\frac{\partial f_s}{\partial t} + \underline{u} \cdot \frac{\partial f_s}{\partial \underline{x}} = \frac{1}{\tau}(m_{s_1} - f_s), \quad (5.57)$$

with the equilibrium function in the form:

$$m_{s_1} = \frac{\rho_s}{\left(2\pi(k_B/m_s)\hat{T}\right)^{3/2}} \exp\left(-\frac{m_s(\underline{u}-\underline{u}_s^{(g)})^2}{2k_B\hat{T}}\right) \frac{m_s}{k_BT_{r_s}} \exp\left(-\frac{m_s I}{k_BT_{r_s}}\right) \times \left(1-\exp\left(-\frac{\theta_{v_s}}{T_{v_s}}\right)\right) \exp\left(-\frac{i\theta_{v_s}}{T_{v_s}}\right). \quad (5.58)$$

Notice that the governing equation reduced to one equilibrium distribution function, similar to the reduction to a single-temperature, single-species model in Eq. (5.53), but the function itself is different. In the current reduction to a monoatomic mixture model, we have kept the distribution defined with the target velocity $\underline{u}_s^{(g)}$ and the target temperature $\hat{T}$, similar to the monoatomic model we are trying to go to: the Groppi et al. model [64], described in Chapter 2. To reduce the equilibrium function we consider the summation over all quantised levels i from 0 to ∞ and then integrating out the rotational energy I as:

$$\frac{\partial F_s}{\partial t} + \underline{u} \cdot \frac{\partial F_s}{\partial \underline{x}} = \frac{1}{\tau}(M_{s_1} - F_s), \tag{5.59}$$

with the equilibrium function in the form:

$$M_{s_1} = \int_0^\infty \sum_{i=0}^{\infty} m_{s_1} dI = \frac{\rho_s}{\left(2\pi(k_B/m_s)\hat{T}\right)^{3/2}} \exp\left(-\frac{m_s(\underline{u} - \underline{u}_s^{(g)})^2}{2k_B\hat{T}}\right) \tag{5.60}$$

Comparing with the expressions in Chapter 2, we conclude that $M_{s_1} \equiv G_s$ and the monoatomic mixture model possessing two correct transport coefficients in the continuum limit is recovered. In this section the governing equations of a new kinetic model for a binary diatomic gas mixture were presented. Furthermore, modelling decisions were discussed and justified. The relaxation process was detailed. The next sections will focus on closing the model by deriving the expressions for the target velocity and species temperatures, demonstrating compatibility of the model, providing the expressions for the transport properties and showing the continuum limit.

5.5 Compatibility

In this section the compatibility property of the model is demonstrated. It is shown that taking moments with respect to the collision invariants of the collision integral on the RHS of the governing equation equals zero. This property was also used in Chapter 2 to provide expressions for the target species velocity $u_s^{(g)}$ and target temperature $\hat{T}$. Similarly, these expressions will be derived for the diatomic mixture model together with the expressions linking the temperatures received by taking moments of the distribution function and the translational-rotational temperature T_{tr} and the equilibrium temperature T. As in Chapter 2 these expressions guarantee the compatibility condition.

5.5.1 Mass Compatibility

The collision term on the RHS of the governing equation is $Q_s = \frac{1}{\tau}(m_{s_1} - f_s) + \frac{1}{Z_r\tau}(m_{s_2} - m_{s_1}) + \frac{1}{Z_v\tau}(m_s^{eq} - m_{s_2})$ and the collision invariant for the mass compatibility is 1, leading to:

$$\begin{aligned}\iiint_{-\infty}^{\infty}\int_0^{\infty}\sum_{i=0}^{\infty} Q_s dI\, d\underline{u} &= \iiint_{-\infty}^{\infty}\int_0^{\infty}\sum_{i=0}^{\infty}\frac{1}{\tau}(m_{s_1} - f_s) + \frac{1}{Z_r\tau}(m_{s_2} - m_{s_1}) + \frac{1}{Z_v\tau}(m_s^{eq} - m_{s_2}) dI\, d\underline{u} \\ &= \frac{1}{\tau}(\rho_s - \rho_s) + \frac{1}{Z_r\tau}(\rho_s - \rho_s) + \frac{1}{Z_v\tau}(\rho_s - \rho_s) \\ &= 0, \end{aligned} \tag{5.61}$$

where even though the model is for a mixture the mass is conserved per species s, since the gas is non-reacting. This will differ for both momentum and energy compatibility equations. The proof of the mass is trivial, since the first moment of all functions is the species density ρ_s and does not impose new conditions between the macroscopic variables.

5.5.2 Momentum Compatibility

The momentum of the diatomic mixture model is conserved for the whole mixture and not per species s. Therefore the sum of the moments of the collision integral Q_s with respect to the collision invariant $\underline{u}$ is assessed:

$$\begin{aligned}&\sum_{s=1}^{2}\iiint_{-\infty}^{\infty}\int_0^{\infty}\sum_{i=0}^{\infty}\underline{u} Q_s dI\, d\underline{u} \\ &\quad= \sum_{s=1}^{2}\iiint_{-\infty}^{\infty}\int_0^{\infty}\sum_{i=0}^{\infty}\underline{u}\frac{1}{\tau}(m_{s_1} - f_s) + \frac{1}{Z_r\tau}(m_{s_2} - m_{s_1}) + \frac{1}{Z_v\tau}(m_s^{eq} - m_{s_2}) dI\, d\underline{u} \\ &\quad= \frac{1}{\tau}\Big((\rho_1\underline{u}_1^{(g)} - \rho_1\underline{u}_1) + \frac{1}{Z_r}(\rho_1\underline{u}_0 - \rho_1\underline{u}_1^{(g)}) + \frac{1}{Z_v}(\rho_1\underline{u}_0 - \rho_1\underline{u}_0)\Big) \\ &\qquad+\frac{1}{\tau}\Big((\rho_2\underline{u}_2^{(g)} - \rho_2\underline{u}_2) + \frac{1}{Z_r}(\rho_2\underline{u}_0 - \rho_2\underline{u}_2^{(g)}) + \frac{1}{Z_v}(\rho_2\underline{u}_0 - \rho_2\underline{u}_0)\Big) \\ &\quad= \frac{1}{\tau}\Big(\Big(\rho_1\underline{u}_1^{(g)} + \rho_2\underline{u}_2^{(g)}\Big) - \Big(\rho_1\underline{u}_1 + \rho_2\underline{u}_2\Big) + \frac{1}{Z_r}\Big(\rho\underline{u}_0 - \rho_1\underline{u}_1^{(g)} - \rho_2\underline{u}_2^{(g)}\Big)\Big) \\ &\quad= 0. \end{aligned} \tag{5.62}$$

Notice that the bracket multiplied with $1/Z_v$ has disappeared in the final expression in Eq. (5.62). Furthermore, for a binary gas mixture with species velocities $\underline{u}_1$ and $\underline{u}_1$ and gas mixture velocity $\underline{u}_0$, the following condition is valid:

$$\rho\underline{u}_0 = \rho_1\underline{u}_1 + \rho_2\underline{u}_2, \tag{5.63}$$

which inserted in Eq. (5.62) leads to a requirement for the target velocity $\underline{u}_s^{(g)}$. This leads to:

$$\Big(1-\frac{1}{Z_r}\Big)(\rho_1\underline{u}_1^{(g)}+\rho_2\underline{u}_2^{(g)}-\rho\underline{u}_0)=0$$
$$\text{OR}$$
$$\rho_1\underline{u}_1^{(g)}+\rho_2\underline{u}_2^{(g)}=\rho\underline{u}_0=\rho_1\underline{u}_1+\rho_2\underline{u}_2 \tag{5.64}$$

Definition of the $u_s^{(g)}$ velocity:

So far we have described the velocity $u_s^{(g)}$ as an equilibrium target velocity for each species representing the velocity in the initial equilibrium distribution function m_{s_1}. However, taking moments of the non-equilibrium distribution function f_s will lead to the species velocity u_s. The gas mixture velocity u_0 can be found using the species velocity u_s and Eq. (5.63). Up until this point, we do not have a mathematical expression for the species target velocity $u_s^{(g)}$. Further to Eq. (5.64), a second velocity relationship is required. This is provided by the same constraint as for the Groppi et al.'s model [64] for the species-velocity equalisation and includes the introduction of the relaxation parameter η:

$$\frac{1}{\rho_1}\iiint_{-\infty}^{\infty}\int_0^{\infty}\sum_{i=0}^{\infty}\underline{u}Q_1 dI\,d\underline{u}-\frac{1}{\rho_2}\iiint_{-\infty}^{\infty}\int_0^{\infty}\sum_{i=0}^{\infty}\underline{u}Q_2 dI\,d\underline{u}=-\eta(\underline{u}_1-\underline{u}_2), \tag{5.65}$$

where Q_1 and Q_2 are the collision terms for species 1 and 2 respectively. Integrating the collision terms with respect to the momentum invariant $\underline{u}$ in Eq. ((5.65)) leads to the following expression:

$$\begin{aligned}&\frac{1}{\rho_1}\Big(\frac{1}{\tau}(\rho_1\underline{u}_1^{(g)}-\rho_1\underline{u}_1)+\frac{1}{Z_r\tau}(\rho_1\underline{u}_0-\rho_1\underline{u}_1^{(g)})+\frac{1}{Z_v\tau}(\rho_1\underline{u}_0-\rho_1\underline{u}_0)\Big)\\&-\frac{1}{\rho_2}\Big(\frac{1}{\tau}(\rho_2\underline{u}_2^{(g)}-\rho_2\underline{u}_2)+\frac{1}{Z_r\tau}(\rho_2\underline{u}_0-\rho_2\underline{u}_2^{(g)})+\frac{1}{Z_v\tau}(\rho_2\underline{u}_0-\rho_2\underline{u}_0)\Big)=-\eta(\underline{u}_1-\underline{u}_2),\end{aligned} \tag{5.66}$$

which reduces to:

$$\begin{aligned}(\underline{u}_1^{(g)}-\underline{u}_1)+\frac{1}{Z_r}(\underline{u}_0-\underline{u}_1^{(g)})-(\underline{u}_2^{(g)}-\underline{u}_2)-\frac{1}{Z_r}(\underline{u}_0-\underline{u}_2^{(g)}) &= -\eta\tau(\underline{u}_1-\underline{u}_2)\\ \underline{u}_1^{(g)}-\underline{u}_2^{(g)}-(\underline{u}_1-\underline{u}_2)+\frac{1}{Z_r}(\underline{u}_0-\underline{u}_1^{(g)}-\underline{u}_0+\underline{u}_2^{(g)}) &= -\eta\tau(\underline{u}_1-\underline{u}_2)\\ \underline{u}_1^{(g)}-\underline{u}_2^{(g)} &= \frac{Z_r(1-\eta\tau)}{(Z_r-1)}(\underline{u}_1-\underline{u}_2)\end{aligned} \tag{5.67}$$

Notice that this equality is possible only if Z_r is common for the two species and not species dependent, while for this formulation Z_v can be species dependent and the same expression will be received. Next, to find $u_s^{(g)}$ velocity we multiply Eq. (5.67) by ρ_2 and sum with the

compatibility equation $\rho_1 \underline{u}_1^{(g)} + \rho_2 \underline{u}_2^{(g)} = \rho \underline{u}_0$ (Eq. (5.64)):

$$\underline{u}_s^{(g)} = (1-\eta\tau)\frac{Z_r}{Z_r-1}\underline{u}_s + \Big(1-(1-\eta\tau)\frac{Z_r}{Z_r-1}\Big)\underline{u}_0 \;\; ; \;\; s=1,2 \tag{5.68}$$

A necessary condition is that $Z_r \neq 1$. In comparison to the monoatomic mixture model (see Eq. (2.10)), where the expression for the velocity has a dependency on the relaxation parameters η and $\nu = 1/\tau$, for the diatomic mixture model a further dependency on the collision number Z_r is present. For typical values of Z_r in the interval $1 < Z_r \leq 5$, then the ratio $Z_r/(Z_r-1)$ will be always bigger than 1 and less than 2. It can be therefore argued that the collision number dependency leads to a small weighted advantage towards the species velocity $\underline{u}_s$ rather than $\underline{u}_0$ in the diatomic mixture model. Also, relatively to the monoatomic model, the same ratio of $\eta/\nu \equiv \eta\tau$ will lead to the value of $\underline{u}_s^{(g)}$ closer to $\underline{u}_s$. Now, all velocities associated with the presented diatomic mixture model are specified and can be computed.

5.5.3 Energy Compatibility

Equivalent to the momentum, the energy of the diatomic mixture is preserved for the sum of all species and not individually. Furthermore, it is preserved for the sum of all types of energy: translational and internal. The sum of the moments of the collision integral Q_s with respect to the collision invariants for the translational, rotational and vibrational energy is:

$$\sum_{s=1}^{2} \iiint_{-\infty}^{\infty} \int_0^{\infty} \sum_{i=0}^{\infty} (\frac{1}{2}|\underline{u}|^2 + I + i\frac{k_B}{m_s}\theta_{v_s}) Q_s dI \, d\underline{u} = 0 \tag{5.69}$$

$$\sum_{s=1}^{2} \iiint_{-\infty}^{\infty} \int_0^{\infty} \sum_{i=0}^{\infty} \Bigg[(\frac{1}{2}|\underline{u}|^2 + I + i\frac{k_B}{m_s}\theta_{v_s}) \times \Big(\frac{1}{\tau}(m_{s_1} - f_s) + \frac{1}{Z_r\tau}(m_{s_2} - m_{s_1}) + \frac{1}{Z_v\tau}(m_s^{eq} - m_{s_2})\Big)\Bigg] dI \, d\underline{u} = 0,$$

where $|\underline{u}|^2 = u^2 + v^2 + w^2$ and after a long but standard integration we reach the following expression:

$$\begin{aligned}
&\sum_{s=1}^{2} \Bigg[\Big(\frac{1}{2}\rho_s \underline{u}_s^{(g)^2} + \frac{3}{2}\rho_s \frac{k_B}{m_s}\hat{T} - \frac{1}{2}\rho_s \underline{u}_s{}^2 - \frac{3}{2}\rho_s \frac{k_B}{m_s} T_{trans_s}\Big) \\
&+ \frac{1}{Z_r}\Big(\frac{1}{2}\rho_s \underline{u}_0{}^2 + \frac{5}{2}\rho_s \frac{k_B}{m_s} T_{tr} - \frac{1}{2}\rho_s \underline{u}_s^{(g)^2} - \frac{3}{2}\rho_s \frac{k_B}{m_s}\hat{T} - \frac{k_B}{m_s} T_{r_s}\rho_s\Big) \\
&+ \frac{1}{Z_v}\Big((\frac{\delta_s(T)}{2} + \frac{5}{2})\rho_s \frac{k_B}{m_s} T - \frac{5}{2}\rho_s \frac{k_B}{m_s} T_{tr} - \frac{\delta_s(T_{v_s})}{2}\frac{k_B}{m_s} T_{v_s}\rho_s\Big)\Bigg] = 0.
\end{aligned} \tag{5.70}$$

The only way to guarantee this expression is equal to 0 for different choices of Z_r and Z_v is if each individual relaxation expression with a different collision number in front of it is 0, leading

to three separate conditions to ensure energy compatibility of the mixture model:

$$\sum_{s=1}^{2}\left[\left(\frac{1}{2}\rho_s\underline{u}_s^{(g)^2}+\frac{3}{2}\rho_s\frac{k_B}{m_s}\hat{T}-\frac{1}{2}\rho_s\underline{u}_s{}^2-\frac{3}{2}\rho_s\frac{k_B}{m_s}T_{tran_s}\right)\right]=0$$
$$\sum_{s=1}^{2}\left[\frac{1}{Z_r}\left(\frac{1}{2}\rho_s\underline{u}_0{}^2+\frac{5}{2}\rho_s\frac{k_B}{m_s}T_{tr}-\frac{1}{2}\rho_s\underline{u}_s^{(g)^2}-\frac{3}{2}\rho_s\frac{k_B}{m_s}\hat{T}-\frac{k_B}{m_s}T_{r_s}\rho_s\right)\right]=0$$
$$\sum_{s=1}^{2}\left[\frac{1}{Z_v}\left(\left(\frac{\delta_s(T)}{2}+\frac{5}{2}\right)\rho_s\frac{k_B}{m_s}T-\frac{5}{2}\rho_s\frac{k_B}{m_s}T_{tr}-\frac{\delta_s(T_{v_s})}{2}\frac{k_B}{m_s}T_{v_s}\rho_s\right)\right]=0 \tag{5.71}$$

These equations resemble Eq. (2.11) in Chapter 2 from which the temperature introduced as a target equilibrium temperature in the equilibrium distribution function was defined. The species translational, rotational and vibrational temperatures T_{tran_s}, T_{r_s} and T_{v_s} are found as moments of the species non-equilibrium distribution functions. Similarly to the monoatomic model, from the energy compatibility, the expressions for $\hat{T}, T_{tr}$ and T are defined from the species temperatures T_{tran_s}, T_{r_s} and T_{v_s}:

$$\hat{T}=\frac{1}{3nk_B}\sum_{s=1}^{2}\left[\rho_s(\underline{u}_s{}^2-\underline{u}_s^{(g)^2})+3n_sk_BT_{tran_s}\right] \tag{5.72}$$

$$T_{tr}=\frac{3}{5}\hat{T}+\frac{1}{5nk_B}\sum_{s=1}^{2}\left[\rho_s(\underline{u}_s^{(g)^2}-\underline{u}_0{}^2)+2n_sk_BT_{r_s}\right] \tag{5.73}$$

$$T=\frac{5nk_BT_{tr}+\sum_{s=1}^{2}(\delta_s(T_{v_s})n_sk_BT_{v_s})}{5nk_B+\sum_{s=1}^{2}(\delta_s(T)n_sk_B)} \tag{5.74}$$

To guarantee positive temperatures, the limit of possible values for the coefficient $\eta\tau=\eta/\nu$ is found, similar to the monoatomic mixture models in Chapter 2. For positive macroscopic values for the temperatures, the expressions in Eq. (5.72) and Eq. (5.74) guarantee positivity without any limitations. From Eq. (5.73) and the known possible values for the rotational collision coefficient Z_r, the coefficient's bounds are $1/Z_r\leq\eta\tau\leq(2Z_r-1)/Z_r$. Inspecting the possible values for Z_r, it follows that $0<\eta\tau<2$, which are similar values to the Groppi et al's model [64] and the Shakhov-based mixture model we developed [88] and detailed in Chapter 2.
Together the 3 equations (Eq. (5.72)-Eq. (5.74)) guarantee energy compatibility of the model, provide expressions for 3 important macroscopic variables for the definition of the equilibrium distribution functions and contribute to the successful closure of the kinetic model.

5.6 Continuum Limit for the Gas Mixture

The continuum limit of the diatomic mixture model and the equations for the mass, momentum and energy conservation are demonstrated in this section. The Chapman-Enskog expansion upto

first order of the species non-equilibrium distribution function f_s is:

$$f_s = m_{s_1} + \frac{1}{Z_r}(m_{s_2} - m_{s_1}) + \frac{1}{Z_v}(m_s^{eq} - m_{s_2}) - \varepsilon\hat{\tau}\Big(\frac{\partial m_s^{eq}}{\partial t} + \underline{u}\cdot\frac{\partial m_s^{eq}}{\partial \underline{x}}\Big) + O(\varepsilon^2), \quad (5.75)$$

where the same approach is followed as for the single-species diatomic models described in this chapter. The order $O(\varepsilon)$ expansion is based solely on the final (Maxwellian) equilibrium distribution function m_s^{eq}, defined by the gas mixture velocity u_0 and the equilibrium temperature T. As with the monoatomic gas mixture and due to the absence of chemistry, the mass conservation is per species s, while the momentum and energy are conserved for the mixture. To receive the complete set of conservation equations, we need to sum over all vibration levels i and integrate the rotational energy I and in the three velocity directions with respect to the collision invariant $\underline{\psi}_s$.

$$\sum_{s=1}^{2}\frac{\partial}{\partial t}\iiint_{-\infty}^{\infty}\int_0^{\infty}\sum_{i=0}^{\infty}\underline{\psi}_s f_s dI\, d\underline{u} + \frac{\partial}{\partial \underline{x}}\iiint_{-\infty}^{\infty}\int_0^{\infty}\sum_{i=0}^{\infty}\underline{u}\underline{\psi}_s f_s dI\, d\underline{u} = 0, \quad (5.76)$$

where the collision invariant is per species and in the form $\psi_1 = [1,0,\underline{u},0,\frac{1}{2}(u^2+v^2+w^2)+I+i\frac{k}{m_s}\theta_{v_1}]^T$ and $\psi_2 = [0,1,0,\underline{u},\frac{1}{2}(u^2+v^2+w^2)+I+i\frac{k}{m_s}\theta_{v_2}]^T$.
Similar to the monoatomic mixture model the drift velocity is a very important quantity. It is found as a moment of the CE-expanded non-equilibrium distribution function f_s as:

$$\begin{aligned}
\rho_s u_s^{\varepsilon} &= \iiint_{-\infty}^{\infty}\int_0^{\infty}\sum_{i=0}^{\infty} u f_s dI\, d\underline{u},\\
\rho_s u_s^{\varepsilon} &= \iiint_{-\infty}^{\infty}\int_0^{\infty}\sum_{i=0}^{\infty} u\Big[m_{s_1} + \frac{1}{Z_r}(m_{s_2} - m_{s_1}) + \frac{1}{Z_v}(m_s^{eq} - m_{s_2}) - \tau\Big(\frac{\partial m_s^{eq}}{\partial t} + \underline{u}\cdot\frac{\partial m_s^{eq}}{\partial \underline{x}}\Big)\Big] dI\, d\underline{u},\\
\rho_s u_s^{\varepsilon} &= \rho_s u_s^{(g)} - \frac{1}{Z_r}(\rho_s u_s^{(g)} - \rho_s u_0) - \tau\Big(\frac{k}{m_s}T\Big(\frac{\partial \rho_s}{\partial x} - \frac{m_s}{m}\frac{\rho_s}{\rho}\frac{\partial \rho}{\partial x}\Big) + \rho_s\frac{k}{m_s}\Big(1 - \frac{m_s}{m}\Big)\frac{\partial T}{\partial x}\Big).
\end{aligned} \quad (5.77)$$

Substituting the expression for $u_s^{(g)}$ as defined in Eq. (5.67) into the above expression leads to:

$$\begin{aligned}
u_s^{\varepsilon} &= u_0 - \frac{\varepsilon kT}{\eta\rho_s}\Big(\frac{1}{m_s}\frac{\partial \rho_s}{\partial x} - \frac{1}{m}\frac{\rho_s}{\rho}\frac{\partial \rho}{\partial x} + \frac{\rho_s}{T}\Big(\frac{1}{m_s} - \frac{1}{m}\Big)\frac{\partial T}{\partial x}\Big),\\
u_s^{\varepsilon} &= u_0 - \frac{\varepsilon kT}{\eta n_s}\Big(\frac{1}{m_s}\frac{\partial n_s}{\partial x} - \frac{n_s}{\rho}\frac{\partial n}{\partial x} + \frac{n_s}{T}\Big(\frac{1}{m_s} - \frac{n}{\rho}\Big)\frac{\partial T}{\partial x}\Big),
\end{aligned} \quad (5.78)$$

where $n_s = \rho_s/m_s$ is the species number density and $n = \rho/m$ is the number density for the gas mixture. Note the relaxation coefficient η is of the same order as $1/\tau$ and therefore $1/\eta = \varepsilon/\hat{\eta}$. In Eq. (5.78) we use this reduced form but instead of $\hat{\eta}$ we have used η by omitting the $\hat{}$ symbol for simplicity. We have used these quantities to derive the species velocity u_s^{ε} in a form allowing comparison with the species velocity for the monoatomic mixture models from Chapter 2. We

find that the monoatomic and diatomic expressions are identical, which is the desired result, since the extra temperatures and relaxation processes should not affect the species velocity u_s^{ε}. The mass conservation equation for the diatomic mixture model is per species s and is in the form:

$$\frac{\partial \rho_s}{\partial t}+\frac{\partial}{\partial x}\Big(\rho_s u_s^{(g)}-\frac{1}{Z_r}(\rho_s u_s^{(g)}-\rho_s u_0)\Big) \\ -\varepsilon\hat{\tau}\frac{\partial}{\partial x}\Big(\frac{k}{m_s}T\Big(\frac{\partial \rho_s}{\partial x}-\frac{m_s}{m}\frac{\rho_s}{\rho}\frac{\partial \rho}{\partial x}\Big)+\rho_s\frac{k}{m_s}\Big(1-\frac{m_s}{m}\Big)\frac{\partial T}{\partial x}\Big)=0, \quad (5.79)$$

which after substituting $u_s^{(g)}$ from Eq. (5.67) and then the expression for u_s^{ε} from Eq. (5.78) reduces the equation to a mass conservation equation which involves the gas mixture velocity u_0.

Mass Conservation:

$$\frac{\partial \rho_s}{\partial t}+\frac{\partial}{\partial x}(\rho_s u_0)-\varepsilon\frac{\partial}{\partial x}\Big(\frac{kT}{\eta}\Big(\frac{1}{m_s}\frac{\partial \rho_s}{\partial x}-\frac{1}{m}\frac{\rho_s}{\rho}\frac{\partial \rho}{\partial x}+\frac{\rho_s}{T}\Big(\frac{1}{m_s}-\frac{1}{m}\Big)\frac{\partial T}{\partial x}\Big)\Big)=0. \quad (5.80)$$

Notice that the diatomic single-species mass equation was equivalent to the monoatomic single-species mass equation. Similarly, the diatomic mixture mass conservation equation is the same as the continuity equation presented in Chapter 2 for the monoatomic gas mixture models. The introduction of molecular collision with internal degrees of freedom has not affected the mass flow and diffusion in the system. The continuity equation can be reduced to a single-species equation for $m_s = m$ and $\rho_s = \rho$, which makes the term of $O(\varepsilon)$ to vanish. The continuum limit for the mass of the system shows consistency with both the monoatomic mixture model and the single-species diatomic model, which is the desired mathematical result.

The momentum is conserved for the mixture and therefore the sum over all species s is required to receive the momentum conservation equation:

$$\frac{\partial}{\partial t}(\rho u_0)+\frac{\partial}{\partial x}\sum_{s=1}^{2}\Bigg(\rho_s(u_s^{(g)})^2+\rho_s\frac{k}{m_s}\hat{T}-\frac{1}{Z_r}\Big(\rho_s(u_s^{(g)})^2+\rho_s\frac{k}{m_s}\hat{T}-\rho_s(u_0)^2-\rho_s\frac{k}{m_s}T_{tr}\Big) \\ -\frac{1}{Z_v}\Big(\rho_s\frac{k}{m_s}T_{tr}-\rho_s\frac{k}{m_s}T\Big)\Bigg) \\ -\tau\frac{\partial}{\partial x}\Bigg(2\rho\frac{k}{m}T\frac{\partial u_0}{\partial x}-\sum_{s=1}^{2}\Bigg\{\rho_s\frac{k}{m_s}\frac{\sum_{s=1}^{2}\Big(\frac{k}{m_s}\rho_s T\Big)}{\sum_{s=1}^{2}\Big(\Big(\frac{5}{2}+\frac{\delta_s^2(T)}{4}\exp\Big(\frac{\theta_{v_s}}{T}\Big)\Big)\frac{k}{m_s}\rho_s\Big)}\Bigg\}\frac{\partial u_0}{\partial x}\Bigg)=0. \quad (5.81)$$

The above equation can be reduced by using:

$$\sum_{s=1}^{2}\Big(\rho_s(u_s^{(g)})^2\Big)-\rho u_0^2=\sum_{s=1}^{2}\Big(\rho_s(u_s^{(g)}-u_0)^2\Big), \quad (5.82)$$

similar to the monoatomic mixture models in Chapter 2. Furthermore, we can show from the velocity expression in Eq. (5.78) that $u_s^{(g)} - u_0 = O(\varepsilon)$ and therefore $(u_s^{(g)} - u_0)^2 = O(\varepsilon^2)$. The continuum limit considered here is upto and including first order terms in ε. Therefore, the momentum equation of the gas mixture is for the whole system and is based on the mixture velocity u_0.

Momentum Conservation:

$$\frac{\partial}{\partial t}(\rho u_0) + \frac{\partial}{\partial x}\left(\rho u_0^2 + \rho \frac{k}{m}\hat{T}\right) - \varepsilon\hat{\tau}\frac{\partial}{\partial x}\left(\frac{1}{\varepsilon Z_r \hat{\tau}}\rho\frac{k}{m}\left(\hat{T} - T_{tr}\right) + \frac{1}{\varepsilon Z_v \hat{\tau}}\rho\frac{k}{m}\left(T_{tr} - T\right)\right.$$
$$\left. + \left(2 - \frac{\rho\frac{k}{m}}{\sum_{s=1}^{2}\left(\left(\frac{5}{2} + \frac{\delta_s^2(T)}{4}\exp\left(\frac{\theta_{v_s}}{T}\right)\right)\frac{k}{m_s}\rho_s\right)}\right)\rho\frac{k}{m}T\frac{\partial u_0}{\partial x}\right) = 0. \tag{5.83}$$

Note that the only difference between the mixture three-temperature momentum conservation and the single-species three-temperature model is the mass m_s and density ρ_s per species s. For $m_s = m$ and $\rho_s = \rho$, the momentum conservation reduces to the single-species three-temperature model. The total energy of the system is conserved for the mixture and we know that:

$$\begin{aligned} e &= \sum_{s=1}^{2}\left[\frac{1}{2}\rho_s(u_s)^2 + \frac{3}{2}\rho_s\frac{k}{m_s}T_{tran_s} + \rho_s\frac{k}{m_s}T_{r_s} + \frac{\delta_s(T_{v_s})}{2}\rho_s\frac{k}{m_s}T_{v_s}\right], \\ e &= \sum_{s=1}^{2}\left[\frac{1}{2}\rho_s u_0^2 + \frac{5}{2}\rho_s\frac{k}{m_s}T + \frac{\delta_s(T)}{2}\rho_s\frac{k}{m_s}T\right]. \end{aligned} \tag{5.84}$$

Furthermore, by inserting Eq. (5.71) we find:

$$e = \sum_{s=1}^{2}\left[\frac{1}{2}\rho_s u_0^2 + \frac{3}{2}\rho_s\frac{k}{m_s}\hat{T} + \rho_s\frac{k}{m_s}T_{r_s} + \frac{\delta_s(T_{v_s})}{2}\rho_s\frac{k}{m_s}T_{v_s}\right], \tag{5.85}$$

which is the form used in the energy conservation expression. After integration the mixture energy conservation equation is based on the $u_s^{(g)}$ velocity and all of the temperatures introduced with the model. We have reduced that expression to a more concise form by using the expressions derived from the energy compatibility, describing the relationships between the different temperatures (Eq. (5.71)) , (Eq. (5.85)) and after expressing $u_s^{(g)}$ as a function of u_s and u_0. Furthermore, all terms of order $O(\varepsilon^2)$ are ignored.

Energy Conservation:

$$\begin{aligned}
&\frac{\partial}{\partial t}\sum_{s=1}^{2}\Big[\frac{1}{2}\rho_s u_0^2+\frac{3}{2}\rho_s\frac{k}{m_s}\hat{T}+\rho_s\frac{k}{m_s}T_{r_s}+\frac{\delta_s(T_{v_s})}{2}\rho_s\frac{k}{m_s}T_{v_s}\Big]\\
&+\frac{\partial}{\partial x}\sum_{s=1}^{2}\left[\frac{1}{2}\rho_s u_0^3+\frac{5}{2}\rho_s u_0\frac{k}{m_s}\hat{T}+\rho_s u_0\frac{k}{m_s}T_{r_s}+\frac{\delta_s(T_{v_s})}{2}\rho_s u_0\frac{k}{m_s}T_{v_s}\right]\\
&-\varepsilon\hat{\tau}\frac{\partial}{\partial x}\left\{\left(2-\frac{\rho\frac{k}{m}}{\sum_{s=1}^{2}\left(\left(\frac{5}{2}+\frac{\delta_s^2(T)}{4}exp\left(\frac{\theta_{v_s}}{T}\right)\right)\frac{k}{m_s}\rho_s\right)}\frac{\partial u_0}{\partial x}\right)\rho u_0\frac{k}{m}T\frac{\partial u_0}{\partial x}\right.\\
&\quad+\sum_{s=1}^{2}\left[\left(\frac{7}{2}+\frac{\delta_s^2(T)}{4}\exp\left(\frac{\theta_{v_s}}{T}\right)\right)\rho_s\frac{k^2}{m_s^2}T\frac{\partial T}{\partial x}+\frac{1}{\varepsilon Z_r\hat{\tau}}\rho_s u_0\frac{k}{m_s}\left(\hat{T}-T_{tr}\right)\right.\\
&\quad+\frac{1}{\varepsilon Z_v\hat{\tau}}\rho_s u_0\frac{k}{m_s}\left(T_{tr}-T\right)-\frac{1}{\varepsilon\hat{\tau}}\Big(\frac{3}{2}\rho_s u_0^2+\frac{5}{2}\rho_s\frac{k}{m_s}\hat{T}+\rho_s\frac{k}{m_s}T_{r_s}\\
&\quad\left.\left.+\frac{\delta_s(T_{v_s})}{2}\rho_s\frac{k}{m_s}T_{v_s}\Big)(u_s-u_0)\right]\right\}=0. \quad (5.86)
\end{aligned}$$

Notice that for the energy conservation equation to reduce to the single-species form will need further requirements than the mass equalisation. Specifically, in the zeroth-order time-derivative and space-derivate terms, the species rotational and vibrational temperatures T_{r_s} and T_{v_s} need to be equal, i.e. $T_{r_1}=T_{r_2}$ and $T_{v_1}=T_{v_2}$. Moreover, the $\delta_s(T_{v_s})$- degrees of freedom dependency, which is defined with the gas-specific characteristic temperature will need to be set to the same value. Only then, the energy conservation model reduces to a single-species model, which is the required reduction to a single-species gas.
Finally, the three-temperature diatomic mixture model can be reduced to a two-temperature and a single-temperature mixture model following the same processes described in the single-species diatomic models.

5.7 Transport Properties for Diatomic Mixture

We will inspect the three equations describing the continuum limit to identify the transport properties. The transport coefficients for the diatomic mixture model inherit the properties of the single-species diatomic model: viscosity, bulk viscosity and thermal conductivity, due to the internal degrees of freedom [125]. Additional properties arise that are mixture related such as the ordinary diffusion, Soret and Dufour effects.

5.7.1 Diffusion

In comparison to the three single-species diatomic models where no mass diffusion behaviour is observed, Eq. (5.80) has a mass flux term, caused by the gradients of the concentration, pressure

and temperature, in comparison to the single-species mass conservation shown in Eq. (5.19). The mass flux term is in the form:

$$j_s = -\varepsilon\frac{k_B T}{\eta}\Big(\frac{1}{m_s}\frac{\partial \rho_s}{\partial x} - \frac{1}{m}\frac{\rho_s}{\rho}\frac{\partial \rho}{\partial x} + \frac{\rho_s}{T}\Big(\frac{1}{m_s} - \frac{1}{m}\Big)\frac{\partial T}{\partial x}\Big), \tag{5.87}$$

which is identical to mass flux of the monoatomic mixture models. Early in this chapter we discussed that expanding from a single-species monoatomic gas to a single-species diatomic gas is known to affect some coefficients, e.g bulk viscosity and thermal conductivity, while others, e.g ordinary viscosity, are unchanged. Diffusion belongs to the latter group and therefore the diffusion effect of the monoatomic mixture and the diatomic mixture are identical [35]. In Chapter 2, as well as here, we ignore the temperature effect (associated with the Soret coefficient), leading our focus to the ordinary diffusion. Therefore, the binary diffusion coefficient $\mathscr{D}_{sr} = \mathscr{D}_{rs}$, where $r \in \{1,2\}$ and $r \neq s$, is such that:

$$\mathscr{D}_{sr} = \frac{\varepsilon k T \rho}{\eta n m_s m_r}, \tag{5.88}$$

similar to expression Eq. (2.62).

5.7.2 Viscosity

For the diatomic mixture model two viscosity coefficients are present: the ordinary viscosity and the bulk viscosity. The momentum equation can be rewritten as:

$$\begin{aligned}\frac{\partial}{\partial t}(\rho u_0) + \frac{\partial}{\partial x}\Big(\rho u_0^2 + \rho\frac{k_B}{m}\hat{T}\Big) - \varepsilon\hat{\tau}\frac{\partial}{\partial x}\Bigg(\frac{4}{3}\rho\frac{k_B}{m}T\frac{\partial u_0}{\partial x} + \frac{1}{\varepsilon Z_r\hat{\tau}}\rho\frac{k_B}{m}\Big(\hat{T} - T_{tr}\Big)\\ + \frac{1}{\varepsilon Z_v\hat{\tau}}\rho\frac{k_B}{m}\Big(T_{tr} - T\Big) + \frac{2}{3}\rho\frac{k_B}{m}T\frac{\partial u_0}{\partial x} - \rho\frac{k_B}{m}T\frac{\rho\frac{k_B}{m}}{\sum_{s=1}^{2}\Big(\Big(\frac{5}{2} + \frac{\delta_s^2(T)}{4}\exp\Big(\frac{\theta_{vs}}{T}\Big)\Big)\frac{k_B}{m_s}\rho_s\Big)}\frac{\partial u_0}{\partial x}\Bigg)\\ = 0,\end{aligned} \tag{5.89}$$

where the ordinary viscosity μ for the diatomic gas mixture considered here is identical to that for the monoatomic model and is expressed as:

$$\mu = \tau\rho\frac{k_B}{m}T. \tag{5.90}$$

Here, we should take a moment to appreciate that the value of $\eta\tau$ is defined from the relationship of the ordinary diffusion and ordinary viscosity coefficients, formulated as [35]:

$$\mu = \frac{5}{3}\frac{m_1 m_2}{(m_1 + m_2)}\frac{n\mathscr{D}_{12}}{A_{12}^*}, \tag{5.91}$$

where A_{12}^* is a non-dimensional coefficient, defined by the ratio of collision integrals and is in general a function of the gas temperature and the force law between molecules. This relationship is identical to the monoatomic gas mixture, as are the ordinary diffusion and viscosity coefficients. Therefore, the expression for $\eta\tau$ is the same and equal to η/ν. Furthermore, the value of $A_{12}^* = 1.10$ is found appropriate [117].

$$\eta\tau = \frac{\eta}{\nu} = \frac{5}{3}\frac{1}{(m_1+m_2)A_{12}^*}\frac{\rho}{n}. \tag{5.92}$$

This coefficient will vary the most in regions of strong non-equilibrium and for bigger mass ratios.

After identifying the ordinary viscosity coefficient, the contribution to the normal stress due to the bulk viscosity is:

$$\begin{aligned}\sigma(\mu_B) = &\frac{1}{Z_r}\rho\frac{k_B}{m}\left(\hat{T}-T_{tr}\right) + \frac{1}{Z_v}\rho\frac{k_B}{m}\left(T_{tr}-T\right) + \frac{2}{3}\tau\rho\frac{k_B}{m}T\frac{\partial u_0}{\partial x} \\ &-\tau\rho\frac{k_B}{m}T\frac{\rho\frac{k_B}{m}}{\sum_{s=1}^{2}\left(\left(\frac{5}{2}+\frac{\delta_s^2(T)}{4}exp\left(\frac{\theta_{vs}}{T}\right)\right)\frac{k_B}{m_s}\rho_s\right)}\frac{\partial u_0}{\partial x} \quad .\end{aligned} \tag{5.93}$$

We observe an expression similar to the single-species three-temperature diatomic model. Again, three temperatures ($\hat{T},\ T_{tr},\ T$) contribute directly to the bulk viscosity expression and the relaxation phenomenon is presented by the collision numbers Z_r and Z_v. The difference with the single-species expression is only in the last term, which is multiplying the derivative of the mixture velocity u_0. There, a mass averaged contribution of the different degrees of freedom is present. In the limiting case where $s = 1$ the normal stress due to bulk viscosity for the mixture will reduce to the single-species expression (Eq. (5.37)). Alternatively, for the limit of no vibrational excitation, the bulk viscosity expression reduces, where:

$$\sigma(\mu_B) = \frac{1}{Z_r}\rho\frac{k_B}{m}\left(\hat{T}-T_{tr}\right) + \frac{4}{15}\tau\rho\frac{k_B}{m}T\frac{\partial u_0}{\partial x}, \tag{5.94}$$

which is identical to the similarly-reduced single-species expression and no mixture contribution is present. Therefore, in the absence of vibrational excitation, the mixture momentum equation up to the Navier-Stokes level is identical to the single-species equation, without any further assumptions or requirements.

5.7.3 Heat Flux

In the energy equation for the gas mixture (Eq. (5.86)), the order $O(\varepsilon)$ expression in the spatial derivative consists of three terms: the work done by the two types of viscosities and the heat flux, which includes the thermal conductivity and the Dufour effect. The heat flux is expressed

as:

$$q = \sum_{s=1}^{2}\Bigg[-\Big(\frac{7}{2}+\frac{\delta_s^2(T)}{4}\exp\Big(\frac{\theta_{v_s}}{T}\Big)\Big)\tau\rho_s\frac{k_B^2}{m_s^2}T\frac{\partial T}{\partial x} + \Big(\frac{3}{2}\rho_s(u_0)^2+\frac{5}{2}\rho_s\frac{k_B}{m_s}\hat{T}+\rho_s\frac{k_B}{m_s}T_{r_s}+\frac{\delta_s(T_{v_s})}{2}\rho_s\frac{k_B}{m_s}T_{v_s}\Big)(u_s-u_0)\Bigg], \quad (5.95)$$

where the term associated with the temperature derivative is the thermal conductivity contribution and the diffusion effect (the term multiplied by the velocity difference) is the Dufour effect. The Dufour effect q_D is:

$$q_D = \sum_{s=1}^{2}\Big(\frac{5}{2}\rho_s\frac{k_B}{m_s}\hat{T}+\rho_s\frac{k_B}{m_s}T_{r_s}+\frac{\delta_s(T_{v_s})}{2}\rho_s\frac{k_B}{m_s}T_{v_s}\Big)(u_s-u_0), \quad (5.96)$$

where contributions from each species temperatures for the rotation T_{r_s}, the vibration T_{v_s} and the common target translational temperature $\hat{T}$ are present, while the velocity contribution sums to 0 for the mixture. This expression of the Dufour effects resembles the monoatomic expression but the additional internal degrees of freedom of the diatomic model give rise to additional terms based on these extra DoF. Note that for the same species mass, the difference between u_s and u_0 vanishes and therefore the Dufour effect disappears.

The other effect in the heat flux expression is the thermal conductivity. The individual contributions of the separate translational, rotational and vibrational DoF to the thermal conductivity are:

$$q^{tran} = -\sum_{s=1}^{2}\frac{5}{2}\Big(\tau\rho_s\frac{k_B^2}{m_s^2}T\Big)\frac{\partial T}{\partial x}, \qquad q^{rot} = -\sum_{s=1}^{2}\frac{2}{2}\Big(\tau\rho_s\frac{k_B^2}{m_s^2}T\Big)\frac{\partial T}{\partial x},$$
$$q^{vib} = -\sum_{s=1}^{2}\Big(\frac{\delta_s(T)^2}{4}\exp\Big(\frac{\theta_{v_s}}{T}\Big)\tau\rho_s\frac{k_B^2}{m_s^2}T\Big)\frac{\partial T}{\partial x}. \quad (5.97)$$

These expression are similar to the thermal conductivity for a single-species diatomic gas and will in fact reduce to it for $m_s = m$, $\rho_s = \rho$ and identical characteristic temperature $\theta_{v_s} = \theta_v$. These equations are consistent with the single-species diatomic model, but the reader should note that in comparison to the expressions in Chapter 2, no Prandtl correction is used in the current diatomic mixture model. This is a drawback of the current kinetic model and should be addressed in the future. However, diatomic mixture models are still a very challenging and active area of research and the introduced model is a strong step in a well-understood, derived and described model for gas mixtures with drift velocity and species-specific rotational and vibrational temperatures.

5.8 Summary of Findings

Three single-species diatomic models with different level of complexity were presented. Furthermore, a diatomic model for binary gas mixture was detailed. The goal was to derive a diatomic model, accounting for the internal degrees of freedom, for a gas mixture through a comprehensive development from a well-known single-species single-temperature model to a mixture three-temperature model and to explore the impact of each change. The continuum limit for each model was demonstrated and compared. The transport properties were discussed separately. The models were shown to have good mathematical properties and more specifically:

- A single-species diatomic model with a single temperature and single-relaxation approach in the governing equation which is well-defined in the literature was summarised and used as a starting point to develop two more detailed single-species models.
- A single-species diatomic model with two temperatures: a common translational and rotational temperature and a separate vibrational temperature was developed and presented. The model also differs from the initial diatomic single-species model by a two-level relaxation approach, allowing for a slower vibrational relaxation.
- A single-species diatomic model with three separate temperatures: translational, rotational and vibrational temperatures was shown. The relaxation was split in three parts, translational, relatively slower rotation and further delayed vibration.
- Both extended models were shown to be consistent with each other and the original model when the temperatures were equalised.
- The mass, momentum and energy conservation was demonstrated. The differences between the conservation equations in the continuum limit due to the introduced temperatures and relaxation differences were detailed and discussed.
- Transport properties were detailed for all models. The ordinary viscosity and the diatomic heat flux, dependent on all excited DoF, were found identical between the models, while the bulk viscosity expression reflected the relaxation of the additional temperatures.
- Based on the three-temperature approach, a diatomic model for a binary gas mixture was developed. Similar to the monoatomic mixture, a new target species velocity and a common target translational temperature were introduced. The rotational and vibrational temperatures were per species, while the three-level relaxation was identical for the two species.
- Species diffusion was accounted for with a relaxation parameter allowing the two species velocities to separate.

- The model was shown to be consistent and to reduce to a single-temperature single-species model. The model was also shown to reduce to the monoatomic mixture, demonstrated in Chapter 2.
- The model was shown to conserve mass, momentum and energy in the continuum limit.
- The ordinary viscosity, bulk viscosity were found identical to the corresponding single-species expressions. The diatomic thermal conductivity was shown dependent on the species mass and concentration, but besides that had a similar expression to the single-species heat flux.
- The mixture transport properties appeared in the continuum limit expressions, similarly to the monoatomic mixture models. The ordinary diffusion coefficient is identical to the monoatomic expression, while the Dufour effect in the energy equation was similar to the monoatomic version, but accounted for the additional internal DoF.

In summary, the developed diatomic model for binary gas mixtures was found consistent and with good mathematical properties. Next, it will be evaluated numerically.

Chapter 6

Numerical Evaluation of the Diatomic Mixture Model *

The purpose of this chapter is to numerically evaluate the diatomic mixture model, which was developed and theoretically evaluated in Chapter 5. The model is applied in a computational setup similar to the setup for the novel monoatomic mixture models in Chapter 3 and a similar approach is utilised for the numerical validation of the model. Starting with the evaluation of the binary mixture model with two gases of equal mass and identical initial conditions, it is numerically verified that the two gases are indifferentiable. The normal shock profile is shown for a gas mixture consisting of nitrogen and oxygen. A parametric study with cases at different Mach numbers, vibrational collision coefficients and species concentrations is presented. A detailed comparison with results, acquired with a DSMC solver under the same conditions, is presented and used for the evaluation of the mixture model. Some of the limitations of the BGK-type model with a uncorrected Prandtl number are observed, while overall the mixture model demonstrates promising results. Finally, the flow around a more complex geometry with a cylindrical body is demonstrated for different Mach numbers and vibrational collision numbers. In summary, the main contribution of this chapter is the numerical application and evaluation of a novel diatomic mixture model with three temperatures per species and velocity diffusion effects. The good agreement of the results when compared with DSMC results at identical conditions is a stepping stone in the development of modelling air flow in rarefied conditions for practical applications using deterministic and efficient kinetic models.

6.1 Numerical Method

The diatomic mixture model is tested and evaluated for the profile of a normal shock wave and a circular cylinder. The computational setup and the problems are detailed in this section.

*Published in AIP Advances.

6.1.1 Discrete Velocity Method

The results of the diatomic kinetic model are acquired using the discrete-velocity method within the Multi Physics Code (M Φ C) in-house framework [112, 118].The method is chosen for its simplicity and accuracy. This is identical to the methodology described in Chapter 3. Since we follow the same approach, only the differences will be detailed here. In the current computational setup, all test cases are considered as two-dimensional (2D) problems. This choice for 2D was based on the planned applications to more complex problems (flow over cylinders, flat plates and ramps). For the current one-dimensional (1D) shock problems, the extra cost was deemed acceptable, since it avoids the development of a separate 1D version of the solver. Code parallelization is required for all cases. As a consequence of using two-dimensional setup, the number of discrete velocities has increased and for the profile of a normal shock wave the number of uniformly spaced discrete velocities in the velocity grid is 48×48 or 2304 for all Mach numbers. Velocity bounds are between $u_{min} = -8$ to $u_{max} = 12$ (i.e. 8 and 12 times the most probable molecular velocity at reference temperature), leading to velocity-step $\Delta u = 0.417$. The local time-step Δt, which is dependent on the local cell size, uses a CFL-based criterion (CFL $= 0.5$) and is limited by the maximum convection speed. The smallest step is at the shock, where the cell are clustered and $\Delta t = 0.004$, which is always smaller than the mean collision time (non-dimensional relaxation time is in the range of 0.075 (post-shock) to 1 (pre-shock)). The number of discrete velocities for the circular cylinder for the $M_\infty = 3$ is 36×36 and it increases correspondingly for $M_\infty = 5$ to 48×48. This is done not to provide a finer velocity grid, but to address the extended minimum and maximum bounds of the range of possible velocities and preserve the uniform velocity mesh at the same Δu (at $M_\infty = 3$, $\Delta u = 0.44$ and at $M_\infty = 5$, $\Delta u = 0.417$ of the most probable speed). The velocity grids are known to be sufficiently refined from the similar tests for the monoatomic setup. Additionally, the $M_\infty = 3$ case is also tested with a finer 48×48 velocity grid, confirming that the 36×36 grid leads to well-converged results in terms of the velocity-space mesh.

Similar to Chapter 3, the evaluation of the distribution functions and the fluxes is performed for each velocity in every cell. The macroscopic variables are obtained from taking corresponding moments of the distribution functions, evaluated using the trapezoidal rule. A finite-volume scheme and a second order Total Variation Diminishing (TVD) time marching method [41], [42] are used to numerically discretise the models' governing equations. The computational time and overhead requirements are again more than a continuum solver, but are also larger than the monoatomic version of the solver due to the extra distribution functions and macroscopic variables related to the internal degrees of freedom of the gas mixture.

6.1.2 Problem setup

The numerical evaluation starts with the study of the profile of a normal shock wave, since it is one of the simplest problems with high levels of non-equilibrium. The normal shock simulations are all performed on a grid with 1152 number of cells, with $x \in [-75L_{ref}, 75L_{ref}]$. In comparison to the monoatomic mixture simulations, the grid is two-dimensional with 4 blocks and a non-uniform physical space, but optimised for the smallest in size cells to gather near the shock, where $\Delta x = 0.125$.

The considered diatomic gases are nitrogen (N_2) and oxygen (O_2) with a concentration ratio similar to air for most cases: 80% and 20% respectively. The normal shock setup is initialised with two Maxwellian equilibrium distributions on each sides of the shock. The equilibrium functions are defined based on the macroscopic variables provided by the modified Rankine-Hugoniot conditions for a diatomic gas with rotational and vibrational excitation. In the test cases studied, pre-shock values are evaluated at a temperature $T_\infty = 288.15K$, for which the level of vibrational excitation is considered negligible and the number of excited vibrational DoF for each species $\delta_s(T_{v_s}) = 0$, while the rotation is taken as fully excited for both gases. Therefore, for the pre-shock values, the ratio of specific heats is taken as $\gamma = 1.4$ and the speed of sound is based on the mass mixture $m_{mix} = \rho/n$. An iterative method is applied to evaluate the jump conditions, described in detail in [1], for each test case.

Even though the main focus of the study is based on the profile of the normal shock wave, the high-speed flow past a cylinder is evaluated and inspected as well. A quarter of a circular cylinder grid is used with symmetry condition imposed on the stagnation line and initialised with free-stream Mach number, species concentration and fixed wall temperature. The same grid as in the monoatomic simulations is used, consisting of 36 blocks and 27864 cells. The rarefaction level is based on the radius of the cylinder ($R = 5.5L_{ref}$) and the Knudsen number is set to $Kn = 0.18$ for all cases. This is a more rarefied case than the case considered in Chapter 3. The reason to inspect test cases with a bigger Knudsen number is the resulting higher level of non-equilibrium, creating a more demanding test case in terms of flow physics, but well-resolved on the relatively fine mesh used here.

Validation of the numerical results for the normal shock are performed by comparing with results acquired by a DSMC solver with the same macroscopic conditions. There are not many validation data for gas mixtures available in the literature with which the accuracy of the model itself can be evaluated. The circular cylinder study demonstrates interesting results, but requires a further validation study.

6.1.3 Dimensional Reduction

The dimensional reduction is a standard and very useful procedure for solvers based on kinetic modelling. As briefly mentioned in Chapter 5, the distribution functions are reduced with respect

to the rotation and the vibration. The functions are reduced as follows:

$$F_s^{tran} = \int_0^\infty \sum_{i=0}^{\infty} f_s \, dI \qquad F_s^{rot} = \int_0^\infty I \sum_{i=0}^{\infty} f_s \, dI \qquad F_s^{vib} = \int_0^\infty \sum_{i=0}^{\infty} i \frac{k_B}{m_s} \theta_{v_s} f_s \, dI \tag{6.1}$$

leading to a set of governing equations per species s that need to be solved together:

$$\begin{aligned}
\frac{\partial F_s^{tran}}{\partial t} + \underline{u} \cdot \frac{\partial F_s^{tran}}{\partial \underline{x}} &= \frac{1}{\tau}(M_{s_1}^{tran} - F_s^{tran}) + \frac{1}{Z_r \tau}(M_{s_2}^{tran} - M_{s_1}^{tran}) + \frac{1}{Z_v \tau}(M_{eq_s}^{tran} - M_{s_2}^{tran}) \\
\frac{\partial F_s^{rot}}{\partial t} + \underline{u} \cdot \frac{\partial F_s^{rot}}{\partial \underline{x}} &= \frac{1}{\tau}(M_{s_1}^{rot} - F_s^{rot}) + \frac{1}{Z_r \tau}(M_{s_2}^{rot} - M_{s_1}^{rot}) + \frac{1}{Z_v \tau}(M_{eq_s}^{rot} - M_{s_2}^{rot}) \\
\frac{\partial F_s^{vib}}{\partial t} + \underline{u} \cdot \frac{\partial F_s^{vib}}{\partial \underline{x}} &= \frac{1}{\tau}(M_{s_1}^{vib} - F_s^{vib}) + \frac{1}{Z_r \tau}(M_{s_2}^{vib} - M_{s_1}^{vib}) + \frac{1}{Z_v \tau}(M_{eq_s}^{vib} - M_{s_2}^{vib}),
\end{aligned} \tag{6.2}$$

where the corresponding equilibrium functions are:

$$\begin{aligned}
M_{s_1}^{tran} &= \frac{n_s}{\left(2\pi(k/m_s)\hat{T}\right)^{3/2}} \exp\left(-\frac{m_s(\underline{u} - \underline{u}_s^{(g)})^2}{2k\hat{T}}\right); \\
M_{s_1}^{rot} &= \frac{kT_{r_s}}{m_s} M_{s_1}^{tran}; \qquad M_{s_1}^{vib} = \frac{\delta_s(T_{v,s})}{2} \frac{k}{m_s} T_{v,s} M_{s_1}^{tran}
\end{aligned} \tag{6.3}$$

The second intermediate function reduces to:

$$\begin{aligned}
M_{s_2}^{tran} &= \frac{n_s}{(2\pi(k/m_s)T_{tr})^{3/2}} \exp\left(-\frac{m_s(\underline{u} - \underline{u}_0)^2}{2kT_{tr}}\right); \\
M_{s_2}^{rot} &= \frac{kT_{tr}}{m_s} M_{s_2}^{tran}; \qquad M_{s_2}^{vib} = \frac{\delta_s(T_{v,s})}{2} \frac{k}{m_s} T_{v,s} M_{s_2}^{tran}
\end{aligned} \tag{6.4}$$

The final equilibrium function reduces to:

$$\begin{aligned}
M_{eq_s}^{tran} &= \frac{n_s}{(2\pi(k/m_s)T)^{3/2}} \exp\left(-\frac{m_s(\underline{u} - \underline{u}_0)^2}{2kT}\right); \\
M_{eq_s}^{rot} &= \frac{kT}{m_s} M_{eq_s}^{tran}; \qquad M_{eq_s}^{vib} = \frac{\delta_s(T)}{2} \frac{k}{m_s} T M_{eq_s}^{tran}
\end{aligned} \tag{6.5}$$

Further to this reduction and similar to the monoatomic solver for gas mixtures, these functions can be further reduced with respect to the $w-$ velocity, since for the two-dimensional setup the mean velocity $w_0 = 0$. This is done by the same approach as in Chapter 3, reducing the distribution functions to a translational G_s component and thermal energy H_s component following:

$$G_s = \int_{-\infty}^{\infty} F_s \, dw \qquad H_s = \int_{-\infty}^{\infty} w^2 F_s \, dw, \tag{6.6}$$

where all distribution functions are reduced translationally, while the thermal component is required only for the kinetic part of the energy equation associated with the first of the set of governing equations in Eq. (6.2). The new and final form of the governing equations is:

$$\begin{aligned}
&\frac{\partial G_s^{tran}}{\partial t}+\underline{u}\cdot\frac{\partial G_s^{tran}}{\partial \underline{x}}=\frac{1}{\tau}(G_{s_1}^{tran}-G_s^{tran})+\frac{1}{Z_r\tau}(G_{s_2}^{tran}-G_{s_1}^{tran})+\frac{1}{Z_v\tau}(G_{eq_s}^{tran}-G_{s_2}^{tran})\\
&\frac{\partial G_s^{rot}}{\partial t}+\underline{u}\cdot\frac{\partial G_s^{rot}}{\partial \underline{x}}=\frac{1}{\tau}(G_{s_1}^{rot}-G_s^{rot})+\frac{1}{Z_r\tau}(G_{s_2}^{rot}-G_{s_1}^{rot})+\frac{1}{Z_v\tau}(G_{eq_s}^{rot}-G_{s_2}^{rot})\\
&\frac{\partial G_s^{vib}}{\partial t}+\underline{u}\cdot\frac{\partial G_s^{vib}}{\partial \underline{x}}=\frac{1}{\tau}(G_{s_1}^{vib}-G_s^{vib})+\frac{1}{Z_r\tau}(G_{s_2}^{vib}-G_{s_1}^{vib})+\frac{1}{Z_v\tau}(G_{eq_s}^{vib}-G_{s_2}^{vib})\\
&\frac{\partial H_s^{tran}}{\partial t}+\underline{u}\cdot\frac{\partial H_s^{tran}}{\partial \underline{x}}=\frac{1}{\tau}(H_{s_1}^{tran}-H_s^{tran})+\frac{1}{Z_r\tau}(H_{s_2}^{tran}-H_{s_1}^{tran})+\frac{1}{Z_v\tau}(H_{eq_s}^{tran}-H_{s_2}^{tran}),
\end{aligned} \tag{6.7}$$

Therefore, the solver uses in total eight governing equations: four for each species. The macroscopic variables are then found by taking moments of the reduced non-equilibrium distribution functions: G_s^{tran}, G_s^{rot}, G_s^{vib} and H_s^{tran}: The macroscopic variables are found as moments of the reduced distribution functions, similarly to the monoatomic solver, finding ρ_s, u_s, T_{tran_s}, T_{r_s} and T_{v_s} from which u_0, $u_s^{(g)}$, $\hat{T}$, T_{tr} and T are expressed. The required moments are:

$$\begin{aligned}
\rho_s &= \iiint_{-\infty}^{\infty} F_s^{tran}\,dudvdw=\iint_{-\infty}^{\infty} G_s^{tran}\,dudv\\
u_s &= \frac{1}{\rho_s}\iint_{-\infty}^{\infty} uG_s^{tran}\,dudv\ ; \qquad v_s=\frac{1}{\rho_s}\iint_{-\infty}^{\infty} vG_s^{tran}\,dudv\\
T_{tran_s} &= \frac{1}{3}\frac{m_s}{\rho_s k_B}\iint_{-\infty}^{\infty}(u^2+v^2)G_s^{tran}\,dudv+\frac{1}{3}\frac{m_s}{\rho_s k_B}\iint_{-\infty}^{\infty} H_s^{tran}\,dudv-\frac{1}{3}\frac{m_s}{k_B}(u_s^2+v_s^2)\\
T_{r_s} &= \frac{m_s}{\rho_s k_B}\iiint_{-\infty}^{\infty} F_s^{rot}\,dudvdw=\frac{m_s}{\rho_s k_B}\iint_{-\infty}^{\infty} G_s^{rot}\,dudv\\
T_{v_s} &= \frac{m_s}{\rho_s k_B}\frac{2}{\delta_s(T_{v_s})}\iiint_{-\infty}^{\infty} F_s^{vib}\,dudvdw=\frac{m_s}{\rho_s k_B}\frac{2}{\delta_s(T_{v_s})}\iint_{-\infty}^{\infty} G_s^{vib}\,dudv,
\end{aligned} \tag{6.8}$$

where the expression for T_{v_s} contains $\delta_s(T_{v_s})$ and an iterative procedure is needed to obtain T_{v_s}. The resulting quasi-two-dimensional functions reduce the computational expense and complexity of the diatomic mixture solver.

6.1.4 Dimensionless Form

The non-dimensionalisation and reference values are summarised here. For the diatomic mixture model including vibrational excitation, the gases in the mixture need to be defined in terms of their respective characteristic temperature, required for the calculation of the number of vibrational degrees of freedom. The focus in the thesis is on air and Therefore, the mixture consists of nitrogen with characteristic temperature $\theta_{v_1} = 3371K$ and oxygen with $\theta_{v_2} = 2256K$. The mass ratio $\beta = m_2/m_1 = 1.14$. The most probable speed u_{ref} for the lighter gas (nitrogen) is used to scale all velocities. The reference values are denoted with ref and are:

$$
\begin{aligned}
u_{ref} &= \sqrt{2kT_{ref}/m_1}, \\
\rho_{ref} &= n_{ref} m_1, \\
G_{tran_{ref}} &= \frac{n_{ref}}{u_{ref}^2} = \frac{n_{ref}}{2kT_{ref}/m_1} \\
G_{rot_{ref}} &= n_{ref} \\
G_{vib_{ref}} &= n_{ref} \\
H_{ref} &= n_{ref} \\
L_{ref} &= \frac{u_{ref}}{t_{ref}} = \frac{u_{ref}}{\tau_{ref}} = \frac{u_{ref}\mu_{ref}}{p_{ref}}.
\end{aligned}
\tag{6.9}
$$

Note that for a hard sphere model, the molecular potential is $\omega = 0.5$ and the expression for the viscosity is:

$$
\mu_{ref} = \frac{5}{16}\lambda_{ref}\rho\sqrt{\frac{2\pi kT}{m_{mix}}}, \tag{6.10}
$$

where the mass of the mixture $m_{mix} = \rho/n$ and the ratio between the kinetic reference length L_{ref} and the mean free-path λ_{ref} is now easily found. It is an important ratio when comparing with the results from DSMC.

6.1.5 Normalised Values

Similar to the results from the monoatomic simualtions, the macroscopic quantities presented for the shock wave are normalised following Kosuge's approach [9] from both the kinetic model and DSMC, where y is the macroscopic variable, Y_- is the pre-shock value of y and Y_+ is post-shock:

$$
\tilde{y} = \frac{y - Y_-}{Y_+ - Y_-}. \tag{6.11}
$$

Note that the tilde is omitted from here on for simplicity. Also, the origin of the plots ($X = 0$) is defined at the location where the total number density is exactly half of the sum of the pre-shock and post-shock values.

6.2 Normal Shock

6.2.1 Single Species Normal Shock Wave

The numerical evaluation of the gas mixture kinetic model begins with the evaluation of the profile of a normal shock wave. Before conducting a thorough test with a gas mixture, however, we will first focus briefly on inspecting numerically the collapse of the mixture model to a single-species diatomic model. We demonstrated this property of the model in Chapter 5 theoretically by reducing it not only to a single-species but also to a single-temperature model. Here, we will solely focus on evaluating the model for a single-species but preserving the three-temperatures and the three-step relaxation. The results will demonstrate the separate rotational and vibrational relaxation processes. We will show that under the same initial conditions, properties and species mass for the two gases, the two gases of the mixture are indifferentiable.

We will show that under the same initial conditions for two identical species and with 50% concentration for each species, the macroscopic variables for both gases are identical throughout the shock wave. Note that further to identical initial conditions, concentration and species mass, the characteristic vibrational temperature for both species has been set for one type of gas only, i.e. the same value is used since two identical gases are considered. In this case, we have selected the characteristic vibrational temperature for nitrogen. To initialize the problem, further to the concentration and the Mach number, the free-stream temperature is defined dimensionally to evaluate the number of vibrationally-excited DoF. The translational and rotational DoF are considered fully excited, which is a reasonable assumption for the considered temperature $T_\infty = 288.15K$. Furthermore, the values of the collision coefficients Z_r and Z_v need to be specified before each simulation. As described during the development of the kinetic model, the two coefficients are considered constants and are not temperature-dependent, which is a simplification to be addressed in future work. The free-stream conditions are: Mach number $M_\infty = 3$, $Z_r = 5$, $Z_v = 25$, free-stream temperature $T_\infty = 288.15K$, hard-sphere potential $\omega = 0.5$ for two N_2 gases with a characteristic temperature $\theta_v = 3371K$.

What we expect to find is all species macroscopic variables equal to each other, i.e $n_1 = n_2$, $u_1 = u_2$, $T_{tran_1} = T_{tran_2}$, $T_{r_1} = T_{r_2}$ and $T_{v_1} = T_{v_2}$, since there is no process to separate the two species. In Fig. 6.1 (a) and (b) these properties are inspected, where the solid coloured lines are used to denote species 1 properties and the black dashed lines with the corresponding coloured symbol indicate results for species 2. In (a) the species number density is in red colour, while the species velocity is in green. In (b) the translational temperature is in red, the rotational temperature is in blue and the vibrational temperature in green. This colour convention for the species temperatures is kept throughout the chapter. It is clear that the two species have identical shock profiles and have collapsed into a single species, which was the desired result. This test shows the consistency of the model numerically. Note, in this section we focus on showing the property of the model to reduce to the same species, while the physical phenomenon observed

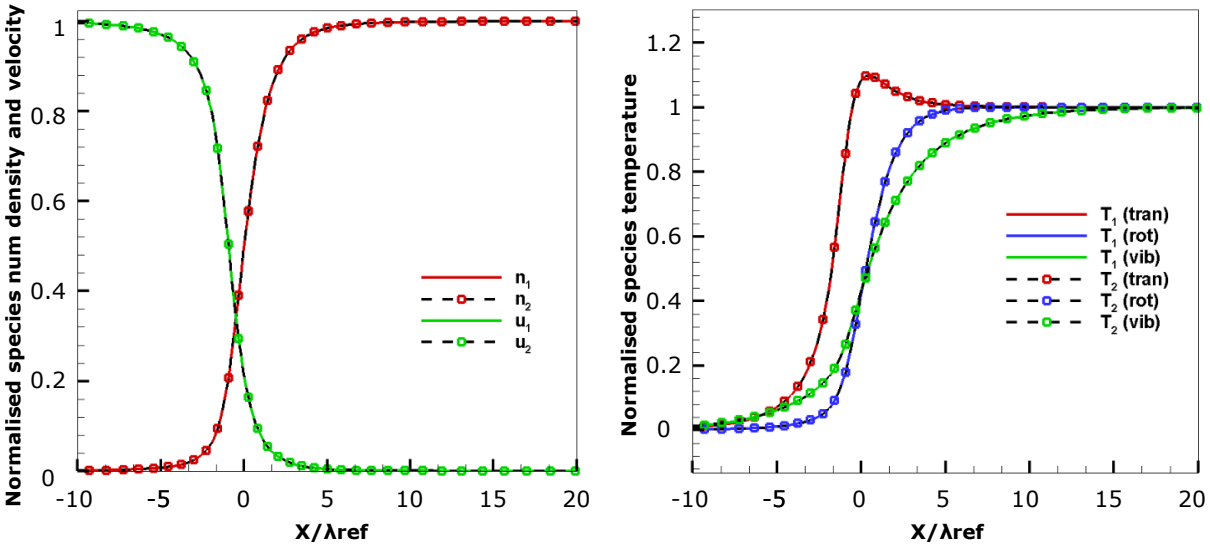

(a) Number density and velocity

(b) Translational, rotational and vibrational temperature

Figure 6.1: Profile of a normal shock wave of a nitrogen gas with a free-stream Mach number 3.0, a mass ratio between species $\beta = 1$ and equal concentration between the species of 50%. Comparison of species macroscopic variables. Results for the species number density and velocity shown in (a), with results translational, rotational and vibrational temperature in (b).

in the results will be discussed in detail in the section concerning the gas mixture.

6.2.2 Gas Mixture Normal Shock Wave: Comparison with DSMC

In this section the diatomic kinetic model is tested for a binary gas mixture. In comparison to the previous section, the effect of diffusion between species is present and the species temperatures can deviate from each other. Further, the characteristic vibrational temperature θ_v is defined per species s to account accurate for the different gas species. Notice that for the practical application of air, the mass ratio between nitrogen and oxygen is quite small ($m_2/m_1 = 1.14$) and is not significant enough to create a big difference between the species in terms of species mean velocities. The non-equilibrium caused by the species mass difference, which we observed in the monoatomic mixture in Chapter 3, is not a dominant effect here. Of course for different gases, e.g. a mixture of hydrogen and nitrogen with mass ratio of 14, the diffusion effect will become very important. Another case where the species diffusion becomes important is when the mixture of a diatomic and monoatomic gas is often considered, which will create in most cases significant mass ratios. For a chemically reacting air, a five-species gas mixture is typically considered with elements N_2, O_2, NO, N and O and therefore a mass ratio of 2 is present. In this case also only some of the gases have rotational and vibrational degrees of freedom and temperatures, while the atoms will have all of their energy stored in the kinetic and translational components. Example application is the atmosphere of different planets beyond the Earth, e.g. Saturn and Jupiter with mostly hydrogen and helium constituents. Therefore, there are a number

of cases in which the diffusion of the gas mixture is significant. At present, the new model can model binary mixture of diatomic gases only. However, when modelling air as a gas mixture the different level of vibrational excitation for each species has the greatest impact on the flow-field. This is due to the different characteristic vibrational temperatures for nitrogen and oxygen. It leads to different expressions for each species equilibrium function and separation between the species. We will focus our attention on demonstrating this difference through the results for the species translational, rotational and vibrational temperatures.

The pre-shock conditions are evaluated at a temperature T_∞ for which the vibrational excitation is negligible, i.e. $T_\infty = 288.15K$, while in comparison the characteristic temperatures for the two gases are $\theta_{v_1} = 3371K$ and $\theta_{v_2} = 2256K$. Throughout the shock, however, the number of excited vibrational DoF, which is a non-integer value changes with the rise in the temperature. The normal shock, reducing the speed to subsonic flow behind it, leads to a jump in the internal energy of the flow, represented by the jump in temperature. Since vibration is present, it absorbs part of the internal energy and the temperature is not as high as for the perfect gas jump. This leads to an increase in the density (and density jump) behind the shock [25].

The information detailed in Table 6.1 describes the initial conditions for the computation of a normal shock for a diatomic gas mixture, including the Mach number, concentration ratio of the two gases, the collision coefficients for rotation and vibration. All other variables are not changed through the simulations, e.g. the free-stream temperature $T_\infty = 288.15K$, the two gas mixture components N_2 and O_2 and their characteristic temperatures. The results from the kinetic model are compared and validated against DSMC simulations under the same conditions. The DSMC simulations and results are provided by Craig White. The DSMC solver used is dsmcFoam+ [124], similar to the monoatomic gas comparison for the circular cylinder. The hard-sphere potential is used for simplicity with $\omega = 0.5$ as in the kinetic model. The number of DSMC particles in steady state are 2.7 million for $M_\infty = 3$ and increase to 3.6 million for the higher Mach number $M_\infty = 5$, with a minimum of 25 particles in each cell. The number of samples in steady state are 35000 and the spatial grid contains 40000 cells. Each point in the results is an average of 80 cells, bringing the resolution to 500 evenly spaced bins for all simulations.

The validation with DSMC allows for a very accurate assessment of the validity of the kinetic model. This is due to the fact that further to initialising the flow with the same initial conditions, including the free-stream temperature, we can also set up constant and identical collision coefficients Z_r and Z_v for both solvers. Currently, available results in the literature do not allow for the same level of comparison, e.g. [31], since the initialisation of the problem is not identical and the collision numbers Z_r and Z_v are not constants typically in the literature.

The jump in the species number density and the mixture number density is shown in Fig. 6.2. The results from DSMC are presented with elements, squares for species 1, triangles for species 2 and circles for the mixture value, while the kinetic model has red lines for species 1, blue for species 2 and green for the mixture values. The number densities are not normalised. It

M_∞	n_1/n	Z_r	Z_v
3	0.8	5	25
3	0.8	5	100
5	0.8	5	25
5	0.8	5	100
5	0.5	5	25

Table 6.1: Test case conditions for a normal shock wave for a diatomic gas mixture

is easier to inspect the results without the normalisation due to the small mass ratio between species and consequent small variation of the normalised results. This also allows us to appreciate the different jump in density for initial velocity or concentration variations. Three cases are shown: $M_\infty = 3$, nitrogen to oxygen concentration 80:20 denoted with $n_1/n = 0.8$ in Fig. 6.2 (a), $M_\infty = 5$, $n_1/n = 0.8$ in Fig. 6.2 (b) and $M_\infty = 5$, $n_1/n = 0.5$ in Fig. 6.2 (c). Further, only results for the vibrational collision coefficient $Z_v = 25$ are shown. Notice that the different coefficients will not lead to a different jump condition and even though it influences the vibrational degrees of freedom and temperatures through the internal part of the shock wave, it has a small effect on the number density. What we observe when we plot the same results for $Z_v = 100$ is almost identical number densities, with the profile of the shock slightly less steep. Notice that even though the mass ratio between the two species is very small, the nitrogen reacts first to the shock wave, since it is the lighter gas. We observe that the number density n_1 (in red) is the first to start rising through the shock, which is consistent with the monoatomic mixture model results.
The jump for the same Mach number ($M_\infty = 5$) but with different concentrations is of similar value, but is not identical as we see when comparing Fig. 6.2 (b) and (c). Having less nitrogen present in (c) leads to a higher jump in number density, since more of the internal energy is absorbed by the easier to excite the vibrational mode for oxygen, which comprises 50% of the gas here. This leads to a lower jump in mixture temperature and higher number density jump, consistent with the discussion earlier in this section and with the literature [25].
Overall, we observe excellent agreement between the results from the diatomic kinetic model and DSMC for all cases. The number densities profiles are mostly identical from the two solvers with only a small difference observed at the second part of the shock. We believe this is caused by the small variation between vibrational temperatures between the results acquired by DSMC and the kinetic model, discussed further when the species temperatures are plotted. Next, the species translational, rotational and vibrational temperatures are plotted and compared with DSMC for all 5 cases defined in Table 6.1. Figure 6.3 (a) and (b) show the profile of the normal shock at Mach number $M_\infty = 3$, 80% N_2 concentration and two different vibrational collision coefficients $Z_v = 25$ and $Z_v = 100$. Figure 6.4 (a) and (b) has the same comparison, but for a higher Mach number $M_\infty = 5$, 80% N_2 concentration and two different vibrational collision coefficients $Z_v = 25$ and $Z_v = 100$. Last, in Fig. 6.5 the focus is on a different concentration with 50% N_2 and 50% O_2 at $M_\infty = 5$ and $Z_v = 25$. The translational temperatures are in red, rotational

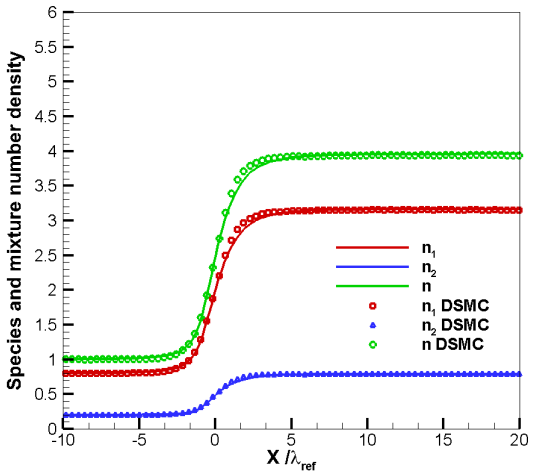

(a) $M_\infty = 3$, $n_1/n = 0.8$

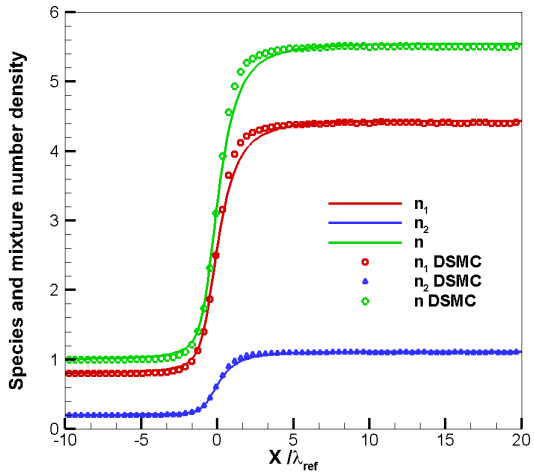

(b) $M_\infty = 5$, $n_1/n = 0.8$

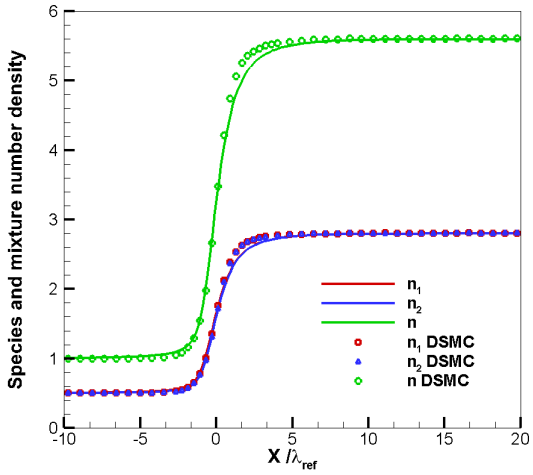

(c) $M_\infty = 5$, $n_1/n = 0.5$

Figure 6.2: Profile of a normal shock wave of a gas mixture consisting of nitrogen and oxygen. Comparison of species number density and the mixture number density between the diatomic kinetic model and DSMC results under different conditions: $M_\infty = 3$, $n_1/n = 0.8$ in (a), $M_\infty = 5$, $n_1/n = 0.8$ in (b) and $M_\infty = 5$, $n_1/n = 0.5$ in (c).

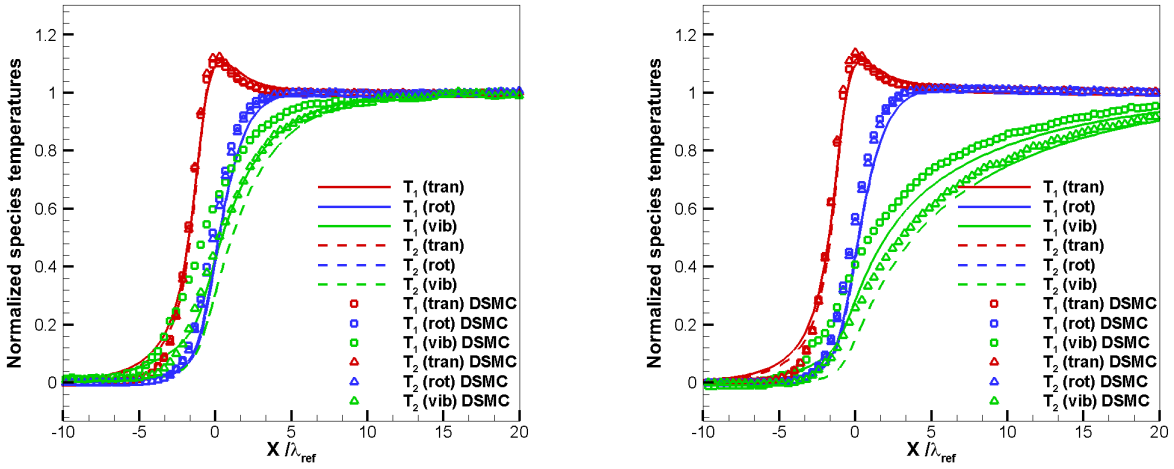

(a) $M_\infty = 3$, $Z_v = 25$, $n_1/n = 0.8$ (b) $M_\infty = 3$, $Z_v = 100$, $n_1/n = 0.8$

Figure 6.3: Profile of a normal shock wave of a gas mixture of nitrogen and oxygen with a free-stream Mach number 3.0 and concentration between the species of 80% N_2 and 20% O_2 .Comparison of species translational, rotational and vibrational temperatures. Results for the collision number $Z_v = 25$ are shown in (a) and for $Z_v = 100$ in (b).

in blue and vibrational temperatures in green for all temperature plots. The kinetic model results are with solid lines for species 1 (nitrogen) and dashed lines for species 2 (oxygen), while the results by acquired with DSMC are presented with symbols and more specifically squares for species 1 and triangles for species 2. All temperatures are normalised, i.e. leading to a value of 0 at pre-shock and 1 at post-shock conditions, respectively.

We observe a good agreement between the results from the kinetic model and DSMC for the structure of the shock. Overall the profile of each temperature jump is steeper when the Mach number is increased and therefore the number of mean free paths for the temperatures to equilibrate post-shock is bigger for the smaller Mach number $M_\infty = 3$, similarly to the monoatomic gas mixture. The translational temperatures for both species have longer upstream tails for the kinetic model in comparison to DSMC. This is a classical characteristic of all BGK-based models for both monoatomic (as observed also in Chapter 3) and diatomic gases. This known disadvantage of BGK models can be avoided if the relaxation time was dependent on the molecular velocity. Another known phenomena that can also be seen here is the overshoot of the translational temperature in all figures, similar to the results from the monoatomic gas mixture. The rotational temperatures lag behind the translational and are excited more slowly with respect to the translational temperatures. For all cases the collisional coefficient $Z_r = 5$ and therefore the rotation's lag is identical for each case. The same is not true for the vibrational temperatures. The change from $Z_v = 25$ in (a) to $Z_v = 100$ in (b) in both Fig. 6.3 and Fig. 6.4 is very significant. The slope of the vibrational temperatures for the bigger Z_v is much more gradual in comparison to the the smaller value. The change between the two Z_v values leads to approximately 15 mean

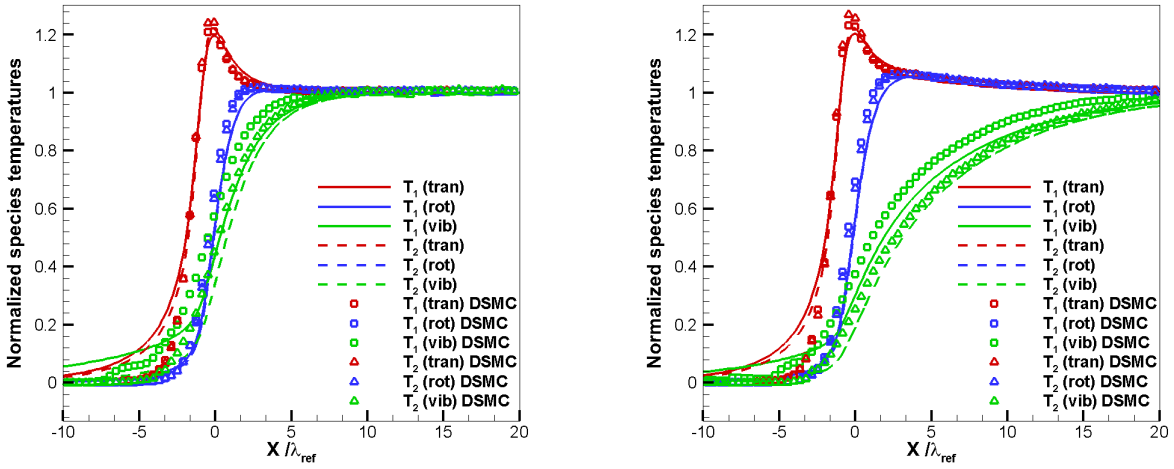

(a) $M_\infty = 5$, $Z_v = 25$, $n_1/n = 0.8$ (b) $M_\infty = 5$, $Z_v = 100$, $n_1/n = 0.8$

Figure 6.4: Profile of a normal shock wave of a gas mixture of nitrogen and oxygen with a free-stream Mach number 5.0 and concentration between the species of 80% N_2 and 20% O_2 .Comparison of species translational, rotational and vibrational temperatures. Results for the collision number $Z_v = 25$ are shown in (a) and for $Z_v = 100$ in (b).

free paths (where λ_{ref} is evaluated at free-stream conditions) difference for the vibrational temperature to reach the equilibrium post-shock temperature for the $M_\infty = 5$ case and approximately 20 mean free paths for the $M_\infty = 3$ case. Moreover, the slope of the rotational temperatures is steeper than the vibrational temperatures, while the translational temperatures have the steepest slope. All of these phenomenon are consistent with non-equilibrium thermodynamics and physical observations.

However, we notice that both the kinetic model and the results for DSMC show that upstream of the shock the vibrational temperatures are not lagging behind the other temperatures. In particular, species 1, which is leading even the translational temperatures. Such a result is surprising, but can be observed in the results by the more detailed General Boltzmann equation (GBE) [31]. Even though further work is required to justify this phenomenon, it is not considered a drawback introduced by the new kinetic model, since it observed by the DSMC and GBE results.

The assumption for a constant Z_v throughout the shock and its value is too big pre-shock, where the free-stream temperature suggest no vibrational excitation. It is also possible that the values post-shock are too low, especially for the case of $Z_v = 25$. It is clear the assumption of a constant Z_v is a simplification, which is reasonable for initial method/ solver development that should be improved upon and addressed in future work.

Until now we were focused on the different types of temperatures. If we turn our attention to the species differences we observe that species 1 (nitrogen) and 2 (oxygen) for both translational and rotational temperatures differ very little for both the kinetic model and DSMC. This is consistent through the different Mach numbers and concentrations. Certainly increasing the mass ratio be-

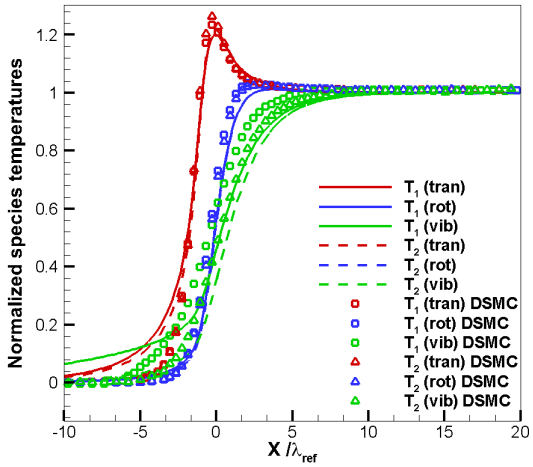

Figure 6.5: Profile of a normal shock wave of a gas mixture of nitrogen and oxygen with a free-stream Mach number 5.0 and concentration between the species of 50% N_2 and 50% O_2 .Comparison of species translational, rotational and vibrational temperatures. Results for the collision number $Z_v = 25$.

tween species will separate the same type of temperature between the two species (specifically the translational and rotational temperatures), as observed for the translational temperature in the monoatomic mixture [88, 112]. The difference between species vibrational temperature is larger, in comparison to the difference between species for the other two types of temperatures, even for the small mass ratio considered here. The number of vibrationally-excited DoF between the oxygen and nitrogen gases is also different, which is a key emphasize of the model. This is due to the different species characteristic vibrational temperatures. It is highly likely that for a species and temperature dependent Z_{v_s} this difference will be more pronounced. Notice that having similarly a species Z_{r_s} for the rotational collision coefficient will separate the two rotational temperatures. Here we observe the biggest difference between the kinetic model and DSMC: in the vibrational temperatures and even here the two numerical models still show good agreement.

This discussion of the results shows that the kinetic model and DSMC results follow the same physical trends, as well as some of the limitations of the current assumptions. It demonstrates that the model itself provides accurate results for the macroscopic variables under strong non-equilibrium conditions, i.e. as created by $M_\infty = 5$ normal shock conditions. The validation and evaluation of the model beyond $M_\infty = 5$ needs further study. Future work will include more and varied numerical cases and further comparison with existing methods, but for now the numerical validation of the diatomic kinetic model for gas mixtures is considered completed and successful.

From here on, the physics of the flow will be investigated further. The vibrational degrees of freedom through the shock are considered. At the considered temperatures, the translational and

rotational degrees of freedom are considered fully excited. In contrast, the vibrational degrees of freedom are species- and temperature-dependent. In Fig. 6.6 the values of the vibrational degrees of freedom $\delta_s(T_{v_s})$ are plotted through the jump for each species s. The results for nitrogen as species 1 are with a solid line and the results for oxygen as species 2 are with a dashed line. To distinguish between the different vibrational collision numbers Z_v, the results for $Z_v = 25$ are solely lines, while results for $Z_v = 100$ have square elements through the lines. Figure 6.6 (a) shows results for $M_\infty = 3$ and concentration ratio 80% : 20% N_2 vs O_2 in red lines, Fig. 6.6 (b) has the same concentration ratio but for a higher Mach number $M_\infty = 5$ in green and Fig. 6.6 (c) shows in blue a variation in concentration with equal parts nitrogen and oxygen at $M_\infty = 5$.
At the specified free-stream temperature, pre-shock values are expected to be negligible. With the rise in temperature through the shock wave, the number of vibrational DoF increase. The non-integer values of $\delta(T)$ in the pre-shock flow-field are close to 0, increase through the shock and reach maximum values post-shock. This maximum value depends on the temperature jump, but asymptotically approaches the value 2 for very high vibrational temperatures. Figure 6.6 shows the values of δ are non-integer values, as expected, and are in the bounds discussed for $\delta(T)$: [0;2). Furthermore, the values of δ for oxygen are much higher than the values of δ for nitrogen for both vibrational collision numbers Z_v. Therefore, we observe that oxygen is more vibrationally-excited than nitrogen at the same temperature, which can be explained from the lower characteristic temperature for O_2. This is consistent with non-equilibrium thermodynamics theory [1, 24, 25, 35]. In Fig. 6.6 (a) and (b) the effect of the larger vibrational collision number $Z_v = 100$ is significant. For the two collision numbers the jump in the value of δ is identical, but for $Z_v = 100$ the slope of the jump is less steep and the number of mean free paths that are required to post-shock equilibrium is much larger than for $Z_v = 25$. Comparing the plots in (a) and (b), it is clear that for larger Mach numbers, the level of excitation of both species is much higher. This is due to the larger temperature jump caused by the $M_\infty = 5$. In contrast, the concentration change in (c) has not really affected the number of vibrational degrees of freedom for either species. The figures demonstrate that there is a significant difference between species in the level of excitation and modelling them separately is important.

6.2.3 Mixture Properties of the Normal Shock Profile

Inspecting the velocity drift between species through the shock demonstrates the importance of having separate species velocity. In Fig. 6.7 the difference between velocities $u_2 - u_1$ is shown for cases when the concentration ratio is 80% N_2 and 20% O_2. The cases considered are $M_\infty = 3$ and $M_\infty = 5$ with vibrational collision numbers $Z_v = 25$ and $Z_v = 100$. The results for $M_\infty = 3$ are in red and for $M_\infty = 5$ are in green, with $Z_v = 25$ displayed with a solid line and $Z_v = 100$ with a dashed line and a symbol. We observe from the figure that the velocity difference does not change when the vibrational coefficient is modified. However, the higher the Mach number, the bigger the velocity difference. This drift velocity will increase with increasing mass ratios

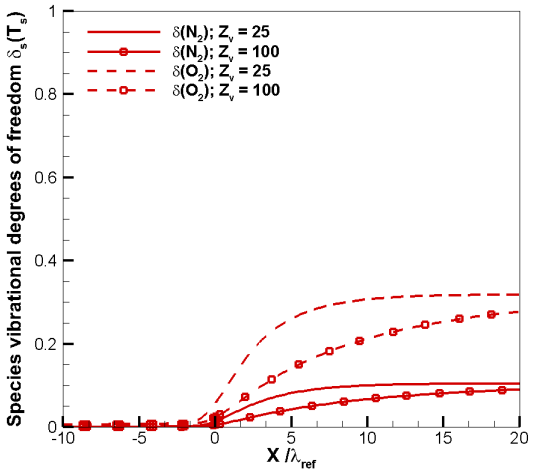

(a) $M_\infty = 3$, $n_1/n = 0.8$;

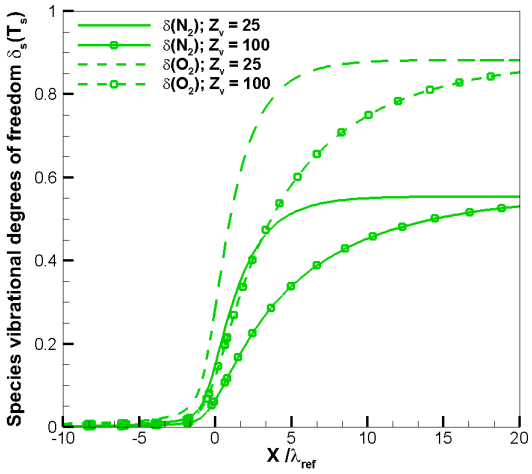

(b) $M_\infty = 5$, $n_1/n = 0.8$

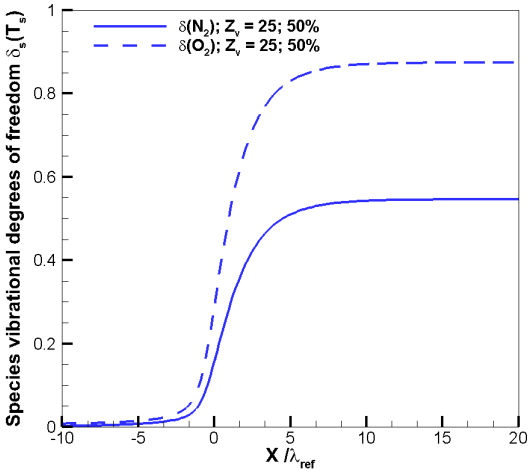

(c) $M_\infty = 5$, $n_1/n = 0.5$

Figure 6.6: Vibrational DoF through a normal shock wave of a gas mixture of nitrogen and oxygen with a free-stream Mach numbers 3.0 and 5.0 and concentration between the species of 80% N_2 and 20% O_2 for the collision numbers $Z_v = 25$ and $Z_v = 100$ in (a) and (b). The vibrational DoF are also evaluated for Mach numbers 5.0, equal species concentration (50%) and $Z_v = 25$ in (c).

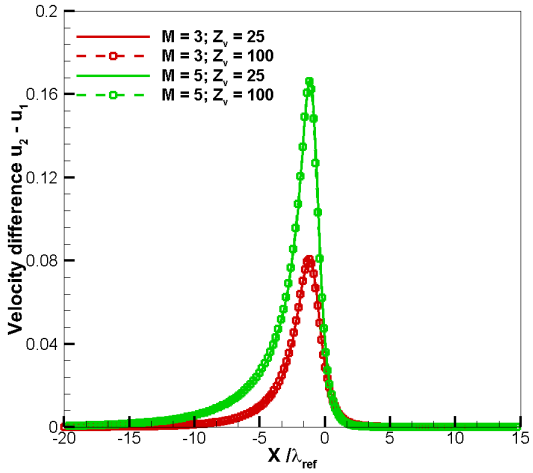

Figure 6.7: Velocity difference through a normal shock wave of a gas mixture of nitrogen and oxygen with a free-stream Mach numbers 3.0 and 5.0 and concentration between the species of 80% N_2 and 20% O_2 for the collision numbers $Z_v = 25$ and $Z_v = 100$.

between species, as it was shown in the parametric study in Chapter 3. It is interesting to compare with the velocity difference $u_2 - u_1$ through the shock for the monoatomic mixture, shown in Fig. 3.7 and Fig. 3.8 (a) in Chapter 3. Figure 3.7 displays a pattern in the lower mass ratios, which is that increasing the mass ratio m_2/m_1 from 2 to 4 is approximately doubling the maximum value of the velocity difference. We know that for a mass ratio of 1, i.e. the species are the same, the difference between velocities is exactly 0. It is hard to predict the value of the velocity difference at $m_2/m_1 = 1.14$ for the monoatomic mixture due to the non-linear response and we expect a velocity difference peak between the values corresponding to $\beta = 0$ and $\beta = 2$. In Fig. 3.8 (a) we observed the change of the velocity difference with the increase of the Mach number at mass ratio 2. Maximum values at $\beta = 2$ for $M_\infty = 3$ is $u_2 - u_1 = 0.3u_{ref}$ and for $M_\infty = 5$ is $u_2 - u_1 = 0.9u_{ref}$ for the monoatomic gas. For the diatomic mixture the maximum values at $\beta = 1.14$ are: at $M_\infty = 3$: $u_2 - u_1 \sim 0.08u_{ref}$ and for $M_\infty = 5$ is $u_2 - u_1 \sim 0.17u_{ref}$, where u_{ref} is the most probable speed for the mixture at free-stream conditions, but is different from the monoatomic mixture value. Qualitatively, the diatomic mixture shows to fit within the bounds of $\beta = 0$ and $\beta = 2$ observed in the results by the monatomic mixture. Note that this discussion is with respect to the corresponding reference velocity u_{ref} for the two kinetic models. No more definitive conclusions can be drawn at this stage for the mass ratio effect on the difference between velocities and comparison between the monoatomic and diatomic mixtures.

6.2.4 Velocity Distribution Functions

Further to the macroscopic variables, the velocity distribution functions reveal interesting facts about the flow-field. There are 4 distribution functions per species: G_s^{tran}, G_s^{rot}, G_s^{vib}, H_s^{tran}.

The flow is initialised with Maxwellian distributions at two different equilibrium positions: pre-shock and post-shock with the corresponding initial macroscopic variables. We observe that their values increase through the shock and reduce after it. The maximum of each distribution function is at the different location, but we have noticed that this physical location matches between species, i.e. X_1 for the maximum value of G^{tran} for nitrogen is the same as X_2 for the maximum value of G^{tran} for oxygen, etc. We have inspected the velocity distribution functions for all test cases and have added a discussion for the differences between them, but have plotted only the case at the highest Mach number $M_\infty = 5$ and the larger vibrational collision number $Z_v = 100$ at $80\% : 20\%$ nitrogen to oxygen concentration ratio in Fig. 6.8 and in Fig. 6.9. In Fig. 6.8 the focus is on comparing the distributions far upstream and far downstream, while Fig. 6.9 shows the behaviour of the distribution functions of the two species through the shock. The pre-shock and post-shock values of the translational, rotational and vibrational distribution functions are shown for the oxygen in Fig. 6.8. Both distributions are Maxwellian and are set by the macroscopic variables defining the shock jump. The pre-shock distribution functions have a sharp peak, which is however low in value in comparison with the post-shock Maxwellian functions. This is due to the higher values of the post-shock macroscopic variables. Here it is important to mention that higher value for the post-shock number density increases the value of distribution function, while high temperature post-shock actually has the opposite effect. We will observe that the first effect seems to dominate here. For this reason the pre-shock values are plotted on a third of the post-shock scale. At the same time, the post-shock distribution functions are more spread out over a larger velocity mesh. This is consistent with theoretical observations: a larger temperature leads to a larger spreading of distribution function. The classical question in applications of kinetic models in DVM solvers for the compromise between velocity bounds (to capture the tails of the post-shock values) and the fine velocity mesh (to capture the sharp spike in the pre-shock values) for the velocity mesh is demonstrated. Through visual observation of the figures, the mesh demonstrates to be adequately selected.

Furthermore, pre-shock values are most prominent for the translational distribution. It has a higher maximum than the rotational and vibrational functions. Notice that the relationship between the reduced translational distribution function and the rotational distribution function, following the expressions in Eq. (6.3) and in non-dimensionalised form $G^{rot} = (T_r/2\beta)G^{tran}$, where T_r is the non-dimensionalised rotational temperature and $\beta = m_2/m_1$ is the mass ratio between species. Since the non-dimensional rotational temperature is taken in the pre-shock as $T_r = T_r(\text{dimensional})/T_\infty = 1$, it follows that $T_r < 2 * \beta$ in the pre-shock then $G^{rot} < G^{tran}$, while post-shock the value of T_r jumps and $G^{rot} > G^{tran}$. Meanwhile, there is no vibrational energy in the pre-shock part of the flow domain. Observe that the colour scale for the vibration is 3 orders of magnitude lower for the purposes of presentation of the figure. The values are approaching zero, consistent with the recognition that no vibrational excitation is present at the pre-shock position. Meanwhile, the biggest pre- and post-shock difference between distribution functions

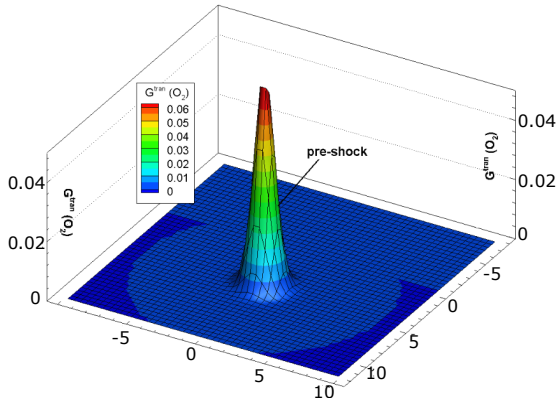

(a) Pre-shock $G^{tran}(O_2)$

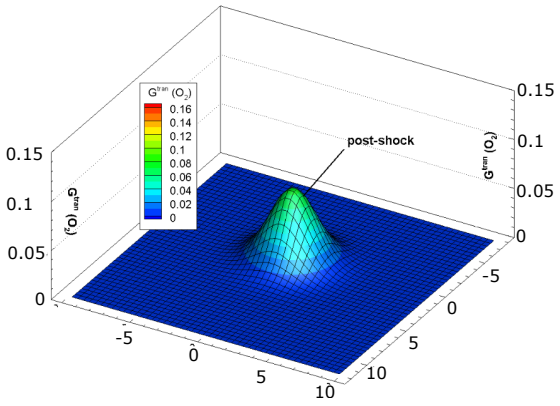

(b) Post-shock $G^{tran}(O_2)$

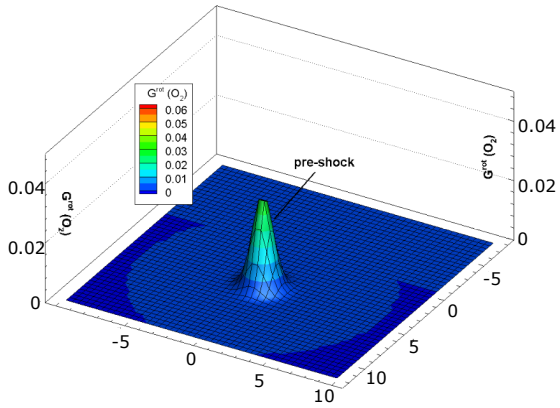

(c) Pre-shock $G^{rot}(O_2)$

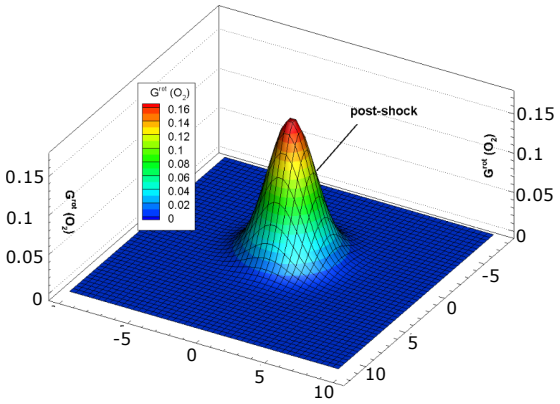

(d) Post-shock $G^{rot}(O_2)$

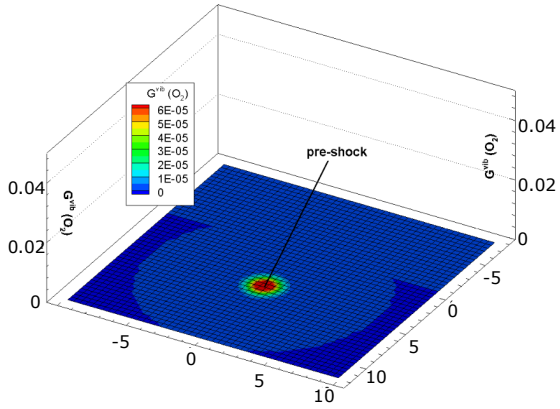

(e) Pre-shock $G^{vib}(O_2)$

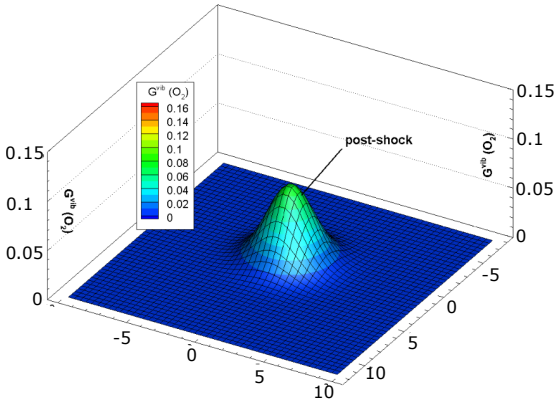

(f) Post-shock $G^{vib}(O_2)$

Figure 6.8: Velocity distribution functions for the case of a normal shock wave of a gas mixture of nitrogen and oxygen with a free-stream Mach number 5.0, concentration between the species of 80% N_2 and 20% O_2 and vibrational collision number $Z_v = 100$ with pre-shock values in the first column and post-shock values in the second column.

is for the vibrational function $G^{vib}(O_2)$, with the highest jump in values of 3 orders in magnitude. The vibrational distribution function is significantly affected by the choice of free-stream temperature. Fig. 6.8 (e) would have a more pronounced peak and shape in the pre-shock for $T_\infty = 1000K$ for example. This selection would also affect the post-shock value dramatically. In Fig. 6.9 the distribution functions for both species: nitrogen (first column) and oxygen (second column) half-way through the shock are shown. The first observation is that the distribution is non-Maxwellian. It has some features of both the pre-shock and post-shock distributions and the transition between them. The values for nitrogen are expectedly higher than the values for the oxygen due to the 4-times higher concentration of nitrogen (i.e. number density multiplied of the distribution), while the shape of the distributions is identical between species. Notice that due to the lower value of excited vibrational degrees of freedom $\delta(N_2)$ as shown in Fig. 6.6 (c), the distribution function of the nitrogen is expected to have lower value of the peak. However, this is compensated by the higher levels of concentration. A clear bimodal behaviour can be observed in Fig. 6.6 (e) and (f) for the two species, suggesting that for $M_\infty = 5$ two most probable velocities can be identified. These two velocities are usually closely related to the pre- and post-shock mean values.

We observe that the maximum values of the distribution functions for the nitrogen gas are higher. This is due to the higher concentration of species 1 in the mixture for the case with $80\% : 20\%$ ratio of nitrogen to oxygen concentration. Furthermore, the displayed results for the distribution functions at $Z_v = 100$ are very close to the values for the lower vibrational collision number $Z_v = 25$. The maximum of the vibrational distribution function G_s^{vib} is achieved further downstream relative for the other distribution functions at $Z_v = 100$, which is consistent with the findings for the macroscopic variables. This is apparent by inspecting the mid-shock value of the distribution functions and compare it with equivalent post-shock distribution function. The maximum value of the translational distribution function is of the same order of magnitude mid-shock and post-shock. The rotational distribution function is 1 order of magnitude smaller mid-shock then post-shock, while the vibrational distribution is at 2 orders of magnitude smaller mid-shock in comparison to the maximum value post-shock. Therefore, the effect of the different relaxation rate of translation, rotation and vibration can be observed in the velocity distribution functions.

Next, comparing the two Mach numbers $M_\infty = 3$ and $M_\infty = 5$, shows that the translational distribution function for both species G_s^{tran} reaches much larger values at $M_\infty = 3$ through the shock, while all other velocity distribution functions: G_s^{rot} and G_s^{vib} have lower maximum values for the lower Mach. Bigger portion of the energy is transformed into internal energy at $M_\infty = 5$ and the effect of the excited vibrational degrees of freedom is more prominent.

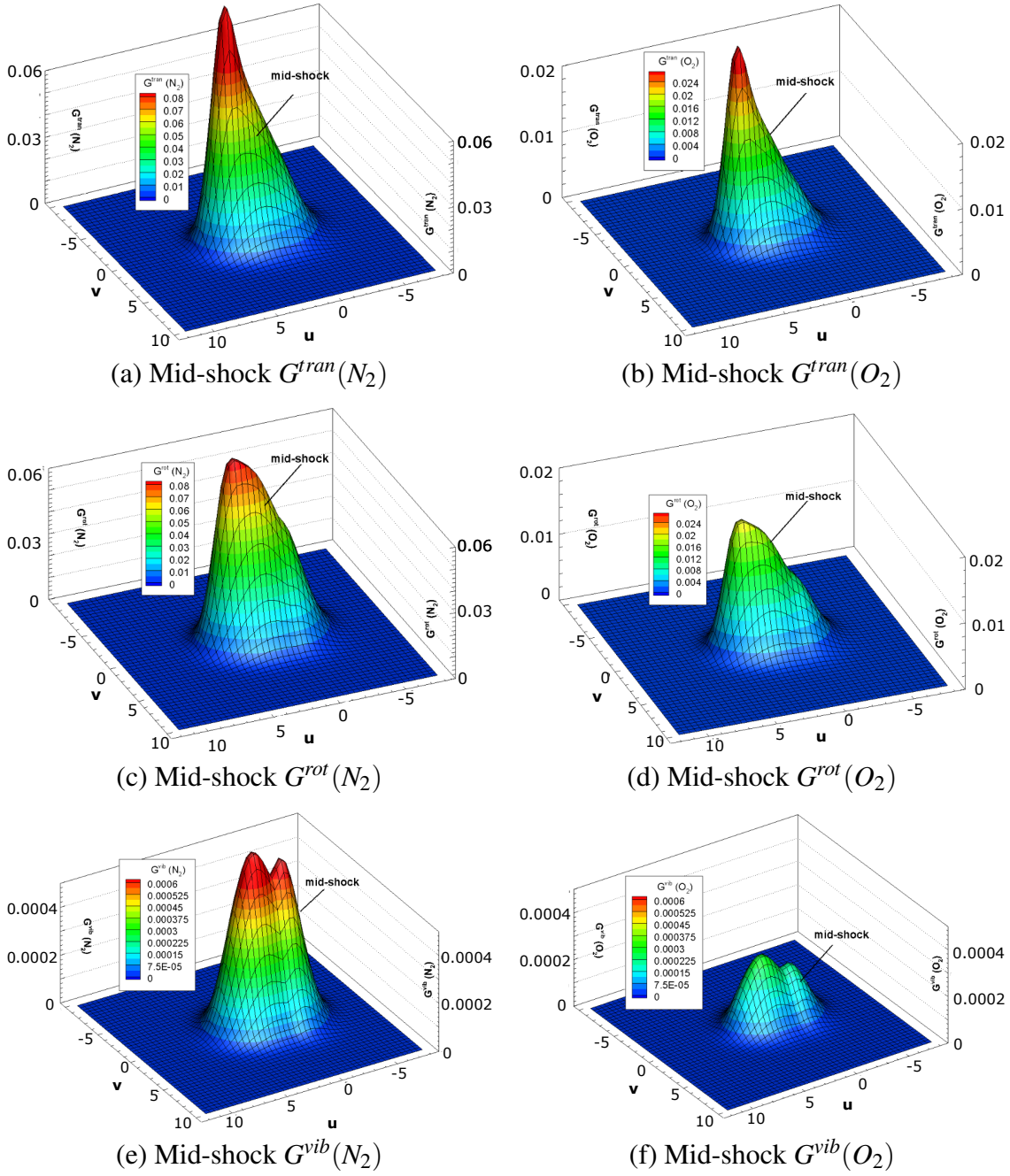

(a) Mid-shock $G^{tran}(N_2)$ (b) Mid-shock $G^{tran}(O_2)$

(c) Mid-shock $G^{rot}(N_2)$ (d) Mid-shock $G^{rot}(O_2)$

(e) Mid-shock $G^{vib}(N_2)$ (f) Mid-shock $G^{vib}(O_2)$

Figure 6.9: Velocity distribution functions through the shock for the case of a normal shock wave of a gas mixture of nitrogen and oxygen with a free-stream Mach number 5.0, concentration between the species of 80% N_2 and 20% O_2 and vibrational collision number $Z_v = 100$ with the nitrogen distribution in the first column and the oxygen distribution in the second column.

6.3 Cylinder

In this section the more complex flow past a circular cylinder is considered. This flow is more complex since it is two-dimensional, with fluxes in the x- and y-directions, unlike the profile of a normal shock. Furthermore, it involves a body and therefore boundary conditions need to be considered for the solid wall. Here fully accommodating diffuse-reflection boundary condition is used. The considered flow field forms a curved shock, incorporating the physics of a normal shock on the stagnation streamline and of an oblique shock with varying shock angles away from stagnation line. This test case is often considered, since the bow shock that appears is of practical application for high-speed vehicles, e.g. re-entry flows.
The flow around a cylinder was previously used as a validation test case for the monoatomic kinetic models for gas mixtures, where it was compared with DSMC results, acquired by Craig White. In this section, the focus is on applying the diatomic kinetic mixture model for this 2-D geometry, inspecting the physics of the flow and the macroscopic variables. Further validation tests for the new kinetic model beyond the profile of a normal shock, presented in this Chapter, form part of the future work. The numerical setup is described in the beginning of the Chapter and the boundary conditions are similarly to Chapter 3, with the main difference of having to consider the rotational and vibrational distribution functions at the wall, which was previously not required. For the rotation and vibration-related governing equations, the corresponding Maxwellian distribution is defined for the prescribed T_{wall}. Similar setup is used for the initialisation of the flow around a cylinder and the details of the initialisation is summarised in Table 6.2. For a gas mixture, an interesting value to inspect is the velocity drift

M_∞	n_1/n	Z_r	Z_v
3	0.8	5	25
3	0.8	5	100
5	0.8	5	100

Table 6.2: Test case conditions for a flow around a cylinder (diatomic gas mixture)

$u_2 - u_1$ between species. In Fig. 6.10 the velocity difference is shown for the three cases from Table 6.2. The velocity difference is zero in the free-stream (where the gas mixture is still in equilibrium at free-stream conditions), increases through the shock to a maximum value (where the species separate the most between each other) and starts decreasing after the shock (where the species equilibrate to a new common and significantly reduced velocity). The vibrational collision number does not affect the velocities and the plots in (a) and (b) are identical. The finding is consistent with the conclusions for the velocity difference through the normal shock wave in Fig. 6.7. The difference increases significantly for the higher Mach number in Fig. 6.10 (c) where the non-equilibrium effect is stronger. Notice that the maximum difference is at the stagnation line, where a normal shock is formed. The maxima also agree with the peak values of the normal shock profile in Fig. 6.7.

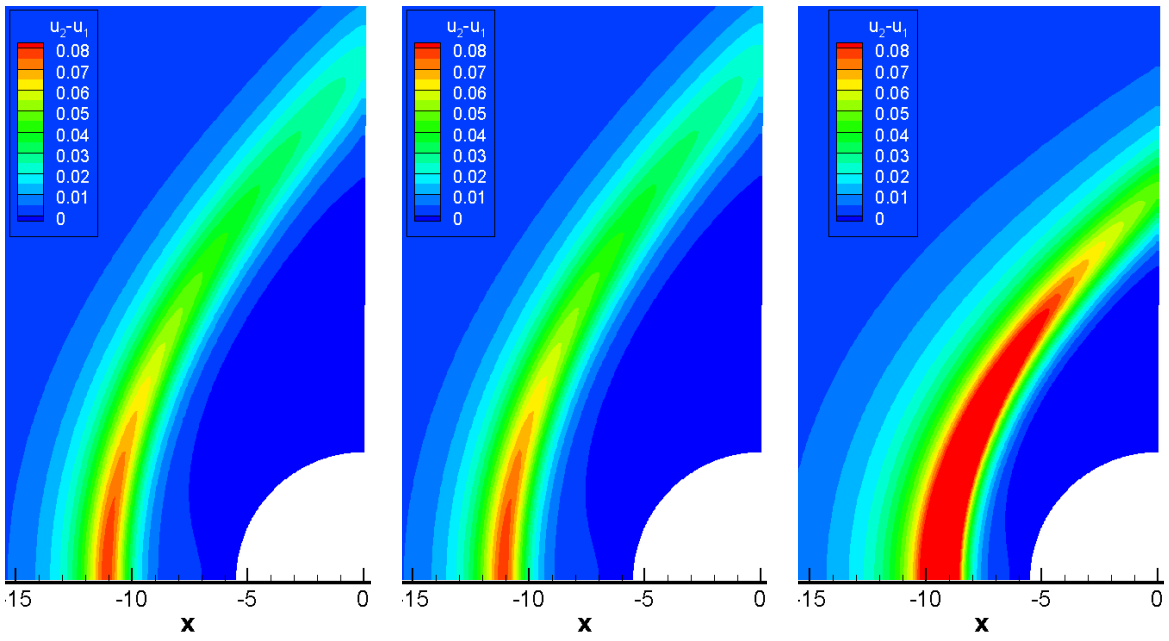

(a) $M_\infty = 3, Z_v = 25$ (b) $M_\infty = 3, Z_v = 100$ (c) $M_\infty = 5, Z_v = 100$

Figure 6.10: Velocity difference between species $u_2 - u_1$ in a binary mixture flow over a cylinder with initial Mach numbers 3 and 5, nitrogen to oxygen concentration 80% : 20%, Knudsen number $Kn = 0.1$ and wall temperature $T_{wall} = 1.5T_\infty$.

The difference between species translation temperatures, species rotational temperatures and species vibrational temperatures follow a similar pattern as the species translational temperatures for the monoatomic gas. Small differences are observed for the different vibrational collision numbers, while higher level of non-equilibrium is brought by the higher Mach number. It is more interesting to inspect the difference between the translational and vibrational temperature. The results are shown in Fig. 6.11 with top figures for species 1 (nitrogen) and bottom figures for species 2 (oxygen). Notice that the colour plots in (c) and (f) are with double the values in the legend, since the difference between the temperatures increases for the high Mach number $M_\infty = 5$. There is a difference between the species. We know that the translational temperatures for the two species are close to each other, while the vibrational temperature deviate between species. Comparing the top and bottom figures in Fig. 6.11 shows the oxygen to have a stronger level of non-equilibrium between the translational and vibrational temperatures for all cases. This is due to the higher level of vibrational excitation of oxygen and the corresponding bigger separation of the vibrational temperature with respect to the translational temperature in comparison to the less vibrationally excited nitrogen.

Furthermore, the vibrational temperature in the case of $Z_v = 25$ in (a) and (d) has the time to develop and reach closer to the value of the translational temperature. However, for the case of $Z_v = 100$ in (b) and (e) the same is not true. The vibrational temperature has a delayed relaxation process and does not approach the value of the translational temperature as closely. As a result the difference between translational and vibrational temperatures is bigger relative to the case

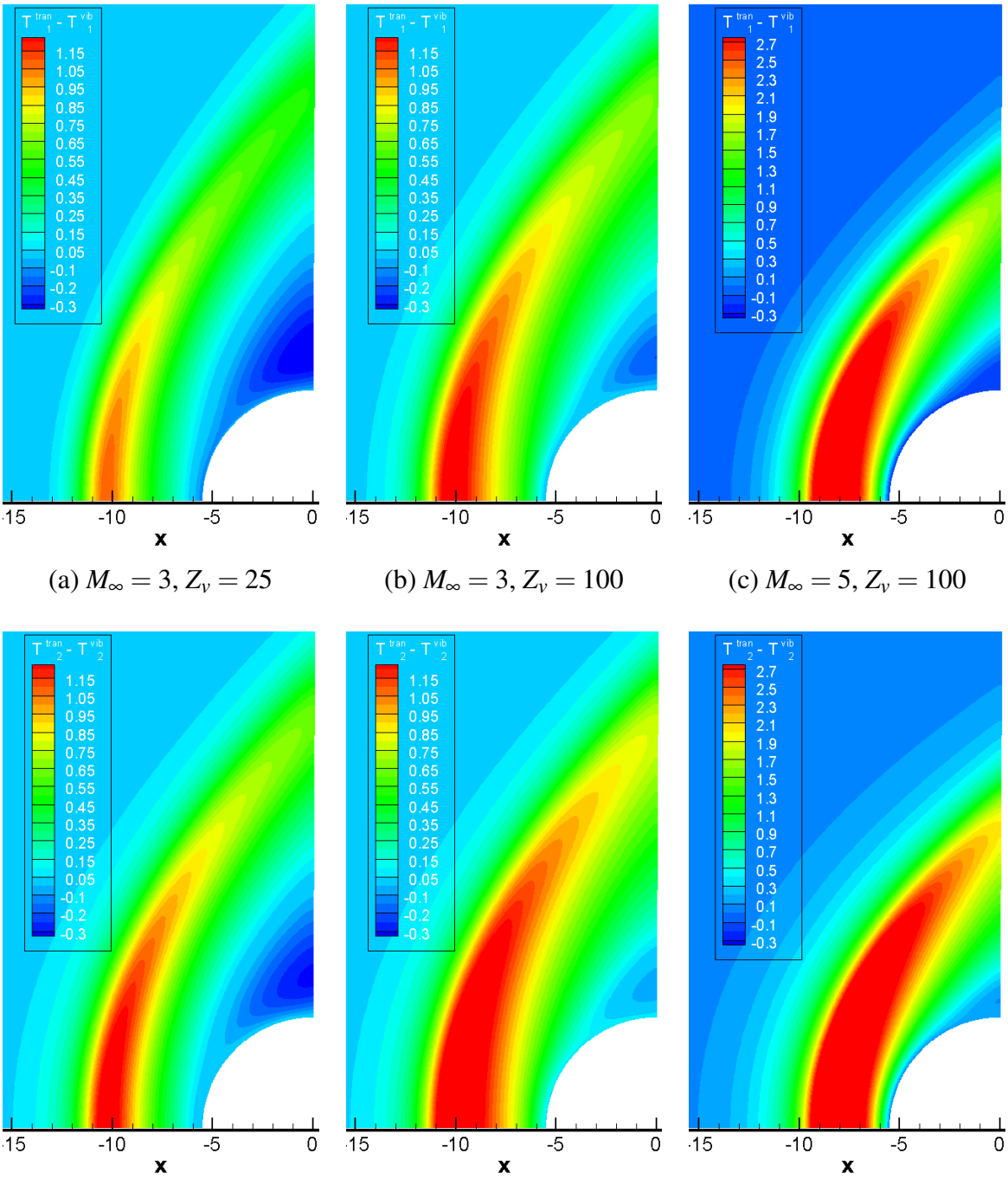

(a) $M_\infty = 3$, $Z_v = 25$ (b) $M_\infty = 3$, $Z_v = 100$ (c) $M_\infty = 5$, $Z_v = 100$

(d) $M_\infty = 3$, $Z_v = 25$ (e) $M_\infty = 3$, $Z_v = 100$ (f) $M_\infty = 5$, $Z_v = 100$

Figure 6.11: Temperature difference between translational and vibrational temperatures per species in a binary mixture flow over a cylinder with initial Mach numbers 3 and 5, nitrogen to oxygen concentration 80% : 20%, Knudsen number $Kn = 0.1$ and wall temperature $T_{wall} = 1.5T_\infty$.

with a same Mach number but lower vibrational collision number Z_v.

In the section for the profile of a normal shock wave, the number of excited vibrational degrees of freedom per species δ_s was considered. This value is also interesting for the cylinder case. In Fig. 6.12 we show the values of δ for nitrogen and in Fig. 6.13 for oxygen for the same 3 cases in Table 6.2. Note that the bottom plots in the two figures ((d) and (e)) are identical to the top plots just above them ((b) and (c) correspondingly), but their legends have different maxima. At the top, the 3 plots have the same legends to allow for easier comparison between cases and drawing conclusions, while the plots below allow for a more detailed evaluation of each case by itself. Notice also that a colour plot is used with the same step size for the top plots in both figures, but the maximum value for the oxygen plots (Fig. 6.13 (a), (b), (c)) is more than 3 times the maximum value of the nitrogen plots (Fig. 6.12 (a), (b), (c)). The vibration degrees of freedom in the free-stream are negligible. This is due to the low free-stream temperature T_∞. The values increase as the flow approaches the cylinder, with a peak at the stagnation streamline, where the bow shock is at 90 degrees and the temperature is at its highest. The values decrease behind the shock as the flow approaches the body of the cylinder, since the temperature decreases to the imposed wall temperature $T_{wall} = 1.5T_\infty = 432.2K$. In all cases, the oxygen reaches much larger values than the nitrogen, consistent with the theory and with the observations in the previous section.

Another consistency is that the higher Mach number $M_\infty = 5$ leads to an increased vibrational excitation, due to the bigger jump in temperature, as seen in Fig. 6.12 (c) and Fig. 6.13 (c). The maximum values for $M_\infty = 3$, $Z_v = 25$ are lower in the case of the cylinder, where $\delta(O_2) = 0.246$, in comparison to the normal shock, with a maximum value of $\delta(O_2) = 0.312$. This is caused by the cylinder wall, which in comparison to the normal shock setup, presents a physical barrier and the provided relaxation for the vibrational DoF is not sufficient to reach equilibrium level. Moreover, notice that for the normal shock the collision number Z_v affected only the length of the excitation process and the maximum value of δ_s was identical downstream. In contrast, the increase of Z_v for the cylinder, reduces the maximum values of the vibrational degrees of freedom in Fig. 6.12 (b), (d) and Fig. 6.13 (b), (d), i.e. $\delta(O_2) = 0.141$. The longer relaxation process does not allow for the vibrational excitation to develop completely, changing the results significantly. Notice also that the region where δ_s is bigger than 0 moves closer to the body with the increase of Z_v, as well as with the increase of the Mach number when considering the flow-field in y-direction. Furthermore, we will inspect the stand-off distance, which is hard to define when the shock structure is resolved. Here it is done by inspecting the position at which the total number density jump is half of its maximum value through the shock. This is similar to the practice established for the normal shock wave in the previous section. For $Z_v = 25$ the number of vibrationally-excited degrees of freedom is higher than for $Z_v = 100$. It follows that for a growing $\delta(T)$, the specific heats ratio γ reduces from $\gamma = 1.4$ for no vibrational excitation to lower values. Therefore, $\gamma\,(Z_v = 25) < \gamma\,(Z_v = 100)$ and for the lower value the shock moves

closer to the body. The change is small and corresponds to 0.5% from the cylinder radius R. This difference will increase for higher vibrational excitation and/or different vibrational collision number. Therefore, the correct vibrational collision number Z_v is of great importance and it will be one of the first objectives to consider in future work.

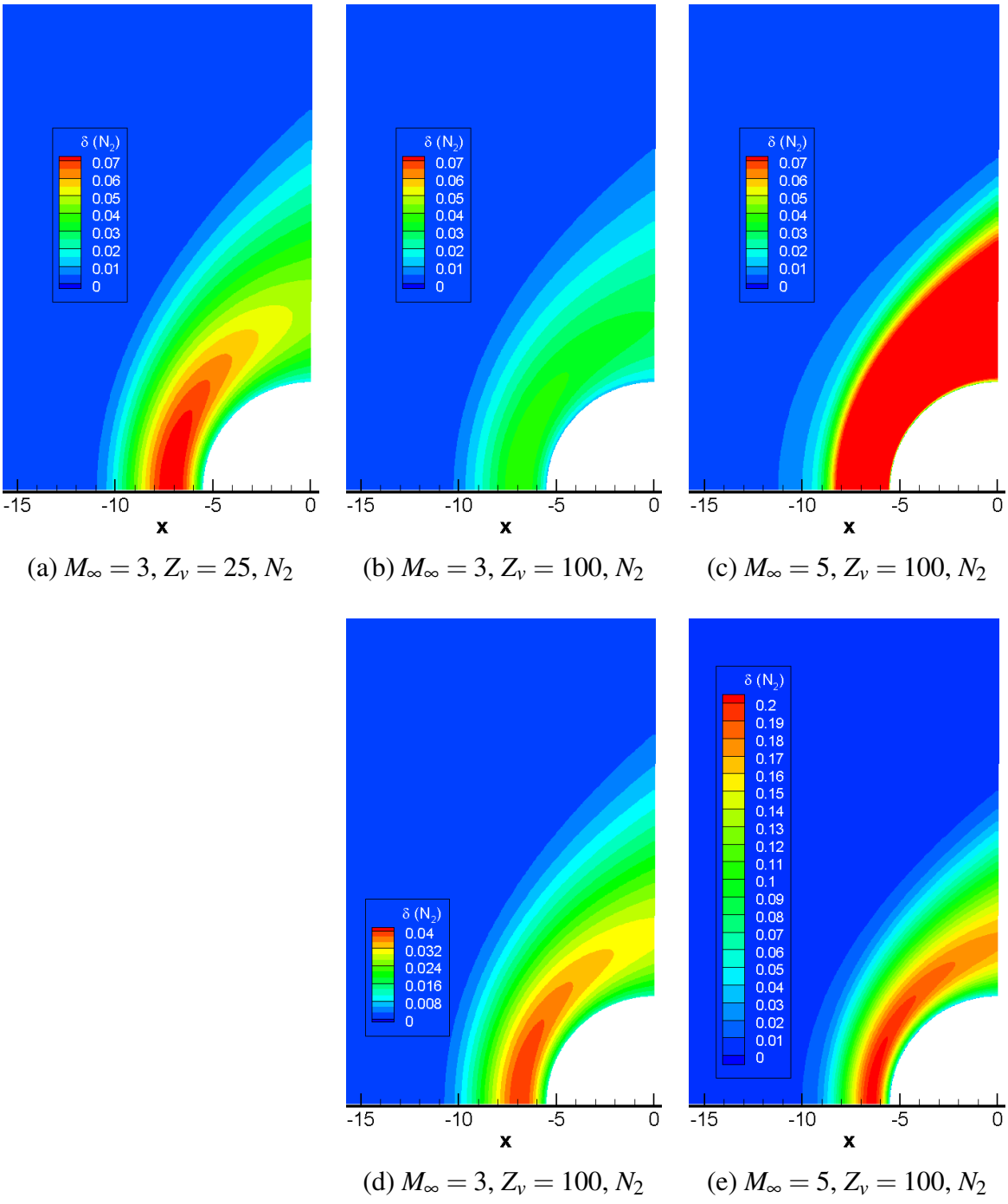

(a) $M_\infty = 3$, $Z_v = 25$, N_2 (b) $M_\infty = 3$, $Z_v = 100$, N_2 (c) $M_\infty = 5$, $Z_v = 100$, N_2

(d) $M_\infty = 3$, $Z_v = 100$, N_2 (e) $M_\infty = 5$, $Z_v = 100$, N_2

Figure 6.12: Vibrational degrees of freedom for nitrogen $\delta(N_2)$ in a binary mixture flow over a cylinder with initial Mach numbers 3 and 5, nitrogen to oxygen concentration 80% : 20%, Knudsen number $Kn = 0.1$ and wall temperature $T_{wall} = 1.5T_\infty$.

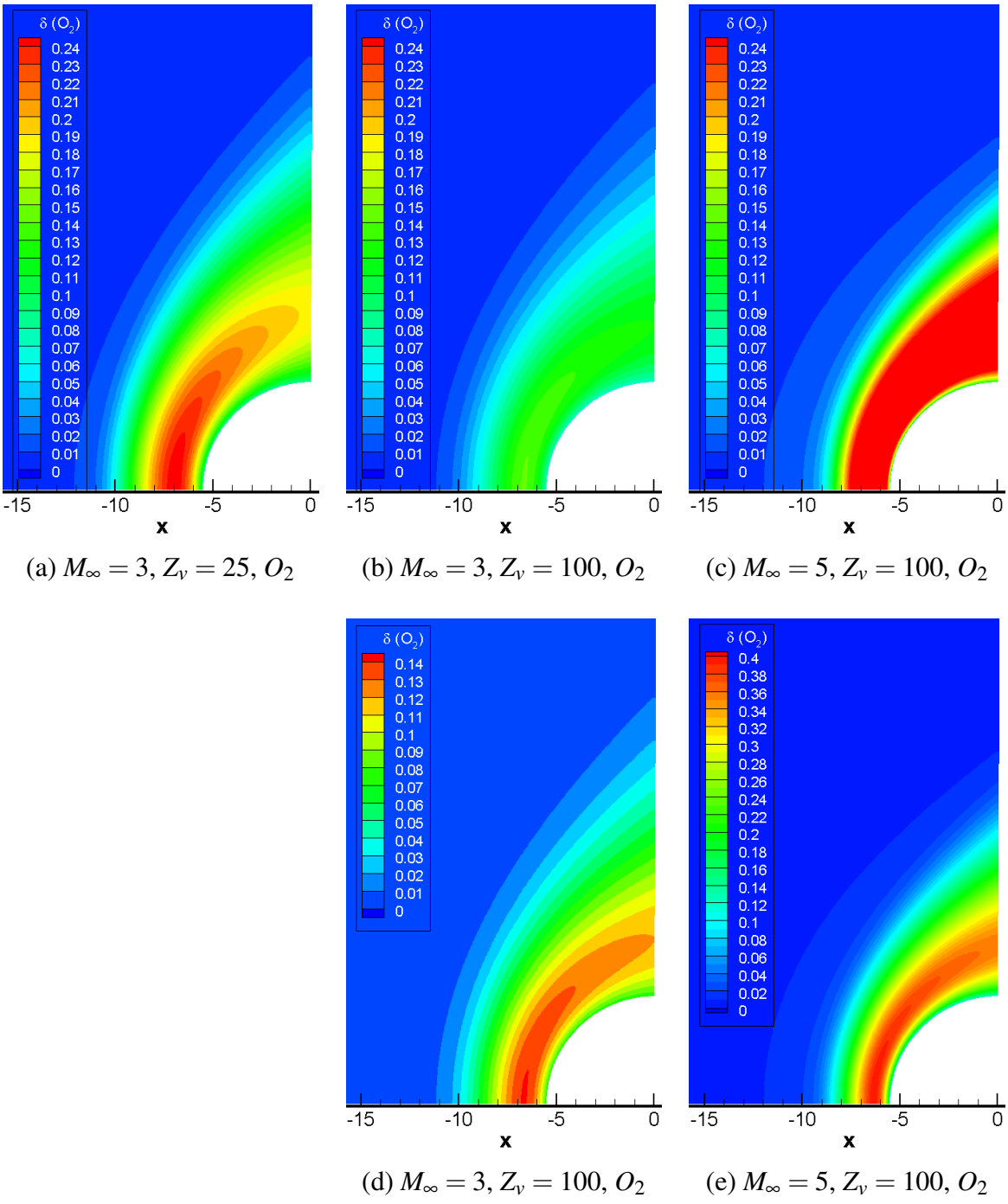

(a) $M_\infty = 3$, $Z_v = 25$, O_2 (b) $M_\infty = 3$, $Z_v = 100$, O_2 (c) $M_\infty = 5$, $Z_v = 100$, O_2

(d) $M_\infty = 3$, $Z_v = 100$, O_2 (e) $M_\infty = 5$, $Z_v = 100$, O_2

Figure 6.13: Vibrational degrees of freedom for oxygen $\delta(O_2)$ in a binary mixture flow over a cylinder with initial Mach numbers 3 and 5, nitrogen to oxygen concentration 80% : 20%, Knudsen number $Kn = 0.1$ and wall temperature $T_{wall} = 1.5T_\infty$.

6.4 Summary of Findings

The new kinetic model for a binary mixture of diatomic gases with species translational, rotational and vibrational temperatures was evaluated numerically for a profile of a normal shock wave and the flow around a circular cylinder. The results are:

- The diatomic mixture solver is shown to produce identical results under the same initial conditions for the two species.
- The profile of a normal shock wave for the gas mixture of nitrogen and oxygen was evaluated.
- A parametric study was conducted varying the free-stream Mach number, the concentration between species and the vibrational collision number. The physics of the flow in the results showed consistency with theoretical observations.
- Validation with DSMC acquired results was demonstrated by inspecting the macroscopic variables: species and total number density, species translational, rotational and vibrational temperatures for all test cases. Very good agreement was observed.
- The vibrational degrees of freedom for the nitrogen and oxygen, which are of particular interest in these test cases, were presented. The vibrational collision number has influenced the results significantly. The importance of treating the gas as a mixture due to the difference in the species vibration DoF was further emphasised.
- The velocity drift between species was shown to increase for higher Mach numbers, but was not affected by the vibrational collision number.
- Beyond the macroscopic variables, the velocity distribution function pre-shock, mid-shock and post-shock was plotted for the case with largest Mach and vibrational collision numbers. The expected non-Maxwellian behaviour through the shock wave appeared, as well as a bi-modal behaviour, most clearly demonstrated by the vibrational distribution.
- The flow around a circular cylinder was demonstrated for 3 cases with varied Mach number and vibrational collision number.
- The species velocity drift again showed no change with the variation of the vibrational collision number, but was significantly affected by the increase of the free-stream Mach number.
- In contrast, the difference between the translational and vibrational temperature was increased by the vibrational collision number, as well as the Mach number. Furthermore, the difference between these two temperatures changed for each species and was more pronounced for the oxygen, which is more vibrationally excited.

- The vibrational DoF for each species was studied for all cases. For the higher vibrational collision number, the flow required more time to be developed and as a results the vibrational DoF did not reach its maximum value.
- The oxygen vibrational DoF were shown to be 3 orders of magnitude higher than the nitrogen under the same condition for the considered Mach numbers.

The kinetic model for a diatomic mixture was numerically evaluated for different cases, under varied conditions. Validation for five cases with DSMC showed good agreement. This initial numerical study of the new kinetic model showed promising results. Future testing will expand the application possibilities and capabilities of the model, but at this stage we are satisfied a gas mixture with air constituents was tested successfully.

Chapter 7

Conclusions and Future Work

7.1 Conclusion

This thesis presents new kinetic models for gas mixtures: first for a binary mixture of monoatomic gases and then for a binary mixture of diatomic gases. The models solved current challenges for Boltzmann relaxation equations for mixtures. The derivation of the models and the consistency with available models in the literature were demonstrated. The continuum limit, compatibility and transport properties of the models were shown. Each species has separate species flow-field properties, e.g. species densities, velocities and temperatures and the relationship between the species macroscopic variables was modelled. Species diffusion was accounted for. Each of the mixture models was shown to reduce to the equivalent single-species model. The models were numerically evaluated and tested.
All objectives of the thesis were satisfied. A detailed summary of findings was provided after each of the chapter and an overview of the main conclusions is as follows:

- A Shakhov-based and an ES-based extensions were applied to a known monoatomic mixture model. As a result, the thermal conductivity coefficient was correctly fitted in the continuum limit, as well as the ordinary diffusion and viscosity coefficients, inherent to the initial mixture model. The Prandtl number was also corrected in the continuum limit, which is a distinct advantage of the two new models.

- The numerical evaluation of the models showed good agreement when compared with results for the flow-field macroscopic variables from the Boltzmann equation for the profile of a normal shock wave and with DSMC results for the flow past a circular cylinder. The influence of the heat flux correction and the actual contribution of the new models were demonstrated when a comparison was presented of the two new models with the uncorrected model and results from the Boltzmann equation. The newly-introduced models showed clear improvement in this comparison. Furthermore, a parametric study showed the importance of modelling the gas as a mixture by varying the mass ratio be-

tween species, level of non-equilibrium caused by the free-stream Mach number and initial species concentrations.

- The derivation of a gas-kinetic scheme based on the Shakhov-based mixture model was detailed. A comprehensive comparison with previously acquired DVM results from the model as a benchmark demonstrated good accuracy and agreement of the gas-kinetic scheme. For moderate levels of rarefaction and moderate level of thermodynamic non-equilibrium, the GKS results showed a good agreement with the corresponding DVM results. For flows with higher Mach numbers and Knudsen numbers differences are to be expected, inherent to the assumptions made in the derivation in the GKS. At the same time a significant speed-up of the computational time was observed, making the GKS a viable method for flows close to equilibrium.

- A new model for diatomic gas mixtures was presented. A detailed derivation procedure from a single-species single-temperature model was included. The model was shown to have species translational, rotational and vibrational temperatures. The model also features a three-step relaxation process, accounting for the different rates of translational, rotational and vibrational effects. Unlike previous diatomic models, species properties and diffusion was accurately represented. These features are major improvements over existing models for diatomic mixtures. A CE-like expansion led to the continuum limit and transport properties of the model.

- A numerical investigation of the diatomic model for a gas mixture showed good agreement with results acquired with DSMC for the profile of a normal shock wave. A parametric study of the shock wave and a flow around a circular cylinder was conducted. The different level of vibrational excitation for each species and under different initial conditions emphasized the importance of modelling flows as mixtures. Also, the different level of vibrational excitation of the normal shock and the cylinder under the same initial conditions highlighted the importance of a correctly modelled vibrational collision number Z_v. The capability to model at the kinetic level the non-reacting flow of air, encountering strong non-equilibrium regions, was created. A gas mixture of nitrogen and oxygen, which is of great relevance to practical applications, was successfully modelled and numerically evaluated.

7.2 Future Work

Based on this thesis and the aforementioned conclusions, the following future work is suggested:

- The transport properties for a mixture of monoatomic gases are a main research point. The Fick, Newton and Fourier coefficients are correctly fitted in the presented models,

but the coupled effects: Dufour and Soret are not addressed in this work. Since they are already included in the continuum limit equations and we know they should have reciprocal quantities, only one extra relaxation coefficient needs to be added to correctly fit all transport coefficients for binary monoatomic gas mixtures.

- The viscosity power law dependence on temperature is used. This is clearly a simplification when binary gas mixtures are considered. Better mixture laws for viscosities are available and should be considered.

- Further validation test cases including a variety of low speed flows and rarefaction levels will enable a more detailed level of evaluation of the new models.

- The limitations of the numerically efficient gas-kinetic scheme should be further studied for a range of Mach numbers and variety of geometries.

- The current GKS scheme is for a monoatomic mixture and an extension to a diatomic mixture will increase the possible applications.

- Implementing the new kinetic models in a more advanced numerical scheme, e.g DUGKS, constitutes an interesting line of research.

- The diatomic mixture model fits only two correct transport coefficients in the continuum limit. Future work is to correct the heat flux and the Prandtl number.

- A model which is capable of simulating gas mixture of a monoatomic and a diatomic gas will increase the domain of applications. Similarly, extending the models to more than two species is part of future work.

- The collision numbers Z_r and Z_v allowing for the different rate of relaxation of the rotational and vibrational DoF are introduced as constants. A more advanced model should define them as functions of the model's temperatures. Furthermore, for the mixture model, Z_r and Z_v should be also species dependent.

- Further validation test cases are required to consider the kinetic model for diatomic gas mixtures fully validated.

- A study inspecting the effect of each new temperature type should be considered. We observed that the species translational temperatures had similar values, as well as the species rotational temperatures for the cases of nitrogen and oxygen components. In order to save computational time, big test cases including air-flow should consider having one translational temperature, one rotational temperature and species vibrational temperatures.

- Test cases with a mixture consistent of other diatomic gases beyond nitrogen and oxygen with higher mass ratio between species should be studied. The mass ratio effect will dominate the difference between species macroscopic properties and will create interesting results.

- Extensions of the model beyond inert mixtures and including chemical reactions, while very challenging, will broaden the capabilities and applications.

Clearly, the area of kinetic models for gas mixtures and their numerical applications is a complex research area with many questions still unanswered. The current thesis makes a strong advance in creating such models for monoatomic and diatomic gas mixtures, enabling the kinetic modelling and simulations of rarefied flows of engineering interest.

Appendices

Appendix A

Standard definite integrals where a and b are constants and $a > 0$ [2] are:

$$\int_{-\infty}^{+\infty} e^{(-a(x-b)^2)}\,dx = \sqrt{\frac{\pi}{a}} \tag{A.1}$$

$$\int_{-\infty}^{+\infty} xe^{(-a(x-b)^2)}\,dx = b\sqrt{\frac{\pi}{a}} \tag{A.2}$$

$$\int_{-\infty}^{+\infty} x^2e^{(-a(x-b)^2)}\,dx = \frac{1}{2a}\sqrt{\frac{\pi}{a}}(2ab^2+1) \tag{A.3}$$

$$\int_{-\infty}^{+\infty} x^3e^{(-a(x-b)^2)}\,dx = \frac{1}{2a}\sqrt{\frac{\pi}{a}}b(2ab^2+3) \tag{A.4}$$

$$\int_{-\infty}^{+\infty} x^4e^{(-a(x-b)^2)}\,dx = \frac{1}{4a^2}\sqrt{\frac{\pi}{a}}(4a^2b^4+12ab^2+3) \tag{A.5}$$

$$\int_{-\infty}^{+\infty} x^5e^{(-a(x-b)^2)}\,dx = \frac{1}{4a^2}\sqrt{\frac{\pi}{a}}b(4a^2b^4+20b^2a+15) \tag{A.6}$$

$$\int_{-\infty}^{+\infty} x^6e^{(-a(x-b)^2)}\,dx = \frac{1}{8a^3}\sqrt{\frac{\pi}{a}}(8a^3b^6+60a^2b^4+90ab^2+15) \tag{A.7}$$

Note: If the limits of the integral are 0 to $+\infty$ all integrals with even powers of x will evaluate to half the value given above. Also, if b=0 integrals with odd powers of x will become 0.

Appendix B

Moments of the Maxwellian distribution function, where $d\underline{u}$ is the infinitesimal change of the element of velocity volume and $d\underline{u} = dudvdw$, are:

$$\iiint_{-\infty}^{+\infty} f^M(\underline{u})\, d\underline{u} = \rho \tag{B.1}$$

$$\iiint_{-\infty}^{+\infty} u f^M(\underline{u})\, d\underline{u} = \rho u_0 \tag{B.2}$$

$$\iiint_{-\infty}^{+\infty} v f^M(\underline{u}) d\underline{u} = \rho v_0 \tag{B.3}$$

$$\iiint_{-\infty}^{+\infty} w f^M(\underline{u})\, d\underline{u} = \rho w_0 \tag{B.4}$$

$$\iiint_{-\infty}^{+\infty} u^2 f^M(\underline{u})\, d\underline{u} = \rho(u_0^2 + RT) \tag{B.5}$$

$$\iiint_{-\infty}^{+\infty} v^2 f^M(\underline{u})\, d\underline{u} = \rho(v_0^2 + RT) \tag{B.6}$$

$$\iiint_{-\infty}^{+\infty} w^2 f^M(\underline{u})\, d\underline{u} = \rho(w_0^2 + RT) \tag{B.7}$$

$$\iiint_{-\infty}^{+\infty} \frac{1}{2}(u^2+v^2+w^2) f^M(\underline{u})\, d\underline{u} = \frac{1}{2}\rho(u_0^2+v_0^2+w_0^2+3RT) \tag{B.8}$$

$$\iiint_{-\infty}^{+\infty} \frac{1}{2}u(u^2+v^2+w^2) f^M(\underline{u})\, d\underline{u} = \frac{1}{2}\rho(u_0^3+v_0^2u_0+w_0^2u_0+5u_0RT) \tag{B.9}$$

The above integrals are of particular interest for the integration of the Maxwellian distribution function $f^M(\underline{u})$.

$$f^M(\underline{u}) = \frac{\rho}{(2\pi RT)^{\frac{3}{2}}} \exp\left[-\frac{1}{2RT}\Big((u-u_0)^2+(v-v_0)^2+(w-w_0)^2\Big)\right] \tag{B.10}$$

It will be shown that:

$$\iiint_{-\infty}^{+\infty} f^M(\underline{u})\, d\underline{u} = \rho \tag{B.11}$$

$$\begin{aligned}
\iiint_{-\infty}^{+\infty} f^M(\underline{u})\, d\underline{u} &= \iiint_{-\infty}^{+\infty} \frac{\rho}{(2\pi RT)^{\frac{3}{2}}} \exp\left[-\frac{1}{2RT}\Big((u-u_0)^2+(v-v_0)^2+(w-w_0)^2\Big)\right] d\underline{u} \\
&= \frac{\rho}{(2\pi RT)^{\frac{3}{2}}} \int_{-\infty}^{+\infty} \exp\left[-\frac{(u-u_0)^2}{2RT}\right] du \int_{-\infty}^{+\infty} \exp\left[-\frac{(v-v_0)^2}{2RT}\right] dv \int_{-\infty}^{+\infty} \exp\left[-\frac{(w-w_0)^2}{2RT}\right] dw \\
&= \frac{\rho}{(2\pi RT)^{\frac{3}{2}}} [\sqrt{2\pi RT}\sqrt{2\pi RT}\sqrt{2\pi RT}] \\
&= \rho
\end{aligned} \tag{B.12}$$

In the above proof of the zeroth order moment of the Maxwellian distribution function, the integral and the exponential function were split into the three directions of the velocity vector c_i. The standard integral (A.1) was applied to all 3 integration functions. The derivation of first and second order moments of the Maxwellian function follows the same procedure as in (B.12) and incorporates more of the standard integrals defined above.

Appendix C

The detailed derivation of the continuum limit of all three models is shown. Note that the mass and momentum limits of the original and Shakhov-based models are the same and is shown only for the corrected Shakhov model G_s^{Sh}.

Mass Equation

The time-derivative term has the following form for all the models:

$$\iiint_{-\infty}^{\infty} \Big\{ G_s^{Sh} - \frac{\varepsilon}{\nu}\Big(\frac{\partial f_s^M}{\partial t} + u\frac{\partial f_s^M}{\partial x}\Big)\Big\} d\underline{u} = n_s \tag{C.1}$$

$$\iiint_{-\infty}^{\infty} \Big\{ G_s^{ES} - \frac{\varepsilon(1-\nu_{ES})}{\nu}\Big(\frac{\partial f_s^M}{\partial t} + u\frac{\partial f_s^M}{\partial x}\Big)\Big\} d\underline{u} = n_s$$

The flux in the x-direction:

$$\iiint_{-\infty}^{\infty} u\Big\{ G_s^{Sh} - \frac{\varepsilon}{\nu}\Big(\frac{\partial f_s^M}{\partial t} + u\frac{\partial f_s^M}{\partial x}\Big)\Big\} d\underline{u} = n_s u_s^{(g)}$$

$$-\varepsilon\frac{kT}{\nu}\Big[\frac{1}{m_s}\frac{\partial n_s}{\partial x} - \frac{n_s}{\rho}\frac{\partial n}{\partial x} + \frac{n_s}{T}\Big(\frac{1}{m_s} - \frac{n}{\rho}\Big)\frac{\partial T}{\partial x}\Big] \tag{C.2}$$

$$\iiint_{-\infty}^{\infty} u\Big\{ G_s^{ES} - \frac{\varepsilon(1-\nu_{ES})}{\nu}\Big(\frac{\partial f_s^M}{\partial t} + u\frac{\partial f_s^M}{\partial x}\Big)\Big\} d\underline{u} = n_s u_s^{(g)}$$

$$-\varepsilon\frac{(1-\nu_{ES})kT}{\nu}\Big[\frac{1}{m_s}\frac{\partial n_s}{\partial x} - \frac{n_s}{\rho}\frac{\partial n}{\partial x} + \frac{n_s}{T}\Big(\frac{1}{m_s} - \frac{n}{\rho}\Big)\frac{\partial T}{\partial x}\Big] \tag{C.3}$$

The mass equation in the continuum limit after substituting the expression for $u_s^{(g)}$ is the same for all three models, as expected.

$$\frac{\partial n_s}{\partial t} + \frac{\partial}{\partial x}\Big\{ n_s u_0 - \varepsilon\frac{kT}{\eta}\Big[\frac{1}{m_s}\frac{\partial n_s}{\partial x} - \frac{n_s}{\rho}\frac{\partial n}{\partial x} + \frac{n_s}{T}\Big(\frac{1}{m_s} - \frac{n}{\rho}\Big)\frac{\partial T}{\partial x}\Big]\Big\} = 0 \tag{C.4}$$

Momentum Equation

The time-derivative term has the following form for all the models:

$$\begin{aligned}
\sum_{s=1}^{2}\iiint_{-\infty}^{\infty} m_s u\Big\{G_s^{Sh}-\frac{\varepsilon}{\nu}\Big(\frac{\partial f_s^M}{\partial t}+u\frac{\partial f_s^M}{\partial x}\Big)\Big\}d\underline{u} &= \sum_{s=1}^{2} m_s n_s u_s^{(g)} \\
&= \sum_{s=1}^{2}\rho_s\Big[\Big(1-\frac{\eta}{\nu}\Big)u_s+\frac{\eta}{\nu}u_0\Big] \\
&= \rho u_0 \\
\sum_{s=1}^{2}\iiint_{-\infty}^{\infty} m_s u\Big\{G_s^{ES}-\frac{\varepsilon(1-\nu_{ES})}{\nu}\Big(\frac{\partial f_s^M}{\partial t}+u\frac{\partial f_s^M}{\partial x}\Big)\Big\}d\underline{u} &= \sum_{s=1}^{2} m_s n_s u_s^{(g)} \qquad \text{(C.5)} \\
&= \sum_{s=1}^{2}\rho_s\Big[\Big(1-\frac{\eta}{\nu}(1-\nu_{ES})\Big)u_s \\
&\qquad +\frac{\eta}{\nu}(1-\nu_{ES})u_0\Big] \\
&= \rho u_0
\end{aligned}$$

Here due to the summation, the contribution from the CE expansion is 0.

The inviscid flux in the x-direction:

$$\begin{aligned}
\sum_{s=1}^{2}\iiint_{-\infty}^{\infty} m_s u^2 G_s^{Sh} d\underline{u} = \sum_{s=1}^{2} m_s n_s\Big(\frac{k\hat{T}}{m_s}+(u_s^{(g)})^2\Big) &= nk\hat{T}+\sum_{s=1}^{2}\rho_s(u_s^{(g)})^2 \\
&= nkT+\rho u_0^2+O(\varepsilon^2) \qquad \text{(C.6)} \\
\sum_{s=1}^{2}\iiint_{-\infty}^{\infty} m_s u^2 G_s^{ES} d\underline{u} = \sum_{s=1}^{2} m_s n_s(\lambda_{11}^s+(u_s^{(g)})^2) &= \sum_{s=1}^{2} m_s n_s\Big(\frac{k\hat{T}}{m_s}-\nu_{ES}\frac{\varepsilon}{\nu}\frac{kT}{m_s}\frac{4}{3}\frac{\partial u_0}{\partial x} \\
&\qquad +(u_s^{(g)})^2+O(\varepsilon^2)\Big) \qquad \text{(C.7)} \\
&= nkT+\rho u_0^2-\nu_{ES}\frac{\varepsilon}{\nu}nkT\frac{4}{3}\frac{\partial u_0}{\partial x}+O(\varepsilon^2)
\end{aligned}$$

The viscous part for all models is similar, with the ES model pre-multiplied as always by $(1-\nu_{ES})$.

$$\sum_{s=1}^{2}\iiint_{-\infty}^{\infty} m_s u^2\Big\{\frac{\varepsilon}{\nu}\Big(\frac{\partial f_s^M}{\partial t}+u\frac{\partial f_s^M}{\partial x}\Big)\Big\}d\underline{u} = \frac{\varepsilon}{\nu}nkT\frac{4}{3}\frac{\partial u_0}{\partial x} \qquad \text{(C.8)}$$

The momentum equation results in:

$$\frac{\partial \rho u_0}{\partial t}+\frac{\partial}{\partial x}\Big\{nkT+\rho u_0^2-\mu\frac{4}{3}\frac{\partial u_0}{\partial x}\Big\}=0 \qquad \text{(C.9)}$$

where the viscosity coefficient $\mu = \frac{\varepsilon}{\nu} nkT$

Energy Equation

The time-derivative term has the form:

$$\begin{aligned}
\sum_{s=1}^{2} \iiint_{-\infty}^{\infty} m_s \frac{1}{2}(u^2+v^2+w^2)\Big\{G_s - \frac{\varepsilon}{\nu}\Big(\frac{\partial f_s^M}{\partial t} + u\frac{\partial f_s^M}{\partial x}\Big)\Big\} d\underline{u} \\
= \sum_{s=1}^{2} \Big\{ n_s m_s \Big(\frac{1}{2}(u_s^{(g)})^2 + \frac{3}{2}\frac{k\hat{T}}{m_s}\Big)\Big\} \qquad \text{(C.10)} \\
\sum_{s=1}^{2} \iiint_{-\infty}^{\infty} m_s \frac{1}{2}(u^2+v^2+w^2)\Big\{G_s^{Sh} - \frac{\varepsilon}{\nu}\Big(\frac{\partial f_s^M}{\partial t} + u\frac{\partial f_s^M}{\partial x}\Big)\Big\} d\underline{u} \\
= \sum_{s=1}^{2} \Big\{ n_s m_s \Big(\frac{1}{2}(u_s^{(g)})^2 + \frac{3}{2}\frac{k\hat{T}}{m_s}\Big)\Big\} \\
\sum_{s=1}^{2} \iiint_{-\infty}^{\infty} m_s \frac{1}{2}(u^2+v^2+w^2)\Big\{G_s^{ES} - \frac{\varepsilon}{\nu}(1-\nu_{ES})\Big(\frac{\partial f_s^M}{\partial t} + u\frac{\partial f_s^M}{\partial x}\Big)\Big\} d\underline{u} \\
= \sum_{s=1}^{2} \Big\{ n_s m_s \Big(\frac{1}{2}(u_s^{(g)})^2 + \lambda_{11}^s + \lambda_{22}^s + \lambda_{33}^s\Big)\Big\} \\
= \sum_{s=1}^{2} \Big\{ n_s m_s \Big(\frac{1}{2}(u_s^{(g)})^2 + \frac{3}{2}\frac{k\hat{T}}{m_s} + O(\varepsilon^2)\Big)\Big\}
\end{aligned}$$

For the 0th-order part of the flux in the $x-$direction this results in,

$$\begin{aligned}
\sum_{s=1}^{2} \iiint_{-\infty}^{\infty} m_s u \frac{1}{2}(u^2+v^2+w^2) G_s d\underline{u} &= \sum_{s=1}^{2} \Big\{ n_s m_s \Big(\frac{1}{2}(u_s^{(g)})^3 + \frac{5}{2}\frac{k\hat{T}}{m_s} u_s^{(g)}\Big)\Big\} \\
\sum_{s=1}^{2} \iiint_{-\infty}^{\infty} m_s u \frac{1}{2}(u^2+v^2+w^2) G_s^{Sh} d\underline{u} &= \sum_{s=1}^{2} \Big\{ n_s m_s \Big(\frac{1}{2}(u_s^{(g)})^3 + \frac{5}{2}\frac{k\hat{T}}{m_s} u_s^{(g)} + \frac{(1-Pr) q_{x_s}^{corr}}{m_s}\Big)\Big\} \\
\sum_{s=1}^{2} \iiint_{-\infty}^{\infty} m_s u \frac{1}{2}(u^2+v^2+w^2) G_s^{ES} d\underline{u} &= \sum_{s=1}^{2} \Big\{ n_s m_s \frac{1}{2}\Big((u_s^{(g)})^2 + 3\lambda_{11}^s + \lambda_{22}^s + \lambda_{33}^s\Big)\Big\} \\
&= \sum_{s=1}^{2} \Big\{ n_s m_s \Big(\frac{1}{2}(u_s^{(g)})^3 + \frac{5}{2}\frac{k\hat{T}}{m_s} u_s^{(g)} \\
&\qquad - \nu_{ES}\frac{\varepsilon}{\nu}\frac{4}{3}\frac{kT}{m_s} u_s^{(g)} \frac{\partial u_0}{\partial x} + O(\varepsilon^2)\Big)\Big\} \qquad \text{(C.11)}
\end{aligned}$$

The 1-st order part of the flux in the x-direction is based on the Maxwellian and is common for all the models, except a multiplication by $(1-\nu_{ES})$ for the ES model. The common part results

in:

$$\sum_{s=1}^{2} \iiint_{-\infty}^{\infty} m_s u \frac{1}{2}\left(u^2+v^2+w^2\right)\left\{\frac{\varepsilon}{\nu}\left(\frac{\partial f_s^M}{\partial t}+u\frac{\partial f_s^M}{\partial x}\right)\right\} d\underline{u}$$

$$= \sum_{s=1}^{2} m_s \frac{\varepsilon}{\nu}\left[\frac{\eta}{\varepsilon} n_s\left(\frac{3}{2}u_0^2+\frac{5}{2}\frac{kT}{m_s}\right)\left(u_0-u_s\right)+\frac{4}{3}n_s\frac{kT}{m_s}u_0\frac{\partial u_0}{\partial x}+\frac{5}{2}n_s\left(\frac{kT}{m_s}\right)^2\frac{1}{T}\frac{\partial T}{\partial x}\right] \quad \text{(C.12)}$$

Combining the time-derivative and the flux terms forms the limit of the energy equation up to order $O(\varepsilon^2)$ for each model as shown in the text.

Bibliography

[1] J. D. Anderson Jr., *Hypersonic and High Temperature Gas Dynamics*. AIAA, 2000.

[2] W. Vincenti and C. Kruger, *Introduction to physical gas dynamics*. Krieger, 1967.

[3] M. Ivanov, Y. Bondar, and G. Markelov, "Recent achievements in the DSMC method and its applications to studying jets in vacuum chamber," *51st IUVSTA Workshop on Modern Problems & Capability of Vacuum Gas Dynamics.*, 2007.

[4] R. E. Cunningham and R. J. J. Williams, *Diffusion in Gases and Porous Media*. Springer, Boston, MA, 1980.

[5] B. N. Todorova and R. Steijl, "Comparison of discrete velocity method and gas-kinetic method for binary gas mixtures," *Journal of Thermophysics and Heat Transfer*, vol. 0, no. 0, pp. 1–12, 2019.

[6] K. Xu, "A gas-kinetic BGK scheme for the Navier–Stokes Equations and its connection with artificial dissipation and Godunov method," *Journal of Computational Physics*, vol. 171, no. 1, pp. 289 – 335, 2001.

[7] J. R. Belcher, W. V. Slaton, R. Raspet, H. E. Bass, and J. Lightfoot, "Working gases in thermoacoustic engines," *The Journal of the Acoustical Society of America*, vol. 105, no. 5, pp. 2677–2684, 1999.

[8] T. Ohwada, "Structure of normal shock waves: Direct numerical analysis of the Boltzmann equation for hard-sphere molecules," *Physics of Fluids A: Fluid Dynamics*, vol. 5, no. 1, pp. 217–234, 1993.

[9] S. Kosuge, K. Aoki, and S. Takata, "Shock-wave structure for a binary gas mixture: finite-difference analysis of the Boltzmann equation for hard-sphere molecules," *European Journal of Mechanics - B/Fluids*, vol. 20, no. 1, pp. 87 – 126, 2001.

[10] K. Champion, A. Cole, and A. Kantor, *Standard and Reference Atmospheres, Handbook of Geophysics and the Space environment*. United States Air Force, Air Force Geophysics Laboratory, 1985.

[11] J. F. Bourgat, P. Le Tallec, B. Perthame, and Y. Qiu, "Coupling Boltzmann and Euler equations without overlapping," *Contemporary Mathematics*, vol. 157, pp. 377–377, 1994.

[12] S. Dellacherie, "Coupling of the Wang Chang–Uhlenbeck equations with the multispecies euler system," *Journal of Computational Physics*, vol. 189, no. 1, pp. 239 – 276, 2003.

[13] A. Patronis, D. A. Lockerby, M. K. Borg, and J. M. Reese, "Hybrid continuum–molecular modelling of multiscale internal gas flows," *Journal of Computational Physics*, vol. 255, pp. 558 – 571, 2013.

[14] W. Yang, X. Gu, L. Wu, D. R. Emerson, Y. Zhang, and S. Tang, "A hybrid approach to couple the discrete velocity method and Method of Moments for rarefied gas flows," *Journal of Computational Physics*, vol. 410, p. 109397, 2020.

[15] K. Xu and J. Huang, "A unified gas-kinetic scheme for continuum and rarefied flows," *Journal of Computational Physics*, vol. 229, no. 20, pp. 7747 – 7764, 2010.

[16] Z. Guo, K. Xu, and R. Wang, "Discrete unified gas kinetic scheme for all Knudsen number flows: Low-speed isothermal case," *Phys. Rev. E*, vol. 88, p. 033305, Sep 2013.

[17] D. Tewari and S. Baul, "Microelectromechanical system market by type, and application: Global opportunity analysis and industry forecast, 2019-2026," technical report, Allied Market Research, 2019.

[18] J. Almquist, M. Cvijovic, V. Hatzimanikatis, J. Nielsen, and M. Jirstrand, "Kinetic models in industrial biotechnology – improving cell factory performance," *Metabolic Engineering*, vol. 24, pp. 38 – 60, 2014.

[19] G. Toscani, "Kinetic models of opinion formation," *Communications in Mathematical Sciences*, vol. 4, pp. 481–496, 09 2006.

[20] S. Cordier, D. Maldarella, L. Pareschi, and C. Piatecki, *Microscopic and kinetic models in financial markets, Mathematical Modeling of Collective Behavior in Socio-Economic and Life Sciences*, pp. 51–80. Boston: Birkhäuser Boston, 2010.

[21] A. Klar and R. Wegener, *Kinetic Traffic Flow Models, Modeling in Applied Sciences: A Kinetic Theory Approach*, pp. 263–316. Boston, MA: Birkhäuser Boston, 2000.

[22] J. D. Anderson Jr., *Modern Compressible Flow: With Historical Perspective*. McGraw-Hill Higher Education, 1982.

[23] G. Bird, *Molecular Gas Dynamics and the Direct Simulation of Gas Flows*. Oxford Science Publications, 1994.

[24] S. Chapman and T. Cowling, *The Mathematical Theory of Non-Uniform Gases*. Cambridge University Press,London, 2 ed., 1952.

[25] J. J. Bertin, *Hypersonic Aerothermodynamics*. American Institute of Aeronautics and Astronautics, 370 L'Enfant Promenade, SW, Washington DC 20024-2518, USA, 1994.

[26] J. M. T. Thompson, J. M. Reese, M. A. Gallis, and D. A. Lockerby, "New directions in fluid dynamics: non-equilibrium aerodynamic and microsystem flows," *Philosophical Transactions of the Royal Society of London. Series A: Mathematical, Physical and Engineering Sciences*, vol. 361, no. 1813, pp. 2967–2988, 2003.

[27] G. E. Karniadakis, A. Beskok, and N. Aluru, *Microflows and Nanoflows: Fundamentals and Simulation*. Springer-Verlag, New York, 2005.

[28] E. Rathakrishnan, *High Enthalpy Gas Dynamics*. John Wiley & Sons, Singapore Pte. Ltd, 2015.

[29] G. Patterson, *Molecular flow of gases*. John Wiley & Sons, Inc.,New York, 1956.

[30] C. W. Chang and G. Uhlenbeck, "Transport phenomena in polyatomic gases," *University of Michigan Research Report*, no. Report No. CM-681, July 1951.

[31] F. G. Tcheremissine and R. K. Agarwal, "Computation of hypersonic shock waves in diatomic gases using the Generalized Boltzmann Equation," *AIP Conference Proceedings*, vol. 1084, no. 1, pp. 427–433, 2008.

[32] P. L. Bhatnagar, E. P. Gross, and M. Krook, "A model for collision processes in gases. I. Small amplitude processes in charged and neutral one-component systems," *Physical Review*, vol. 94, pp. 511–525, May 1954.

[33] E. M. Shakhov, "Generalization of the Krook kinetic relaxation equation," *Fluid Dynamics*, vol. 3, no. 5, pp. 95–96, 1968.

[34] L. H. Holway, "New statistical models for kinetic theory: Methods of construction," *The Physics of Fluids*, vol. 9, no. 9, pp. 1658–1673, 1966.

[35] J. O. Hirschfelder, C. F. Curtiss, and R. B. Bird, *Molecular theory of gases and liquids*. Wiley, New York, 1 ed., 1954.

[36] J. C. Maxwell, "VII. On stresses in rarefied gases arising from inequalities of temperature," *Philosophical Transactions of the Royal Society of London*, vol. 170, pp. 231–256, 1879.

[37] L. Wu and H. Struchtrup, "Assessment and development of the gas kinetic boundary condition for the Boltzmann equation," *Journal of Fluid Mechanics*, vol. 823, p. 511–537, 2017.

[38] C. Hirsch, "Numerical computation of internal and external flows, Volume 1: Fundamentals of numerical discretization," *John Wiley and Sons*, vol. 9, p. 10, 1988.

[39] R. Sanders and K. Prendergast, "The possible relation of the 3-kiloparsec arm to explosions in the galactic nucleus," *The Astrophysical Journal*, vol. 188, 1974.

[40] A. W. Date, *Introduction to Computational Fluid Dynamics*. Cambridge University Press, New York, 2005.

[41] A. Harten, "High resolution schemes for hyperbolic conservation laws," *Journal of Computational Physics*, vol. 49, no. 3, pp. 357 – 393, 1983.

[42] S. Chigullapalli, A. Venkattraman, M. Ivanov, and A. Alexeenko, "Entropy considerations in numerical simulations of non-equilibrium rarefied flows," *Journal of Computational Physics*, vol. 229, no. 6, pp. 2139 – 2158, 2010.

[43] K. Xu, "Gas-kinetic schemes for fluid simulations," *Computational Fluid Dynamics 2000*, pp. 14–27, 2001.

[44] K. H. Prendergast and K. Xu, "Numerical hydrodynamics from gas-kinetic theory," *Journal of Computational Physics*, vol. 109, no. 1, pp. 53 – 66, 1993.

[45] K. Xu and K. H. Prendergast, "Numerical navier-stokes solutions from gas kinetic theory," *Journal of Computational Physics*, vol. 114, no. 1, pp. 9 – 17, 1994.

[46] K. Xu, M. Mao, and L. Tang, "A multidimensional gas-kinetic BGK scheme for hypersonic viscous flow," *Journal of Computational Physics*, vol. 203, no. 2, pp. 405 – 421, 2005.

[47] S. Chen, K. Xu, and Q. Cai, "A comparison and unification of Ellipsoidal Statistical and Shakhov BGK models," *Advances in Applied Mathematics and Mechanics*, vol. 7, no. 2, pp. 245–266, 2015.

[48] P. Andries, P. L. Tallec, J. Perlat, and B. Perthame, "The Gaussian-BGK model of Boltzmann equation with small Prandtl number," *European Journal of Mechanics - B/Fluids*, vol. 19, no. 6, pp. 813 – 830, 2000.

[49] S. Brull and J. Schneider, "A new approach for the Ellipsoidal Statistical Model," *Continuum Mechanics and Thermodynamics*, vol. 20, no. 2, pp. 63 – 74, 2008.

[50] S. Brull and J. Schneider, "On the Ellipsoidal Statistical Model for polyatomic gases," *Continuum Mechanics and Thermodynamics*, vol. 20, no. 8, pp. 489 – 508, 2009.

[51] E. P. Gross and M. Krook, "Model for collision processes in gases: Small-amplitude oscillations of charged two-component systems," *Phys. Rev.*, vol. 102, no. 3, pp. 593 – 604, 1956.

[52] L. Sirovich, "Kinetic modeling of gas mixtures," *The Physics of Fluids*, vol. 5, no. 8, pp. 908–918, 1962.

[53] T. F. Morse, "Kinetic model equations for a gas mixture," *The Physics of Fluids*, vol. 7, no. 12, pp. 2012–2013, 1964.

[54] B. Hamel, "Kinetic model for binary gas mixtures," *The Physics of Fluids*, vol. 8, no. 3, pp. 418–425, 1965.

[55] E. Goldman and L. Sirovich, "Equations for gas mixtures," *The Physics of Fluids*, vol. 10, no. 9, pp. 1928–1940, 1967.

[56] V. Garzo, A. Santos, and J. J. Brey, "A kinetic model for a multicomponent gas," *Physics of Fluids A: Fluid Dynamics*, vol. 1, no. 2, pp. 380–383, 1989.

[57] P. Andries, K. Aoki, and B. Perthame, "A consistent BGK-type model for gas mixtures," *Journal of Statistical Physics*, vol. 106, no. 5, pp. 993–1018, 2002.

[58] R. Wang and K. Xu, "Unified gas-kinetic scheme for multi-species non-equilibrium flow," *AIP Conference Proceedings*, vol. 1628, no. 1, pp. 970–975, 2014.

[59] Y. Zhang, L. Zhu, R. Wang, and Z. Guo, "Discrete unified gas kinetic scheme for all Knudsen number flows. III. Binary gas mixtures of Maxwell molecules," *Physical Review E*, vol. 97, p. 053306, 2018.

[60] C. Klingenberg, M. Pirner, and G. Puppo, "A consistent kinetic model for a two-component mixture with an application to plasma," *Kinetic & Related Models*, vol. 10, no. 2, pp. 445–465, 2017.

[61] J. R. Haack, C. D. Hauck, and M. S. Murillo, "A conservative, entropic multispecies BGK model," *Journal of Statistical Physics*, vol. 168, no. 4, pp. 826–856, 2017.

[62] C. Klingenberg and M. Pirner, "Existence, uniqueness and positivity of solutions for BGK models for mixtures," *Journal of Differential Equations*, vol. 264, pp. 702–727, 2018.

[63] A. V. Bobylev, M. Bisi, M. Groppi, G. Spiga, and I. F. Potapenko, "A general consistent BGK model for gas mixtures," *Kinetic & Related Models*, vol. 11, no. 6, pp. 1377 – 1393, 2018.

[64] M. Groppi, S. Monica, and G. Spiga, "A kinetic ellipsoidal BGK model for a binary gas mixture," *EPL (Europhysics Letters)*, vol. 96, no. 6, p. 64002, 2011.

[65] S. Brull, V. Pavan, and J. Schneider, "Derivation of a BGK model for mixtures," *European Journal of Mechanics - B/Fluids*, vol. 33, pp. 74 – 86, 2012.

[66] S. Brull, "An Ellipsoidal Statistical Model for gas mixtures," *Communications in Mathematical Sciences*, vol. 13, no. 1, pp. 1 – 13, 2015.

[67] F. Sharipov and D. Kalempa, "Separation phenomena for gaseous mixture flowing through a long tube into vacuum," *Physics of Fluids*, vol. 17, no. 12, p. 127102, 2005.

[68] M. Sabouri and M. Darbandi, "Numerical study of species separation in rarefied gas mixture flow through micronozzles using DSMC," *Physics of Fluids*, vol. 31, no. 4, p. 042004, 2019.

[69] F. Sharipov and J. L. Strapasson, "Benchmark problems for mixtures of rarefied gases. I. Couette flow," *Physics of Fluids*, vol. 25, no. 2, p. 027101, 2013.

[70] T. M. M. Homolle and N. G. Hadjiconstantinou, "A low-variance deviational simulation Monte Carlo for the Boltzmann equation," *Journal of Computational Physics*, vol. 226, no. 2, pp. 2341 – 2358, 2007.

[71] Y. Zhang, L. Zhu, P. Wang, and Z. Guo, "Discrete unified gas kinetic scheme for flows of binary gas mixture based on the McCormack model," *Physics of Fluids*, vol. 31, no. 1, p. 017101, 2019.

[72] S. Lorenzani, "A microchannel flow application of a linearized kinetic Bhatnagar-Gross-Krook-type model for inert gas mixtures with general intermolecular forces," *Physics of Fluids*, vol. 31, no. 7, p. 072001, 2019.

[73] M. Bisi and S. Lorenzani, "High-frequency sound wave propagation in binary gas mixtures flowing through microchannels," *Physics of Fluids*, vol. 28, no. 5, p. 052003, 2016.

[74] R. E. Center, "Measurement of shock wave structure in helium argon mixtures," *The Physics of Fluids*, vol. 10, no. 8, pp. 1777–1784, 1967.

[75] L. N. Harnett and E. P. Muntz, "Experimental investigation of normal shock wave velocity distribution functions in mixtures of argon and helium," *The Physics of Fluids*, vol. 15, no. 4, pp. 565–572, 1972.

[76] A. Raines, "Study of a shock wave structure in gas mixtures on the basis of the Boltzmann equation," *European Journal of Mechanics - B/Fluids*, vol. 21, no. 5, pp. 599 – 610, 2002.

[77] L. Wu, J. Zhang, J. M. Reese, and Y. Zhang, "A fast spectral method for the Boltzmann equation for monatomic gas mixtures," *Journal of Computational Physics*, vol. 298, pp. 602 – 621, 2015.

[78] F. Sharipov and F. C. Dias, "Temperature dependence of shock wave structure in helium and neon," *Physics of Fluids*, vol. 31, no. 3, p. 037109, 2019.

[79] V. Titarev, A. Frolova, V. Rykov, P. Vashchenkov, A. Shevyrin, and Y. Bondar, "Comparison of the Shakhov kinetic equation and DSMC method as applied to space vehicle aerothermodynamics," *Journal of Computational and Applied Mathematics*, vol. 364, p. 112354, 2020.

[80] S. Colonia, R. Steijl, and G. Barakos, "Kinetic models and gas-kinetic schemes for hybrid simulation of partially rarefied flows," *AIAA Journal*, vol. 54, pp. 1264–1276, April 2016.

[81] J. Huang, K. Xu, and P. Yu, "A unified gas-kinetic scheme for continuum and rarefied flows II: Multi-dimensional cases," *Communications in Computational Physics*, vol. 12, no. 3, p. 662–690, 2012.

[82] S. Liu, P. Yu, K. Xu, and C. Zhong, "Unified gas-kinetic scheme for diatomic molecular simulations in all flow regimes," *Journal of Computational Physics*, vol. 259, pp. 96 – 113, 2014.

[83] Z. Wang, H. Yan, Q. Li, and K. Xu, "Unified gas-kinetic scheme for diatomic molecular flow with translational, rotational, and vibrational modes," *Journal of Computational Physics*, vol. 350, pp. 237 – 259, 2017.

[84] Z. Guo, R. Wang, and K. Xu, "Discrete unified gas kinetic scheme for all Knudsen number flows. II. Thermal compressible case," *Physical Review E*, vol. 91, p. 033313, Mar 2015.

[85] K. Xu, "BGK-based scheme for multicomponent flow calculations," *Journal of Computational Physics*, vol. 134, no. 1, pp. 122 – 133, 1997.

[86] Y. Lian and K. Xu, "A gas-kinetic scheme for multimaterial flows and its application in chemical reactions," *Journal of Computational Physics*, vol. 163, no. 2, pp. 349–375, 2000.

[87] L. Pan, J. Cheng, S. Wang, and K. Xu, "A two-stage fourth-order gas-kinetic scheme for compressible multicomponent flows," *Communications in Computational Physics*, vol. 22, no. 4, p. 1123–1149, 2017.

[88] B. Todorova and R. Steijl, "Derivation and numerical comparison of Shakhov and Ellipsoidal Statistical kinetic models for a monoatomic gas mixture," *European Journal of Mechanics - B/Fluids*, vol. 76, pp. 390 – 402, 2019.

[89] T. F. Morse, "Kinetic model for gases with internal degrees of freedom," *The Physics of Fluids*, vol. 7, no. 2, pp. 159–169, 1964.

[90] V. A. Rykov, "A model kinetic equation for a gas with rotational degrees of freedom," *Fluid Dynamics*, vol. 10, no. 6, pp. 959–966, 1975.

[91] C. Park, "Assessment of two-temperature kinetic model for ionizing air," *Journal of Thermophysics and Heat Transfer*, vol. 3, no. 3, pp. 233–244, 1989.

[92] S. Kosuge, H. Kuo, and K. Aoki, "A kinetic model for a polyatomic gas with temperature-dependent specific heats and its application to shock-wave structure," *Journal of Statistical Physics*, vol. 177, no. 2, pp. 209–251, 2019.

[93] J. Wu, A. Peng, Z. Li, and X. Jiang, "Kinetic models for thermodynamic non-equilibrium effects of polyatomic gases and preliminary application in gas-kinetic unified algorithm," *AIP Conference Proceedings*, vol. 2132, no. 1, p. 060006, 2019.

[94] P. Ao-Ping, L. Zhi-Hui, W. Jun-Lin, and J. Xin-Yu, "Validation and analysis of gas-kinetic unified algorithm for solving Boltzmann model equation with vibrational energy excitation (in Chinese)," *Acta Physica Sinica*, vol. 66, no. 20, p. 204703, 2017.

[95] V. Titarev and A. Frolova, "Application of model kinetic equations to calculations of super- and hypersonic molecular gas flows," *Fluid Dynamics*, vol. 53, no. 4, pp. 536–551, 2018.

[96] J. Mathiaud and L. Mieussens, "BGK and Fokker-Planck models of the Boltzmann equation for gases with discrete levels of vibrational energy," *Journal of Statistical Physics*, 2020.

[97] C. Baranger, Y. Dauvois, G. Marois, J. Mathé, J. Mathiaud, and L. Mieussens, "A BGK model for high temperature rarefied gas flows," *European Journal of Mechanics - B/Fluids*, vol. 80, pp. 1 – 12, 2020.

[98] C. Klingenberg, M. Pirner, and G. Puppo, "A consistent kinetic model for a two-component mixture of polyatomic molecules," *Communications in Mathematical Sciences*, vol. 17, no. 1, pp. 149 – 173, 2019.

[99] F. Bernard, A. Iollo, and G. Puppo, "BGK Polyatomic Model for Rarefied Flows," *Journal of Scientific Computing, Springer Verlag*, vol. 78, no. 3, pp. 1893 – 1916, 2019.

[100] M. Bisi and M. J. Cáceres, "A BGK relaxation model for polyatomic gas mixtures," *Communications in Mathematical Sciences*, vol. 14, pp. 297–325, 2016.

[101] M. Bisi, R. Monaco, and A. J. Soares, "A BGK model for reactive mixtures of polyatomic gases with continuous internal energy," *Journal of Physics A*, vol. 51, p. 125501, 2018.

[102] M. Bisi and G. Spiga, "Hydrodynamic limits of kinetic equations for polyatomic and reactive gases," *Communications in Applied and Industrial Mathematics*, vol. 8, no. 1, pp. 23 – 42, 2017.

[103] M. Bisi and R. Travaglini, "A BGK model for mixtures of monoatomic and polyatomic gases with discrete internal energy," *Physica A: Statistical Mechanics and its Applications*, vol. 547, p. 124441, 2020.

[104] A. B. Huang, P. F. Hwang, D. P. Giddens, and R. Srinivasan, "High-speed leading edge problem," *The Physics of Fluids*, vol. 16, no. 6, pp. 814–824, 1973.

[105] C. Tantos, D. Valougeorgis, and A. Frezzotti, "Conductive heat transfer in rarefied polyatomic gases confined between parallel plates via various kinetic models and the DSMC method," *International Journal of Heat and Mass Transfer*, vol. 88, pp. 636 – 651, 2015.

[106] C. Tantos, G. P. Ghiroldi, D. Valougeorgis, and A. Frezzotti, "Effect of vibrational degrees of freedom on the heat transfer in polyatomic gases confined between parallel plates," *International Journal of Heat and Mass Transfer*, vol. 102, pp. 162 – 173, 2016.

[107] I. Larina and V. Rykov, "Kinetic model of the Boltzmann equation for a diatomic gas with rotational degrees of freedom," *Computational Mathematics and Mathematical Physics*, vol. 50, no. 12, pp. 2118–2130, 2010.

[108] V. Rykov, V. Titarev, and E. Shakhov, "Shock wave structure in a diatomic gas based on a kinetic model," *Fluid Dynamics*, vol. 43, no. 2, pp. 316–326, 2008.

[109] K. Xu, X. He, and C. Cai, "Multiple temperature kinetic model and gas-kinetic method for hypersonic non-equilibrium flow computations," *Journal of Computational Physics*, vol. 227, no. 14, pp. 6779 – 6794, 2008.

[110] G. Cao, H. Liu, and K. Xu, "Physical modeling and numerical studies of three-dimensional non-equilibrium multi-temperature flows," *Physics of Fluids*, vol. 30, no. 12, p. 126104, 2018.

[111] B. N. Todorova, C. White, and R. Steijl, "Discrete-velocity simulations of high-speed flows based on binary gas mixture kinetic models," *AIP Conference Proceedings*, vol. 2132, no. 1, p. 060009, 2019.

[112] B. N. Todorova, C. White, and R. Steijl, "Numerical evaluation of novel kinetic models for binary gas mixture flows," *Physics of Fluids*, vol. 32, no. 1, p. 016102, 2020.

[113] B. N. Todorova, C. White, and R. Steijl, "Modelling of nitrogen and oxygen gas mixture with a novel diatomic kinetic model," *Physics of Fluids (under review)*, 2020.

[114] E. Goldman and L. Sirovich, "The structure of shock-waves in gas mixtures," *Journal of Fluid Mechanics*, vol. 35, no. 3, pp. 575–597, 1969.

[115] F. S. Sherman, "Shock-wave structure in binary mixtures of chemically inert perfect gases," *Journal of Fluid Mechanics*, vol. 8, no. 3, pp. 465–480, 1960.

[116] P. Andries and B. Perthame, "The ES-BGK model equation with correct Prandtl number," *AIP Conference Proceedings*, vol. 585, no. 1, pp. 30–36, 2001.

[117] S. Weissman and E. A. Mason, "Determination of gaseous-diffusion coefficients from viscosity measurements," *The Journal of Chemical Physics*, vol. 37, no. 6, pp. 1289–1300, 1962.

[118] R. Steijl and G. Barakos, "Coupled Navier–Stokes/molecular dynamics simulations in nonperiodic domains based on particle forcing," *International Journal for Numerical Methods in Fluids*, vol. 69, no. 8, pp. 1326–1349, 2012.

[119] G. A. Bird, "Definition of mean free path for real gases," *The Physics of Fluids*, vol. 26, no. 11, pp. 3222–3223, 1983.

[120] C. K. Chu, "Kinetic-theoretic description of the formation of a shock wave," *The Physics of Fluids*, vol. 8, no. 1, pp. 12–22, 1965.

[121] H. Alsmeyer, "Density profiles in argon and nitrogen shock waves measured by the absorption of an electron beam," *Journal of Fluid Mechanics*, vol. 74, no. 3, p. 497–513, 1976.

[122] S. Liu, Y. Yang, and C. Zhong, "An extended gas-kinetic scheme for shock structure calculations," *Journal of Computational Physics*, vol. 390, pp. 1 – 24, 2019.

[123] C. D. Wilson, R. K. Agarwal, and F. G. Tcheremissine, "Computation of hypersonic shock waves in inert gas mixtures using the Generalized Boltzmann equation," *AIP Conference Proceedings*, vol. 1333, no. 1, pp. 152–157, 2011.

[124] C. White, M. Borg, T. Scanlon, S. Longshaw, B. John, D. Emerson, and J. Reese, "dsmcFoam+: An OpenFOAM based direct simulation Monte Carlo solver," *Computer Physics Communications*, vol. 224, pp. 22 – 43, 2018.

[125] V. M. Zhdanov, "The kinetic theory of a polyatomic gas," *Journal of Experimental and Theoretical Physics*, vol. 26, no. 6, pp. 1187–1191, 1968.

[126] B. Sharma and R. Kumar, "Estimation of bulk viscosity of dilute gases using a nonequilibrium molecular dynamics approach," *Physical Review E*, vol. 100, p. 013309, Jul 2019.

[127] G. Emanuel, "Bulk viscosity in the Navier–Stokes equations," *International Journal of Engineering Science*, vol. 36, no. 11, pp. 1313 – 1323, 1998.

[128] K. Xu and E. Josyula, "Continuum formulation for non-equilibrium shock structure calculation," *Communications in Computational Physics*, vol. 1, no. 3, pp. 425–448, 2006.

[129] J. G. Parker, "Rotational and vibrational relaxation in diatomic gases," *The Physics of Fluids*, vol. 2, no. 4, pp. 449–462, 1959.

[130] P. Valentini, C. Zhang, and T. E. Schwartzentruber, "Molecular dynamics simulation of rotational relaxation in nitrogen: Implications for rotational collision number models," *Physics of Fluids*, vol. 24, no. 10, p. 106101, 2012.